Hyperfine Interactions 123/124 (1999) 127–274

Coherent γ-ray optics

J.P. Hannon and G.T. Trammell

Physics Department, Rice University, Houston, TX 77005-1892, USA

With the advent of high brightness synchrotron radiation sources, an important new field has been opened up involving *coherent* nuclear excitations induced by synchrotron radiation *pulses* traversing a piece of matter. We review the theory of coherent resonant γ-ray optics, including some of the interesting new phenomena which occur when systems of nuclei are excited by synchrotron radiation pulses, such as the creation of nuclear exciton states, superradiant and subradiant decay, spatially coherent quantum beats, and temporal Pendellösung. We also discuss the relation between the nuclear exciton states and multi-photon Dicke superradiance and γ-ray lasers, and comment on neutron phasors and neutron superradiance in resonant neutron optics. The interesting features of coherent enhancement, superradiant decay, and dynamical beats are discussed from the fundamental perspective of the radiative normal modes of a system of nuclear resonators.

AMS subject classification: PACS numbers: 73.20.Hb, 31.50.+w, 79.20.Rf, 79.20.-m

1. Introduction

For most Mössbauer transitions, the γ-ray wavelength ($\lambda_0 \approx 0.1$–1.0 Å) is well suited for diffraction experiments. Tuned to resonance, the scattering amplitude f is proportional to λ_0, and can be very large, $\approx 400 r_0$ for the 14.4 keV ^{57}Fe transition. The linewidths are exceedingly sharp ($\approx 10^{-9}$–10^{-6} eV), allowing the easy variation of the phase and amplitude of the resonantly scattered wave by Doppler shifting, with negligible variation of the nonresonant electronically scattered wave. Correspondingly, the time response of the resonant nuclear scattering is very long, $\approx 10^{-9}$–10^{-6} s (compared to $\approx 10^{-15}$ s for a 1 eV width atomic resonance, and $\approx 10^{-14}$ s for characteristic crystal vibration times). The signal emitted by a "nuclear oscillator" over a duration of $\tau \approx 10^{-7}$ s has a longitudinal coherence length $l_c \approx c\tau \approx 30$ m, or a "quality factor" $Q \approx 10^{12}$, the number of perfectly spaced radiation crests in the signal, comparable to the highest precision optical lasers. In magnetic crystals, and in the presence of crystal electric fields, there is hyperfine splitting of the nuclear resonances, and the amplitude and polarization of the resonantly scattered photons are strongly dependent upon the directions of the local fields. Mössbauer transitions also occur with well-defined multipolarity E1, M1, E2 (and in a few cases M1–E2), in contrast to the electronic response of atoms which occurs as a hierarchy of multipole contributions E1 $\gg$ E2 $\gg$ M1, etc. These unique features – large scattering amplitudes, the long scattering time, the sharp variation with frequency near resonance, the sensitivity to crystalline electric

and magnetic fields, and the well defined multipolarities – give rise to important applications for chemical and magnetic structure determinations, new possibilities for long coherence length X-ray interferometry, time-resolved spectroscopy on the nanosecond scale, and interesting optical effects such as strong Faraday-type effects and higher multipole Borrmann effects.

Because of the low brightness of most radioactive Mössbauer sources, however, until recently nearly all Mössbauer experiments involved only resonance absorption, which, while valuable, does not exhibit to the fullest the interesting effects due to coherence in the emission or scattering of γ-rays from a system of nuclei. This situation has changed dramatically with the advent of high brightness synchrotron radiation sources, and an active field of coherent γ-ray optics utilizing nuclear excitation by synchrotron radiation pulses has emerged.

We review the theory of coherent resonant γ-ray optics, and discuss some of the interesting new phenomena which occur when systems of nuclei are excited by synchrotron radiation pulses, such as the creation of nuclear exciton states, superradiant and subradiant decay, spatially coherent quantum beats, and temporal Pendellösung. We also discuss the relation between the nuclear exciton states and multi-photon Dicke superradiance and γ-ray lasers, and comment on neutron phasors and neutron superradiance in resonant neutron optics. In the final section, we discuss one of the most unique and fundamental aspects of Mössbauer γ-ray optics – collective nuclear states established by the radiative interaction between the nuclei.

2. Simple features of resonant γ-ray scattering

In this section we discuss some of the simple features of resonant nuclear scattering, and make comparisons with atomic X-ray scattering.

2.1. Atomic scattering

The usual X-ray scattering from an atom consists of three contributions: the direct A^2 interaction, which gives the "free electron" Thomson scattering f_0, and two virtual excitation/deexcitation diagrams (with photon absorption preceding or following emission), which give the "anomalous scattering" $f' + \mathrm{i}f''$,

$$f_{\mathrm{e}} = -\frac{Ze^2}{m_{\mathrm{e}}c^2}F(\theta) + \sum_n \frac{\lambda\!\!\!^{-}_0 \Gamma_{\mathrm{R}}}{(E_n - E_0) - \hbar\omega - \mathrm{i}\Gamma_{\mathrm{T}}/2} + \sum_n \frac{\lambda\!\!\!^{-}_0 \Gamma_{\mathrm{R}}}{(E_n - E_0) + \hbar\omega}$$
$$= f_0 + \left(f' + \mathrm{i}f''\right). \tag{2.1}$$

These contributions are indicated schematically in figure 1.

In the anomalous dispersion contribution, $\Gamma_{\mathrm{R}}/\hbar$ is the rate for the radiative decay $\psi_{\mathrm{n}} \rightarrow \psi_0$, with Γ_{R} proportional to the square of the electric dipole moment, $\Gamma_{\mathrm{R}} \propto |\langle\psi_{\mathrm{n}}|x|\psi_0\rangle|^2$, and $\Gamma_{\mathrm{T}}/\hbar$ is the total decay rate of the intermediate excited state ψ_{n} due to all possible radiative and nonradiative decay processes (such as the Auger emission

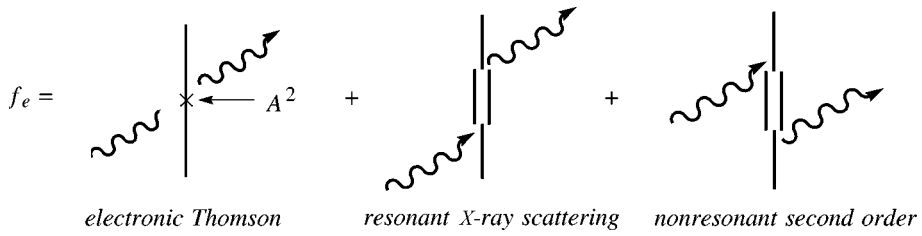

Figure 1. X-ray scattering contributions.

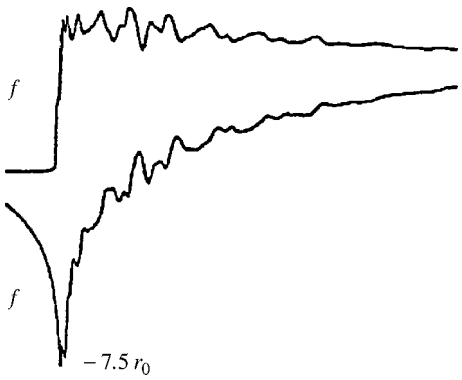

Figure 2. Cu K-edge.

process, in which the excitation energy of ψ_n is transferred via the Coulomb interaction to an outer electron which is ejected into the continuum). Typically, $\Gamma_R \approx 0.01$–0.1 eV, while $\Gamma_T \approx 1$–10 eV. (For simplicity, we have omitted the polarization dependence, and a statistical/angular momentum factor ≈ 1. Also, λ_0 is the resonance wavelength and $\lambda\!\!\!^{-}_0 \equiv \lambda_0/2\pi$.)

The Thomson scattering $f_0 \approx Zr_0$, where $r_0 = e^2/m_e c^2$ is the "classical electron radius", while the resonant contribution to the anomalous scattering has a peak amplitude $\approx \lambda\!\!\!^{-}_0(\Gamma_R/\Gamma_T)$, which, as for any resonant scattering, is independent of r_0, and instead is determined entirely by the resonance wavelength λ_0 and the branching ratio Γ_R/Γ_T. Typically $\Gamma_R/\Gamma_T \approx 10^{-3}$–$10^{-2}$, while $\lambda\!\!\!^{-}_0/r_0 \approx 5 \times 10^3$ for 1 Å radiation, so that the peak value of $(f' + \mathrm{i}f'') \approx 1 - 10r_0$ near an absorption edge. Since there is a "continuum" of resonators above the absorption edge, rather than a sharp resonance response, $(f' + \mathrm{i}f'')$ exhibits a "distributed" resonance response, spread over 10–100 eV, such as the well-known Cu K-edge spectrum shown in figure 2.

2.2. Nuclear scattering

The scattering of a photon by a nucleus is determined by the same three diagrams, where the A^2 interaction is now for the protons of the nucleus, and the ψ_n are the

virtual excited states of the nucleus, so again

$$f_{\rm n} = -\frac{Ze^2}{m_{\rm p}c^2} + \sum_n \frac{\lambda\!\!\!^{-}_0 \Gamma_\gamma}{(E_n - E_0) - \hbar\omega - {\rm i}\Gamma/2} + \sum_n \frac{\lambda\!\!\!^{-}_0 \Gamma_\gamma}{(E_n - E_0) + \hbar\omega}, \qquad (2.2)$$

where the first term is the nuclear Thomson scattering, the second term is the resonant γ-ray scattering, and the third term is the nonresonant second order contribution. For nuclear scattering, we use the notation $\Gamma_{\rm R} \equiv \Gamma_\gamma$ and $\Gamma_{\rm T} \equiv \Gamma$.

Now, however, the relative magnitude of the three contributions and the nature of the response are very different from the atomic scattering for two reasons: First, the nuclear Thomson scattering involves the proton mass $m_{\rm p}$ rather than the electron mass $m_{\rm e}$, and hence, is down by $m_{\rm e}/m_{\rm p} \approx 1/2000$, so the nuclear Thomson scattering is typically $\approx 0.01 r_0$ and can usually be ignored. Secondly, the nuclear resonances are dramatically sharper than the atomic resonances, typically, $\Gamma \approx 10^{-8}$ eV (and $\Gamma_\gamma \approx 10^{-9}$ eV) in contrast to $\Gamma_{\rm T} \approx$ 1–10 eV for atomic excited states. As a consequence, there is no appreciable scattering from the nucleus unless the incident photon energy is tuned to within a few widths $\Gamma \approx 10^{-8}$ eV of a nuclear resonance, in which case

$$f_{\rm n} \approx \lambda\!\!\!^{-}_0 \frac{\Gamma_\gamma}{\Gamma} \frac{1}{(x - {\rm i})},$$

where $x = [(E_n - E_0) - \hbar\omega]/(\Gamma/2)$ is the deviation from resonance in units of the halfwidth. At resonance, the scattering amplitude peaks to

$$f_{\rm n} \approx {\rm i}\lambda\!\!\!^{-}_0 \frac{\Gamma_\gamma}{\Gamma},$$

which can be very large. For the 14.4 keV ^{57}Fe transition, $\Gamma_\gamma/\Gamma \approx 1/9$, and $|f_{\rm n}| \approx 440 r_0$ at resonance!

Also, in contrast to the continuum distribution of oscillators above an atomic absorption edge, the nuclear excited states $\psi_{\rm n}$ are separated by 10's or 100's of keV. As a consequence, the nuclear scattering exhibits a strikingly simple Lorentzian response, with $f''_{\rm n} = \lambda\!\!\!^{-}_0(\Gamma_\gamma/\Gamma)/(x^2+1)$ peaking to $\lambda\!\!\!^{-}_0(\Gamma_\gamma/\Gamma) \approx 440 r_0$ at resonance, and $f'_{\rm n} = \lambda\!\!\!^{-}_0(\Gamma_\gamma/\Gamma)x/(x^2+1)$ varying from $+220 r_0$ to $-220 r_0$ as $\hbar\omega$ is tuned from $-\Gamma/2 \rightarrow +\Gamma/2$ about resonance, as shown in figure 3.

The narrow linewidths ($\approx 10^{-9}$–10^{-6} eV) allow the easy variation of the phase and amplitude of the resonantly scattered wave by Doppler shifting, with negligible variation of the electronic scattering amplitude $f_{\rm e}$.

Complementary to the exceedingly sharp frequency response, the time response of the resonant nuclear scattering is very slow, $\tau \approx 10^{-9}$–10^{-6} s (compared to $\approx 10^{-15}$ s for a 1 eV width atomic resonance, and $\approx 10^{-14}$ s for characteristic crystal vibration times). The signal emitted by a "nuclear oscillator" over a duration of $\tau \approx 10^{-7}$ s has a longitudinal coherence length $l_{\rm c} = c\tau \approx 30$ m, or a "quality factor" $Q \approx 10^{12}$, the number of perfectly spaced radiation crests in the signal, comparable to that of the highest precision optical lasers.

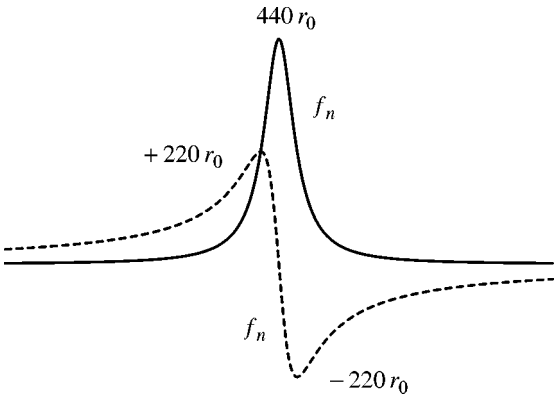

Figure 3. Lorentzian response of ^{57}Fe.

The striking difference in the sharpness of a nuclear γ-ray resonance compared to an atomic X-ray resonance is primarily a size effect:

$$\Gamma_{\mathrm{R}} \propto \left|\langle\psi_{\mathrm{n}}|x|\psi_0\rangle\right|^2 \propto (\text{radius})^2,$$

and thus,

$$\frac{\Gamma_{\mathrm{R}}(\text{nucleus})}{\Gamma_{\mathrm{R}}(\text{atom})} \approx \left(\frac{R(\text{nucleus})}{R(\text{atom})}\right)^2 \approx 10^{-8}.$$

That is, the dipole moment for a nuclear transition is about four orders of magnitude smaller than that for an atomic transition, leading to a radiative decay rate eight orders of magnitude smaller.

In magnetic crystals, and in the presence of crystal electric fields, there is hyperfine splitting of the nuclear resonances, and the amplitude and polarization of the resonantly scattered photons are strongly dependent upon the directions of the local fields. Mössbauer transitions also occur with well-defined multipolarity E1, M1, E2 (and in a few cases, M1–E2), in contrast to the electronic response of atoms, which occurs as a hierarchy of multipole contributions E1 $\gg$ E2 $\gg$ M1, etc.

The best known Mössbauer resonance is the 14.4 keV ($\lambda_0 = 0.86$ Å) transition of ^{57}Fe, indicated schematically in figure 4. This is an M1 transition from a ground state $j_0 = 1/2$ to an excited state $j_1 = 3/2$. The lifetime of the excited state is $\tau = \hbar/\Gamma = 141$ ns. In a magnetic material the spin polarized 3d electrons induce, via exchange, a net spin polarization of the s-electron density at the nucleus, which, by the Fermi contact interaction, gives a strong magnetic field at the nucleus, $B_{\mathrm{int}} \approx$ 30–40 T, resulting in Zeeman splitting of the ground and excited levels, $\Delta E(m_j) = -m_j\gamma_j B_{\mathrm{int}}$. In α-Fe, $B_{\mathrm{int}} = 32.2$ T and $j\gamma_j = 0.09\mu_{\mathrm{N}}$ and $-0.15\mu_{\mathrm{N}}$ ($\mu_{\mathrm{N}} =$ nuclear magneton), respectively for the ground and excited states, so the separation between levels is $g_0 = 39.7\Gamma$ for the ground state, and $g_1 = 22.4\Gamma$ for the excited state. Since the transition is M1, the selection rule is $\Delta j_z = 0, \pm 1$, and there are six allowed transitions. In the presence of crystal fields, the coupling of the

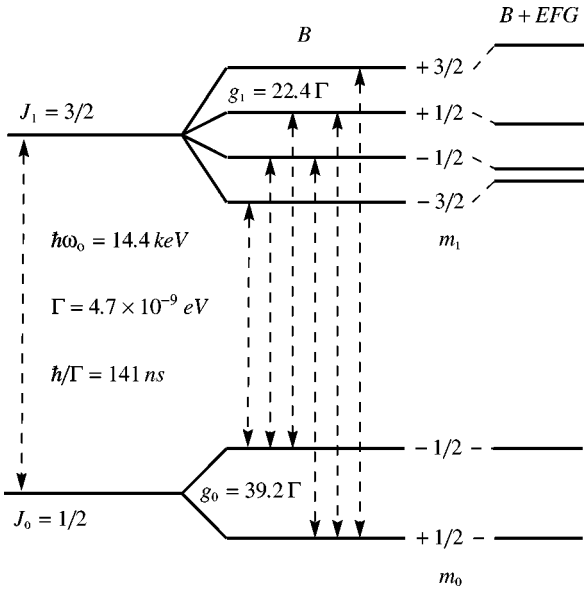

Figure 4. ^{57}Fe Mössbauer transition.

Figure 5. Decay from an excited nucleus.

quadrupole moment of the nucleus in the state ψ_n to the electric field gradient (EFG) gives an additional shift to the nuclear levels, typically on the order of 10–20Γ. The coherent elastic scattering amplitude f_n is then a superposition of six sharp resonance contributions, the separation between the resonances being typically on the order of 20–40Γ.

In an excited state ψ_n, a nucleus will decay via radiative decay (at the rate $\Gamma_\gamma/\hbar$), or more likely, by internal conversion decay (at the rate $\Gamma_\alpha/\hbar$), which is the direct analogue of Auger decay: the excitation energy of ψ_n is transferred via the Coulomb interaction to an outer electron, which is ejected into the continuum, as indicated in figure 5. The total decay width is $\Gamma = \Gamma_\gamma + \Gamma_\alpha$. For the 14.4 keV level of ^{57}Fe, $\Gamma_\alpha/\Gamma_\gamma \approx 8$ so that an *isolated* excited nucleus is eight times more likely to give up its energy via conversion. However, for a collection of nuclei, as we will discuss in section 4.1, the probability for radiative decay can be greatly enhanced by spatial coherence.

2.3. Fast versus slow scattering

The effect of zero point motion and temperature motion of a scatterer bound in a solid on the X-ray or γ-ray coherent elastic scattering amplitude f depends on whether the collision time is short or long relative to the characteristic vibration time, ω_m^{-1} ($\approx 10^{-14}$–10^{-13} s), of the scatterer about its mean position.

For nonresonant Thomson scattering, the A^2 scattering is "instantaneous", and the scattering amplitude f_0 will contain the factor $\exp[-\mathrm{i}(\mathbf{k}_\mathrm{f} - \mathbf{k}_0)\cdot\mathbf{r}]$, where $\mathbf{r}$ is the position of the nucleus of the scatterer relative to its mean position. When averaged over a Gibbs ensemble this gives the Debye–Waller factor

$$f_\mathrm{D}(\theta) = \big\langle \exp\big[-\mathrm{i}(\mathbf{k}_\mathrm{f} - \mathbf{k}_0)\cdot\mathbf{r}\big]\big\rangle = \exp\left[-\frac{1}{2}\big\langle\big[(\mathbf{k}_\mathrm{f} - \mathbf{k}_0)\cdot\mathbf{r}\big]^2\big\rangle\right]. \tag{2.3}$$

For resonant scattering, the coherent elastic scattering amplitude can be put in the time-dependent representation [1],

$$f_\mathrm{res} = \left(\frac{\Gamma_\gamma}{2\mathrm{i}k}\right)\int_0^\infty \mathrm{d}t\, \mathrm{e}^{\mathrm{i}(\omega-\omega_0)t}\mathrm{e}^{-(\Gamma/2\hbar)t}\big\langle \mathrm{e}^{-\mathrm{i}\mathbf{k}_\mathrm{f}\cdot\mathbf{r}(t)}\mathrm{e}^{\mathrm{i}\mathbf{k}_0\cdot\mathbf{r}(0)}\big\rangle, \tag{2.4}$$

where $\mathbf{r}(t)$ is the nuclear center of mass operator in the Heisenberg representation.

For resonant X-ray scattering, the characteristic scattering times are $\hbar/\Gamma \approx 10^{-16}$–$10^{-15}$ s and, hence, *fast* compared to ω_m^{-1}. Then effectively $t \approx 0$, which gives the Debye–Waller factor

$$\big\langle \exp\big[-\mathrm{i}\mathbf{k}_\mathrm{f}\cdot\mathbf{r}(t\approx 0)\big]\exp\big[\mathrm{i}\mathbf{k}_0\cdot\mathbf{r}(0)\big]\big\rangle \approx f_\mathrm{D}(\theta). \tag{2.5}$$

On the other hand, for Mössbauer resonances, the scattering is very *slow*, $\hbar/\Gamma \approx 10^{-9}$–$10^{-6}$ s $\gg \omega_m^{-1}$, so that effectively $t \approx \infty$ and the motions $\mathbf{r}(\infty)$ and $\mathbf{r}(0)$ are uncorrelated, giving the Lamb–Mössbauer factor

$$\big\langle \exp\big[-\mathrm{i}\mathbf{k}_\mathrm{f}\cdot\mathbf{r}(t\approx\infty)\big]\exp\big[\mathrm{i}\mathbf{k}_0\cdot\mathbf{r}(0)\big]\big\rangle \approx \big\langle \exp\big[-\mathrm{i}\mathbf{k}_\mathrm{f}\cdot\mathbf{r}\big]\big\rangle\big\langle \exp[\mathrm{i}\mathbf{k}_0\cdot\mathbf{r}]\big\rangle = f_\mathrm{M}. \tag{2.6}$$

Interesting cases of intermediate scattering times $\approx \omega_m^{-1}$ can occur for neutron resonance scattering as discussed in section 5.

2.4. Polarization response of resonant scattering

The nonresonant Thomson scattering has a simple $\mathbf{e}_\mathrm{f}^*\cdot\mathbf{e}_0$ polarization dependence, so there is no orthogonal $\hat{\sigma} \leftrightarrow \hat{\pi}$ scattering, and no sensitivity to local fields. On the other hand, resonant X-ray and γ-ray scattering is generally sensitive to the directions of the local fields (**B** and EFG axis) at the scatterer, and as a consequence, the scattering necessarily has a strong tensor component in the polarization response (giving, e.g., strong orthogonal scattering).

For a pure QL multipole transition (2^L – pole electric (Q = E) or magnetic (Q = M) multipole; thus, E1 = electric dipole, etc.), with quantization axis $\mathbf{z}_J$ (for

simplicity, we assume J_z is a good quantum number), the coherent elastic scattering amplitude is [2–7] (see appendices A.1 and A.2)

$$f_{\rm n}(\mathbf{e}_{\rm f}\mathbf{k}_{\rm f};\mathbf{e}_0\mathbf{k}_0) = 4\pi\lambda\bar{} \sum_{M=-L}^{L} \left[\mathbf{e}_{\rm f}^{*}\cdot\mathbf{Y}_{LM}^{(q)}\left(\hat{k}_{\rm f}\right)\mathbf{Y}_{LM}^{(q)}\left(\hat{k}_0\right)^{*}\cdot\mathbf{e}_0\right]F_{LM}^{(q)}, \tag{2.7}$$

where

$$F_{LM}^{(q)} = \frac{f_{\rm M}}{(2j_0+1)}\frac{\Gamma_\gamma}{\Gamma}\sum_{m_0=-j_0}^{j_0}\frac{C(j_0Lj_1;m_0M)^2}{x(m_0M)-{\rm i}}. \tag{2.8}$$

The $\mathbf{Y}_{LM}^{(q)}$ with $q = e$ or m are the vector spherical harmonics [8], $x(m_0M) = 2\,[\,E(j_1;m_0+M) - E(j_0;m_0) - \hbar\omega]/\Gamma$ and $f_{\rm M}$ is the Lamb–Mössbauer factor, m_0 runs over the $(2j_0+1)$ hyperfine levels of the ground state, and M gives the ΔJ_z change $(m_1 - m_0)$. The scattering amplitude is a coherent superposition of resonances, such as the six allowed transitions for ^{57}Fe.

For a $\Delta J_z = M$ resonance line of a qL-multipole transition, the polarization response

$$\mathbf{e}_{\rm f}^{*}\cdot\mathbf{Y}_{LM}^{(q)}\left(\hat{k}_{\rm f}\right)\mathbf{Y}_{LM}^{(q)}\left(\hat{k}_0\right)^{*}\cdot\mathbf{e}_0 \tag{2.9}$$

is precisely the polarization response of a qL, $\Delta J_z = M$ *classical oscillator*. For example, for an E1 transition, there are three types of oscillators: $M = 0$ which is a *linear* electric dipole oscillation along the quantization axis $\mathbf{z}_J$, $M = +1$ is a *right-hand circular* oscillation about the $+\mathbf{z}_J$ axis, and $M = -1$ is a *left-hand circular* oscillation about $\mathbf{z}_J$. If the resonances are well separated ($\Delta\Omega \gg \Gamma$), then there is necessarily strong orthogonal scattering and a strong dependence on the direction of the local fields ($\mathbf{z}_J$). For example (see figure 6), tuning in to an $M = +1$, E1 resonance, regardless of the incident polarization (as long as $\mathbf{e}_0$ drives the oscillator), the scattered radiation will be RH circular for $\mathbf{k}_{\rm f}$ in the direction $+\mathbf{z}_J$, LH circular in the $-\mathbf{z}_J$ direction, linear for $\mathbf{k}_{\rm f} \perp \mathbf{z}_J$, and elliptical for all other directions; and the whole pattern will rotate with $\mathbf{z}_J$ if the direction of $\mathbf{z}_J$ is changed.

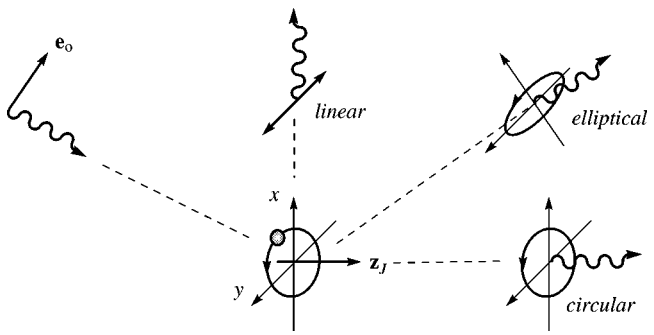

Figure 6. $M = +1$ electric dipole oscillator.

The overall form of the polarization response is dictated by symmetry considerations and can depend only on $\mathbf{e}_0$, $\mathbf{k}_0$, $\mathbf{e}_\mathrm{f}^*$, $\mathbf{k}_\mathrm{f}$ and $\mathbf{z}_J$ since these are the only defined directions of the scattering (in the absence of crystal fields). For an E1 transition, the explicit $\mathbf{Y}_{1M}^{(e)}$ expressions give the scattering amplitude [3]

$$f_{\mathrm{E1}} = A_0 \mathbf{e}_\mathrm{f}^* \cdot \mathbf{e}_0 + \mathrm{i}A_1\big(\mathbf{e}_\mathrm{f}^* \times \mathbf{e}_0\big) \cdot \mathbf{z}_J + A_2\big(\mathbf{e}_\mathrm{f}^* \cdot \mathbf{z}_J\big)(\mathbf{e}_0 \cdot \mathbf{z}_J), \tag{2.10}$$

where factors A_0, A_1 and A_2 are combinations of the $F_{1M}^{(e)}$ (see appendix A.2). But the general form can be deduced entirely by symmetry arguments: the lowest order E1 approximation is made by replacing $\exp(\pm\mathrm{i}\mathbf{k}\cdot\mathbf{x}) \rightarrow 1$, and the resonant scattering amplitude f_{E1} is then proportional to $\langle\psi_0|\mathbf{p}\cdot\mathbf{e}_\mathrm{f}^*|\psi_\mathrm{n}\rangle\langle\psi_\mathrm{n}|\mathbf{p}\cdot\mathbf{e}_0|\psi_0\rangle$. Thus, f_{E1} is a *scalar* which is *linear* in the components of $\mathbf{e}_0$ and $\mathbf{e}_\mathrm{f}^*$, and *independent* of $\mathbf{k}_0$ and $\mathbf{k}_\mathrm{f}$. In the absence of crystal fields, the only defined directions which enter into f_{E1} are $\mathbf{e}_0$, $\mathbf{e}_\mathrm{f}^*$ and $\mathbf{z}_J$, the direction of the quantization axis defined by the local moment of the ion, as indicated in figure 7. Thus the distinct polarization responses possible are the various scalar products which can be constructed from $\mathbf{e}_0$, $\mathbf{e}_\mathrm{f}^*$ and $\mathbf{z}_J$, with $\mathbf{e}_0$ and $\mathbf{e}_\mathrm{f}^*$ occurring linearly, and with $\mathbf{z}_J$ allowed to any order. These combinations are simply $\mathbf{e}_\mathrm{f}^* \cdot \mathbf{e}_0$, $\mathrm{i}(\mathbf{e}_\mathrm{f}^* \times \mathbf{e}_0) \cdot \mathbf{z}_J$ and $(\mathbf{e}_\mathrm{f}^* \cdot \mathbf{z}_J)(\mathbf{e}_0 \cdot \mathbf{z}_J)$. In the linear term, the factor i is required for time-reversal invariance.

For a magnetic dipole transition (M1), similar arguments show that the same form holds, but with the E-polarization vector $\mathbf{e}$ replaced by the B-polarization vector $\mathbf{b} = \hat{\mathbf{k}} \times \mathbf{e}$.

For an E2 transition, the scattering amplitude is linear in both $\mathbf{e}$ and $\mathbf{k}$. Thus, for E2 scattering the defined vectors are $\mathbf{e}_0$, $\mathbf{k}_0$, $\mathbf{e}_\mathrm{f}^*$, $\mathbf{k}_\mathrm{f}$ and $\mathbf{z}_J$. The scattering amplitude f_{E2} is a scalar comprised of products of these vectors, with each term linear in $\mathbf{e}_0$, $\mathbf{k}_0$, $\mathbf{e}_\mathrm{f}^*$ and $\mathbf{k}_\mathrm{f}$, and containing $\mathbf{z}_J$ to any order [3–5].

The explicit expressions for the electronic and nuclear contributions f_e and f_n to the elastic scattering amplitude are given in appendices A.1 and A.2 (for E1, M1, E2 and mixed M1–E2 nuclear transitions, assuming good J_z). The modifications of f_n when the electric field gradient (EFG) is noncoaxial with B_{int} are also discussed in appendix A.2.

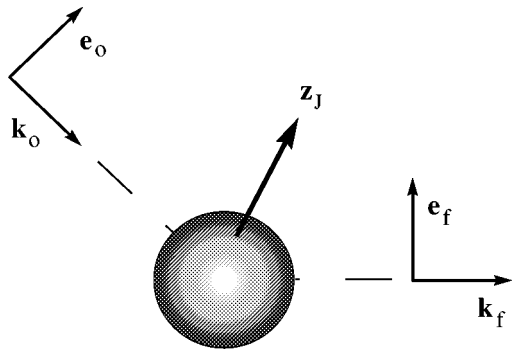

Figure 7. Scattering geometry.

3. Dynamical theory of Mössbauer optics

3.1. Basic equations

The quantum theory of crystal optics is most conveniently developed using the Green-function techniques of quantum electrodynamics [9].[1] Using the simple intuitive Feynman procedures, basic equations are obtained bearing a close formal relation to those of classical optics [10].

For an incident photon [9][2]

$$A^0_\mu(x) = \left[\frac{4\pi\hbar c^2}{2\omega_0}\right]^{1/2} e^0_\mu \exp(-\mathrm{i}\omega_0 t_x + \mathrm{i}\mathbf{k}_0\cdot\mathbf{x}), \tag{3.1}$$

the *induced current* for *coherent elastic scattering* is

$$c^{-1}J_\mu(x) = \int \mathrm{d}^4 y M_{\mu\upsilon}(x,y)A^0_\upsilon(y), \tag{3.2}$$

where $M_{\mu\upsilon}(x,y)$ is the *coherent elastic scattering operator*

$$M_{\mu\upsilon}(x,y) = M_{\mu\upsilon}(\mathbf{x},\mathbf{y},t_x - t_y) = -\frac{\mathrm{i}}{\hbar c^2}\big\langle\langle\varphi_0|T\big[j_\mu(x)j_\upsilon(y)\big]|\varphi_0\rangle\big\rangle. \tag{3.3}$$

Here $j_\mu(x)$ is the Heisenberg current operator, T is the time-ordering operator, φ_0 is the initial Heisenberg state vector for the system, and the outer brackets $\langle\cdots\rangle$ indicate an ensemble average over the initial state of the system φ_0.

The *Feynman photon potential* for the *coherent elastic scattered wave*[3] is then

$$\begin{aligned} A^{\mathrm{s}}_\mu(\mathbf{z};\omega) &= c^{-1}\int \frac{\exp[\mathrm{i}(k|\mathbf{z}-\mathbf{x}|)]}{|\mathbf{z}-\mathbf{x}|} J_\mu(\mathbf{x},\omega)\,\mathrm{d}\mathbf{x}, \\ &= \int\int \frac{\exp[\mathrm{i}(k|\mathbf{z}-\mathbf{x}|)]}{|\mathbf{z}-\mathbf{x}|} M_{\mu\upsilon}(\mathbf{x},\mathbf{y},\omega)A^0_\upsilon(\mathbf{y},\omega)\,\mathrm{d}\mathbf{x}\,\mathrm{d}\mathbf{y}, \end{aligned} \tag{3.4}$$

or in obvious matrix notation

$$A^{\mathrm{s}} = \delta^+ M A^0. \tag{3.5}$$

[1] We make extensive use of the Feynman techniques and nomenclature as given in his book [9].

[2] We use the four-vector conventions of [9]. x, y are four-vectors $(ct_x,\mathbf{x})$, $(ct_y,\mathbf{y})$. Four-vector contractions are denoted as either $kx = (ck_4t_x - \mathbf{k}\cdot\mathbf{x})$ or by repeated indices $A_\mu B_\mu = A_4B_4 - \mathbf{A}\cdot\mathbf{B}$. The four-dimensional gradient operator used later is $\partial\mu = [(1/c)(\partial/\partial t), -\nabla]$.

[3] As we have discussed in [10], at large distances from the source the "Feynman potential" is $\mathbf{A}_\perp(\mathbf{x},t) = \langle 0|\hat{\mathbf{A}}_\perp(\mathbf{x})|\psi(t)\rangle$, where $\hat{\mathbf{A}}_\perp(\mathbf{x})$ is the usual transverse vector potential operator at the point $\mathbf{x}$, $|\psi(t)\rangle$ represents the electromagnetic field state vector at t, and $|0\rangle$ represents the vacuum state. More generally, the "Feynman potential" is a photon Green's function as discussed in [10, appendix A]. Our treatment and nomenclature are designed to maintain a close correspondence with the conventional semiclassical treatment of X-ray optics.

Here the index ω indicates the Fourier transform. For coherent elastic scattering, the final state of the system is unchanged, $\varphi_{\mathrm{f}} = \varphi_0$, and consequently, A^{s} is *coherent* with the primary wave A^0. The *total Feynman potential* at z is then

$$A_\mu(z) = A^0_\mu(z) + A^{\mathrm{s}}_\mu(z). \tag{3.6}$$

The Feynman potential may be used to compute the scattering cross-section in the following manner: at large distances from the scatterer the expected energy flux is given by

$$\mathbf{S} = \frac{c}{2\pi}\mathrm{Re}\big(\mathbf{E} \times \mathbf{B}^*\big), \tag{3.7}$$

where **E** and **B** are computed from the potential $A^s_\mu(z)$ in the usual manner. The quantum flux is $(\hbar\omega)^{-1}\mathbf{S}$. Dividing by the incident quantum flux, the *coherent elastic scattering cross-section* is

$$\frac{\mathrm{d}\sigma}{\mathrm{d}\Omega} = \lim_{R\to\infty} \frac{R^2|\mathbf{A}^s_\perp(\mathbf{z};\omega_0)|^2}{|\mathbf{a}^0_\perp|^2}. \tag{3.8}$$

We have assumed an incident photon of well-defined energy $\hbar\omega_0$. However, if the incident wave packet is a *time varying signal*,

$$A^0_\mu(z) = \int A^0_\mu(\mathbf{z},\omega)\mathrm{e}^{-\mathrm{i}\omega t_z}\,\mathrm{d}\omega, \tag{3.9}$$

then the *time-dependent* coherent elastic *scattered wave packet* is

$$A^{\mathrm{s}}_\mu(z) = \int A^{\mathrm{s}}_\mu(\mathbf{z},\omega)\mathrm{e}^{-\mathrm{i}\omega t_z}\,\mathrm{d}\omega. \tag{3.10}$$

For time-dependent scattering, the *expected flux* (probability/cm^2/s) for a photon at $(\mathbf{z}, t)$ is

$$n(\mathbf{z},t) = \frac{\omega_0}{2\pi\hbar c}\big|\mathbf{A}_\perp(\mathbf{z},t)\big|^2, \tag{3.11}$$

where ω_0 is now the central resonance frequency of the Mössbauer transition, and the *frequency spectrum* (probability/cm^2/unit frequency interval) for a photon at $(\mathbf{z},\omega)$ is

$$n(\mathbf{z},\omega) = \frac{\omega_0}{4\pi^2\hbar c}\big|\mathbf{A}_\perp(\mathbf{z},\omega)\big|^2. \tag{3.12}$$

As discussed in [10], for scattering from a *single atom*, the scattering matrix M includes all internal processes involving virtual photon exchange, e.g., radiative reaction, virtual internal conversion, virtual photoelectric and Auger absorption, etc. When calculated exactly, M gives all contributions for the coherent elastic scattering amplitude f for the atom.

Similarly, for scattering from a *multiatom system*, in addition to the complete radiative processes for each atom, M now also includes all possible virtual photon exchanges between atoms, and the resulting coherent elastic scattered wave A^{s} includes

all possible single and multiple scattering processes which leave the final state of the system unchanged, $\varphi_{\rm f} = \varphi_0$.

The basic problem for coherent X-ray and γ-ray optics is to obtain the coherent elastic scattering operator M for the system. As discussed in the following section, the scattering operator M can be developed in terms of single atom scattering operators leading to simple multiple scattering equations which determine the coherent elastic wave.

3.2. Multiple scattering equations

The scattering amplitude f for resonant X-ray or γ-ray optics gives strong tensor scattering (e.g., $\sigma \leftrightarrow \pi$). The appropriate dynamical theory to handle this complication has already been developed in connection with Mössbauer optics, and can be taken over intact for resonant X-ray optics.

The multiple scattering equations for X-ray or γ-ray optics are developed in terms of the scattering operators M^j of the individual atoms. In terms of M^j, the coherent elastic scattering amplitude $f^j(\mathbf{k}_{\rm f}\mathbf{e}_{\rm f};\mathbf{k}_0\mathbf{e}_0)$ for atom j to scatter an incident $|\mathbf{k}_0\mathbf{e}_0\rangle$ photon into a $|\mathbf{k}_{\rm f}\mathbf{e}_{\rm f}\rangle$ photon is given by (see [10])

$$f^j(\mathbf{k}_{\rm f},\mathbf{e}_{\rm f};\mathbf{k}_0,\mathbf{e}_0) = f^j_{\rm e} + f^j_{\rm n} = \left(\mathbf{e}^*_{\rm f}\right)_\mu \cdot M^j_{\mu\upsilon}(\mathbf{k}_{\rm f},\mathbf{k}_0;\omega)\cdot(\mathbf{e}_0)_\upsilon, \tag{3.13}$$

including all atomic and nuclear scattering processes. For an arbitrary incident field A^j, M^j determines the scattering response of the jth atom, i.e., the coupling to the incident wave, and the amplitude and polarization of the scattered photon. As noted, this response can be quite complex, depending on the direction of incidence, the polarization and frequency of the incident photon, the direction and time-dependence of the local fields, and the direction of the scattered photon.

For a system of scatterers, a simple set of multiple scattering equations determine the coherent elastic wave (see [10])

$$A_\mu(\mathbf{z},\omega) = A^0_\mu(\mathbf{z},\omega) + \sum_i \frac{\exp(\mathrm{i}k|\mathbf{z}-\mathbf{R}_i|)}{|\mathbf{z}-\mathbf{R}_i|} M^i_{\mu\upsilon}\left(\overleftarrow{\mathbf{k}}_i,\overrightarrow{\mathbf{k}}_i;\omega\right) A^i_\upsilon(\mathbf{R}_i,\omega), \tag{3.14}$$

where M^i is the coherent elastic atomic scattering operator for atom i, and A^i is the coherent elastic wave incident on atom i. A^i satisfies

$$A^i_\mu(\mathbf{R}_i,\omega) = A^0_\mu(\mathbf{R}_i,\omega) + \sum_{j\neq i} \frac{\exp(\mathrm{i}k|\mathbf{R}_i-\mathbf{R}_j|)}{|\mathbf{R}_i-\mathbf{R}_j|} M^j_{\mu\upsilon}\left(\overleftarrow{\mathbf{k}}_j,\overrightarrow{\mathbf{k}}_j;\omega\right) A^j_\upsilon(\mathbf{R}_j,\omega). \tag{3.15}$$

Here $\overleftarrow{\mathbf{k}}_j = \mathrm{i}\overleftarrow{\nabla}_j$ and $\overrightarrow{\mathbf{k}}_j = -\mathrm{i}\overrightarrow{\nabla}_j$, where the gradient is with respect to $\mathbf{R}_j$, the equilibrium position of atom j, and the gradients operate on the factors to the left or right as indicated. In obvious matrix notation, these equations become

$$A = A^0 + \sum_i \delta^+_{z,i} M^i A^i \tag{3.16}$$

and

$$A^i = A^0 + \sum_{j \neq i} \delta_{ij}^{+} M^j A^j, \tag{3.17}$$

where $\delta_{ij}^{+} = \exp(\mathrm{i}kR_{ij})/R_{ij}$. Equations (3.17) are a set of coupled equations which determine the incident fields A^i, and then (3.16) gives the coherent elastic wave A at $(\mathbf{z}, \omega)$. Equation (3.17) simply says that the total field incident on the ith atom is the primary field A^0, plus the scattered waves emanating from all the other atoms j under the inluence of the total fields A^j incident at those sites. Equation (3.16) then gives the total field incident at $\mathbf{r}$ as the primary field $A^0(\mathbf{r}, t)$ plus the scattered waves emanating from all the atoms j under the inluence of the total fields A^j incident at those sites.

Equations (3.16) and (3.17) are the *basic optical equations for coherent X-ray and γ-ray optics*. These equations are identical in form to the semiclassical equations used to develop the dynamical theory of X-ray diffraction (the important distinction between the classical and quantum equations is that the *quantum field equations* are *complex*, while the classical equations are real). Except for a small inaccuracy in accounting for "mirror terms" [10, appendix B], eqs. (3.16) and (3.17) are the exact single-quantum coherent scattering equations from a collection of scatterers.

Using these equations, the dynamical theory for X-ray or γ-ray optics has been developed using a *generalized Darwin–Prins* approach, which is applicable even to monolayer films [2,11–13]. An alternative *generalized Laue* development of Mössbauer optics has been given by Afanas'ev and Kagan [14–16].[4] In the following subsection we review the Darwin–Prins approach.

The resulting optics is very rich because of the exceeding sharpness of the nuclear resonances, the well defined multipolarity of the transitions, and the strong dependence of the scattering on the directions of the local fields. There are strong *magneto-optical effects* (Kerr, Faraday, etc.), and striking dynamical effects such as the strong *coherent enhancement* of the radiative width $\Gamma_\gamma \rightarrow (\Gamma_\mathrm{c} + \Gamma'_\gamma)$, which occurs for Bragg excitation, and, in the Laue geometry, the *nuclear Borrmann effect*, which involves quite different modes of the radiation field than the X-ray Borrmann effect because of the higher multipolarity of the nuclear resonators, and which has a much deeper penetration depth because of the long scattering times (because the Lamb–Mössbauer factor replaces the Debye–Waller factor in the scattering amplitude) [14,17].

3.3. Generalized Darwin–Prins dynamical theory

The multiple scattering equations which describe the interaction of a γ-ray with a Mössbauer medium are given by eqs. (3.16) and (3.17). These equations are identical in form to the semiclassical equations used to develop the dynamical theory of X-ray

[4] The generalized Laue development is also given in [2, appendix D], starting from the basic multiple scattering equations (3.16) and (3.17).

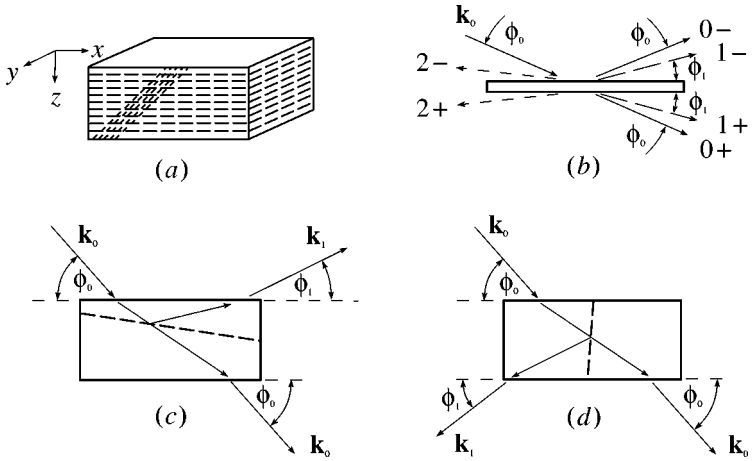

Figure 8. (a) Schematic representation of the crystal geometry used in developing the dynamical theory (dashed lines indicate crystal planes); (b) representation of open radiation channels for a plane layer; (c) Bragg reflection; (d) Laue transmission.

diffraction,[5] and as a consequence, much of the X-ray theory can be taken over directly. However, it is necessary to generalize the X-ray theory to account for the very strong polarization mixing which occurs in Mössbauer optics.

We will generally limit our discussion here to perfect single crystals (except for the cases of critical reflection and transmission off-Bragg, where the expressions are independent of crystal structure). The reflection and transmission coefficients depend somewhat on the shape of the crystal, and, as in the usual X-ray development, we take the form shown in figure 8: we assume that some set of infinite crystalline planes is parallel to the surface, which we take as the xy plane, and that the crystal is of finite thickness l in the z direction, $l = Md$, where M is the number of "planes", and d is the interplanar distance. The thickness of the layers is rather arbitrary, but they must be sufficiently thin so that the Born approximation is good within the layer. We generally assume a unit cell thickness (chemical or magnetic, whichever is larger). For example, if there is a magnetic spiral axis $\hat{\theta}$ which is commensurate with the crystal structure, it is convenient to use the magnetic unit cell, which contains the full spiral, so that each "plane" of the crystal has the same internal field structure.

If a photon $A^0_\mu(\mathbf{z}, t) = a^0_\mu \exp[\mathrm{i}(\mathbf{k}_0 \cdot \mathbf{z} - \omega t)] = A^0_\mu(\mathbf{z}) \exp(-\mathrm{i}\omega t)$ is incident on a plane layer (at $z = 0$), then in the Born approximation the coherent elastic photon amplitude at $\mathbf{R}$ is given by[6]

$$A_\mu(\mathbf{R}) = A^0_\mu(\mathbf{R}) + A^{\mathrm{s}}_\mu(\mathbf{R}), \tag{3.18}$$

[5] For a discussion of the Darwin–Prins and Laue formulations of the dynamical theory of X-ray diffraction, see [18].

[6] An exact treatment of planar scattering, i.e., including multiple scattering within the plane, is given in [11] and discussed in section 6. For most cases the planar self-action contribution is negligible.

where $A^{\mathrm{s}}_{\mu}(\mathbf{R})$ is the scattered wave,

$$A^{\mathrm{s}}_{\mu}(\mathbf{R}) = \sum_{s} \frac{\mathrm{i}\lambda_0 n'}{\sin\phi_s} \mathrm{e}^{\mathrm{i}[g_s|z| + (\mathbf{k}^0_{xy} + \vec{\tau}_s)\cdot\mathbf{R}]} M_{\mu\upsilon}\big(-\mathrm{i}\overleftarrow{\nabla}_{\mathbf{R}}, \mathbf{k}_0\big) a^0_{\upsilon} \tag{3.19}$$

with

$$g_s = \sqrt{k_0^2 - \big(\mathbf{k}^0_{xy} + \vec{\tau}_s\big)^2}, \tag{3.20}$$

$$\sin\phi_s = \frac{g_s}{k_0}, \tag{3.21}$$

and n' is the *planar* density of unit cells (number/cm^2). $M_{\mu\upsilon}$ is understood to be the coherent scattering operator of the *unit cell*

$$M_{\mu\upsilon}\big(\mathbf{k}', \mathbf{k}\big) = \sum_{\rho} \big[M^{(\rho)}_{\mu\upsilon}\big(\mathbf{k}', \mathbf{k}\big)\big]_{\mathrm{c}} \mathrm{e}^{-\mathrm{i}(\mathbf{k}'-\mathbf{k})\cdot\vec{\rho}}. \tag{3.22}$$

In deriving (3.19), we used the planar relation

$$\sum_{j} \frac{\mathrm{e}^{\mathrm{i}k|\mathbf{R}-\mathbf{R}_j|}\mathrm{e}^{\mathrm{i}\mathbf{k}^0_{xy}\cdot\mathbf{R}_j}}{|\mathbf{R}-\mathbf{R}_j|} = \mathrm{i}2\pi n' \sum_{s} (1/g_s) \mathrm{e}^{\mathrm{i}[g_s|z| + (\mathbf{k}^0_{xy} + \vec{\tau}_s)\cdot\mathbf{R}]}. \tag{3.23}$$

The $\vec{\tau}_s$ in eqs. (3.19) and (3.20) are the *planar* reciprocal lattice vectors for the unit cells, and the sum is over all $\vec{\tau}_s$ for which g_s is real (the sum over the $\vec{\tau}_s$ for which g_s is imaginary gives an exponentially damped contribution on the order of $\mathrm{e}^{-k_0|z|}/k_0|z|$). The scattered photon amplitude is thus a superposition of a *finite* number of plane-wave channels ($s\pm$) having wave vectors $\mathbf{k}_{(s\pm)} = (\mathbf{k}^0_{xy} + \vec{\tau}_s, \pm g_s)$. These channels are symmetric about the scattering plane, i.e., for each forward scattered wave in the $\mathbf{k}_{(s+)}$ direction (the $(s+)$ channel), there is a reflected wave in the $\mathbf{k}_{(s-)}$ direction (the $(s-)$ channel) (see figure 8(b)). Finally, we note that the operator $-\mathrm{i}\overleftarrow{\nabla}_{\mathbf{R}}$ in eq. (3.19) operates on the exponential plane-wave factor to the left of $M_{\mu\upsilon}$, and is replaced by the wave vector $\mathbf{k}_{(s+)} = (\mathbf{k}^0_{xy} + \vec{\tau}_s,\ g_s)$ if $z > 0$ (corresponding to forward scattering $\mathbf{k}_0 \rightarrow \mathbf{k}_{(s+)}$), and by $\mathbf{k}_{(s-)} = (\mathbf{k}^0_{xy} + \vec{\tau}_s, -g_s)$ if $z < 0$ (corresponding to reflection $\mathbf{k}_0 \rightarrow \mathbf{k}_{(s-)}$).

In a crystal of finite thickness, any wave of appreciable magnitude is built up by constructive interference of the planar radiation channels. All the (open) planar channels contribute to the general dynamical equations (eqs. (3.24), (3.34), (3.35) below), but in the usual approximation, only constructively interfering channels need be considered open for the crystal. Thus, there will generally only be one or two radiation channels open in a crystal (off-Bragg, only the $(0+)$ channel is open, for a single Bragg reflection, the $(0+)$ and a $(1-)$ channel are open, and for Laue transmission, the $(0+)$ channel and a $(1+)$ channel are open).

This approach to the problem follows the Darwin–Prins development of the dynamical X-ray diffraction. The alternative Laue formulation for γ-ray optics is dis-

cussed in [14–16]. For a discussion of the Darwin–Prins and Laue formulations of the dynamical theory of X-ray diffraction, see, for example, [18].

The generalization of the Darwin–Prins dynamical equations is straightforward: denoting by $A_\mu^{(m)}(\mathbf{k}_{(s+)})$ the wave incident on the mth plane (from "above") in the $(s+)$ channel, and similarly, by $A_\mu^{(m)}(\mathbf{k}_{(s-)})$ the wave incident on the mth plane (from "below") in the $(s-)$ channel, then the waves incident from *above* on the mth plane are related to the waves incident on the $(m-1)$th plane as

$$A_\mu^{(m)}(\mathbf{k}_{(s+)}) = \mathrm{e}^{\mathrm{i}g_s d}\Bigg[A_\mu^{(m-1)}(\mathbf{k}_{(s+)}) + \frac{\mathrm{i}\lambda_0 n d}{\sin\phi_s}\sum_{s'}\sum_{\eta=\pm} M_{\mu\upsilon}^{(m-1)}\big(\mathbf{k}_{(s+)},\mathbf{k}_{(s'\eta)}\big)A_\upsilon^{(m-1)}\big(\mathbf{k}_{(s'\eta)}\big)\Bigg], \quad (3.24)$$

where d is the interplanar distance and n is the unit-cell density (cm^{-3}). $M_{\mu\upsilon}^{(m-1)}$ is the unit-cell scattering operator of the $(m-1)$th plane. We will generally limit our considerations to uniform Mössbauer crystals (i.e., crystals with a uniform distribution of Mössbauer atoms, and for which the unit-cell internal field structure is the same throughout the crystal) for which the plane designation of the scattering operator can be omitted. Equation (3.24) is an obvious result: the amplitude of a wave $A_\mu^{(m)}(\mathbf{k}_{(s+)})$ incident on the mth plane (from above) in the $(s+)$ channel is equal to the amplitude $A_\mu^{(m-1)}(\mathbf{k}_{(s+)})$ of such a wave incident on the $(m-1)$th plane, plus the forward scattering

$$\mathrm{i}\frac{\lambda_0 n d}{\sin\phi_s} M_{\mu\upsilon}^{(m-1)}\big(\mathbf{k}_{(s+)},\mathbf{k}_{(s+)}\big)A_\upsilon^{(m-1)}\big(\mathbf{k}_{(s+)}\big) \quad (3.25)$$

of this wave by the $(m-1)$th plane, plus the amplitudes of all other channels incident on the $(m-1)$th plane scattered into the $(s+)$ channel by this plane. These effects are propagated to the mth plane by the phase factor $\mathrm{e}^{\mathrm{i}g_s d}$.

Similarly, the waves incident on the mth plane from *below* are related to the waves incident on the $(m+1)$th plane, with $A_\mu^{(m)}(\mathbf{k}_{(s-)})$ given by eq. (3.24) with the replacements $(s+)\to(s-)$, $(m-1)\to(m+1)$.

Denoting the first plane as the $m=0$ plane, and the last plane as the $m=M$ plane (the total number of planes is $M+1$), the general boundary conditions to be satisfied are

$$A_\mu^{(m=0)}(\mathbf{k}_{(s+)}) = \delta_{s0}a_\mu^0\mathrm{e}^{\mathrm{i}\mathbf{k}_0\cdot\mathbf{R}_0}, \quad (3.26)$$

$$A_\mu^{(m=M)}(\mathbf{k}_{(s-)}) = 0. \quad (3.27)$$

That is, the only wave incident from above on the first plane is A_μ^0, and there are no waves incident from below on the last plane.

It has already been implicitly assumed in deriving eq. (3.24) that $k_0 d \gg 1$, which is well satisfied for Mössbauer frequencies. Thus, the longitudinal and scalar components need not be considered and it is convenient to express eq. (3.24) in terms of orthogonal transverse amplitudes.

We define by $\mathbf{e}_x^{(s\eta)}$, $\mathbf{e}_y^{(s\eta)}$ ($\eta = +$ or $-$) any convenient orthogonal basis perpendicular to $\mathbf{k}_{(s\eta)}$. In terms of this basis, the transverse part of $A_\mu^{(m)}(\mathbf{k}_{(s\eta)})$ is given by

$$A_\mu^{(m)}(\mathbf{k}_{(s+)}) = \left(\mathbf{e}_x^{(s+)} T_{x,m}^{(s)} + \mathbf{e}_y^{(s+)} T_{y,m}^{(s)}\right) \mathrm{e}^{\mathrm{i}\mathbf{k}_{xy}^{(s+)}\cdot\mathbf{R}_m}, \tag{3.28}$$

$$A_\mu^{(m)}(\mathbf{k}_{(s-)}) = \left(\mathbf{e}_x^{(s-)} R_{x,m}^{(s)} + \mathbf{e}_y^{(s-)} R_{y,m}^{(s)}\right) \mathrm{e}^{\mathrm{i}\mathbf{k}_{xy}^{(s-)}\cdot\mathbf{R}_m}, \tag{3.29}$$

where

$$T_{x,m}^{(s)} = \mathbf{e}_x^{(s+)*} \cdot \mathbf{A}^{(m)}(\mathbf{k}_{(s+)}) \mathrm{e}^{-\mathrm{i}\mathbf{k}_{xy}^{(s+)}\cdot\mathbf{R}_m},$$

etc., so that $T_{x,m}^{(s)}$ gives the scalar amplitude of a photon $|\mathbf{e}_x^{(s+)}, \mathbf{k}_{(s+)}\rangle$ incident on the mth layer from above, etc. We will denote the $(s+)$ channels by the index t, and the $(s-)$ channels by r, and define the column vectors $\mathbf{T}_m^t$, $\mathbf{R}_m^r$ as

$$\mathbf{T}_m^t = \begin{pmatrix} T_{x,m}^{(t)} \\ T_{y,m}^{(t)} \end{pmatrix}, \tag{3.30}$$

$$\mathbf{R}_m^r = \begin{pmatrix} R_{x,m}^{(r)} \\ R_{y,m}^{(r)} \end{pmatrix}. \tag{3.31}$$

The "planar" scattering matrix $\widetilde{F}^{ss'}$ (and $\tilde{f}^{ss'}$) ($s, s' = t$ or r) for scattering an (s') channel into an (s) channel is defined by

$$\widetilde{F}^{ss'} \equiv \frac{d}{\sin\phi_s} \tilde{f}^{ss'} = \begin{pmatrix} F_{xx}^{ss'} & F_{xy}^{ss'} \\ F_{yx}^{ss'} & F_{yy}^{ss'} \end{pmatrix}, \tag{3.32}$$

where

$$F_{\lambda\lambda'}^{ss'} \equiv \frac{d}{\sin\phi_s} f_{\lambda\lambda'}^{ss'} = \frac{d}{\sin\phi_s} \lambda_0 n f\left(\mathbf{k}_s, \mathbf{e}_\lambda^s; \mathbf{k}_{s'}, \mathbf{e}_\lambda^{s'}\right), \tag{3.33}$$

$\lambda, \lambda' = x$ or y, and where $f(\mathbf{k}_s, \mathbf{e}_\lambda^s; \mathbf{k}_{s'}, \mathbf{e}_\lambda^{s'})$ is the unit cell coherent elastic scattering amplitude as given by eqs. (3.13) and (3.22). The planar scattering amplitudes $F^{ss'}$ are dimensionless, while the amplitudes $f^{ss'}$ have the dimensions of a linear mass absorption coefficient, i.e., length^{-1}.

In terms of these matrix quantities, the dynamical equations for Mössbauer optics are given by the coupled equations

$$\mathbf{T}_m^t = \mathrm{e}^{\mathrm{i}g_t d}\left(\mathbf{T}_{m-1}^t + \mathrm{i}\sum_{t'} \widetilde{F}^{tt'} \mathbf{T}_{m-1}^{t'} + \mathrm{i}\sum_r \widetilde{F}^{tr} \mathbf{R}_{m-1}^r\right), \tag{3.34}$$

$$\mathbf{R}_m^r = \mathrm{e}^{\mathrm{i}g_r d}\left(\mathbf{R}_{m+1}^r + \mathrm{i}\sum_{r'} \widetilde{F}^{rr'} \mathbf{R}_{m+1}^{r'} + \mathrm{i}\sum_t \widetilde{F}^{rt} \mathbf{T}_{m+1}^t\right), \tag{3.35}$$

with the boundary conditions

$$\mathbf{T}_0^t = \delta_{t0}\mathbf{a}_0\big(\hat{k},\omega\big), \tag{3.36}$$

$$\mathbf{R}_M^r = 0. \tag{3.37}$$

Equations (3.34), (3.35) are the generalization of the Darwin–Prins equations of X-ray optics. These equations include not only the polarization mixing effects, but by including the contribution of all (open) planar radiation channels, the scattering from any set of Bragg planes can be computed.

3.4. General solution

For a uniform Mössbauer crystal it is straightforward to obtain a general solution from eqs. (3.34)–(3.37) for the amplitude and polarization of the reflected and transmitted waves by making the substitutions

$$\mathbf{T}_m^t = \sum_{k'} \mathbf{T}_{k'}^t \mathrm{e}^{\mathrm{i}mk'd} \equiv \sum_{k'} \begin{pmatrix} T_{x,k'}^{(t)} \\ T_{y,k'}^{(t)} \end{pmatrix} \mathrm{e}^{\mathrm{i}mk'd}, \tag{3.38}$$

$$\mathbf{R}_m^r = \sum_{k'} \mathbf{R}_{k'}^r \mathrm{e}^{\mathrm{i}mk'd} \equiv \sum_{k'} \begin{pmatrix} R_{x,k'}^{(r)} \\ R_{y,k'}^{(r)} \end{pmatrix} \mathrm{e}^{\mathrm{i}mk'd}. \tag{3.39}$$

Substitution of (3.38), (3.39) into (3.34)–(3.37) gives

$$\big[\mathrm{e}^{-\mathrm{i}(g_t-k')d} - 1\big]\mathbf{T}_{k'}^t - \mathrm{i}\sum_{t'} \widetilde{F}^{tt'}\mathbf{T}_{k'}^{t'} - \mathrm{i}\sum_{r} \widetilde{F}^{tr}\mathbf{R}_{k'}^r = 0, \tag{3.40}$$

$$\big[\mathrm{e}^{-\mathrm{i}(g_r+k')d} - 1\big]\mathbf{R}_{k'}^r - \mathrm{i}\sum_{r'} \widetilde{F}^{rr'}\mathbf{R}_{k'}^{r'} - \mathrm{i}\sum_{t} \widetilde{F}^{rt}\mathbf{T}_{k'}^t = 0, \tag{3.41}$$

and the boundary conditions

$$\sum_{\lambda}\sum_{k'} T_{\lambda,k'}^{(t)}\mathbf{e}_\lambda^{(t)} = \delta_{t0}\mathbf{a}_0\big(\hat{k}_0,\omega_0\big), \tag{3.42}$$

$$\sum_{k'} R_{\lambda,k'}^{(r)}\mathrm{e}^{\mathrm{i}k'Md} = 0. \tag{3.43}$$

The dispersion equation to determine the allowed values of k' is then

$$\det\big[\widetilde{C}\big(k'\big)\big] = 0, \tag{3.44}$$

where $\widetilde{C}(k')$ is the coefficient matrix of eqs. (3.40) and (3.41),

$$\widetilde{C}(k')=\begin{pmatrix} [(\mathrm{e}^{-\mathrm{i}(g_0-k')d}-1)\tilde{I}-\mathrm{i}\widetilde{F}^{00}] & -\mathrm{i}\widetilde{F}^{0t} & \cdot \\ -\mathrm{i}\widetilde{F}^{t0} & [(\mathrm{e}^{-\mathrm{i}(g_t-k')d}-1)\tilde{I}-\mathrm{i}\widetilde{F}^{tt}] & \\ \vdots & \vdots & \\ -\mathrm{i}\widetilde{F}^{r0} & -\mathrm{i}\widetilde{F}^{rt} & \\ \vdots & \vdots & \\ \cdot & -\mathrm{i}\widetilde{F}^{0r} & \cdot \\ \cdot & -\mathrm{i}\widetilde{F}^{tr} & \cdot \\ \cdot & \vdots & \cdot \\ \cdot & [(\mathrm{e}^{-\mathrm{i}(g_r+k')d}-1)\tilde{I}-\mathrm{i}\widetilde{F}^{rr}] & \cdot \\ \cdot & \vdots & \cdot \end{pmatrix}. \tag{3.45}$$

Here $\tilde{I}$ is the 2×2 unit matrix and the $\widetilde{F}^{ss'}$ are the dimensionless planar scattering matrices defined in eq. (3.33). $\widetilde{C}(k')$ includes the (0+) channel, and all other transmission channels (t) and reflection channels (r) that are open. If there are n open channels, then eq. (3.44) gives $2n$ values of k' (which are independent of the polarization basis of representation). There are then $4n^2$ amplitudes $T^{(t)}_{\lambda,k'}$, $R^{(r)}_{\lambda,k'}$ to be determined from the $4n^2$ linear relationships given by eqs. (3.40)–(3.43). In particular, for a given value of k', the $2n-1$ independent equations (3.40), (3.41) give the determinate solutions

$$T^{(t)}_{\lambda,k'}=D^{t0}_{\lambda x}\big(k'\big)T^{(0)}_{x,k'},\qquad R^{(r)}_{\lambda,k'}=D^{r0}_{\lambda x}\big(k'\big)T^{(0)}_{x,k'},$$

in terms of $T^{(0)}_{x,k'}$. The $2n$ values of $T^{(0)}_{x,k'}$ are then determined from the boundary conditions (3.42), (3.43). The reflected and transmitted waves are then given by

$$\mathbf{R}^r=\sum_{\lambda}\sum_{k'}\mathbf{e}^{(r)}_{\lambda}R^{(r)}_{\lambda,k'}, \tag{3.46}$$

$$\mathbf{T}^t=\sum_{\lambda}\sum_{k'}\mathbf{e}_{\lambda}(t)T^{(t)}_{\lambda,k'}\mathrm{e}^{\mathrm{i}k'Md}. \tag{3.47}$$

Actually, eqs. (3.46) and (3.47) give $\mathbf{R}^r_0$, the wave *incident from below* on the first plane ($m=0$), and $\mathbf{T}^t_M$, the wave *incident from above* on the last plane ($m=M$). The exact reflected and transmitted waves $\mathbf{R}^r$ and $\mathbf{T}^t$ can then be calculated from equations (3.34), (3.35) with the boundary conditions (3.36), (3.37):

$$\mathbf{R}^r=\mathbf{R}^r_0+\mathrm{i}\sum_{r'}\widetilde{F}^{rr'}\mathbf{R}^{r'}_0+\mathrm{i}\widetilde{F}^{r0}\mathbf{T}^0_0, \tag{3.48}$$

$$\mathbf{T}^t=\mathbf{T}^t_M+\mathrm{i}\sum_{t'}\widetilde{F}^{tt'}\mathbf{T}^{t'}_M. \tag{3.49}$$

Usually, however, the scattering effects of a single plane can be neglected (unless we are interested in the scattering from very thin films, say $M\approx$ 1–10), and it suffices to use $\mathbf{R}^r=\mathbf{R}^r_0$ and $\mathbf{T}^t=\mathbf{T}^t_M$ as given by eqs. (3.46) and (3.47).

The reflection and transmission coefficients are then given by

$$R^r = g \int \mathrm{d}\omega_0 \, \mathrm{d}\Omega_{k_0} \frac{|\mathbf{R}^r|^2}{I_0}, \qquad T^t = g \int \mathrm{d}\omega_0 \, \mathrm{d}\Omega_{k_0} \frac{|\mathbf{T}^t|^2}{I_0}, \tag{3.50}$$

where

$$I_0 = \int \mathrm{d}\omega_0 \, \mathrm{d}\Omega_{k_0} \left|\mathbf{a}_0\left(\omega_0, \hat{k}_0\right)\right|^2,$$

$g = \sin\phi_s / \sin\phi_0$ (figure 8(c,d)) is the Jacobian $|\Omega_{k_0}/\Omega_{k_s})|$ for $s = r$ or t, respectively, and the integration range is taken sufficiently small that the relative variation of g and ω_0 is negligible.

The coherent elastic wave scattered into the $\mathbf{k}_s$-channel is linear in the incident photon potential $\mathbf{a}_0$ ($= a_0\mathbf{e}_0$) and can always be expressed in the general form

$$\mathbf{S}\left(\omega; \hat{k}_s, \hat{k}_0; \mathbf{e}_0\right) = \widetilde{S}\left(\omega; \hat{k}_s, \hat{k}_0\right)\mathbf{a}_0, \tag{3.51}$$

where $\mathbf{S} = \mathbf{R}^r$ or $\mathbf{T}^t$ for reflection or transmission channels, respectively. The components of the 2×2 scattering matrix $\widetilde{S}$ ($= \widetilde{R}$ or $\widetilde{T}$), which directly relates the coherent elastic wave scattered into the $\mathbf{k}_s$-channel to the incident photon $\mathbf{a}_0$, can be extracted directly from the solutions for $\mathbf{R}^r$ and $\mathbf{T}^t$.

The *internal field* in the crystal can be expressed as a superposition of *radiation eigenwave* contributions,

$$\mathbf{A}(\mathbf{r}) = \sum_{k'} \mathbf{A}_{k'}(\mathbf{r}), \tag{3.52}$$

where the k' eigenwave contribution is

$$\mathbf{A}_{k'}(\mathbf{r}) = \mathrm{e}^{\mathrm{i}k'z}\left[\sum_t \mathbf{T}^t_{k'} \mathrm{e}^{\mathrm{i}(\mathbf{k}_t)_{xy}\cdot\mathbf{r}} + \sum_r \mathbf{R}^r_{k'} \mathrm{e}^{\mathrm{i}(\mathbf{k}_r)_{xy}\cdot\mathbf{r}}\right]. \tag{3.53}$$

In certain cases it is convenient to solve in terms of eigenwaves, e.g., off-Bragg (section 3.5), Laue (section 3.8), and multibeam Borrmann (section 3.9).

3.5. Off-Bragg

Off-Bragg, to a very good approximation, we only need consider the (0+) channel open. This channel only involves forward scattering amplitudes, and the optical solutions are thus valid for a noncrystalline medium as well as for a crystal. A complicating, but interesting feature of γ-ray optics is the presence of strong optical activity, which gives strong polarization mixing (i.e., orthogonal scattering $\hat{\mathbf{e}}_x \leftrightarrow \hat{\mathbf{e}}_y$) and Faraday-type effects [10,13,19,20].

3.5.1. Eigenwaves

Keeping only the (0+) channel in (3.40) and taking

$$e^{i(k'-g_0)d} = 1 + \frac{i f_\eta d}{\sin\phi_0}, \tag{3.54}$$

the eigenpolarizations and indices of refraction are determined by the eigenvalue equation

$$\begin{pmatrix} f_{xx} & f_{xy} \\ f_{yx} & f_{yy} \end{pmatrix} \begin{pmatrix} T_{x,k'} \\ T_{y,k'} \end{pmatrix} = f_\eta \begin{pmatrix} T_{x,k'} \\ T_{y,k'} \end{pmatrix}, \tag{3.55}$$

where f_{xx}, f_{yy}, etc. are the planar forward-scattering amplitudes defined by (3.33) and again we have used $\mathbf{e}_x$, $\mathbf{e}_y$ to denote *any* two *orthogonal* polarizations perpendicular to $\mathbf{k}_0$; f_{ab} ($a, b = x$ or y) is related to the unit-cell coherent forward scattering amplitude by

$$f_{ba}(\mathbf{k},\omega) = \lambda n \sum_\rho f^{(\rho)}(\mathbf{e}_b, \mathbf{k}; \mathbf{e}_a, \mathbf{k}), \tag{3.56}$$

where n is the unit-cell density, the sum is over the unit cell, and $f^{(\rho)}(\mathbf{e}_b, \mathbf{k}; \mathbf{e}_a, \mathbf{k})$ is the coherent elastic scattering amplitude of atom ρ for scattering an $|\mathbf{e}_a, \mathbf{k}\rangle$ photon into an $|\mathbf{e}_b, \mathbf{k}\rangle$ photon.

From (3.55) we obtain (for $\eta = 1$ or 2)

$$\begin{aligned} f_\eta &= \frac{1}{2}\mathrm{Tr}\big(\tilde{f}\,\big) + (-1)^{(\eta+1)}\left\{\left[\frac{1}{2}\mathrm{Tr}\big(\tilde{f}\,\big)\right]^2 - \det\big(\tilde{f}\,\big)\right\}^{1/2} \\ &= \frac{1}{2}(f_{xx} + f_{yy}) + (-1)^{(\eta+1)}\left[\frac{1}{4}(f_{xx} - f_{yy})^2 + f_{xy}f_{yx}\right]^{1/2}, \end{aligned} \tag{3.57}$$

where the square root is taken to have a positive imaginary part. The corresponding eigenpolarizations $\mathbf{e}_\eta$ are given by[7]

$$\mathbf{e}_\eta\big(\hat{k},\omega\big) = K_{(\eta,x)}\left[\mathbf{e}_x + \frac{(f_\eta - f_{xx})}{f_{xy}}\mathbf{e}_y\right], \tag{3.58}$$

where

$$K_{(\eta,x)} = \left[1 + \left|\frac{(f_\eta - f_{xx})}{f_{xy}}\right|^2\right]^{-1/2}. \tag{3.59}$$

[7] There are, of course, a number of alternative forms for $\mathbf{e}_\eta$ which are obtained by using the determinant equation (3.55), i.e., $(f_{xx} - f_\eta)(f_{yy} - f_\eta) - f_{xy}f_{yx} = 0$, and by modifying the factor $K_{(\eta,x)}$. In particular, we can interchange all x and y subscripts in (3.58) and (3.59). In going from one basis to another, over-all phase factors are absorbed into $K_{(\eta,x)}$.

From (3.54) we see that $k'_\eta d = g_0 d + f_\eta d/\sin\phi_0 + \mathrm{O}(f_\eta d)^2$, so the $\mathbf{e}_\eta$ eigenwave propagates in the medium (to first order) as $\exp(\mathrm{i}n_\eta \mathbf{k}_0 \cdot \mathbf{r})$, with the complex index of refraction given by

$$n_\eta = 1 + \lambda_0 f_\eta. \tag{3.60}$$

We note that since the scattering matrix in (3.55) is, generally, non-Hermitian [2, 19], the eigenwaves $\mathbf{e}_\eta$ are, generally, nonorthogonal. Only in limiting cases will the eigenwaves be strictly orthogonal: well-isolated resonances (splitting large compared to Γ); unsplit resonances (splitting small compared to Γ); or otherwise, if J_z is a good quantum number, and $\hat{k}_0 \cdot \hat{z}_J = 0, \pm 1$. Although it is not immediately obvious, it can be verified that $\mathbf{e}_\eta$ and f_η are invariant with respect to the choice of orthogonal basis $\mathbf{e}_x, \mathbf{e}_y$, as they must be.

3.5.2. Transmission through a Mössbauer film

The polarization and intensity of the coherent elastic wave transmitted through a Mössbauer medium are easily obtained using the eigenwaves $\mathbf{e}_\eta$. The polarization and amplitude of the $(\hat{k}, \omega)$ component of the incident photon we write as

$$\mathbf{a}_0(\hat{k}, \omega) = a_{0x}(\hat{k}, \omega)\mathbf{e}_x(\hat{k}) + a_{0y}(\hat{k}, \omega)\mathbf{e}_y(\hat{k}) = \begin{pmatrix} a_{0x} \\ a_{0y} \end{pmatrix}, \tag{3.61}$$

where $\mathbf{e}_x(\hat{k})$ and $\mathbf{e}_y(\hat{k})$ are an orthogonal polarization basis perpendicular to the momentum vector $\mathbf{k}$ of the incident photon.

Expressing $\mathbf{e}_x$ and $\mathbf{e}_y$ in terms of the eigenwaves $\mathbf{e}_1$ and $\mathbf{e}_2$ by inverting (3.58), the $(\hat{k}, \omega)$ component of the wave transmitted through a Mössbauer film of normal thickness l is then given by

$$\mathbf{T}(\hat{k}, \omega) = \widetilde{T}(\hat{k}, \omega; l)\mathbf{a}_0(\hat{k}, \omega), \tag{3.62}$$

where the 2×2 transmission matrix is given by

$$\begin{aligned} \widetilde{T}(\hat{k}, \omega; l) &= \begin{pmatrix} T_{xx} & T_{xy} \\ T_{yx} & T_{yy} \end{pmatrix} \\ &= \begin{pmatrix} \dfrac{1}{2}\left[e_{(+)} + e_{(-)}\left(\dfrac{f_{xx} - f_{yy}}{f_1 - f_2}\right)\right] & e_{(-)}\left(\dfrac{f_{xy}}{f_1 - f_2}\right) \\ e_{(-)}\left(\dfrac{f_{yx}}{f_1 - f_2}\right) & \dfrac{1}{2}\left[e_{(+)} - e_{(-)}\left(\dfrac{f_{xx} - f_{yy}}{f_1 - f_2}\right)\right] \end{pmatrix}. \end{aligned} \tag{3.63}$$

Here

$$e_{(\pm)}(\hat{k}, \omega; l) = \left(\mathrm{e}^{\mathrm{i}f_1 l_\parallel} \pm \mathrm{e}^{\mathrm{i}f_2 l_\parallel}\right)\mathrm{e}^{\mathrm{i}g_0 l}, \tag{3.64}$$

where $l_\parallel = l/\sin\phi_0$ is the thickness along the direction of propagation.

The intensity of the transmitted packet is then given by

$$I = \int \mathrm{d}\omega\, \mathrm{d}\Omega_k \left|T(\hat{k}, \omega)\right|^2. \tag{3.65}$$

If the incident packet is unpolarized or partially polarized, one can use the density matrix formalism discussed in [13].

The transmitted wave $\mathbf{T}(\hat{k},\omega)$ is a superposition of eigenwaves $\mathbf{e}_1$ and $\mathbf{e}_2$. Since the indices of refraction of the two waves are different, i.e.,

$$n_1 - n_2 = 2\lambda\left[\frac{1}{4}(f_{xx} - f_{yy})^2 + f_{xy}f_{yx}\right]^{1/2}, \tag{3.66}$$

there are Faraday effects involved in the transmission through a Mössbauer medium. The real part of $n_1 - n_2$ gives the usual Faraday rotation effect, while the imaginary part gives a "selective absorption" effect. Since the electronic scattering gives essentially no contribution to (3.66) (assuming the Mössbauer resonance frequency is far from any X-ray absorption edges of the atom), $n_1 - n_2$ depends upon the nuclear scattering amplitude and is primarily imaginary at resonance, while the real part dominates off-resonance. Thus, at resonance the Faraday effect in Mössbauer optics is primarily one of selective absorption. That is, if the resonances are well separated and if the incident frequency (packet) is within a few widths of a resonance, so that $I(f_1) \gg I(f_2)$, the $\mathbf{e}_1$ eigenwave is damped out much more rapidly. For such a case, the thickness l of the polarizing medium can be chosen sufficiently thick that almost all of the $\mathbf{e}_1$ wave is absorbed, but still sufficiently thin that the $\mathbf{e}_2$ wave is only slightly attenuated, and the transmitted wave is nearly $\mathbf{e}_2$ polarized. If the incident frequency is adjusted off-resonance (within a few Γ), the real part of $n_1 - n_2$ dominates and the optical activity is primarily Faraday rotation.

3.5.3. Blume–Kistner approach

An alternative approach to treating off-Bragg transmission is to convert the finite difference equation (3.34) to a differential equation. This is essentially the approach of Blume and Kistner [19]. With only the (0+) channel open, (3.34) is

$$\mathbf{T}_m^{(0)} = \mathrm{e}^{\mathrm{i}g_0 d}\left[1 + \mathrm{i}\widetilde{F}^{00}\right]\mathbf{T}_{m-1}^{(0)}. \tag{3.67}$$

Treating the interplanar separation d as an infinitesimal (i.e., $d \to \mathrm{d}z$, $md \to z$, $\mathbf{T}_m^{(0)} \to \mathbf{T}(z)$, and $\widetilde{F}^{00} \to \mathrm{d}z\tilde{f}/\sin\phi_0$), and taking normal incidence for simplicity (i.e., $\phi_0 = \pi/2$ so $\sin\phi_0 = 1$, $g_0 = k_0$ and $l_{\|} = l$), eq. (3.67) becomes the differential equation

$$\frac{\mathrm{d}\mathbf{T}(z)}{\mathrm{d}z} = \mathrm{i}k_0\tilde{n}\mathbf{T}(z), \tag{3.68}$$

where $\tilde{n} = [1 + \lambda_0\tilde{f}\,]$ is the 2×2 index of refraction operator, defined in (3.60), which, combined with the boundary condition (3.36), gives the solution for the transmitted wave amplitude

$$\mathbf{T}\big(\hat{k},\omega\big) = \mathbf{T}(z = l) = \widetilde{T}\big(\hat{k},\omega;l\big)\mathbf{a}_0\big(\hat{k},\omega\big), \tag{3.69}$$

where the 2×2 transmission matrix is now given by

$$\widetilde{T}\big(\hat{k},\omega;l\big) = \exp\big(\mathrm{i}k_0\tilde{n}l\big) = \exp\big[\mathrm{i}\big(k_0 + \tilde{f}\,\big)l\big]. \tag{3.70}$$

Expressing the 2×2 planar scattering matrix $\tilde{f}$ in terms of the Pauli matrices, i.e., $\tilde{f} = a+\mathbf{b}\cdot\vec{\sigma}$, and making use of the operator identity $\exp(\mathrm{i}\mathbf{b}\cdot\vec{\sigma}z) = \cos(bz)+\mathrm{i}(\hat{b}\cdot\vec{\sigma})\sin(bz)$, $\widetilde{T}(\hat{k},\omega;l)$ can be expressed as

$$\widetilde{T}\big(\hat{k},\omega;l\big) = \mathrm{e}^{\mathrm{i}(k_0+a)l}\big[\cos(bl)+\mathrm{i}\big(\hat{b}\cdot\vec{\sigma}\big)\sin(bl)\big], \tag{3.71}$$

where

$$a=\frac{1}{2}(f_{xx}+f_{yy}),\quad b_x=\frac{1}{2}(f_{xy}+f_{yx}),\quad b_y=\frac{\mathrm{i}}{2}(f_{xy}-f_{yx}),\quad b_z=\frac{\mathrm{i}}{2}(f_{xx}-f_{yy}), \tag{3.72}$$

and

$$b=\sqrt{\mathbf{b}\cdot\mathbf{b}}=\sqrt{\frac{1}{4}(f_{xx}-f_{yy})^2+f_{xy}f_{yx}},\qquad \hat{b}\cdot\vec{\sigma}=\frac{1}{b}\begin{pmatrix} b_z & b_x-\mathrm{i}b_y \\ b_x+\mathrm{i}b_y & -b_z\end{pmatrix}.$$

Noting that $b=(f_1-f_2)/2$ and that $\exp[\mathrm{i}(k_0+a)l]\cos(bl) = e_{(+)}(\hat{k},\omega;l)/2$ and $\exp[\mathrm{i}(k_0+a)l]\sin(bl) = -\mathrm{i}e_{(-)}(\hat{k},\omega;l)/2$ (assuming normal incidence), it is easy to verify the equivalence of the two expressions (3.63) and (3.71) for the transmission matrix $\widetilde{T}(\hat{k},\omega;l)$.

3.6. Bragg

For a single-Bragg reflection from a Mössbauer crystal, two channels are open: the $t_0=(0+)$ channel and a "reflection" channel r (Bragg case, shown in figure 8(c)), or a "transmission" channel t (Laue case, shown in figure 8(d)). In this section we consider the Bragg case.

The general dynamical equations (3.40), (3.41) now contain only the two amplitudes $\mathbf{T}^0_{k'}$ and $\mathbf{R}^r_{k'}$,

$$\widetilde{C}\big(k'\big)\begin{pmatrix}\mathbf{T}^0_{k'}\\ \mathbf{R}^r_{k'}\end{pmatrix}=0, \tag{3.73}$$

where the coefficient matrix $\widetilde{C}(k')$ is now the 4×4 matrix,

$$\widetilde{C}\big(k'\big)=\begin{pmatrix}(\mathrm{e}^{-\mathrm{i}(g_0-k')d}-1)\tilde{I}-\mathrm{i}\widetilde{F}^{00} & -\mathrm{i}\widetilde{F}^{0r}\\ -\mathrm{i}\widetilde{F}^{r0} & [(\mathrm{e}^{-\mathrm{i}(g_r+k')d}-1)\tilde{I}-\mathrm{i}\widetilde{F}^{rr}\end{pmatrix}. \tag{3.74}$$

The dispersion equation (3.44) is now of the fourth order, and except for a few special cases, there is no simple analytical solution. Of course, the numerical solution is easily obtained, as outlined in section 3.4.

The special cases occur when the 2×2 forward scattering matrices $\widetilde{F}^{00}$ and $\widetilde{F}^{rr}$, and the reflection matrices $\widetilde{F}^{r0}$ and $\widetilde{F}^{0r}$ can be simultaneously diagonalized with an appropriate choice of orthogonal polarization bases $\mathbf{e}^{(0)}_{\lambda}$ and $\mathbf{e}^{(r)}_{\lambda'}$ (λ and $\lambda'=x,y$). Three important cases where this is possible are the following:

1. In the "*isotropic limit*" (magnetically disordered state for which the splittings are negligible compared to Γ, e.g., ^{57}Fe in stainless steel), the polarization response of

the resonant Mössbauer scattering amplitude, given by eqs. (A.47)–(A.49) of appendix A.2 for E1, M1, and E2 nuclear transitions, respectively, is that of a *free classical oscillator* of the corresponding multipolarity. For example, for an E1 resonance, $f_{\rm E1} \propto \hat{\mathbf{e}}_{\rm f}^{*} \cdot \hat{\mathbf{e}}_0$, which is the response of a free electric dipole oscillator: the incident $\hat{\mathbf{e}}_0$ polarized **E** field drives the oscillator with an acceleration $\mathbf{a} \propto \hat{\mathbf{e}}_0 \exp(-{\rm i}\omega t)$, and the emitted radiation in the $\hat{\mathbf{k}}_{\rm f}$ direction is proportional to the transverse projection $\mathbf{a}_{\perp}$ of the acceleration relative to the $\hat{\mathbf{k}}_{\rm f}$ direction.

For the "isotropic limit", we also assume that the resonance energy of the Mössbauer transition is far removed from any atomic absorption edges, so that the electronic contribution to the scattering amplitude has the simple limiting form of eq. (A.13), i.e., $f_{\rm e} \propto \hat{\mathbf{e}}_{\rm f}^{*} \cdot \hat{\mathbf{e}}_0$. We make this same assumption for the other two special cases discussed below.

For Bragg scattering from a crystal of isotropic scatterers, there is no orthogonal scattering between the σ and π polarizations ($\widehat{\sigma}_0 = \widehat{\sigma}_r$ is the unit vector lying parallel to $\mathbf{k}_r \times \mathbf{k}_0$, while $\hat{\pi}_s$ ($s = 0, r$) lies in the $(\mathbf{k}_r, \mathbf{k}_0)$ scattering plane and perpendicular to $\mathbf{k}_s$, with the convention that $(\hat{\pi}_s, \widehat{\sigma}_s, \mathbf{k}_s)$ forms a right-hand coordinate system). That is, in the isotropic limit, π polarization scatters only into π polarization (both for forward scattering $0 \rightarrow 0$, $r \rightarrow r$ and for reflections $0 \leftrightarrow r$), and σ polarization scatters only into σ polarization. With the x, y polarization basis perpendicular to $\mathbf{k}_s$ taken as $(\mathbf{e}_x^{(s)}, \mathbf{e}_y^{(s)}) = (\hat{\pi}_s, \widehat{\sigma}_s)$, there is no polarization mixing $x \leftrightarrow y$, and the four coupled linear equations of eq. (3.73) separate into two sets of 2×2 coupled linear equations, one set containing only the x amplitudes and the second only the y amplitudes.

2. A second special case occurs when J_z is *conserved*, and the quantization axis $\hat{\mathbf{z}}_J$ (direction of the internal magnetic field and symmetry axis of the quadrupole field) at each Mössbauer nucleus is *perpendicular* to the scattering plane $(\mathbf{k}_r, \mathbf{k}_0)$.

Each hyperfine split resonance is now a good ΔJ_z transition. As discussed in section 2.4, for elastic scattering, the polarization response of a pure qL multipole transition with $\Delta J_z = M$ is precisely that of a qL, $\Delta J_z = M$ *classical oscillator*, with symmetry axis along the quantization axis $\hat{\mathbf{z}}_J$ (which is *perpendicular* to the scattering plane $(\mathbf{k}_r, \mathbf{k}_0)$). In this situation, there is no polarization mixing $x \leftrightarrow y$ if the polarization basis is again taken as $(\mathbf{e}_x^{(s)}, \mathbf{e}_y^{(s)}) = (\hat{\pi}_s, \widehat{\sigma}_s)$.

For example, for an E1 resonance, the $\Delta J_z = \pm 1$ resonances correspond to right$(+)$ and left$(-)$ hand-side circularly polarized electric dipole oscillations about $+\hat{\mathbf{z}}_J$, while $\Delta J_z = 0$ resonances correspond to linear oscillation along $\pm\hat{\mathbf{z}}_J$. With $\hat{\mathbf{z}}_J \perp (\mathbf{k}_r, \mathbf{k}_0)$, incident $\hat{\pi}_0$ polarized radiation couples only to the $\Delta J_z = \pm 1$ oscillators, which emit $\hat{\pi}_{\rm f}$ polarized radiation in the $(\mathbf{k}_r, \mathbf{k}_0)$ plane, and incident $\widehat{\sigma}$ radiation couples only to the $\Delta J_z = 0$ oscillators, which emit $\widehat{\sigma}$ polarized radiation in the $(\mathbf{k}_r, \mathbf{k}_0)$ plane.

3. A third interesting special case where it is possible to simultaneously diagonalize the scattering matrices is for a *pure magnetic reflection* from a *simple antiferromagnet*, under the conditions that J_z is *conserved*, and that the quantization axis $\hat{\mathbf{z}}_J$ at each Mössbauer nucleus lies *in* the $(\mathbf{k}_r, \mathbf{k}_0)$ scattering plane.

This is a more complex situation because for *forward scattering* ($0 \to 0$ or $r \to r$) $\hat{\pi}$ polarized radiation scatters only into $\hat{\pi}$, and $\widehat{\sigma}$ scatters only into $\widehat{\sigma}$, but for *reflection* ($0 \leftrightarrow r$), $\hat{\pi}$ scatters into $\widehat{\sigma}$, and $\widehat{\sigma}$ scatters into $\hat{\pi}$.

To see this, consider the simple case of an E1 Mössbauer transition ($f_{\mathrm{E1}} = A_0 \mathbf{e}_{\mathrm{f}}^* \cdot \mathbf{e}_0 + \mathrm{i}A_1(\mathbf{e}_{\mathrm{f}}^* \times \mathbf{e}_0) \cdot \hat{\mathbf{z}}_J + A_2(\mathbf{e}_{\mathrm{f}}^* \cdot \hat{\mathbf{z}}_J)(\mathbf{e}_0 \cdot \hat{\mathbf{z}}_J)$), with two atoms ($\pm\hat{\mathbf{z}}_J$) in the magnetic unit cell. The *unit cell* forward scattering amplitude is then proportional to $2A_0\mathbf{e}_{\mathrm{f}}^* \cdot \mathbf{e}_0 + 2A_2(\mathbf{e}_{\mathrm{f}}^* \cdot \hat{\mathbf{z}}_J)(\mathbf{e}_0 \cdot \hat{\mathbf{z}}_J)$ (plus an electronic contribution proportional to $\mathbf{e}_{\mathrm{f}}^* \cdot \mathbf{e}_0$, assuming the resonance energy is far removed from any atomic absorption edges), while for a pure magnetic reflection, the unit cell reflection amplitude is proportional to $2A_1(\mathbf{e}_{\mathrm{f}}^* \times \mathbf{e}_0) \cdot \hat{\mathbf{z}}_J$ (for a pure magnetic reflection, the electronic contribution vanishes, as do the resonant terms of f_{E1} which contain even powers of $\hat{\mathbf{z}}_J$). With $\hat{\mathbf{z}}_J$ in the $(\mathbf{k}_r, \mathbf{k}_0)$ scattering plane, $\hat{\mathbf{z}}_J \cdot \widehat{\sigma} = 0$, and it is easy to verify that the polarization response for forward scattering and reflection from the unit cell is that discussed above.

Because for forward scattering the polarization state ($\hat{\pi}$ or $\widehat{\sigma}$) is conserved, while reflection changes the state ($\hat{\pi} \to \widehat{\sigma}$ or $\widehat{\sigma} \to \hat{\pi}$), it follows that if we take the **x**, **y** basis vectors for the $(0+)$ and (r) channels as $(\mathbf{e}_x^{(0)}, \mathbf{e}_y^{(0)}) = (\hat{\pi}_0, \widehat{\sigma})$ and $(\mathbf{e}_x^{(r)}, \mathbf{e}_y^{(r)}) = (\widehat{\sigma}, -\hat{\pi}_r)$, there is no polarization mixing $x \leftrightarrow y$.

For all cases where there is no polarization mixing $x \leftrightarrow y$, the four coupled linear equations of (3.73) separate into two sets of 2×2 coupled linear equations, one set containing only the x amplitudes and the other only the y amplitudes. There is then a simple analytical solution for the reflected and transmitted waves:

If the incident radiation is near a Bragg angle for a reflection channel $r = (1-)$ as shown in figure 8(c), then

$$(g_0 + g_1)d = 2n\pi + 2\delta. \tag{3.75}$$

We note that with g_0 and g_1 given by eq. (3.20), eq. (3.75) defines δ in terms of the angle of incidence ϕ_0 and, for asymmetric reflections, the x, y orientation of $\mathbf{k}_0$. For a symmetric reflection ($r = (0-)$), $\delta = k_0 d \cos\phi_0 \delta\phi$, where ϕ_0 is now understood to be the exact Bragg angle, and $\delta\phi$ is the deviation of the incidence angle from exact Bragg.

The dispersion equation then gives two values of k'_λ ($\lambda = x, y$),

$$k'_\lambda = \frac{g_0 d - \delta + \alpha_\lambda \pm \beta_\lambda}{d}, \tag{3.76}$$

where

$$\alpha_\lambda = \frac{1}{2}\left(F_{\lambda\lambda}^{00} - F_{\lambda\lambda}^{11}\right), \tag{3.77}$$

$$\beta_\lambda = \sqrt{\eta_\lambda^2 - F_{\lambda\lambda}^{01} F_{\lambda\lambda}^{10}}, \quad \mathrm{Im}\beta_\lambda > 0, \tag{3.78}$$

$$\eta_\lambda = \delta + \frac{1}{2}\left(F_{\lambda\lambda}^{00} + F_{\lambda\lambda}^{11}\right), \tag{3.79}$$

and where the $F_{\lambda\lambda}^{ss'}$ are the planar scattering amplitudes defined by eq. (3.33).

The reflected wave in the $\mathbf{k}_1$ channel is then given by

$$\mathbf{R}^{(1)}(\delta,\omega) = \widetilde{R}\big(\omega;\hat{k}_1,\hat{k}_0;M\big)\mathbf{a}_0\big(\hat{k}_0,\omega\big), \tag{3.80}$$

where the 2×2 reflection matrix $\widetilde{R}$ is diagonal,

$$\big(\widetilde{R}\big(\omega;\hat{k}_1,\hat{k}_0;M\big)\big)_{\lambda\lambda} = \mathrm{i}m_\lambda F^{10}_{\lambda\lambda} \tag{3.81}$$

with m_λ given by

$$m_\lambda = \frac{\mathrm{i}}{\eta_\lambda + \mathrm{i}\beta_\lambda \cot(M\beta_\lambda)}. \tag{3.82}$$

Here $(M+1)$ is the number of layers. As noted before in eqs. (3.46) and (3.48), $R_\lambda(\delta,\omega)$ is strictly the wave incident from below on the first plane ($m=0$).

For *thick crystals* (such that $\mathrm{Im}(M\beta_\lambda)\gg 1$), $m_\lambda \approx \mathrm{i}/(\eta_\lambda+\beta_\lambda)$, and

$$R_\lambda(\delta,\omega) \approx -\frac{F^{10}_{\lambda\lambda}}{\eta_\lambda+\beta_\lambda}\,\mathbf{e}^{(0)*}_\lambda\cdot\mathbf{a}_0\big(\omega,\hat{k}\big), \tag{3.83}$$

which is the usual Darwin thick-crystal expression.[8] In the opposite limit of *thin films* (and very near Bragg), such that $|M\beta_\lambda|\ll 1$, then $m_\lambda \approx M/(1-\mathrm{i}M\eta_\lambda)$, and

$$R_\lambda(\delta,\omega) \approx \frac{\mathrm{i}MF^{10}_{\lambda\lambda}}{1-\mathrm{i}M\eta_\lambda}\mathbf{e}^{(0)*}_\lambda\cdot\mathbf{a}_0\big(\omega,\hat{k}\big). \tag{3.84}$$

The transmitted wave in the $\mathbf{k}_0$ channel is given by

$$\mathbf{T}^{(0)}(\delta,\omega) = \widetilde{T}\big(\omega;\hat{k}_0,\hat{k}_0;M\big)\mathbf{a}_0\big(\hat{k}_0,\omega\big), \tag{3.85}$$

where the diagonal 2×2 transmission matrix $\widetilde{T}$ is

$$\big(\widetilde{T}\big(\omega;\hat{k}_0,\hat{k}_0;M\big)\big)_{\lambda\lambda} = Q_\lambda^{-1}\exp\big[\mathrm{i}M(\alpha_\lambda+\beta_\lambda+g_0d-\delta)\big]. \tag{3.86}$$

Here

$$Q_\lambda = \frac{\eta_\lambda+\beta_\lambda}{2\beta_\lambda}\left[1-\mathrm{e}^{\mathrm{i}2M\beta_\lambda}\frac{\eta_\lambda-\beta_\lambda}{\eta_\lambda+\beta_\lambda}+\mathrm{i}m_\lambda(\eta_\lambda-\beta_\lambda)\big(1-\mathrm{e}^{\mathrm{i}2M\beta_\lambda}\big)\right]. \tag{3.87}$$

The denominator Q_λ has simple limiting forms for thick and thin crystals: $Q_\lambda = 1$ for *thick* films, and $Q_\lambda = [1-\mathrm{i}M(\eta_\lambda-\beta_\lambda)]$ for *thin* films.

3.6.1. Coherent enhancement

One of the most interesting features of resonant γ-ray optics is the phenomenon of "coherent enhancement" near a Bragg excitation – under proper conditions, a strong enhancement of the coherent radiative width occurs, due to a constructive collective interaction between the nuclei interacting through the resonant radiation field [11]. The

[8] In comparing with the standard results, e.g., [18, p. 428], note that the $|\gamma_m|$, $|\gamma_0|$ factors which appear in the X-ray results for asymmetrical reflections are the same as the $\sin\phi_{(s)}$ factors which are included in the $F^{ss'}_{\lambda\lambda}$.

integrated intensity of the reflected wave then maximizes near resonance, in optimum cases approaching 100% reflectivity, and also the transmitted intensity, although minimizing near resonance, is generally much greater than the off-Bragg intensity. (This occurs because the transmitted wave depends primarily on the $e^{iM\beta_\lambda}$ factor in (3.86), and β_λ, which depends on the square root of the difference between $\frac{1}{4}(F^{00}_{\lambda\lambda}+F^{11}_{\lambda\lambda})^2$ and $F^{01}_{\lambda\lambda}F^{10}_{\lambda\lambda}$, generally has a much smaller imaginary part than $F^{00}_{\lambda\lambda}$, which determines the off-Bragg transmission.)

The optimum conditions are to have a highly enriched crystal in which the resonant nuclear contribution to the coherent elastic scattering amplitude strongly dominates the nonresonant electronic contribution; to have a symmetric Bragg reflection (i.e., the $r=(0-)$ channel) so that $F^{11}_{\lambda\lambda}=F^{00}_{\lambda\lambda}$ and $F^{10}_{\lambda\lambda}=F^{01}_{\lambda\lambda}$; and to have a situation where the resonant nuclear scattering is isotropic in the $(\mathbf{k}_0,\mathbf{k}_1)$ scattering plane, so that $F^{10}_{\lambda\lambda}=F^{00}_{\lambda\lambda}$ for the nuclear scattering. These conditions optimize the radiative coupling between the contributing planes.

To illustrate coherent enhancement, we consider the particularly simple case of an "isotropic" M1 Mössbauer transition and a simple cubic lattice containing a fraction C of the resonant nuclei. We assume incident $\hat{\pi}$-polarized radiation (the incident **B** field, which couples to the M1 transition, is then $\hat{\sigma}$-polarized and the scattering is isotropic in the $(\mathbf{k}_0,\mathbf{k}_1)$ scattering plane), and a symmetric Bragg reflection. For this case we have (with $\mathbf{e}^{(s)}_x=\hat{\pi}^{(s)}$ for $s=0,1$)

$$\begin{aligned} F^{00}_{xx}&=F^{11}_{xx}=F_{\rm n}+F_{\rm e},\\ F^{10}_{xx}&=F^{01}_{xx}=F_{\rm n}+r_{\rm e}\cos(2\phi_0), \end{aligned} \tag{3.88}$$

where $2\phi_0$ is the scattering angle (ϕ_0 is the angle of incidence with respect to the xy planes), and

$$\begin{aligned} F_{\rm n}&=\frac{\lambda nd}{\sin\phi_0}f_{\rm n}=\frac{\lambda nd}{\sin\phi_0}\,\frac{1}{2}\lambda C f_{\rm M}\frac{2J_1+1}{2J_0+1}\,\frac{\Gamma_\gamma}{\Gamma}\,\frac{1}{[x(J_0,J_1)-{\rm i}]},\\ F_{\rm e}&=\frac{\lambda nd}{\sin\phi_0}f_{\rm e}(0)=\frac{\lambda nd}{\sin\phi_0}\left(-Zr_0+{\rm i}\frac{\sigma_{\rm e}}{4\pi\lambda}\right),\\ r_{\rm e}&=\frac{\lambda nd}{\sin\phi_0}f_{\rm e}(2\phi_0)=\frac{\lambda nd}{\sin\phi_0}\left(-F(2\phi_0)r_0+{\rm i}\frac{\sigma_{\rm e}}{4\pi\lambda}\right), \end{aligned} \tag{3.89}$$

where $x(J_0,J_1)=[E(J_1)-E(J_0)-\hbar\omega]/(\Gamma/2)$. $F_{\rm e}$ and $r_{\rm e}$ in (3.89) should, of course, be the coherent average of the Mössbauer and non-Mössbauer atoms. For a numerical estimate we take a thin iron crystal with $M\approx 10^4$ plane layers, containing 65% ^{57}Fe. Then for $\mathbf{e}_x=\hat{\pi}$ polarized resonant radiation incident at Bragg (with $C/\sin\phi_0=1$), we have $T\approx 0.04$, $R\approx 0.67$; while off-Bragg, $T\approx 2\times10^{-4}$ and $R\approx 2\times10^{-7}$. Thus, at Bragg, the reflectivity is increased by six orders of magnitude, and the transmitted intensity, although still small, is increased by two orders of magnitude compared to off-Bragg.

This enhancement of the coherent scattered radiation can be viewed as due to an enhancement of the partial width $\Gamma_{\rm c}$ for coherent scattering. For a highly enriched

crystal for which we can neglect $F_{\rm e}$ and $r_{\rm e}$ with respect to $F_{\rm n}$ near resonance, we have, in the thin-crystal limit of eq. (3.84),

$$R_x(\omega,\delta) \approx \frac{1}{1-{\rm i}M\delta}\,\frac{{\rm i}(\Gamma_{\rm c}/2)}{[\omega_0-\omega-{\rm i}(\Gamma/2)-({\rm i}\Gamma_{\rm c}/2)/(1-{\rm i}M\delta)}, \tag{3.90}$$

where the partial width for spatially coherent scattering is

$$\Gamma_{\rm c} = 2\pi n \lambda\!\!\!^{-2} l_{\parallel}(\mathbf{k}_0)\Gamma_{\rm coh}. \tag{3.91}$$

Here $\Gamma_{\rm coh} = [f_M C(2j_1+1)\Gamma_\gamma/(4j_0+2)]$ and $l_{\parallel}(\mathbf{k}_0) = Md/\sin\phi_0$ is the thickness of the crystal in the direction of $\mathbf{k}_0$. (Strictly, the total width $\Gamma = \Gamma_\gamma + \Gamma_\alpha$ in the denominator of (3.90) should be $\Gamma'_\gamma + \Gamma_\alpha$, where Γ'_γ is the partial width for *spatially incoherent* radiative decay and Γ_α is the partial width for internal conversion decay.)

Thus, the effect of the coherent interaction is to enhance the resonance width to Γ',

$$\Gamma' = \Gamma'_\gamma + \Gamma_\alpha + \frac{\Gamma_{\rm c}}{1+(M\delta)^2} = \Gamma'_\gamma + \Gamma_\alpha + \Gamma_{\rm c} \quad \text{at exact Bragg } (\delta = 0), \tag{3.92}$$

and additionally to shift the resonance frequency about Bragg,

$$\omega'_0 = \omega_0 + \Delta\omega_{\rm c}(\delta) = \omega_0 + \frac{M\delta}{1+(M\delta)^2}\frac{\Gamma_{\rm c}}{2}. \tag{3.93}$$

The enhancement of $\Gamma_{\rm c}$ is proportional to the number of layers of the crystal, and for sufficiently thick crystals, typically $M \approx 10^3 - 10^4$ layers, $\Gamma_{\rm c}$ will exceed $(\Gamma'_\gamma + \Gamma_\alpha)$ and coherent decay will dominate incoherent decay.

3.6.2. Nuclear excitons, superradiance and coherent enhancement

That radiative coupling can radically alter the radiative decay rate of an excited system relative to that of an isolated atom is well known [11,21–25]. Following [11], consider two identical nuclei with nondegenerate ground states a_1 and a_2 and excited states b_1 and b_2. Because of the radiative coupling between the nuclei, the exponentially decaying states (normal modes) are not b_1a_2 or a_1b_2, but rather the symmetric and antisymmetric combinations $(b_1a_2 \pm a_1b_2)/\sqrt{2}$. If Γ_γ is the partial width for radiative decay from either nucleus alone, the radiative decay rates of these two modes are

$$\Gamma_\pm = \frac{1}{2}\Gamma_\gamma\overline{|1 \pm \exp({\rm i}\mathbf{k}\cdot\mathbf{R})|^2} = \Gamma_\gamma\left(1 \pm \frac{\sin kR}{kR}\right), \tag{3.94}$$

where $\mathbf{k}$ is the wave vector of the emitted radiation, and $\mathbf{R}$ is the relative displacement between the two nuclei. For $kR \ll 1$, we have $\Gamma_+ \approx 2\Gamma_\gamma$ and $\Gamma_- \approx 0$. In this limit, the symmetric mode has an enhanced decay rate while the antisymmetric mode becomes nonradiative. We call the phenomenon that a collective state of a system has a radiative decay rate larger than that of a single nucleus "superradiance". If the decay rate is smaller than that of a single nucleus, the mode is "subradiant".

This behavior is easy to understand classically. The symmetric mode corresponds to two oscillators oscillating together in-phase, which, for $kR \ll 1$, doubles the dipole moment. The radiation fields are doubled and the radiation power is increased to four times that of a single oscillator. Since the total mechanical energy ε_{T} is also doubled, the decay rate for the system is $-(\mathrm{d}\varepsilon_{\mathrm{T}}/\mathrm{d}t)/\varepsilon_{\mathrm{T}} = 2\Gamma_\gamma$. In contrast, in the antisymmetric mode, the oscillators move 180° out of phase and the radiation fields from the two oscillators interfere destructively, giving a very weak (electric quadrupole) radiative decay.

In addition to the altered decay rates, the normal modes also exhibit shifted resonance frequencies. For the two-nuclei system, the resonance shifts are (averaged over the direction $\widehat{R}$)

$$\Delta\omega_{\pm} \approx \mp\Gamma_\gamma \frac{\cos(kR)}{kR}, \tag{3.95}$$

which will give large resonance shifts for $kR \ll 1$, with the symmetric mode oscillating at the lower frequency.

For a crystal of resonant nuclei, the effects can be much more pronounced. As a first approximation, the wave functions for the exponentially decaying excited states (normal modes) in a crystal might be expected to be of the form of Bloch waves,

$$\big|\psi_{\mathrm{e}}(\mathbf{q})\big\rangle = \frac{1}{\sqrt{N}} \sum_{l=1}^{N} \mathrm{e}^{\mathrm{i}\mathbf{q}\cdot\mathbf{R}_l} |e_l\rangle \big|G_0(l)\big\rangle, \tag{3.96}$$

where $|e_l\rangle|G_0(l)\rangle$ represents the state in which the lth nucleus is excited while all other nuclei remain in their ground states, $\mathbf{R}_l$ is the position of the lth nucleus and $\mathbf{q}$ is the Bloch vector. The partial width for the radiative decay of this "$\mathbf{q}$th mode" is (in the Golden Rule approximation)

$$\Gamma_{\mathrm{c}}(\mathbf{q}) = \frac{\Gamma_\gamma}{4\pi N} \int \mathrm{d}\Omega(\mathbf{n}) \left| \sum_{l=1}^{N} \exp\big[-\mathrm{i}(\mathbf{k}-\mathbf{q})\cdot\mathbf{R}_l\big] \right|^2, \tag{3.97}$$

where $\mathbf{k} = (\omega_0/c)\mathbf{n}$ is the wave vector of the outgoing radiation (ω_0 is the resonance frequency of the nuclei). Most states $|\psi_{\mathrm{e}}(\mathbf{q})\rangle$ are subradiant, with $\Gamma_{\mathrm{c}}(\mathbf{q})$ on the order of Γ_γ/N. However, if for some specific emission direction $\mathbf{n}$, the condition $\mathbf{k} - \mathbf{q} = \boldsymbol{\tau}$ holds, where $\boldsymbol{\tau}$ is a reciprocal vector of the crystal lattice, then the mode $|\psi_{\mathrm{e}}(\mathbf{q})\rangle$ will have a highly directional coherent decay about the $\mathbf{q} + \boldsymbol{\tau}$ direction at an enhanced decay rate

$$\Gamma_{\mathrm{c}} = \pi n \lambda\!\!\!^{-2} l_{\parallel}(\mathbf{q}+\boldsymbol{\tau})\Gamma_\gamma, \tag{3.98}$$

where $l_{\parallel}(\mathbf{q}+\boldsymbol{\tau})$ is the thickness of the crystal in the direction of $(\mathbf{q}+\boldsymbol{\tau})$ and n is the number of nuclei per unit volume. We will give a more detailed discussion of this result in section 4.1.4. For $\lambda = 1$ Å, $n = 0.1$ Å^{-3}, we get a decay rate $\Gamma_{\mathrm{c}} = \Gamma_\gamma$ for a crystal with a thickness of only 100 Å. Thus, in such a superradiant mode, if a crystal

is sufficiently thick, the coherent decay rate will dominate the incoherent radiative decay rate Γ_γ and the the decay rate due to internal conversion Γ_α.

Now, in fact, the Bloch waves $|\psi_e(\mathbf{q})\rangle$ are generally not the true radiative normal modes in a crystal. As discussed in [11] and shown in section 6, the proper forms of the eigenmodes for a parallel sided crystal have a sine or cosine modulation (coming in from the crystal faces) with a complex wave vector. Generally, the Bloch state $|\psi_e(\mathbf{q})\rangle$ is a superposition of these radiative eigenmodes, which have a spread of eigenfrequencies and decay rates. The important exception is the case in which $|\mathbf{q}| = \omega_0/c$ and $\mathbf{q}$ satisfies a Bragg condition $\mathbf{q}\cdot\boldsymbol{\tau} = (1/2)\boldsymbol{\tau}^2$, where $\boldsymbol{\tau}$ is a reciprocal lattice vector which is perpendicular to the parallel faces. In this case, $|\psi_e(\mathbf{q})\rangle$ is a superradiant eigenmode, radiating at the natural resonance frequency ω_0, and decaying at an enhanced decay rate including the contributions from coherent decay into both the $\mathbf{q}$ and $\mathbf{q}+\boldsymbol{\tau}$ directions,

$$\Gamma_c(\mathbf{q}) = \pi n\lambda^2\big[l_\parallel(\mathbf{q}) + l_\parallel(\mathbf{q}+\boldsymbol{\tau})\big]\Gamma_\gamma. \tag{3.99}$$

An important general result is that the eigenmodes are not Hermitian orthogonal, and, as a consequence, the decay of a general superposition state depends upon the spread of mode eigenfrequencies as well as the individual eigenmode decay rates.

This issue is of considerable current interest because it is now possible to create spatially coherent single exciton nuclear states $|\psi_e(\mathbf{k}_0)\rangle$ of the Bloch form by illuminating crystals containing resonant Mössbauer nuclei (e.g., ^{57}Fe) with synchrotron radiation pulses [26–28]. The resulting state has $\mathbf{k}_0 = (\omega_0/c)\mathbf{n}_0$, where ω_0 is the resonance frequency and $\mathbf{n}_0$ is the incidence direction of the synchrotron pulse. By proper choice of $\mathbf{n}_0$, $\mathbf{k}_0$ will satisfy a Bragg condition and the state $|\psi_e(\mathbf{k}_0)\rangle$ becomes a superradiant eigenmode decaying into the $\mathbf{k}_0$ and $\mathbf{k}_0+\boldsymbol{\tau}$ directions. For $\mathbf{k}_0$ off-Bragg, $|\psi_e(\mathbf{k}_0)\rangle$ is a superposition of various normal modes of different eigenfrequencies and decay rates. Nevertheless, as we will discuss in section 4.1.4, such a state still has an *initial* superradiant decay into the "forward" $\mathbf{k}_0$ direction, with Γ_c given by eq. (3.98) with $\boldsymbol{\tau} = 0$.

The normal mode breakup gives a different perspective on the scattering of external resonant radiation at Bragg and the coherent enhancement effect given in eqs. (3.90)–(3.93): the intermediate excited states in the scattering process are now the collective normal mode exciton states, and at exact Bragg ($\delta = 0$) for a symmetric Bragg reflection, the phasing is such that *only* the superradiant *eigenmode* state $|\psi_e(\mathbf{q}=\mathbf{k}_0)\rangle$ is excited, with resonance occurring at the natural resonance frequency ω_0, and with the coherent decay rate Γ_c given by eq. (3.99) (which agrees with eq. (3.91), noting that for the symmetric Bragg reflection $l_\parallel(\mathbf{k}_0+\boldsymbol{\tau}) = l_\parallel(\mathbf{k}_0)$). Rocking off-Bragg, in addition to the superradiant eigenmode, various other normal mode states are virtually excited, the weighted resonance energy is shifted from ω_0, and the effective width is decreased.

3.6.3. Thick crystal reflectivity curves

A qualitative insight into the dependence of the integrated reflected resonance scattering on the beam collimation, the rocking angle, the frequency, and the enrichment C of Mössbauer atoms is obtained by examining the angular dependence of the reflectivity curves $|R_\lambda(\delta,\omega)|^2$ for different incidence frequencies ω. In figures 9(a) and (b) we plot $|R_\lambda(\delta,\omega)|^2$ as a function of δ for a symmetric Bragg reflection from a thick crystal of ^{57}Fe in stainless steel, with enrichment concentrations $C = 0.02, 0.65$, respectively, and with $\phi_0 = 10°$. The incident polarization is $\mathbf{e}_x = \hat{\pi}$. $R_x(\delta,\omega)$ is then given by eq. (3.83), with the planar scattering amplitudes given by eqs. (3.88) and (3.89).

The curves labeled $x = \infty$ are the purely electronic scattering curves. As is well known, the reflected intensity for this case has a region of near total reflection for $\delta \propto -\Re(F_\mathrm{e} \pm r_\mathrm{e})$, where F_e and r_e are given by eq. (3.89).

In figure 9(a), the crystal has a weak concentration of Mössbauer atoms, $C = 0.02$. For this case, $F_\mathrm{n} \approx 1.1\times10^{-4}(x-\mathrm{i})^{-1}$ while $F_\mathrm{e} \approx -6.1\times10^{-4}+\mathrm{i}2.0\times10^{-5}$ and $r_\mathrm{e} \approx -3.3\times10^{-4}+\mathrm{i}2.0\times10^{-5}$. Thus, even at resonance, the dominant contributions to the coherent scattering amplitudes are the real parts of F_e and r_e, and the region of maximum scattering is still contained within the region $\delta \propto -\Re(F_\mathrm{e} \pm r_\mathrm{e})$. As the frequency of the incident radiation nears the resonance frequency, F_n is primarily imaginary and acts as an absorptive contribution to F_e and r_e. As shown in figure 9(a), the intensity within the maximum scattering region is strongly decreased, and it is clear that the integrated intensity will exhibit a minimum in the resonance region.

In figure 9(b), C is taken as 0.65, for which $F_\mathrm{n} \approx 3.5\times10^{-3}(x-\mathrm{i})^{-1}$, and F_n gives the dominant contribution to the scattering amplitudes near resonance. For this case the region of strong scattering is greatly broadened near resonance, with a maximum spread on the order of $|F_\mathrm{n}|_{\omega=\omega_0}$. This broadening of the scattering region can lead to a strong maximum for the integrated intensity. Of course, within the region $\delta \propto -\Re(F_\mathrm{e} \pm r_\mathrm{e})$,

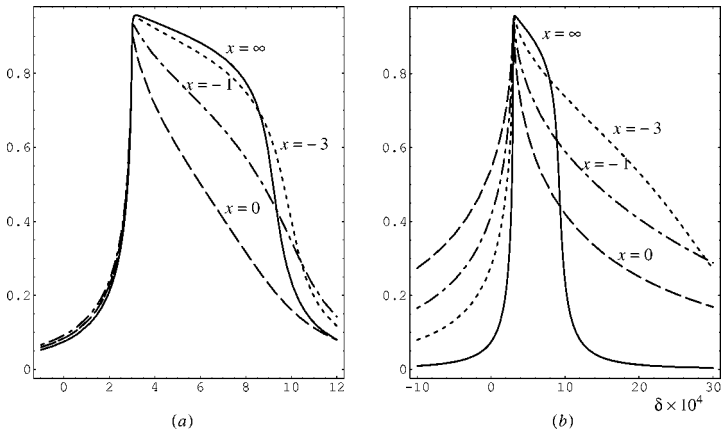

Figure 9. Thick crystal reflectivity curves for ^{57}Fe stainless steel with enrichments (a) $C = 0.02$, and (b) $C = 0.65$.

$|R_x(\delta,\omega)|^2$ as a function of frequency again strongly decreases near resonance, so if the incident beam is collimated to this region, a minimum will occur (for the case being considered, this corresponds to an angular collimation $\approx 4\times 10^{-4}$ rad). Qualitatively then, the reflected wave will maximize near resonance if the rms spread $\langle\delta\rangle$ satisfies $\langle\delta\rangle > |F_{\rm n}|_{\omega=\omega_0} > |r_{\rm e}|$, i.e., the most favorable conditions for a maximum are for highly enriched crystals, large scattering angles, and collimation spread larger than the region $\delta \propto -\Re(F_{\rm e} \pm r_{\rm e})$.

Finally, we note that polarization is important. For example, in the simple case considered above, for incident $\mathbf{e}_y = \widehat{\sigma}$ polarization, $R_y(\delta,\omega)$ is given by eq. (3.83) with the planar scattering amplitudes

$$\begin{aligned} F_{yy}^{00} &= F_{yy}^{11} = F_{\rm n} + F_{\rm e}, \\ F_{yy}^{10} &= F_{yy}^{01} = F_{\rm n}\cos(2\phi_0) + r_{\rm e}. \end{aligned} \tag{3.100}$$

An interesting point is that the reflected intensity will always minimize near resonance for a Bragg angle of $\phi_0 = 45^\circ$. This occurs because $\cos(2\phi_0) = 0$, so that the numerator of $R_y(\delta,\omega)$ only contains $r_{\rm e}$ and is frequency independent, while the denominator contains $F_{\rm n}$ and maximizes at resonance. This is analogous to the Brewster angle effect in optics, but modified by the multipolarity of the scattering: for $\phi_0 = 45^\circ$ and incident $\mathbf{e}_y = \widehat{\sigma}$, the magnetic dipoles respond to the incident $\hat{\pi}_0$ polarized **B** field, and hence oscillate in the direction of the reflected wave and do not contribute to the scattered field. Thus, the scattered wave is produced entirely by the electrons, which do strongly scatter the incident $\widehat{\sigma}$-polarized **E** field. However, the reflected wave from a layer will interact with the magnetic dipoles in upper layers, and this interaction dissipates energy from the reflected wave.

3.7. Grazing incidence

For grazing incidence reflection, there are again two channels open: the $t_0 = (0+)$ channel and the symmetric reflection channel $r = (0-)$. Grazing incidence reflection is, in fact, a special case of Bragg reflection with Bragg angle $\phi_{\rm B} = 0$.

If the incident photon is near grazing incidence with respect to the xy planes, the four scattering matrices $\widetilde{F}^{s's}$ $(s', s = 0, r)$ in eq. (3.74) can be taken equal to the forward scattering matrix $\widetilde{F}^{00}$ to order ϕ (where ϕ is the angle of grazing incidence). In this approximation, the matrices can all be simultaneously diagonalized, and the equations separate into two sets of Darwin–Prins equations, as in the special Bragg cases considered in section 3.6. Furthermore, since only $\widetilde{F}^{00}$ enters, the diagonalizing bases are the off-Bragg nonorthogonal eigenwaves $\mathbf{e}_\eta(\hat{k},\omega)$ given by eq. (3.58). Since only forward scattering amplitudes are involved, the optical solutions are valid for noncrystalline films as well as for crystals. The equivalence of this "two-wave" dynamical theory approach and the "one-wave" index of refraction approach is discussed in [29, appendix A].

The Bragg reflection solutions of section 3.6 can then be used, with appropriate modifications for the nonorthogonality of the bases. For an incident $\mathbf{e}_0 = \mathbf{e}_\eta(\hat{k}_0, \omega)$ photon, the reflected wave is given by eq. (3.83), which after some manipulation becomes

$$\mathbf{R}(\hat{k}_r, \omega) = R_\eta \mathbf{e}_\eta(\hat{k}_r, \omega), \tag{3.101}$$

$$R_\eta = \frac{1 - (1 + 2\lambda f_\eta/\phi^2)^{1/2}}{1 + (1 + 2\lambda f_\eta/\phi^2)^{1/2}}, \tag{3.102}$$

where f_η is given by eq. (3.57). For the special cases for which the eigenbases are orthogonal, the reflected wave for an incident photon of arbitrary polarization is given by

$$\mathbf{R}(\hat{k}_r, \omega) = \sum_{\eta=1,2} (\mathbf{e}^*_\eta \cdot \mathbf{e}_0) R_\eta \mathbf{e}_\eta. \tag{3.103}$$

For the general case where the $\mathbf{e}_\eta$ are nonorthogonal, the development follows the off-Bragg treatment, and the reflected wave is given by

$$\mathbf{R}(\hat{k}_r, \omega) = \widetilde{R}(\hat{k}_r, \hat{k}_0, \omega) \mathbf{a}_0(\hat{k}_0, \omega), \tag{3.104}$$

where the incident wave $\mathbf{a}_0$ is taken as a two-component column vector as in eq. (3.61), and the 2×2 reflection matrix is given by

$$\begin{aligned} \widetilde{R}(\hat{k}_r, \hat{k}_0, \omega) &= \begin{pmatrix} R_{xx} & R_{xy} \\ R_{yx} & R_{yy} \end{pmatrix} \\ &= \begin{pmatrix} \frac{1}{2}\left(R_{(+)} + R_{(-)} \frac{f_{xx} - f_{yy}}{f_1 - f_2} \right) & R_{(-)} \frac{f_{xy}}{f_1 - f_2} \\ R_{(-)} \frac{f_{yx}}{f_1 - f_2} & \frac{1}{2}\left(R_{(+)} - R_{(-)} \frac{f_{xx} - f_{yy}}{f_1 - f_2} \right) \end{pmatrix}, \end{aligned} \tag{3.105}$$

where

$$R_{(\pm)} = R_1 \pm R_2. \tag{3.106}$$

Here f_η and R_η ($\eta = 1, 2$) are given by eqs. (3.57) and (3.102).

In figure 10(a) we plot $|\mathbf{R}(\hat{k}_r, \omega)|^2$ as a function of ϕ for for several different frequencies about a resonance. Here we consider only a *single* resonance so that $f_\mathrm{n} = f_0/(x - \mathrm{i})$ with $x = 2(E_\mathrm{res} - \hbar\omega)/\Gamma$, and for f_0 we use the factors appropriate for grazing incidence of right-circular-polarized radiation in near resonance with the $m_0 = +1/2 \leftrightarrow m_1 = +3/2$ resonance of ^{57}Fe with $\mathbf{B} \parallel \mathbf{k}_0$. Off resonance there is a region of near total reflection for $\phi < \phi_\mathrm{c} = [-2\lambda \Re(f_\eta)]^{1/2} \approx 3.8 \times 10^{-3}$ rad. In the resonance region, the scattering amplitude f_η becomes primarily imaginary, and there

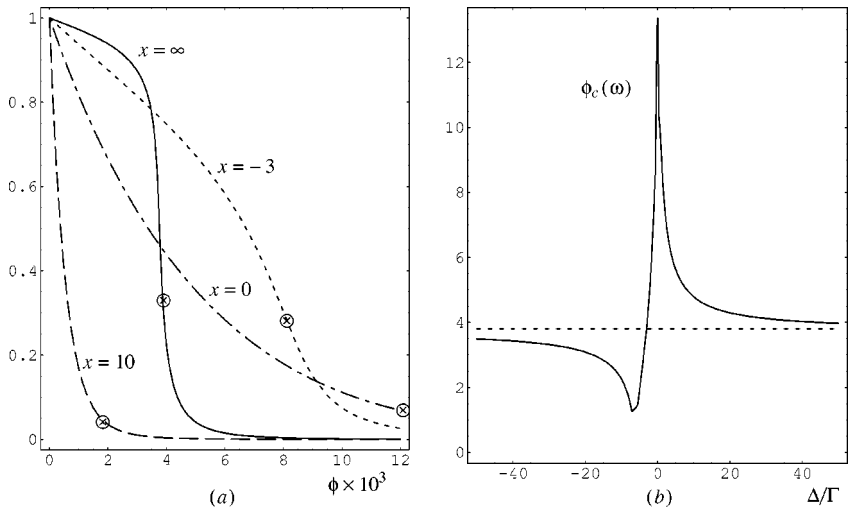

Figure 10. (a) $|R(\omega,\phi)|^2$ vs. ϕ for reflection from a resonant ^{57}Fe mirror for several different frequencies. The crosses indicate the angles $\phi_c(\omega)$. The X-ray critical angle is $\phi_c = 3.8$ mrad. (b) $\phi_c(\omega)$ vs. $\Delta/\Gamma = (\hbar\omega - E_{res})/\Gamma$. The scale is mrad, and the dotted line indicates the X-ray critical angle ϕ_c.

is no well-defined critical angle. Nevertheless, a rough characterization of the curves is given by the "frequency-dependent critical angle" $\phi_c(\omega)$,

$$\phi_c(\omega) = \max\left\{\sqrt{|2\chi\Re(f_\eta)|},\ \sqrt{2\chi\Im(f_\eta)}\right\}.$$

In figure 10(a) the positions of $\phi_c(\omega)$ are indicated by crosses. The region $\phi < \phi_c(\omega)$ is a region of strong scattering for a wave of frequency ω. In figure 10(b) we plot $\phi_c(\omega)$ for the same resonance. $\phi_c(\omega)$ is enhanced on the high-frequency side of the resonance, where the nuclear contribution to the index of refraction interferes constructively with the electronic contribution, and the angular region of strong reflection is much broader than far off resonance (ϕ_c). Correspondingly, there is a minimum for $\phi_c(\omega)$ on the low-frequency side of the resonance, where the nuclear scattering interferes destructively with the electronic scattering, and the angular region of strong scattering is much smaller than ϕ_c.

From figure 10(a) it is clear that if the beam is incident below the electronic ϕ_c, then as a function of frequency the reflected intensity will exhibit a sharp *minimum* on the low-frequency side of the resonance (where $\phi_c(\omega)$ minimizes). Similarly, if $\phi > \phi_c$, the reflected intensity will have a sharp *maximum* on the high-frequency side of the resonance.

In figures 11(a) and (b) we plot $|R(\omega,\phi)|^2$ vs. ω for grazing-incidence reflection from ^{57}Fe at angles $\phi = 3.0$ and 4.4 mrad, which lie below and above the electronic critical angle $\phi_c = 3.8$ mrad. Here the magnetic field at the nucleus lies in the plane of the film and perpendicular to $\mathbf{k}_0$, so the eigenpolarizations are the linear basis $\hat{\pi}, \hat{\sigma}$. The solid lines give the response to incident $\hat{\sigma}$. The two $M = 0$ transitions couple only to $\hat{\pi}$ radiation, and the four $M = \pm 1$ transitions couple only to $\hat{\sigma}$ radiation.

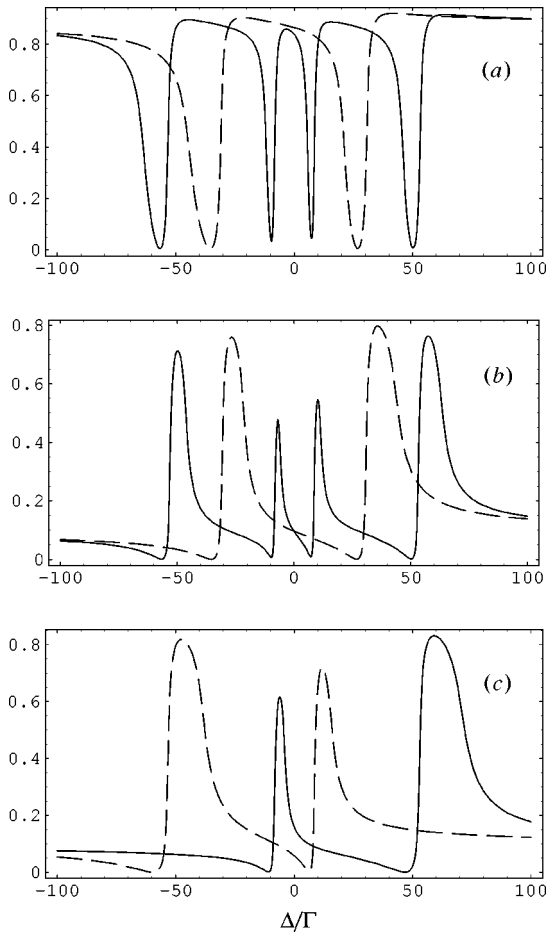

Figure 11. (a) $|R(\omega,\phi)|^2$ vs. ω for reflection from a resonant ^{57}Fe mirror for (a) $\mathbf{B}\perp\mathbf{k}_0$, $\phi = 3.0$ mrad, and (b) $\phi = 4.4$ mrad. The solid line gives the response for incident $\widehat{\sigma}$ polarization, the dashed line for incident $\hat{\pi}$. In (c), $\mathbf{B}\parallel\mathbf{k}_0$, $\phi = 4.4$ mrad. The solid line is for incident $\mathbf{e}_{(+1)}$, the dashed line for incident $\mathbf{e}_{(-1)}$.

The strongest polarization coupling is that of $\hat{\pi}$ polarization to the linear $M = 0$ oscillators ($|\hat{\pi}\cdot\widehat{\mathbf{Y}}^{(m)}_{10}(\hat{k}_0)|^2 = 1$, while $|\widehat{\sigma}\cdot\widehat{\mathbf{Y}}^{(m)}_{1\pm1}(\hat{k}_0)|^2 = 1/2$). The Clebsch–Gordan coefficients are $C^2 = 2/3$ for the two $M = 0$ transitions, $C^2 = 1$ or $1/3$ for the two $M = +1$ transitions (the strongest is the $+1/2 \leftrightarrow +3/2$ transition), and similarly $C^2 = 1$ or $1/3$ for the two $M = -1$ transitions. For this geometry, the strongest oscillator strengths then occur for the $M = 0$ transitions ($C^2|\hat{\pi}\cdot\widehat{\mathbf{Y}}^{(m)}_{10}|^2 = 2/3$, while $C^2|\widehat{\sigma}\cdot\widehat{\mathbf{Y}}^{(m)}_{1\pm1}|^2 = 1/2$ or $1/6$), and we see in figure 11(b) that the strongest effects (higher peak reflectivities and broader widths) occur near these resonances. In agreement with our earlier discussion, for $\phi < \phi_c$, a sharp minimum occurs on the low-frequency side of each resonance, while for $\phi > \phi_c$ a sharp maximum occurs on the high-frequency side of each resonance.

In figure 11(c) we give the corresponding results for $\phi = 4.4$ mrad with **B** parallel to $\mathbf{k}_0$, for which the eigenpolarizations are the circular basis $\mathbf{e}_{(\pm1)}$. Now the solid line gives the response for $\mathbf{e}_{(+1)}$ radiation, and the dashed line for $\mathbf{e}_{(-1)}$ radiation. In this geometry the $M = +1$ transitions couple only to $\mathbf{e}_{(+1)}$ radiation, the $M = -1$ transitions couple only to $\mathbf{e}_{(-1)}$ radiation, and the $M = 0$ transitions are unexcited. The polarization coupling is now maximal, $|\mathbf{e}^*_{(\pm1)} \cdot \widehat{\mathbf{Y}}^{(m)}_{1\pm1}|^2 = 1$, and the oscillator strengths are $C^2|\mathbf{e}^*_{(\pm1)} \cdot \widehat{\mathbf{Y}}^{(m)}_{1\pm1}|^2 = 1$ or $1/3$. We note that in this geometry the oscillator strengths for the two strong $M = \pm1$ transitions ($\pm1/2 \leftrightarrow \pm3/2$, for which $C^2 = 1$) are stronger than those of the $M = 0$ transitions with $\mathbf{B} \perp \mathbf{k}_0$, and, in fact, this geometry gives the maximum possible oscillator strength in the case of hyperfine splitting. The only stronger coupling is for the unsplit case, for which the oscillator strength is increased from 1 to $4/3$.

An important extension of these considerations is grazing incidence reflection from multilayer media of resonant and nonresonant films, discussed by Röhlsberger [30] and Chumakov et al. [31] (in this issue), and in [29,32,33]. Thin-film interference techniques are of fundamental importance in modern optics. In the optical region, thin dielectric films are used to produce antireflection coatings, broad and narrow bandpass frequency filters, polarizers, dichroic mirrors for color-selective beam splitting, and multilayer high-reflectance dielectric mirrors. Many of these techniques have been extended to the UV and X-ray regions. For γ-ray optics, the important point is that if one or more of the films are highly enriched Mössbauer films, the index of refraction for near resonant radiation differs strongly from the index of refraction far off resonance, and as a consequence it is possible to use thin-film interference techniques to strongly suppress the off-resonance grazing incidence reflectivity while maintaining a very "bright" reflection for near resonance radiation, offering an "ultranarrow" bandpass filter for synchrotron radiation. By using different combinations of films and substrates, the response can be tailored to give narrow bandpass widths $\Delta\omega \approx \Gamma$ and correspondingly long delayed scattering times to optimize time filtering, or at the other extreme, to produce filters of very broad resonance width with $\Delta\omega \approx 100\Gamma$, which would be ideal for a high resolution X-ray source [32,33].

3.8. Laue

For a Laue-case Bragg reflection from a Mössbauer crystal, the two open channels are the $t_0 = (0+)$ incidence channel, and a "transmission" channel $t_1 = (1+)$, as shown in figure 8(d).

In parallel to the Bragg case, the general dynamical equations (3.40), (3.41) now contain only the two amplitudes $\mathbf{T}^0_{k'}$ and $\mathbf{T}^1_{k'}$,

$$\widetilde{C}(k') \begin{pmatrix} \mathbf{T}^0_{k'} \\ \mathbf{T}^1_{k'} \end{pmatrix} = 0, \tag{3.107}$$

where the coefficient matrix $\widetilde{C}(k')$ is now the 4×4 matrix

$$\widetilde{C}(k') = \begin{pmatrix} \left(\mathrm{e}^{-\mathrm{i}(g_0-k')d} - 1\right)\tilde{I} - \mathrm{i}\widetilde{F}^{00} & -\mathrm{i}\widetilde{F}^{01} \\ -\mathrm{i}\widetilde{F}^{10} & \left(\mathrm{e}^{-\mathrm{i}(g_1-k')d} - 1\right)\tilde{I} - \mathrm{i}\widetilde{F}^{11} \end{pmatrix}. \tag{3.108}$$

As in the Bragg case, the dispersion equation (3.44) is again of fourth order and, except for a few special cases, there is no simple analytical solution, but the numerical solution is easily obtained, as outlined in section 3.4.

The special cases again occur when the 2×2 forward scattering matrices $\widetilde{F}^{00}$ and $\widetilde{F}^{11}$, and the reflection matrices $\widetilde{F}^{10}$ and $\widetilde{F}^{01}$ can be simultaneously diagonalized with an appropriate choice of orthogonal polarization bases $\mathbf{e}_{\lambda}^{(0)}$ and $\mathbf{e}_{\lambda'}^{(1)}$ (λ and $\lambda' = x, y$). For these special cases, there is no polarization mixing $x \leftrightarrow y$, the four coupled linear equations of (3.107) separate into two sets of 2×2 coupled linear equations, and the resulting transmission matrices are diagonal.

If the incident radiation is near a Bragg angle for a transmission channel $t = (1+)$, as shown in figure 8(d), then

$$(g_0 - g_1)d = 2n\pi + 2\delta, \tag{3.109}$$

and the dispersion equation then gives ($\lambda = x, y$)

$$k'_{\lambda} = (g_0 d - \delta + \alpha_{\lambda} \pm \beta_{\lambda})/d, \tag{3.110}$$

where, for the Laue case,

$$\alpha_{\lambda} = \frac{1}{2}\left(F_{\lambda\lambda}^{00} + F_{\lambda\lambda}^{11}\right), \tag{3.111}$$

$$\beta_{\lambda} = \sqrt{\nu_{\lambda}^2 + F_{\lambda\lambda}^{01}F_{\lambda\lambda}^{10}}, \tag{3.112}$$

$$\nu_{\lambda} = \delta + \frac{1}{2}\left(F_{\lambda\lambda}^{00} - F_{\lambda\lambda}^{11}\right). \tag{3.113}$$

The square root is again taken so that $\Im(\beta_{\lambda}) > 0$.

The transmitted waves in the $\mathbf{k}_0$ and $\mathbf{k}_1$ channels are then given by

$$\mathbf{T}^{(0)}(\delta, \omega) = \widetilde{T}\left(\omega; \hat{k}_0, \hat{k}_0; l\right)\mathbf{a}_0\left(\hat{k}_0, \omega\right), \tag{3.114}$$

$$\mathbf{T}^{(1)}(\delta, \omega) = \widetilde{T}\left(\omega; \hat{k}_1, \hat{k}_0; l\right)\mathbf{a}_0\left(\hat{k}_0, \omega\right), \tag{3.115}$$

where the 2×2 transmission matrices $\widetilde{T}$ are diagonal,

$$\left(\widetilde{T}\left(\omega; \hat{k}_0, \hat{k}_0; l\right)\right)_{\lambda\lambda} = \left(\cos M\beta_{\lambda} + \mathrm{i}\nu_{\lambda}\frac{\sin M\beta_{\lambda}}{\beta_{\lambda}}\right)\mathrm{e}^{\mathrm{i}M(\alpha_{\lambda}+g_0 d-\delta)}, \tag{3.116}$$

$$\left(\widetilde{T}\left(\omega; \hat{k}_1, \hat{k}_0; l\right)\right)_{\lambda\lambda} = \left(\mathrm{i}F_{\lambda\lambda}^{10}\frac{\sin M\beta_{\lambda}}{\beta_{\lambda}}\right)\mathrm{e}^{\mathrm{i}M(\alpha_{\lambda}+g_0 d-\delta)}. \tag{3.117}$$

From eqs. (3.116) and (3.117), we see that for a *thin crystal*, very near Bragg, $T_{\lambda}^{(1)} \approx \mathrm{i}MF_{\lambda\lambda}^{10}$ and $T_{\lambda}^{(0)} \approx (1 + \mathrm{i}M\alpha_{\lambda})$. As a function of frequency, the $\mathbf{k}_1$ wave in this

case will exhibit a maximum in the region of constructive interference between the electronic and nuclear scattering, while the $\mathbf{k}_0$ wave exhibits a weak minimum.

For a *thick crystal* the dominant contributions to $T_\lambda^{(1)}$ and $T_\lambda^{(0)}$ come from the exponential term depending on the difference between α_λ and β_λ, i.e.,

$$\begin{aligned} T_\lambda^{(1)}(\delta,\omega) &\approx -\frac{1}{2}\mathbf{e}_\lambda^{(0)*}\cdot\mathbf{a}_0\frac{F_{\lambda\lambda}^{10}}{\beta_\lambda}\mathrm{e}^{\mathrm{i}M(\alpha_\lambda-\beta_\lambda+g_0d-\delta)}, \\ T_\lambda^{(0)}(\delta,\omega) &\approx \frac{1}{2}\mathbf{e}_\lambda^{(0)*}\cdot\mathbf{a}_0\left(1-\frac{\nu_\lambda}{\beta_\lambda}\right)\mathrm{e}^{\mathrm{i}M(\alpha_\lambda-\beta_\lambda+g_0d-\delta)}. \end{aligned} \tag{3.118}$$

The exponent in (3.118) determines the Laue penetration depth l_λ for the radiation field,

$$l_\lambda(\delta) = d\big[\Im(\alpha_\lambda-\beta_\lambda)\big]^{-1}. \tag{3.119}$$

Since the imaginary part of $\alpha_\lambda-\beta_\lambda$ will generally maximize in the resonance region, it is clear that, as a function of frequency, both the $\mathbf{k}_0$ and $\mathbf{k}_1$ waves will exhibit a minimum in the resonance region for a thick crystal (and it is only for the thin-film limit that a maximum will occur). Nevertheless, because the penetration depth depends on the difference between α_λ and β_λ, the transmitted intensity for the Laue case is greater than for the off-Bragg case, and for certain high symmetry situations in simple crystals, it is possible to strongly suppress either the nonresonant photoelectric absorption (X-ray Borrmann effect), or the resonant internal conversion absorption (γ-ray suppression effect).

3.8.1. X-ray Borrmann effect

For a symmetric Laue reflection for which the scattering planes are perpendicular to the crystal surface, $\phi_1=\phi_0$ and $F_{\lambda\lambda}^{11}=F_{\lambda\lambda}^{00}$. If, furthermore, there is only one atom per unit cell, then $F_{\lambda\lambda}^{01}=F_{\lambda\lambda}^{10}$. Under these conditions, at exact Bragg ($\delta=0$), the penetration depth for $\mathbf{e}_\lambda^{(0)}$ incident radiation is

$$l_\lambda(\delta=0) = d\big[\Im\big(F_{\lambda\lambda}^{00}-F_{\lambda\lambda}^{10}\big)\big]^{-1}. \tag{3.120}$$

If the frequency of the radiation is large compared to any of the atomic absorption edge frequencies, the coherent elastic X-ray scattering amplitude is given to good approximation by the isotropic limit, eq. (A.13). When this holds, the imaginary part of $F_{\lambda\lambda}^{10}$ differs from the imaginary part of $F_{\lambda\lambda}^{00}$ by two factors: the Debye–Waller factor $f_{\mathrm{D}}(\theta)$ and the polarization factor $\mathbf{e}_{\mathrm{f}}^*\cdot\mathbf{e}_0$, which is 1 for $\widehat{\sigma}$ polarization and $\cos(\theta)$ for $\hat{\pi}$ polarization. The Laue penetration depths are then

$$\begin{aligned} l_\sigma(\delta=0) &= \frac{2\cos(\theta/2)}{n\sigma_{\mathrm{e}}}\frac{1}{1-f_{\mathrm{D}}(\theta)}, \\ l_\pi(\delta=0) &= \frac{2\cos(\theta/2)}{n\sigma_{\mathrm{e}}}\frac{1}{1-\cos(\theta)f_{\mathrm{D}}(\theta)}. \end{aligned} \tag{3.121}$$

For $\hat{\sigma}$ polarization, the Laue penetration depth is greatly enhanced over the off-Bragg penetration depth,

$$l_{\mathrm{OB}} = \frac{2\cos(\theta/2)}{n\sigma_{\mathrm{e}}}, \tag{3.122}$$

the enhancement being

$$\frac{l_\sigma}{l_{\mathrm{OB}}} = \left[1 - f_{\mathrm{D}}(\theta)\right]^{-1} \approx \frac{1}{2\sin^2(\theta/2)}\frac{\lambda^2}{\langle x^2\rangle} = \frac{1}{2m^2\pi^2}\frac{d_{\mathrm{B}}^2}{\langle x^2\rangle}, \tag{3.123}$$

where x is the displacement of an atom from its equilibrium position due to zero point and thermal motion, and where, in the last expression, we have used the Bragg condition $k\sin\theta = m\pi/d_{\mathrm{B}}$, where d_{B} is the interplanar distance for the particular set of Bragg planes. For $\hat{\pi}$ polarization, the enhancement is

$$\frac{l_\pi}{l_{\mathrm{OB}}} = \left[1 - \cos(\theta) f_{\mathrm{D}}(\theta)\right]^{-1} \approx \left[2\sin^2(\theta/2)\right]^{-1}. \tag{3.124}$$

For an iron lattice at liquid-He temperature, and $\theta = 20^\circ$, the l_σ enhancement is $\approx 2.2 \times 10^2$, and the l_π enhancement is ≈ 17.

The deep penetration of the $\hat{\sigma}$ polarization occurs because for this polarization the radiation field establishes a standing wave pattern in the crystal with nodes at the lattice sites, greatly reducing the photoabsorption.

When the difference between the wave vectors $\mathbf{k}_0$ and $\mathbf{k}_1$ of two plane waves in the crystal is very nearly equal to a reciprocal lattice vector $\vec{\tau}$, as shown in figure 12(a), the waves satisfy the Bragg condition for reflection from the set of planes associated with $\vec{\tau}$ and will be strongly reflected one into the other. Neither the wave in $\mathbf{k}_0$ nor that in $\mathbf{k}_1$ by itself constitutes an eigenwave of the radiation field in the crystal; rather, the eigenwaves are linear combinations of the waves in these two channels. There are two linearly independent polarization vectors associated with each beam in the mode, $\hat{\pi}$ and $\hat{\sigma}$, and thus there are four eigenmodes associated with each two-beam Laue reflection. When the Bragg condition is satisfied exactly, the wave field of these eigenmodes within the crystal consists of traveling waves along the direction of propagation (along $\mathbf{k}_0 + \mathbf{k}_1$) and standing waves perpendicular to that direction.

At exact Bragg ($\delta = 0$) for a symmetric Laue reflection, incident $\hat{\sigma}$-polarized radiation is a superposition of two eigenmodes:

$$E_0\hat{\sigma}_0 \mathrm{e}^{\mathrm{i}\mathbf{k}_0\cdot\mathbf{r}} = \frac{1}{\sqrt{2}}\left(\mathbf{E}_{|2\sigma\rangle_2} + \mathbf{E}_{|1\sigma\rangle_2}\right), \tag{3.125}$$

where the eigenmodes are

$$\mathbf{E}_{|2\sigma\rangle_2} = \frac{E_0}{\sqrt{2}}\left(\hat{\sigma}_0 \mathrm{e}^{\mathrm{i}\mathbf{k}_0\cdot\mathbf{r}} + \hat{\sigma}_1 \mathrm{e}^{\mathrm{i}\mathbf{k}_1\cdot\mathbf{r}}\right) = \frac{E_0}{\sqrt{2}}\mathrm{e}^{\mathrm{i}kz\cos(\theta/2)} 2\mathrm{i}\hat{y}\sin\left(\frac{m\pi x}{d_{\mathrm{B}}}\right), \tag{3.126}$$

$$\mathbf{E}_{|1\sigma\rangle_2} = \frac{E_0}{\sqrt{2}}\left(\hat{\sigma}_0 \mathrm{e}^{\mathrm{i}\mathbf{k}_0\cdot\mathbf{r}} - \hat{\sigma}_1 \mathrm{e}^{\mathrm{i}\mathbf{k}_1\cdot\mathbf{r}}\right) = \frac{E_0}{\sqrt{2}}\mathrm{e}^{\mathrm{i}kz\cos(\theta/2)} 2\hat{y}\cos\left(\frac{m\pi x}{d_{\mathrm{B}}}\right). \tag{3.127}$$

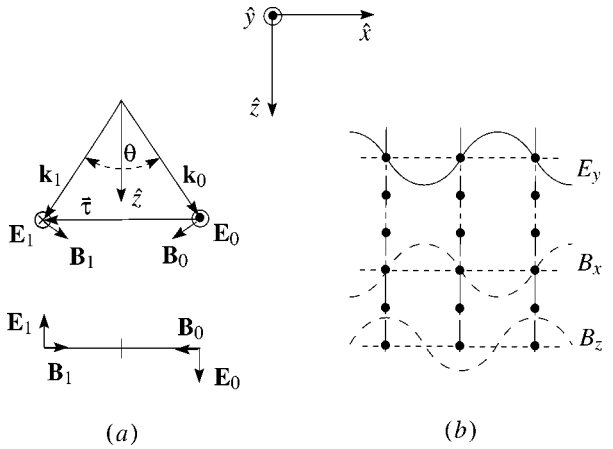

Figure 12. (a) Structure of the two-beam symmetric $\widehat{\sigma}$ eigenmode $|2\sigma\rangle_2$, corresponding to the reciprocal lattice vector $\vec{\tau}$, where the relative phase of the two beams is that which occurs at an atomic site. The lower figure shows a projection of the mode onto the plane perpendicular to the symmetry axis $\hat{z}$ of the mode. (b) Standing-wave fields produced within the crystal in mode $|2\sigma\rangle_2$. The solid vertical lines through the lattice points denote planes of nodal **E**.

Here we have used the geometry shown in figure 12 (and figure 14 in the next section).

In figure 12(b) we plot the standing waves of $\mathbf{E}_{|2\sigma\rangle_2}$ and its associated magnetic field $\mathbf{B}_{|2\sigma\rangle_2}$,

$$\begin{aligned}\mathbf{B}_{|2\sigma\rangle_2} &= \frac{E_0}{\sqrt{2}}\left(-\hat{\pi}_0 \mathrm{e}^{\mathrm{i}\mathbf{k}_0\cdot\mathbf{r}} - \hat{\pi}_1 \mathrm{e}^{\mathrm{i}\mathbf{k}_1\cdot\mathbf{r}}\right) \\ &= \frac{-E_0}{\sqrt{2}}\mathrm{e}^{\mathrm{i}kz\cos(\theta/2)}\left[2\mathrm{i}\hat{x}\cos\left(\frac{\theta}{2}\right)\sin\left(\frac{m\pi x}{d_\mathrm{B}}\right) - 2\hat{z}\sin\left(\frac{\theta}{2}\right)\cos\left(\frac{m\pi x}{d_\mathrm{B}}\right)\right].\end{aligned} \tag{3.128}$$

Note that, in this mode, the equilibrium position of each atom in the crystal lies within a nodal plane of the electric field. In contrast, for the $\mathbf{E}_{|1\sigma\rangle_2}$ mode, eq. (3.127), each atom is in an antinode of the electric field.

At typical X-ray energies, photoabsorption is predominantly electric dipole, so the photoabsorption rate is proportional to the average squared electric field at the atom, $\langle|\mathbf{E}|^2\rangle$. In the Borrmann mode ($|2\sigma\rangle_2$), each atom lies in a region of low electric field and the photoabsorption rate of this mode is reduced from the off-Bragg value of $\mu_\mathrm{OB} = n\sigma_\mathrm{e}$ to a value

$$\mu = g_\mathrm{e}\mu_\mathrm{OB} = g_\mathrm{e} n\sigma_\mathrm{e}, \tag{3.129}$$

where, to first order,

$$g_\mathrm{e}\left(|2\sigma\rangle_2\right) = 2k^2\sin^2(\theta/2)\left\langle x^2\right\rangle. \tag{3.130}$$

The factor $k^2 \sin^2(\theta/2)\langle x^2\rangle$ is the product of the mean-square amplitude of oscillation of the atom about its equilibrium position and the square of the x, y component of each wave vector in the mode. This occurs because the atoms oscillate about their equilibrium positions, and the electrons sample the nonzero electric field on either side of the node. Comparing eqs. (3.130) and (3.123), we see that $g_e(|2\sigma\rangle_2) = l_{OB}/l_\sigma$; $g_e(|2\sigma\rangle_2)$ can be quite small ($\approx$0.1–0.01), and radiation in the Borrmann mode will penetrate 10–100 times further in a good crystal than will radiation off-Bragg in the same material.

In contrast, the $|1\sigma\rangle_2$ mode has an enhanced **E**-field at each site, giving

$$g_e\big(|1\sigma\rangle_2\big) = 2, \tag{3.131}$$

and the two $\hat{\pi}$ modes also have nonzero **E**-fields at the lattice sites, giving

$$g_e\big(|2\pi\rangle_2\big) = 2\sin^2(\theta/2), \tag{3.132}$$

$$g_e\big(|1\pi\rangle_2\big) = 2\cos^2(\theta/2), \tag{3.133}$$

and as a consequence, the penetration depths ($= l_{OB}/g_e$) of these modes are much less than for the two-beam Borrmann mode $|2\sigma\rangle_2$. The **E** and **B** standing waves of the $|2\pi\rangle_2$ mode are shown in figure 13.

Returning to eq. (3.125), incident $\hat{\sigma}$ polarization is a superposition of $\mathbf{E}_{|2\sigma\rangle_2}$ and $\mathbf{E}_{|1\sigma\rangle_2}$. Within the crystal, the $\mathbf{E}_{|1\sigma\rangle_2}$ component is rapidly absorbed out, leaving the $\mathbf{E}_{|2\sigma\rangle_2}$ pattern deep in the crystal. The transmitted field at the bottom surface is then $\mathbf{E}_{|2\sigma\rangle_2}$, which then divides into two equal amplitude channels $\mathbf{k}_0$ and $\mathbf{k}_1$, each carrying 25% of the incident intensity (if $l \ll l_\sigma$). This is just the solution for $T_\sigma^{(0)}$ and

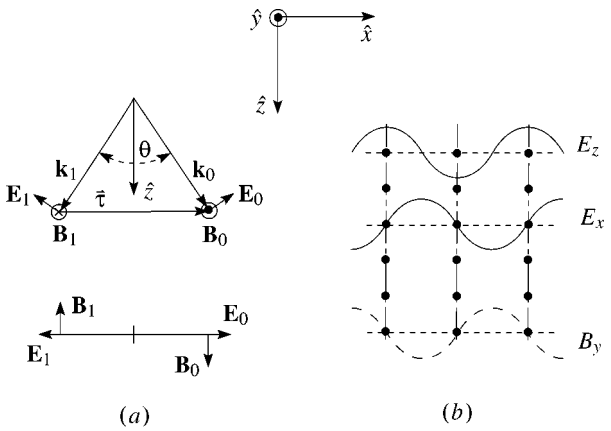

Figure 13. (a) Structure of the two-beam symmetric $\hat{\pi}$ eigenmode $|2\pi\rangle_2$, corresponding to the reciprocal lattice vector $\vec{\tau}$, where the relative phase of the two beams is that which occurs at an atomic site. The lower figure shows a projection of the mode onto the plane perpendicular to the symmetry axis $\hat{z}$ of the mode. (b) Standing-wave fields produced within the crystal in mode $|2\pi\rangle_2$. The solid vertical lines through the lattice points denote planes of nodal **B**.

$T_\sigma^{(1)}$ given by eq. (3.118) at exact Bragg, for the highly symmetric situation considered here.

3.8.2. γ-ray suppression effect

For the resonant Mössbauer nuclei, the effect is even more striking: because the resonant nuclear transitions take place over times much longer than crystal vibration times (10^{-8} s or longer as compared to 10^{-13} s), in contrast to the electronic interactions, which occur over a much shorter time period ($\approx 10^{-16}$ s), it is possible for the nuclei to effectively decouple from a two-beam Laue mode. Under these conditions, there is a complete suppression of all elastic and inelastic resonant γ-ray processes, and the nuclei become completely transparent to the mode. However, because the multipolarity of the Mössbauer transition is generally M1 or higher, the suppression effect mode will generally be different from the E1 Borrmann mode $|2\sigma\rangle_2$. This effect was first discussed by Afanas'ev and Kagan [14,34,35].

As for the X-ray Borrmann effect, the suppression effect is optimal in a simple crystal with one atom per unit cell (so $F_{\lambda\lambda}^{01} = F_{\lambda\lambda}^{10}$ for the "isotropic" limits) and for a symmetric Laue reflection (so $\phi_1 = \phi_0$ and $F_{\lambda\lambda}^{11} = F_{\lambda\lambda}^{00}$). Then at exact Bragg ($\delta = 0$), the penetration depth l_λ again depends inversely on $\Im(F_{\lambda\lambda}^{00} - F_{\lambda\lambda}^{10})$, as given by eq. (3.120), but now the planar scattering amplitudes F contain both the nuclear and electronic scattering amplitudes, $F = n\lambda d(f_\mathrm{e} + f_\mathrm{n})/\sin\phi_0$. Assuming the simplest situation of an unsplit Mössbauer line, the nuclear scattering amplitudes f_n are given by the isotropic limits given in eqs. (A.47)–(A.49) for E1, M1 and E2 transitions, respectively.

Because the resonant scattering is slow compared to crystal vibration times, the nuclear scattering amplitude contains the Mössbauer phonon factor $f_\mathrm{M} = \exp(-k^2\langle x^2\rangle)$ for both $\mathbf{k}_0 \to \mathbf{k}_1$ scattering and for forward scattering $\mathbf{k}_0 \to \mathbf{k}_0$. Thus, in contrast to the electronic scattering, which contains the Debye phonon factor $f_\mathrm{D}(\theta)$, $F_{\lambda\lambda}^{10}(n)$ differs from $F_{\lambda\lambda}^{00}(n)$ only by the *polarization factor* of the nuclear scattering.

As a consequence, for the nuclear scattering it is possible to have a complete equality of the $0 \to 1$ and the $0 \to 0$ scattering amplitudes, $F_{\lambda\lambda}^{10}(n) = F_{\lambda\lambda}^{00}(n)$. When this occurs, the nuclei become completely transparent to the deeply penetrating Laue mode – i.e., there is a complete suppression of all resonant nuclear scattering and absorption in this mode. The penetration depth of the suppression effect mode (SE mode) is determined entirely by photoabsorption, $l_\lambda = d/\Im(F_{\lambda\lambda}^{00}(e) - F_{\lambda\lambda}^{10}(e))$.

If the Mössbauer transition is E1 (e.g., the 6.25 keV transition of ^{181}Ta or the 25.7 keV transition of ^{161}Dy), then $f_\mathrm{n} \propto \mathbf{e}_\mathrm{f}^* \cdot \mathbf{e}_0$ for an unsplit line, just as for f_e in the isotropic limit. Then for incident $\widehat{\sigma}_0$ radiation, $F_{\sigma\sigma}^{10}(n) = F_{\sigma\sigma}^{00}(n)$, and the deeply penetrating SE mode is just the Borrmann $|2\sigma\rangle_2$ mode with nodes of the **E** field at the lattice sites, with penetration depth given by eq. (3.121). The other two-beam Laue modes ($|1\sigma\rangle_2$, $|2\pi\rangle_2$, $|1\pi\rangle_2$), which all have antinodes of **E** at the nuclei, are strongly absorbed at resonance.

Most Mössbauer transitions, however, are M1 or E2. For an M1 Mössbauer transition, for an unsplit line, $f_\mathrm{n} \propto \mathbf{b}_\mathrm{f}^* \cdot \mathbf{b}_0$, where $\mathbf{b} = (\hat{k} \times \mathbf{e})$ is the magnetic

polarization vector of the radiation field. Thus, an M1 transition responds to the **b** vector of the radiation field just as an E1 transition responds to the **e** vector. As a consequence, it is for $\mathbf{e} = \hat{\pi}$ radiation (for which $\mathbf{b} = \hat{\sigma}$), that the SE condition holds, i.e., $F^{10}_{\pi\pi}(n) = F^{00}_{\pi\pi}(n)$. The penetration depth l_π is strongly limited by photoabsorption, however, as given by eq. (3.123).

The effective decoupling of the $\hat{\pi}$ polarization from the M1 nuclear resonance occurs because for this polarization the radiation field is able to establish a standing wave pattern in the crystal with nodes of the *magnetic field* at the lattice sites. At exact Bragg ($\delta = 0$) for a symmetric Laue reflection, incident $\hat{\pi}$-polarized radiation is a superposition of two eigenmodes,

$$E_0\hat{\pi}_0 \mathrm{e}^{\mathrm{i}\mathbf{k}_0\cdot\mathbf{r}} = \frac{1}{\sqrt{2}}\big(\mathbf{E}_{|2\pi\rangle_2} + \mathbf{E}_{|1\pi\rangle_2}\big), \tag{3.134}$$

in parallel to eq. (3.125). The structure of the $|2\pi\rangle_2$ mode is shown in figure 13. Note that in this mode, the equilibrium position of each atom in the crystal lies within a nodal plane of the magnetic field, but in an antinode of the electric field. In the $|1\pi\rangle_2$ mode, there is a 180° phase change of the $\mathbf{k}_1$ wave, and the resulting standing wave patterns are shifted by 90° from the $|2\pi\rangle_2$ mode, so the $|1\pi\rangle_2$ mode has antinodes of both **E** and **B** at the lattice sites. Thus, at resonance, the $|1\pi\rangle_2$ component of the incident radiation is rapidly absorbed out by resonant nuclear absorption, leaving the $|2\pi\rangle_2$ pattern deep in the crystal. Resonant nuclear transitions take place over times much longer than crystal vibration times (10^{-8} s or longer as compared to 10^{-13} s), in contrast to the electronic interactions, which occur over a much shorter time period ($\approx 10^{-16}$ s). The coupling between the radiation mode and the nuclei is, thus, proportional to the *square of the average* of the appropriate component of the field at the nucleus, in this case $|\langle\mathbf{B}\rangle|^2 = 0$, rather than the average of the square $\langle|\mathbf{B}|^2\rangle$ as one would expect for a fast process [1].

Note that the M1 suppression effect mode $|2\pi\rangle_2$ is not a Borrmann mode, since it has a nonzero electric field at the equilibrium site of the atom and thus couples strongly to the electrons. Conversely, the Borrmann mode $|2\sigma\rangle_2$ will couple strongly to M1 Mössbauer nuclei, since, in this mode, each nucleus lies in a region of strong magnetic field (see eq. (3.128) and figure 12(b)). This mode will couple to higher-multipole transitions as well since the electric field gradient (EFG) and higher derivatives of the field are also large at the oscillator. In general, *it is not possible to obtain simultaneous suppression of both the nuclear and electronic coupling in the two-beam case for Mössbauer transitions of multipolarity M1 or higher in the absence of Zeeman splitting*. As we shall see in the next section, this is possible for multibeam modes.

For an unsplit E2 Mössbauer transition,

$$f_\mathrm{n} \propto \big(\hat{k}_\mathrm{f}\cdot\hat{k}_0\big)\big(\mathbf{e}^*_\mathrm{f}\cdot\mathbf{e}_0\big) + \big(\hat{k}_\mathrm{f}\cdot\mathbf{e}_0\big)\big(\hat{k}_0\cdot\mathbf{e}^*_\mathrm{f}\big).$$

Because f_n depends on the directions of both the wave vector $\hat{k}$ and of the polarization **e**, the E2 scattering is anisotropic for both $\hat{\sigma}$ and $\hat{\pi}$ polarizations, $F^{10}_{\sigma\sigma}(n) = F^{00}_{\sigma\sigma}(n)\cos(\theta)$ and $F^{10}_{\pi\pi}(n) = F^{00}_{\pi\pi}(n)\cos(2\theta)$, where θ is the scattering angle $\mathbf{k}_0 \to \mathbf{k}_1$.

The classical radiation pattern being produced by the "isotropic" E2 oscillator driven by incident $|\mathbf{k}_0\mathbf{e}_0\rangle$ radiation is a fourfold E2 pattern, with lobes along $\pm\mathbf{e}_0$ and $\pm\hat{k}_0$. Thus, for incident $\widehat{\sigma}_0$, which lies perpendicular to the $(\mathbf{k}_0, \mathbf{k}_1)$ scattering plane, $F^{10}_{\sigma\sigma}(n) = F^{00}_{\sigma\sigma}(n)$ only for 180° backscattering, $\mathbf{k}_1 = -\mathbf{k}_0$; while for incident $\hat{\pi}_0$, which lies in the $(\mathbf{k}_0, \mathbf{k}_1)$ scattering plane, $F^{10}_{\pi\pi}(n) = F^{00}_{\pi\pi}(n)$ for 90° scattering as well as for 180° scattering. As a consequence, there is no suppression effect possible for an unsplit E2 transition, except for the very special situation of a 90° Bragg angle, in which case the SE condition holds for $\hat{\pi}$ radiation, $F^{10}_{\pi\pi}(n) = F^{00}_{\pi\pi}(n)$.

Higher multipoles will also exhibit anisotropic scattering in any scattering plane, so *in the absence of hyperfine splitting, there can be no two-beam suppression effect for transitions of multipolarity E2 or higher, except for certain accidental situations where a Bragg angle coincides with a scattering symmetry.*

To this point we have assumed that there is no hyperfine splitting. If there is hyperfine splitting, then it is possible to have a two-beam suppression effect for selected ΔJ_z nuclear transitions for any multipole order and it is also possible to obtain a simultaneous suppression of both the electronic and nuclear coupling in the two-beam case:

The simplest situation is to have the local quantization axis $\mathbf{z}_J$ of each nucleus oriented parallel to the symmetry axis $\hat{z}$ of the symmetric Laue channel (i.e., the sample is ferromagnetically ordered in the $\hat{z}$ direction). For this symmetrical arrangement, $\mathbf{k}_0$ and $\mathbf{k}_1$ each make a polar angle $\theta/2$ relative to $\mathbf{z}_J$ (see figure 12), and the axial angles ϕ_0 and ϕ_1 differ by π, so that $\exp[\mathrm{i}M(\phi_1 - \phi_0)] = (-1)^M$. It then follows that the couplings of the oscillator to the two channels are related by

$$\mathbf{e}^{(1)}_\lambda \cdot \mathbf{Y}^{(q)}_{LM}(\hat{k}_1) = (-1)^M \mathbf{e}^{(0)}_\lambda \cdot \mathbf{Y}^{(q)}_{LM}(\hat{k}_0), \tag{3.135}$$

for $\mathbf{e}_\lambda = \widehat{\sigma}$ or $\hat{\pi}$ (see, e.g., the explicit $\mathbf{Y}^{(q)}_{LM}$ expressions for E1, M1 and E2 given in eqs. (A.22)–(A.24)). As a consequence, using the simple interference criteria discussed in the following section, *for even order transitions* ($\Delta J_z = 0, \pm 2, \ldots$), *there is no coupling to either* $|1\sigma\rangle_2$ *or* $|1\pi\rangle_2$; and *for odd order transitions* ($\Delta J_z = \pm 1, \pm 3, \ldots$), *there is no coupling to either the two-beam Borrmann mode* $|2\sigma\rangle_2$ *or to the mode* $|2\pi\rangle_2$.

Thus, simultaneous SE and Borrmann effects occur for any *well-isolated* odd order ΔJ_z transition (symmetrically oriented as discussed above), for example, for an M1 transition with $\Delta J_z = +1$. From the semiclassical point of view, the **B**-field standing wave of the $|2\sigma\rangle_2$ mode is in the $\hat{z}$ direction, as shown in figure 12, which is *orthogonal* to the $(\hat{x}, \hat{y})$-oscillation plane of the M1, $\Delta J_z = +1$ oscillator, so the $|2\sigma\rangle_2$ mode does not couple to this nuclear transition. However, the mode does couple to the $\Delta J_z = 0$ components, so strong resonance absorption will occur if the frequency is shifted to a $\Delta J_z = 0$ resonance.

3.8.3. Interferometry, Borrmann and suppression

The photon mode established deep in the crystal by the scattering/absorption in the upper layers (the $|2\sigma\rangle_2$ mode for the Borrmann case, or the $|2\pi\rangle_2$ mode for the isotropic M1 suppression effect) is a coherent two-channel mode. This is exactly

the situation produced in Bonse–Hart X-ray interferometry in the final plate of the interferometer where the two beams are brought back together.

The suppression of absorption (and scattering) that occurs in the Borrmann and SE effects is due to destructive interference between competing quantum processes.

Consider an atom which can be moved about the unit cell (for example, on the lower surface of the crystal). Let its equilibrium position be $\mathbf{r}$, with $\mathbf{r} = 0$ a lattice site (or extended lattice site on the lower surface). If the photon is in the $|2\sigma\rangle_2$ state, then the transition matrix element for K-shell photoabsorption is

$$\begin{aligned}\langle\Psi_\mathrm{f}|H_I|\Psi_0\rangle \propto{}& \langle\psi_{\mathbf{k}_\mathrm{e}}|\mathbf{p}\cdot\widehat{\sigma}_0|\psi_K\rangle\big\langle\chi_\mathrm{f}\big|\mathrm{e}^{\mathrm{i}(\mathbf{k}_0-\mathbf{k}_\mathrm{e})\cdot\mathbf{x}}\big|\chi_0\big\rangle\mathrm{e}^{\mathrm{i}(\mathbf{k}_0-\mathbf{k}_\mathrm{e})\cdot\mathbf{r}}\\ &+\langle\psi_{\mathbf{k}_\mathrm{e}}|\mathbf{p}\cdot\widehat{\sigma}_1|\psi_K\rangle\big\langle\chi_\mathrm{f}\big|\mathrm{e}^{\mathrm{i}(\mathbf{k}_1-\mathbf{k}_\mathrm{e})\cdot\mathbf{x}}\big|\chi_0\big\rangle\mathrm{e}^{\mathrm{i}(\mathbf{k}_1-\mathbf{k}_\mathrm{e})\cdot\mathbf{r}},\end{aligned}\tag{3.136}$$

where $\mathbf{k}_\mathrm{e}$ is the wave vector of the ejected photoelectron, and χ_0 and χ_f denote the initial and final crystal vibrational states. Since $\widehat{\sigma}_1 = -\widehat{\sigma}_0$, there will be destructive interference between the two processes if the atom is located at a lattice site ($\mathbf{r} = 0$), while at an interstitial, the two absorption amplitudes interfere constructively. The resulting total photoabsorption cross-section is then

$$\sigma = \sigma_\mathrm{e}\big[1 - f_\mathrm{D}(\mathbf{k}_1 - \mathbf{k}_0)\cos(\mathbf{k}_1 - \mathbf{k}_0)\cdot\mathbf{r}\big],\tag{3.137}$$

where σ_e is the usual photoabsorption cross-section, and $f_\mathrm{D}(\mathbf{k}_1 - \mathbf{k}_0) = f_\mathrm{D}(\theta)$ is the Debye phonon factor for photon scattering $\mathbf{k}_0 \rightarrow \mathbf{k}_1$. Thus, at a lattice site, photoabsorption is suppressed by the factor $[1 - f_\mathrm{D}(\theta)] \approx 2\sin^2(\theta/2)\langle x^2\rangle/\lambda^2$. For an iron lattice at liquid-He temperature, with 14.4 keV radiation and $\theta = 20^\circ$, the suppression is $\approx 4.5\times10^{-3}$.

Scattering is also suppressed in the Borrmann effect. The scattering amplitude for photon scattering $|2\sigma\rangle_2 \rightarrow |\mathbf{k},\mathbf{e}\rangle$ from an atom located at a position $\mathbf{r}$ within the unit cell is

$$\langle\mathbf{k},\mathbf{e}|\tilde{f}_\mathrm{e}(\mathbf{r})|2\sigma\rangle_2 = \frac{1}{\sqrt{2}}\big[f_\mathrm{e}(\mathbf{k},\mathbf{e};\mathbf{k}_0,\widehat{\sigma}_0)\mathrm{e}^{\mathrm{i}(\mathbf{k}_0-\mathbf{k})\cdot\mathbf{r}} + f_\mathrm{e}(\mathbf{k},\mathbf{e};\mathbf{k}_1,\widehat{\sigma}_1)\mathrm{e}^{\mathrm{i}(\mathbf{k}_1-\mathbf{k})\cdot\mathbf{r}}\big],\tag{3.138}$$

which is the coherent superposition of the two scattering processes $|\mathbf{k}_0,\widehat{\sigma}_0\rangle \rightarrow |\mathbf{k},\mathbf{e}\rangle$ and $|\mathbf{k}_1,\widehat{\sigma}_1\rangle \rightarrow |\mathbf{k},\mathbf{e}\rangle$. These two contributions interfere destructively if the atom is located at a lattice site ($\mathbf{r} = 0$) and if f_e is given by the isotropic limit (A.14), but the cancelation is not as complete as for photoabsorption: in addition to having different phonon factors as in eq. (3.136), the real parts also have different form factors, $\langle n(\mathbf{Q}_0)\rangle$ and $\langle n(\mathbf{Q}_1)\rangle$. The resulting cross-section for scattering is then suppressed by a factor $\approx[1 - \int\langle n(\mathbf{Q}_0)\rangle\langle n(\mathbf{Q}_1)\rangle\,\mathrm{d}\Omega_k/\int\langle n(\mathbf{Q}_0)\rangle^2\,\mathrm{d}\Omega_k]$, typically $\approx 10^{-1}$.

For the nuclear scattering and absorption processes, it is possible to have complete suppression. This occurs for two reasons. First, the Mössbauer phonon factor $f_\mathrm{M} = \exp(-k^2\langle x^2\rangle)$ replaces the Debye–Waller factor $f_\mathrm{D}(\mathbf{Q}) = \exp(-\frac{1}{2}Q^2\langle x^2\rangle)$. The important point is that f_M is essentially isotropic, while f_D depends on the momentum transfer and, hence, varies with the scattering angle θ. Secondly, there is no $\mathbf{Q}$-dependent form factor for nuclear scattering. Instead, the angular dependence is determined entirely by the multipole pattern of the particular Q_{LM} os-

cillator. Thus, for a properly oriented nuclear oscillator, it is possible to have $f_{\rm n}(\mathbf{k},\mathbf{e};\mathbf{k}_0,\mathbf{e}_0) = f_{\rm n}(\mathbf{k},\mathbf{e};\mathbf{k}_1,\mathbf{e}_1)$, and complete suppression can be achieved.

For resonant scattering or absorption, the transition amplitude has the general form

$$\sum_n \frac{\langle\Psi_{\rm f}|H_I|\Psi_{\rm n}\rangle\langle\Psi_{\rm n}|H_I(em)|\Psi_0\rangle}{[E_{\rm n}-E_0-\hbar\omega-{\rm i}\Gamma_{\rm n}/2]}, \tag{3.139}$$

where $H_I(em) = -c^{-1}\int {\rm d}\mathbf{x}\,\mathbf{j}_{\rm n}(\mathbf{x})\cdot\mathbf{A}(\mathbf{x})$ is the electromagnetic interaction potential for the nucleus, and H_I is the appropriate interaction potential for the decay. If the incident photon is in a coherent two-beam superposition state $|m\lambda\rangle_2$ ($m = 1$ or 2, $\lambda = \sigma$ or π), then the photon absorption part of the resonant amplitude (3.139) has the form

$$\langle 0|H_I(em)|m\lambda\rangle_2 \propto J^{(q)}_{LM}\big[\mathbf{Y}^{(q)*}_{LM}(\hat{k}_0)\cdot\mathbf{e}^{(0)}_\lambda + (-1)^m\mathbf{Y}^{(q)*}_{LM}(\hat{k}_1)\cdot\mathbf{e}^{(1)}_\lambda\big], \tag{3.140}$$

where we have assumed that the nuclear transition is a pure Q_{LM} multipole transition, and that the nucleus is located at a lattice site. Substituting (3.140) into (3.139), the resonant transition amplitude becomes a coherent superposition of two competing amplitudes, arising from the incident photon being in the $\mathbf{k}_0$- or the $\mathbf{k}_1$-channel, respectively. Complete destructive interference between these two amplitudes occurs if

$$\big[\mathbf{Y}^{(q)*}_{LM}(\hat{k}_0)\cdot\mathbf{e}^{(0)}_\lambda + (-1)^m\mathbf{Y}^{(q)*}_{LM}(\hat{k}_1)\cdot\mathbf{e}^{(1)}_\lambda\big] = 0. \tag{3.141}$$

If the local quantization axis $\mathbf{z}_J$ of each nucleus is oriented parallel to the symmetry axis $\hat{z}$ of the symmetric Laue channel (i.e., the sample is ferromagnetically ordered in the $\hat{z}$-direction), then $\mathbf{Y}^{(q)*}_{LM}(\hat{k}_0)\cdot\mathbf{e}^{(0)}_\lambda$ and $\mathbf{Y}^{(q)*}_{LM}(\hat{k}_1)\cdot\mathbf{e}^{(1)}_\lambda$ are related by eq. (3.135), leading to the following conclusions: *for even order transitions* ($\Delta J_z = 0, \pm2, \ldots$), *there is a complete suppression of resonant scattering and absorption in both the* $|1\sigma\rangle_2$ *and the* $|1\pi\rangle_2$ *modes*; and *for odd order transitions* ($\Delta J_z = \pm1, \pm3, \ldots$), *there is complete suppression in the two-beam Borrmann mode* $|2\sigma\rangle_2$ *and in the* $|2\pi\rangle_2$ *mode*.

Since the even and odd ΔJ_z transitions couple to different sets of modes, it is generally not possible to have an SE effect if there is no hyperfine splitting, except for E1 or M1 transitions. For an unsplit E1 transition, if we take $\mathbf{z}_J$ parallel to $\hat{z}$ as above, the $\Delta J_z = 0$ transitions correspond to a classical charge oscillating along the $\hat{z}$ axis and there is no coupling to $\widehat{\sigma}$-polarization. Thus the $|2\sigma\rangle_2$ mode will not couple to the $\Delta J_z = 0$ transitions and, as discussed above, suppression holds for this mode for the remaining $\Delta J_z = \pm1$ transitions. Similarly, for an unsplit M1 transition, the SE effect holds for the $|2\pi\rangle_2$ mode because the $\Delta J_z = 0$ transitions will not couple to $\hat{\pi}$-polarization, and suppression holds for the $\Delta J_z = \pm1$ transitions in this mode.

3.8.4. Enhancement and suppression

The enhancement effect and the nuclear Borrmann effect are distinct effects, but there is an aspect linking the two effects. In the Russian literature, the anomalous transmission at Laue, and the near total reflection occurring at Bragg in a thick crystal,

are both considered aspects of a single effect, the "suppression of inelastic channels" [14,15]. We use the term "suppression effect" to mean specifically the nuclear Borrmann effect.

For the nuclear Borrmann effect, which occurs in the symmetric Laue geometry, there is a *complete suppression* of all *elastic* and *inelastic* resonant processes. This is a quantum interference effect in which the photon is first put into a coherent two-beam symmetric Laue state (the $|2\sigma\rangle_2$ state for E1 Borrmann or the $|2\pi\rangle_2$ state for M1 Borrmann) by scattering and absorption from the atoms in the upper layers of the crystal. Once the mode is established, which requires 50% absorption of the incident $|\mathbf{k}_0, \mathbf{e}_\lambda^{(0)}\rangle$ radiation, there is a complete suppression of all further resonant scattering or absorption processes for a Mössbauer atom placed at a lattice site. This occurs because there are two coherent amplitudes leading to any final state $|\Psi_\mathrm{f}\rangle$ – either the absorbed photon is incident in the $|\mathbf{k}_0, \mathbf{e}_\lambda^{(0)}\rangle$ channel, or it is incident in the $|\mathbf{k}_1, \mathbf{e}_\lambda^{(1)}\rangle$ channel – and there is complete destructive interference between the two amplitudes.

The nuclear Borrmann effect is not a collective effect of coupled resonators. Once the coherent photon state is established, suppression occurs equally well for a *single* Mössbauer atom at a lattice site as for a collection of Mössbauer atoms at different lattice sites. Furthermore, the resonators need play no role in establishing the coherent two-beam photon state. For example, for E1 resonators, the $|2\sigma\rangle_2$ mode can be established by normal X-ray scattering and absorption in the upper layers, with the Mössbauer isotope atoms only being introduced at depths on the order of the Borrmann penetration depth, or at extended lattice sites on the exit surface.

The enhancement effect, on the other hand, is manifestly a collective effect between the interacting resonators: when a crystal of Mössbauer atoms is excited resonantly by an external monochromatic plane wave at a Bragg angle (in the Bragg geometry), there is an enhancement of the partial width for emission via coherent decay ($\Gamma_\mathrm{c} = 2\pi n\lambda^2 l_\parallel(\mathbf{k}_0)$) and a consequent suppression of the probability for incoherent decay ($P_{\gamma'} = \Gamma'_\gamma/(\Gamma_\mathrm{c} + \Gamma'_\gamma + \Gamma_\alpha)$), and of the probability for internal conversion decay ($P_\alpha = \Gamma_\alpha/(\Gamma_\mathrm{c} + \Gamma'_\gamma + \Gamma_\alpha)$). In the most ideal case, a single superradiant normal mode of the system of nuclei is excited. Γ_c is proportional to the thickness of the crystal, so for sufficiently thick crystals the probability for coherent decay approaches unity. From the temporal standpoint, the time scales for the various decay modes are $\hbar/\Gamma_\mathrm{c}$, $\hbar/\Gamma'_\gamma$ and $\hbar/\Gamma_\alpha$, respectively, so if the crystal is sufficiently thick that $\Gamma_\mathrm{c} \gg (\Gamma'_\gamma + \Gamma_\alpha)$, then with high probability the excited state decays "quickly" by coherent emission, rather than by the "slow" incoherent, inelastic decay processes.

This suppression of the *inelastic* processes which occurs at Bragg does have a "standing wave" interference aspect, analogous to the X-ray Borrmann and nuclear Borrmann effects: at exact Bragg, the excitation amplitudes of the nuclei are uniform throughout the crystal, each reduced to $1/M$ (relative to "unity" in the incident plane wave $\mathbf{E}_0$ alone). This occurs because in each layer, the wave $\mathbf{T}_m$ incident from above and the wave $\mathbf{R}_m$ incident from below almost cancel, the total field at the plane being reduced by $1/M$. For example, for a system of E1 resonators, with the incident field $\mathbf{E}_0$ being $\widehat{\sigma}$ polarized, $\mathbf{T}_m + \mathbf{R}_m = \pm(1/M)\mathbf{E}_0$. (At the bottom layer, $\mathbf{R}_M = 0$

and $\mathbf{T}_M = \pm(1/M)\mathbf{E}_0$; at the top layer, $\mathbf{T}_0 = \mathbf{E}_0$ and $\mathbf{R}_0 = -(1 - 1/M)\mathbf{E}_0$.) Thus, for *thick crystals*, the *local* field which each nucleus is subjected to is very nearly a $|2\sigma\rangle_2$ mode, which is the E1 Borrmann mode. (The propagation direction now lies in the plane in the direction of $(\mathbf{k}_0)_{xy}$, with "nodal" planes coinciding with the M layers.) The *probability* of incoherent scattering or absorption from each nucleus is then reduced by $(1/M)^2$. But there is, of course, no suppression of the coherent elastic scattering by the crystal: the *amplitude* for elastic scattering by each nucleus is reduced by $1/M$, but these amplitudes *add coherently* over the entire crystal, resulting in the enhanced coherent decay rate Γ_c and near total reflection.

In the enhancement effect, there is a strong enhancement of coherent elastic scattering, and correspondingly, a strong suppression of the inelastic processes; in the nuclear Borrmann effect, there is a complete suppression of all processes, elastic as well as inelastic.

For a system of resonators, there is a fundamental distinction between the Bragg and Laue geometries: for Bragg excitation, a superradiant normal mode is excited, while for Laue or off-Bragg excitation this is not the case. The normal modes of decay for a crystal of parallel planes are necessarily Bragg geometry modes because for a normal mode all planes must be *mutually coupled* – i.e., the upper planes must communicate to lower planes (T-channels) and the lower planes must communicate to the upper planes (R-channels). For the Laue case, and for off-Bragg, there is only forward communication (T-channels). Radiative normal modes are discussed in section 6.

When a crystal is excited by a *synchrotron pulse* rather than by a monochromatic plane wave, we also use the term "*coherent enhancement*" to describe the superradiant decay of the resulting nuclear exciton $|\psi_e(\mathbf{k}_0)\rangle$, because this is again a collective effect involving the same enhancement of the coherent decay rate, $\Gamma_c(\mathbf{k}_0) = m \cdot \pi n \lambda^2 l_{\|}(\mathbf{k}_0)\Gamma_\gamma$, where $\mathbf{k}_0$ is the phasing vector ($= (\omega_0/c)\mathbf{n}_0$), and m is the number of open channels. But there is an important difference now: the initial decay is superradiant regardless of the orientation of $\mathbf{k}_0$ – i.e., whether $\mathbf{k}_0$ satisfies Bragg-, off-Bragg-, or Laue-conditions. But the origin of the superradiance, and the delayed decay ($t > \hbar\Gamma_c^{-1}$), is radically different depending on whether or not $\mathbf{k}_0$ satisfies the Bragg condition. In all cases, there is also a suppression of inelastic processes, but this is now accomplished by the speedup of the coherent decay mode relative to the unaltered decay rates into the inelastic modes (there is no standing wave interference involved here). These aspects are discussed in section 6.

3.9. Multibeam Borrmann

In the two-beam Borrmann modes, the electric field is zero at the equilibrium position of each atom in the crystal, but the magnetic field and higher derivatives of the field (electric field gradient, magnetic field gradient, ...) are generally quite large in the vicinity of the atoms. Other modes exist in which the magnetic field is zero at each atomic site, but which have a large electric field near the atoms. Although there

are no *two-beam* modes in which the electric and magnetic fields are *simultaneously* zero at the atomic sites, there are *multibeam* modes, which occur when three or more beams simultaneously satisfy the Bragg condition, which do have both the electric and magnetic fields (or, in some cases, other higher-multipole derivatives of the field) simultaneously zero at the lattice sites. Other multibeam Borrmann modes exist in which the magnetic field (and other field derivatives) are enhanced near the vicinity of the atoms. (We use the term "Borrmann mode" to refer to any mode in which the *electric* field is zero at each atomic site in the crystal.)

As discussed by Hutton et al. [17], these properties of multibeam modes, coupled with the well-defined multipolarity of Mössbauer transitions, lead to three particularly interesting effects which occur at multibeam points of good single crystals containing Mössbauer nuclei:

(1) Certain multibeam Borrmann modes exhibit suppressed coupling both to the electrons and to the nuclei and will be anomalously transmitted at resonance, even when the nuclear transition is of multipolarity M1 or higher and there is no Zeeman splitting. Such simultaneous suppression is not possible in the usual two-beam case.

(2) Other multibeam Borrmann modes exhibit particularly strong coupling to the nuclei, so that nuclear absorption is greatly enhanced.

(3) Excited Mössbauer nuclei located at lattice sites within a crystal will have enhanced emission into certain of these weakly attenuated multibeam Borrmann modes ("anomalous emission").

While these last two effects can also occur in the two-beam case, greater enhancements are possible in multibeam modes, since the coupling is proportional to the number of beams in the mode.

3.9.1. Multibeam modes

Multibeam modes of the radiation field occur when the Bragg condition is satisfied simultaneously by three or more plane waves (beams) within the crystal. Except for certain very special frequencies, all the reciprocal lattice vectors involved in such a mode will be coplanar such that their endpoints lie on a circle. The wave vectors then lie on the surface of a cone whose base is defined by this circle, as shown in figure 14. The difference between any two of these vectors is then nearly equal to a reciprocal lattice vector and the wave in each channel will, in general, be strongly reflected into each of the others. For multibeam modes, we take θ to be the half-apex angle of the cone, as shown in figure 14 (previously, θ was the scattering angle $\mathbf{k}_0 \rightarrow \mathbf{k}_1$). Again, there are two linearly independent polarization vectors associated with each beam, so there are $2m$ eigenmodes associated with each m-beam point.

We restrict our consideration here to modes formed about high-symmetry axes. In our analysis we assume a perfect crystal which contains resonant nuclei located at lattice sites. Finally, we limit our discussion to that point in phase space where the

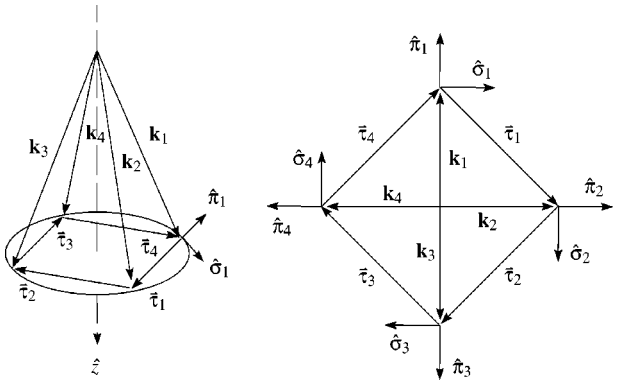

Figure 14. General structure of a multibeam mode, showing the polarization basis chosen for each beam. The $\widehat{\sigma}$'s lie in the plane containing the reciprocal lattice vectors (along $\hat{\phi}$(**k**) in the spherical coordinate system $(\hat{k}, \hat{\theta}, \hat{\phi})$, where now θ is the angle from the symmetry axis $\hat{z}$ to the wave vector **k**), and the $\hat{\pi}$'s lie out of this plane, along the $\hat{\theta}$(**k**) direction. The figure on the right shows a projection of the mode onto the plane perpendicular to $\hat{z}$. The four-beam case is shown, but similar modes exist for other numbers of beams.

Bragg condition is satisfied exactly for all the reflections in the mode and we restrict our attention to those modes whose structure is fully determined by the symmetry of the crystal [36].

The symmetry of a mode is determined by the symmetry of the axis of the reciprocal lattice about which it is formed. When there is no hyperfine splitting, the symmetry group of a mode centered about an n-fold rotation axis of the reciprocal lattice is the group of an n-sided regular polygon, that is, the group of rotations and reflections which leave that polygon invariant. When there is Zeeman splitting, with $\mathbf{z}_J$ parallel to the mode symmetry axis $\hat{z}$, reflections are no longer valid symmetry operations and the group reduces to the group of rotations which leaves the n-sided polygon invariant.

The set of eigenmodes associated with an m-beam case whose cone is centered about an m-fold rotation axis of the reciprocal lattice will contain either two (if m is odd) or four (if m is even) eigenmodes which are fully determined by symmetry,[9] and as such will be identical to the corresponding eigenmodes in the X-ray case, as determined by Joko and Fukuhara [37]. In complete analogy to the two-beam

[9] The set of $2m$ basis vectors $\{|\pi_s\rangle, |\sigma_s\rangle\}$, which spans the space of an m-beam mode, defines a *regular* representation of the symmetry group C_{mv}. In such a case, the number of times each irreducible representation appears among the eigenmodes is equal to the dimension of that representation (see, e.g., L.D. Landau and E.M. Lifshitz, *Quantum Mechanics. Non-Relativistic Theory* (Pergamon, Oxford, 1965)). One-dimensional irreducible representations appear only once and the structure of the eigenmodes to which they correspond is fully determined by symmetry. C_{mv} has either two (if m is odd) or four (if m is even) such one-dimensional irreducible representations. C_{mv} ($m > 2$) also has one or more two-dimensional irreducible representations. The modes to which they correspond are *not* fully determined by symmetry and their structure thus depends upon the multipolarity of the nuclear transition and the relative strength of the nuclear and electronic responses.

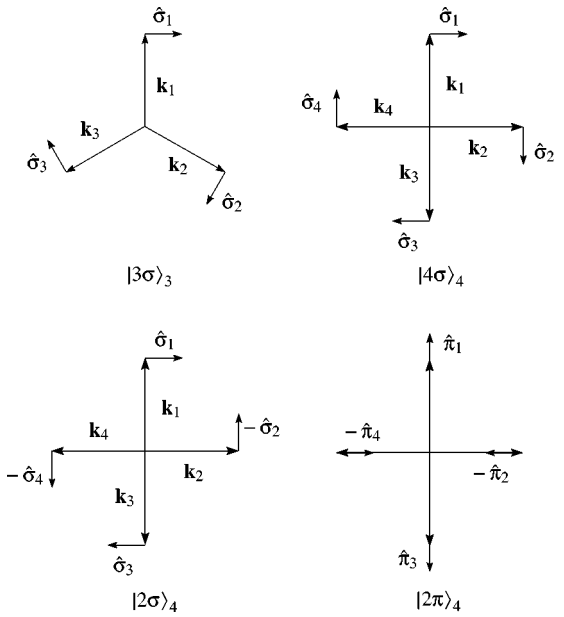

Figure 15. Structure of the three- and four-beam $|m\sigma\rangle_m$, $|(m/2)\sigma\rangle_m$ and $|(m/2)\pi\rangle_m$ Borrmann modes. In each case, the excitation pattern shown is that which occurs at an atomic site.

results, these modes have either all $\widehat{\sigma}$ or all $\hat{\pi}$ polarization channels excited with equal amplitude. $|m\sigma\rangle_m$ and $|m\pi\rangle_m$ have neighboring beams in phase so that they are invariant under a rotation of $2\pi/m$ about the cone axis (the notation used for the modes is that of Afanas'ev and Kohn [38][10]). In contrast, $|(m/2)\sigma\rangle_m$ and $|(m/2)\pi\rangle_m$ have neighboring beams π out of phase, so that they change sign under such a rotation [38]. $|(m/2)\sigma\rangle_m$ and $|(m/2)\pi\rangle_m$ exist only when m is even and are Borrmann modes for $m \geqslant 4$, while $|m\sigma\rangle_m$ is always a Borrmann mode; $|m\pi\rangle_m$ is never a Borrmann mode. The structure of the three- and four-beam $|m\sigma\rangle_m$, $|(m/2)\sigma\rangle_m$, and $|(m/2)\pi\rangle_m$ Borrmann modes are shown in figure 15.

3.9.2. Photoabsorption in the multibeam Borrmann modes

As for the two-beam Borrmann case, in the multibeam Borrmann modes each atom lies in a region of low electric field and the photoabsorption rate is reduced to $\mu = g_{\mathrm{e}} n \sigma_{\mathrm{e}}$, where the electronic coupling factors g_{e} for these modes are, to first order,

$$g_{\mathrm{e}} = \begin{cases} \frac{m}{2} k^2 \langle x^2 \rangle \sin^2\theta, & |m\sigma\rangle_m, \ \left|\frac{m}{2}\sigma\right\rangle_m, \\ \frac{m}{2} k^2 \langle x^2 \rangle \cos^2\theta \sin^2\theta, & \left|\frac{m}{2}\pi\right\rangle_m, \end{cases} \tag{3.142}$$

where θ is now the half-apex angle of the cone, as shown in figure 14. These modes differ in symmetry from the two-beam Borrmann mode in that here each atom lies on

[10] The subscript denotes the number of beams, the Greek letter denotes the polarization, while the first number gives the symmetry of the mode.

a *nodal line* of the electric field, rather than in a nodal plane. This accounts for the additional factor 2 in eq. (3.130).[11]

3.9.3. Multipole coupling to the multibeam Borrmann modes

Multibeam modes couple only to particular ΔJ_z components of multipole transition currents (where ΔJ_z is the change of angular momentum about the symmetry axis of the mode, which we take to be the $\hat{z}$ axis). As a consequence of this and certain polarization properties discussed below, multibeam modes couple only to particular electric multipole transitions of order L (EL) and particular magnetic multipole transitions (ML). The rules for coupling the multibeam Borrmann modes considered above to multipole currents may be summarized as follows:[12]

Mode	Couples only to	Couples to multipole
$\|m\sigma\rangle_m$	$\Delta J_z = 0, \pm m, \pm 2m, \ldots$	ML: $L \geqslant 1$; EL: $L \geqslant m$
$\|(m/2)\sigma\rangle_m, \|(m/2)\pi\rangle_m$	$\Delta J_z = \pm m/2, \pm 3m/2, \ldots$	ML: $L \geqslant m/2$; EL: $L \geqslant m/2$

As discussed below, these results are an immediate consequence of the rotational symmetries and polarization properties of the multibeam Borrmann modes and of the multipole radiation fields emitted by the various ΔJ_z transitions.

The radiation pattern of $|m\sigma\rangle_m$ is invariant under rotation by $2\pi/m$ about the symmetry axis of the mode, while the amplitude of the radiation field emitted by a ΔJ_z transition transforms as exp(i$\Delta J_z \phi$). Hence, $|m\sigma\rangle_m$ can couple only to $\Delta J_z = 0, \pm m, \pm 2m, \ldots$ transitions. For magnetic multipole transitions (ML), $|m\sigma\rangle_m$ couples to all orders (L) through the $\Delta J_z = 0$ components. This is easy to see physically since the circulating radiation pattern associated with these modes is polarized entirely along $\widehat{\sigma}$ and, for example in the M1 case, corresponds exactly to that of a classical magnetic dipole oscillating along the z axis. The radiation pattern associated with $\Delta J_z = 0$ components of electric transitions, on the other hand, is polarized entirely along $\hat{\pi}$ and is thus everywhere orthogonal to the field in $|m\sigma\rangle_m$. Thus, these modes do not couple to any electric transition (EL) with $L < m$. For example, $|3\sigma\rangle_3$ does not couple to E1 or E2 transitions, but will couple to E3 transitions through their $\Delta J_z = \pm 3$ components. Similarly, $|4\sigma\rangle_4$ will couple to E4 transitions, but not to E1, E2, or E3.

Similarly, the radiation patterns of $|(m/2)\sigma\rangle_m$ and $|(m/2)\pi\rangle_m$ change sign under a rotation by $2\pi/m$ about the symmetry axis of the mode, so these modes couple only to $\Delta J_z = \pm m/2, \pm 3m/2, \ldots$ components of multipole currents, which have radiation

[11] E1 polarization response goes as $\mathbf{e}_1^* \cdot \mathbf{e}_2$, so that to this order, $|4\sigma\rangle_4$ and $|2\sigma\rangle_4$ may be regarded as two independent $|2\sigma\rangle_2$ modes. Thus g_e for these two modes must equal that for $|2\sigma\rangle_2$, hence, the additional factor 2 in eq. (3.130).

[12] Other modes exist (see [17,37,38]) which couple to components of multipole currents other than $\Delta J_z = 0, \pm m/2, \pm m, \ldots$. For example, there exist four- and six-beam modes which couple only to $\Delta J_z = \pm 1, \pm(m+1), \ldots$ components, such as the $|1\sigma, \pi\rangle_4$ mode discussed in [17]. Similarly, there are six-beam modes which couple only to $\Delta J_z = \pm 2, \pm 8, \ldots$ components.

patterns that go as exp[i$(\pm m/2)\phi$] and exp[i$(\pm 3m/2)\phi$], ..., respectively. Thus, $|2\sigma\rangle_4$ and $|2\pi\rangle_4$ couple to M2, E2, and higher multipole nuclear transitions, but do not couple to M1 or E1. Similarly, $|3\sigma\rangle_6$ and $|3\pi\rangle_6$ couple to M3 and E3 transitions, but not to M1, E1, M2, or E2.

A nuclear coupling factor $g_{\rm n}$ may be defined in a manner exactly analogous to that used to define $g_{\rm e}$ in eqs. (3.129) and (3.142), so that the rate at which a mode is absorbed by the nuclei is given by

$$\mu_{\rm n} = g_{\rm n} n \sigma_{\rm n}, \tag{3.143}$$

The nuclear coupling factor $g_{\rm n}$ is given by

$$g_{\rm n} = \frac{\Im(\langle\psi_{\rm B}|\tilde{f}_{\rm n}|\psi_{\rm B}\rangle)}{\Im(\langle\psi_{\rm OB}|\tilde{f}_{\rm n}|\psi_{\rm OB}\rangle)}, \tag{3.144}$$

where $|\psi_{\rm B}\rangle$ is a multibeam eigenmode of the crystal such as those considered above, consisting of a coherent superposition of single plane waves, $|\mathbf{k}_i, \mathbf{e}_\lambda^{(i)}\rangle$, given by

$$|\psi_{\rm B}\rangle = \sum_{i\lambda} \psi_{i\lambda} \big|\mathbf{k}_i, \mathbf{e}_\lambda^{(i)}\big\rangle, \tag{3.145}$$

with

$$\sum_{i\lambda} |\psi_{i\lambda}|^2 = 1. \tag{3.146}$$

$|\psi_{\rm OB}\rangle = |\mathbf{k}, \mathbf{e}\rangle$ is a single plane wave off-Bragg. If there is no Zeeman splitting, then $\langle\psi_{\rm OB}|\tilde{f}_{\rm n}|\psi_{\rm OB}\rangle$ is independent of $\hat{\mathbf{k}}$ and $\mathbf{e}$.

The $g_{\rm n}$'s for coupling the Borrmann modes described above to the first few nuclear multipole transitions are given in table 1. The expression $g_{\rm n,M2}$ for $|2\sigma\rangle_2$ differs from that for the other $|m\sigma\rangle_m$ modes because $|2\sigma\rangle_2$ couples both to $\Delta J_z = 0$ and to $\Delta J_z = \pm 2$ components, which are allowed for M2 transitions, while the other $|m\sigma\rangle_m$ modes couple only to $\Delta J_z = 0$.

Table 1
$g_{\rm n}$'s for coupling Borrmann modes to good multipole nuclear transitions. Only the first two or three nonzero coupling factors are shown in each case. The symbols C and S used in the table refer to $\cos\theta$ and $\sin\theta$, respectively. Note that since these are Borrmann modes, none of them couple to E1 nuclear transitions.

	Transition					
Mode	E1	M1	E2	M2	E3	M3
$\|2\sigma\rangle_2$	0	$2S^2$	$2S^2$	$4S^2C^2$		
$\|m\sigma\rangle_m$	0	mS^2	0	$(3/2)mS^2$		
$\|2\sigma\rangle_4$	0	0	$4S^2$	$4S^2C^2$		
$\|2\pi\rangle_4$	0	0	$4S^2C^2$	$4S^2$		
$\|3\sigma\rangle_6$	0	0	0	0	$(45/8)S^4$	$(45/8)S^4C^2$
$\|3\pi\rangle_6$	0	0	0	0	$(45/8)S^4C^2$	$(45/8)S^4$

3.9.4. Multibeam Borrmann modes in γ-ray optics

These properties of multibeam modes, coupled with the well-defined multipolarity of Mössbauer transitions, lead to three particularly interesting effects which occur at multibeam points of good single crystals containing Mössbauer nuclei:

Simultaneous suppression of electronic and nuclear coupling. It follows immediately from the simple coupling rules given above that certain multibeam Borrmann modes do not couple to Mössbauer transitions of particular multipolarities (see table 1). Since both the electric field and the multipole component of the electromagnetic field driving the nuclear transition are zero at the equilibrium site of the atoms in such a mode, the coupling to both the electrons and the nuclei will be suppressed, regardless of whether or not there is Zeeman splitting of the nuclear transition. As noted before, this is not possible in the two-beam case.

For example, in the $|2\sigma\rangle_4$ Borrmann mode, there is no coupling to an M1 Mössbauer transition. This mode may be regarded as two independent $|2\sigma\rangle_2$ modes, rotated by 90° from each other and 180° out of phase. As a consequence, the nonzero magnetic standing wave B_z of the $|2\sigma\rangle_2$ mode, shown in figure 12, is canceled, so the electric and magnetic fields are simultaneously zero at the lattice site in the $|2\sigma\rangle_4$ Borrmann mode.

It is also interesting to note that for any $|m\sigma\rangle_m$ Borrmann mode with $m \geqslant 3$, there is no coupling to an E2 Mössbauer transition. In contrast, in the two-beam case there is no E2 suppression effect if there is no Zeeman splitting.

Enhanced nuclear absorption in multibeam Borrmann modes. While some Borrmann modes do not couple to particular nuclear transitions, others have an enhanced coupling and will be absorbed more strongly than will off-Bragg modes. While enhanced absorption occurs in the two-beam case [12,13,39,41], much greater enhancements are possible for multibeam modes.

For example, for an unsplit M1 transition, the coupling to the $|m\sigma\rangle_m$ Borrmann mode is $g_{\mathrm{n}} = m \sin^2\theta$, directly proportional to the number of beams. This occurs because the M1 multipole couples to the mode through the $\Delta J_z = 0$ transition which is driven by the B_z component of the incident radiation, and for the $|m\sigma\rangle_m$ mode, the m separate contributions to B_z coming from the m beams of the mode all add constructively at the lattice sites, leading to the m-fold enhancement of the resonant cross-section (m rather than m^2 because there is also a factor $1/\sqrt{m}$ in the normalization of the photon state $|m\sigma\rangle_m$).

Anomalous emission in multibeam Borrmann modes. It may be shown by applying the reciprocity theorem that the factor g_{n}, which gives the coupling between a radiation mode and a nuclear absorber, also describes the coupling between that mode and a nuclear emitter at the same site (section 3.10.2). Thus, $|m\sigma\rangle_m$ modes are fed by M1 and higher-order magnetic multipole emitters, $|3\sigma\rangle_6$ and $|3\pi\rangle_6$ by E3 and higher, etc. The fact that M1 and higher multipolarity excited nuclei can emit into certain of these weakly attenuated Borrmann modes is responsible for the predicted "anomalous

emission effect", in which waves emerge from a crystal from sources located at lattice sites deep within the crystal [13,17,39].

3.9.5. Multibeam Borrmann modes and crystalline γ-ray lasers

If a γ-ray laser can be achieved, it will necessarily have to rely upon the Mössbauer effect [42], so that the resonant nuclei must reside in a cool solid. There are important practical difficulties associated with pumping such a system while maintaining the conditions necessary for an appreciable recoilless fraction [43]. If these difficulties can be overcome, then there are significant advantages to be obtained by using a single crystal [40,41,44,45,48].

Lasing requires that the gain from stimulated emission exceed the losses from nonresonant absorption. The Schallow–Townes [46] steady-state lasing condition is $K \geqslant 0$, where K is the net gain in intensity per unit length, which for a γ-ray laser is given by

$$K = K_0 - \mu_\mathrm{e} = \sigma_\mathrm{n} g'_\mathrm{n} \Delta n - \sigma_\mathrm{e} g'_\mathrm{e} n_0. \tag{3.147}$$

For simplicity, we have assumed no hyperfine splitting. According to the linearized theory [47], the wave in the lasing mode will then amplify by e^{Kl} on traversing a distance l through the crystal.

In eq. (3.147) n_0 is the number density of atoms in the crystal, while σ_e is the nonresonant atomic absorption cross-section, which for Mössbauer energies (10–100 keV) will be almost entirely due to the electric dipole contribution to photoelectric absorption, σ_n is the nuclear absorption-stimulated emission cross-section at exact resonance, given by

$$\sigma_\mathrm{n} = \frac{2\pi \lambda\!\!\!^{-2} f_\mathrm{M}}{(1+\alpha)(1+a)} \frac{\Gamma_1}{\Gamma_1 + \Gamma_2}. \tag{3.148}$$

Here α is the internal conversion coefficient, while $(1 + a)$ represents the effects of inhomogeneous broadening. Γ_1 and Γ_2 are the total widths of the upper and lower lasing levels, respectively. $\Delta n = n_1 - (g_1/g_2)n_2$ is the population-inversion density, where n_1 and n_2 are the population densities in the upper and lower lasing levels, while $g_1 = 2j_1 + 1$ and $g_2 = 2j_2 + 1$ are the spin degeneracy factors. g'_e and g'_n describe the coupling of the electromagnetic field of the lasing mode to the atomic electrons and the nuclear resonators, respectively, and are related to g_e and g_n as given by eqs. (3.142) and (3.144) by

$$g'_s = \frac{g_s}{\cos\theta}, \quad s = \mathrm{e \text{ or } n}. \tag{3.149}$$

Here θ is the angle between the beams in the eigenmode and the direction of energy propogation (i.e., the symmetry axis of the eigenmode, as noted in figure 14). The factor $1/\cos\theta$ gives the increase in path length of the radiation in the mode as compared to a single plane wave traveling along the mode axis. In effect, the crystal consists of a series of weakly reflecting mirrors so that it acts as an etalon at the Bragg angles.

Setting $K = 0$ in eq. (3.147) and solving for Δn yields the threshold population-inversion density $\Delta n_{\rm t}$ given by

$$\Delta n_{\rm t} = \frac{g_{\rm e}}{g_{\rm n}} \frac{\sigma_{\rm e}}{\sigma_{\rm n}} n_0. \tag{3.150}$$

Equation (3.147) may thus be rewritten as

$$K = \sigma_{\rm n} \frac{g_{\rm n}}{\cos\theta} (\Delta n - \Delta n_{\rm t}). \tag{3.151}$$

The *threshold condition* (3.150) favors minimizing the photoabsorption coupling $g_{\rm e}$, hence Borrmann modes, and maximizing the coupling $g_{\rm n}$ to the lasing nuclei, hence the strongest anomalous emission mode (which will be the mode with the largest number of beams). Thus, for a crystal containing M1 Mössbauer nuclei, the favored lasing mode will be the $|m\sigma\rangle_m$ mode with maximum m.

Above threshold, the *gain* (3.151) is proportional to $g_{\rm n}/\cos\theta$, which favors either the anomalous emission mode with the largest number of beams, or the mode with the largest cone angle θ, to maximize the etalon effect of the crystal. A number of examples are discussed in [41,45,48].

Now in fact, as discussed in [44,45,48], once the population inversion has been established to make a practical γ laser, the threshold for Dicke superradiance will also have been surpassed. Since the time required to superradiate is much shorter than the time required to lase, the system will predominantly de-excite by superradiant, rather than stimulated, emission. The same factors, $g_{\rm n}/g_{\rm e}$, that determine the favored Borrmann lasing modes, however, will also determine the superradiant modes. Thus, the advantages of using a crystalline sample apply whether the system lases or superradiates.

3.10. Internal sources

When an emitting atom is located within a crystal, the emitted photon is diffracted by the surrounding lattice and the radiation pattern outside the crystal exhibits a set of light and dark Kossel cones, whose positions and intensities are determined by the crystal structure. The theory of the Kossel effect for X-rays and its application to crystal structure determinations have been discussed extensively in the literature (see, e.g., [21, pp. 430–448]). The γ-ray emission problem has been discussed in detail by the authors [12,13,49–52] and by Alexandrov and Kagan [16]. Of particular interest are the anomalous emission effect, magnetic Kossel cones, and phase determination using the holographic nature of the Kossel cones.

For γ-ray optics, the source can be a radioactive isotope, or alternatively, the wave arising from incoherent scattering, e.g., nuclear spin-flip (Raman) scattering by a Mössbauer atom or the isotope effect. For X-ray optics, the source is normally fluorescence radiation following photoabsorption.

Historically, the internal-source problem for X-ray optics was first discussed by von Laue by using the classical reciprocity theorem. A similar approach can be taken

in Mössbauer optics, using a more general form of the theorem to treat the higher-order multipolarity of the sources and the magnetic nature of the medium. However, it is also straightforward to obtain a direct solution to the problem without recourse to reciprocity. The direct solution adds considerable insight to the problem and is more convenient for treating the anomalous emission effect, magneto-optical effects, and polarization effects.

3.10.1. Direct solution

The spherical wave emanating from an emitting atom at $\mathbf{R}_j$ may be expressed as a sum of plane waves in accordance with

$$\frac{\exp(\mathrm{i}k|\mathbf{R}-\mathbf{R}_j|)}{|\mathbf{R}-\mathbf{R}_j|} = S_1 + S_2, \tag{3.152}$$

where

$$S_1 = \frac{\mathrm{i}k}{2\pi}\int_+ \exp\left[\mathrm{i}\mathbf{k}\cdot(\mathbf{R}-\mathbf{R}_j)\right]\mathrm{d}\Omega_k \tag{3.153}$$

and

$$S_2 = k\int_0^\infty \exp\left(-k|z-z_j|\tau\right)J_0\left(k|\vec{\rho}-\vec{\rho}_j|\sqrt{1+\tau^2}\right)\mathrm{d}\tau. \tag{3.154}$$

In eq. (3.154) $\vec{\rho}$ is the component of $\mathbf{R}$ in the xy plane. In eq. (3.153) the integration over the solid angles of the $\mathbf{k}$ vector is over the upper hemisphere $k_z > 0$ if $(z-z_j) > 0$, and over the lower hemisphere $k_z < 0$ if $(z-z_j) < 0$. The contribution S_1 to (3.152) is a sum of plane waves $\mathbf{k}$, whereas the contribution S_2 is a sum of exponentially damped waves as a function of $|z-z_j|$.

In sections 3.5–3.9 we obtained the response of a crystal to plane waves incident upon a crystal surface. These expressions can be used to immediately give the response of the crystal to S_1.

The contribution of S_2 to the field in the crystal is, in fact, generally very small except in the near zone, $kR \leqslant 1$, of the radiating atom. For X-ray wavelengths this means that it can be neglected relative to the radiation field, S_1, except in computing the scattering and absorption processes occurring within the radiating atom itself. These intra-atomic processes determine the internal conversion width of the decaying nucleus, and give rise to small ($\xi \approx 10^{-3}$) multipolarity dependent phase shifts of the waves emitted by the atom, as discussed in appendix A.2.4.

In the radiation zone, keeping only S_1 in eq. (3.152), the emitted radiation field of a decaying atom located at $\mathbf{R}_j$ is

$$\mathbf{A}^0(\mathbf{R},\omega;j) = \frac{\mathrm{i}k}{2\pi}\int_+ \exp\left[\mathrm{i}\mathbf{k}\cdot(\mathbf{R}-\mathbf{R}_j)\right]\mathbf{J}_\perp^{f0}(-\mathbf{k},\omega;j)\,\mathrm{d}\Omega_k. \tag{3.155}$$

Here $\mathbf{J}_{\perp}^{f0}(-\mathbf{k},\omega;j)$ is the component of the transition current at $\mathbf{R}_j$ perpendicular to $\mathbf{k}$,

$$\mathbf{J}_{\perp}^{f0}(-\mathbf{k},\omega;j)=\frac{\langle\chi_{\mathrm{f}}|\mathrm{e}^{-\mathrm{i}\mathbf{k}\cdot\mathbf{r}_j}|\chi_0\rangle\mathbf{j}_{\perp}^{f0}(-k)}{\omega+E_{\mathrm{f}}+\varepsilon_{\mathrm{f}}-E_0-\varepsilon_0+\mathrm{i}\Gamma/2}, \tag{3.156}$$

where the first factor gives the usual recoil factor, $\mathbf{j}^{f0}(-\mathbf{k})=c^{-1}\int \mathrm{d}\mathbf{x}\langle\phi_{\mathrm{f}}|\mathrm{e}^{-\mathrm{i}\mathbf{k}\cdot\mathbf{x}}\mathbf{j}(\mathbf{x})|\phi_0\rangle$ is the Fourier transform of the current density of the atom $\mathbf{R}_j$, and in the resonance denominator E gives the internal state energy of the atom and ε gives the vibrational state energy of the crystal.

The general multiple scattering equations are now given by eqs. (3.16) and (3.17), with $\mathbf{A}^0$ now given by eq. (3.155). The propagation of each plane wave contribution through the crystal can be obtained directly from our previous results.

If a wave vector $\mathbf{k}_0$ is incident on the mth layer, then, as discussed in section 3.3, there will be waves $\mathbf{k}_{s\pm}$ scattered from that layer,

$$\mathbf{k}_{s\pm}=\pm g_s\hat{z}+\mathbf{k}_{0xy}+\vec{\tau}_s, \tag{3.157}$$

with

$$g_s=\sqrt{k_0^2-(\mathbf{k}_{0xy}+\vec{\tau}_s)^2}. \tag{3.158}$$

As before, the $\vec{\tau}_s$ are *planar* reciprocal-lattice vectors, with $\vec{\tau}_0\equiv 0$.

Within a crystal, for each component $\mathbf{k}_0$, there will be additional waves traveling between the crystal planes with all these wave vectors $\mathbf{k}_{s\eta}$ ($\eta=+$ or $-$), and waves with wave vectors $\mathbf{k}_{s+}$ and $\mathbf{k}_{s-}$ emerging from the top and bottom faces of the crystal, respectively; but, as discussed in section 3.3, it is only when the Bragg condition is nearly satisfied that a $\mathbf{k}_{s\eta}$ wave will be built up by constructive interference to an appreciable magnitude. The near Bragg condition is

$$\mathbf{k}_{s\eta}-\mathbf{k}_0\approx\vec{\tau}_s+\frac{2\pi n}{d}\hat{z}, \tag{3.159}$$

or

$$g_s-g_0\approx\frac{2\pi n}{d}\quad\text{(Laue case)}, \tag{3.160}$$

$$g_s+g_0\approx\frac{2\pi n}{d}\quad\text{(Bragg case)}. \tag{3.161}$$

The right-hand side of (3.159) with $\vec{\tau}_s$ a *planar* reciprocal-lattice vector is, of course, a *crystal* reciprocal-lattice vector. If (3.159) is satisfied by a particular $\mathbf{k}_0$, then it is satisfied by all the $\mathbf{k}_0$'s making the same angle with the reciprocal lattice vector as the original $\mathbf{k}_0$. The $\mathbf{k}_0$'s and $\mathbf{k}_{s\eta}$'s then form a double cone, the Kossel cone, whose axis is along the reciprocal-lattice vector. The Laue case holds for those points for which $(\mathbf{k}_{s\eta})_z$ and $(\mathbf{k}_0)_z$ are of the same sign, the Bragg case when they are of opposite sign. In the Laue case the two waves arising from each other by internal Bragg reflections will emerge from the crystal through the same surface (top or bottom), as shown in

figure 16; while in the Bragg case they will emerge through opposite surfaces, as shown in figure 17. A given Kossel cone can be purely Laue, purely Bragg, or both.

Equation (3.157) gives the wave vectors $\mathbf{k}_{s\eta}(\mathbf{k}_0)$ of the various waves arising by scattering if a given $\mathbf{k}_0$ is incident on the crystal. This relation can be inverted to give $\mathbf{k}_0^{s\eta}(\mathbf{k})$, representing the various incident waves which can give rise to a wave vector $\mathbf{k}$:

$$\mathbf{k}_0^{s\eta}(\mathbf{k}) = \eta\sqrt{k^2 - (\mathbf{k}_{xy} - \vec{\tau}_s)^2}\,\hat{z} + \mathbf{k}_{xy} - \vec{\tau}_s. \tag{3.162}$$

In our case the "incident" wave is the spherical wave $\mathbf{A}^0$ given by (3.155). We are interested in obtaining the wave emerging from the upper face of the crystal, which is layer M using the emission geometry shown in figures 16 and 17 ($\hat{z}$ is now "up",

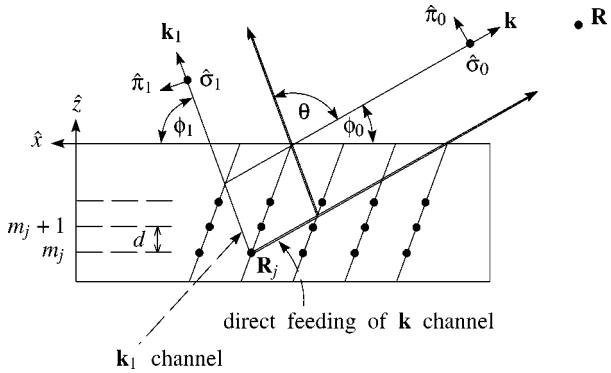

Figure 16. Schematic representation of a Laue emission channel. The wave fed directly into the **k** channel by the source is indicated by the double line, and the wave reflected into the **k** channel from the $\mathbf{k}_1$ channel which interferes with the direct wave is indicated by the single line.

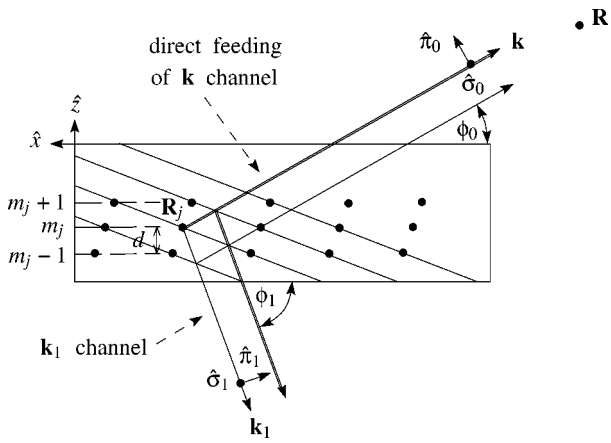

Figure 17. Schematic representation of a Bragg emission channel. The wave fed directly into the **k** channel by the source is indicated by the double line, and the wave reflected into the **k** channel from the $\mathbf{k}_1$ channel which interferes with the direct wave is indicated by the single line.

the emitting atom is located in layer m_j, the bottom layer is $m = 0$, and the top layer is $m = M$). If we write this emergent wave as

$$\mathbf{A}_M(\mathbf{R}) = \frac{\mathrm{i}k}{2\pi} \int_{k_z>0} \mathbf{A}_M(\mathbf{k}) \exp\left[\mathrm{i}\mathbf{k}\cdot\left(\mathbf{R} - z_M\hat{z}\right)\right] \mathrm{d}\Omega_k, \quad z > z_M, \tag{3.163}$$

then

$$\mathbf{A}_M(\mathbf{k}) = \sum_{s,\eta} \widetilde{D}_j^M\left(\mathbf{k}, \mathbf{k}_0^{s\eta}(\mathbf{k})\right) \mathbf{J}_\perp\left(-\mathbf{k}_0^{s\eta}(\mathbf{k}), \omega; j\right), \tag{3.164}$$

where we have used (3.155) for the source of the incident waves and the sum is over those $\vec{\tau}_s$'s for which $k_{0z}^{s\eta}$ is real (open channels). For large R ($kR \gg 1$),

$$\mathbf{A}_M(\mathbf{R}) \sim \mathbf{A}_M(\mathbf{k}) \frac{\mathrm{e}^{\mathrm{i}kR}}{R}, \tag{3.165}$$

where $\mathbf{k} = k\widehat{R}$, so that the direction of observation $\widehat{R}$ determines the "channel" $\mathbf{k} = k\widehat{R}$ at the top of the crystal which contributes to $\mathbf{A}_M(\mathbf{R})$. The γ-ray flux may be obtained by inserting these expressions for $\mathbf{A}_M(\mathbf{R})$ into (3.12).

Equation (3.164) represents the wave $\mathbf{A}_M(\mathbf{k})$ emerging from the crystal in the "$\mathbf{k}$ channel" as resulting from the coherent "feeding" of the channels $\mathbf{k}_0^{s\eta}(\mathbf{k})$ by the source currents at $\mathbf{R}_j$. The 2×2 matrix $\widetilde{D}_j^M\left(\mathbf{k}, \mathbf{k}_0^{s\eta}(\mathbf{k})\right)$ gives the amplitude of the coherent wave in the $\mathbf{k}$ channel at layer M, which arises, due to scattering within the medium, from the wave in the $\mathbf{k}_0^{s\eta}$ channel at layer m_j. The amplitude with which the $\mathbf{k}_0^{s\eta}$ channel is being fed at the m_j layer is given by $\mathbf{J}_\perp(-\mathbf{k}_0^{s\eta}(\mathbf{k}), \omega; j)$. The sum is over all the open channels $\mathbf{k}_0^{s\eta}$ that reflect into the $\mathbf{k}$ channel. As indicated, the propagation matrix $\widetilde{D}_j^M$ is a function of the frequency ω, the thickness of the crystal, the position at which the photon is being emitted, which channel is being fed (i.e., the $\mathbf{k}_0^{s\eta}$ channel), and the final direction $\mathbf{k}$. Now $\widetilde{D}_j^M(\mathbf{k}, \mathbf{k}_0^{s\eta}(\mathbf{k}))$ is negligible unless (3.159) is satisfied (using $\mathbf{k}$ as the independent variable, (3.159) takes the form $\mathbf{k} - \mathbf{k}_0^{s\eta} \approx \vec{\tau}_s + (2\pi n/d)\hat{z}$, similarly for (3.160) and (3.161)). In particular, the propagation matrix depends upon whether the $\mathbf{k}$ channel satisfies the conditions for Laue, Bragg, off-Bragg, or grazing emission.

Off-Bragg emission. For nearly all $\mathbf{k}$'s (3.159) is satisfied only for $s = 0$, $\eta = +$, $n = 0$ for which $\mathbf{k}_0^{0+}(\mathbf{k}) = \mathbf{k}$, and (3.164) becomes

$$\mathbf{A}_M(\mathbf{k}) = \widetilde{D}_j^M(\mathbf{k}, \mathbf{k})\mathbf{J}_\perp(-\mathbf{k}, \omega; j) \quad \text{(off-Bragg)}. \tag{3.166}$$

$\widetilde{D}_j^M(\mathbf{k}, \mathbf{k})$ is simply the off-Bragg transmission matrix which propagates a photon from the emission position $\mathbf{R}_j$ to the top surface of the crystal, i.e.,

$$\widetilde{D}_j^M(\mathbf{k}, \mathbf{k}) = \widetilde{T}\left(\hat{k}, \omega; l_j\right), \tag{3.167}$$

where $\widetilde{T}(\hat{k}, \omega; l_j)$ is given by eq. (3.63) with $l_j = z_M - z_j = (M - m_j)d \equiv M_j d$.

Laue emission. If **k** is near a Bragg angle for the Laue case, then $\mathbf{k}_1(\mathbf{k})$ is given by (eq. (3.162))

$$\mathbf{k}_1 = \sqrt{k^2 - (\mathbf{k}_{xy} - \vec{\tau}_1)^2}\,\hat{z} + \mathbf{k}_{xy} - \vec{\tau}_1, \tag{3.168}$$

where $\vec{\tau}_1$ is some *planar* reciprocal lattice vector. The near-Laue condition (3.160) becomes

$$(g - g_1)d = 2\pi m + 2\delta, \tag{3.169}$$

where $g \equiv k_z = (k^2 - \mathbf{k}_{xy}^2)^{1/2}$ and δ is small ($\delta = 0$ is the exact Bragg condition). In terms of the deviation $\Delta\phi = (\phi - \phi_{\mathrm{B}})$ of the rocking angle ϕ ($\equiv \phi_0$) from the exact Bragg angle ϕ_{B}, δ is given by $\delta = (kd\sin\theta)\Delta\phi/2\sin\phi_1$, where θ is the scattering angle (figure 16).

If (3.168) and (3.169) are satisfied, we say that **k** and $\mathbf{k}_1$ are "Laue emission channels". In this case we have

$$\mathbf{A}_M(\mathbf{k}) = \widetilde{D}_j^M(\mathbf{k},\mathbf{k})\mathbf{J}_\perp(-\mathbf{k},\omega;j) + \widetilde{D}_j^M(\mathbf{k},\mathbf{k}_1)\mathbf{J}_\perp(-\mathbf{k}_1,\omega;j) \quad \text{(Laue)}, \tag{3.170}$$

and channel **k** at the top of the crystal is "fed" coherently by the waves emitted by the atom at $\mathbf{R}_j$ into both the channel **k** and the channel $\mathbf{k}_1$. This is shown schematically in figure 16. For **k** in the vicinity of a Laue channel, $\widetilde{D}_j^M(\mathbf{k},\mathbf{k})$ and $\widetilde{D}_j^M(\mathbf{k},\mathbf{k}_1)$ are rapidly varying functions of $\hat{k}$ and give rise to the appearance of the (Laue) Kossel cones in these directions.

The Laue coherent wave propagation matrices $\widetilde{D}_j^M$ are given in terms of the Laue transmission matrices $\widetilde{T}$ by (see [13])

$$\widetilde{D}_j^M(\mathbf{k},\mathbf{k}) = \widetilde{T}\big(\omega;\hat{k},\hat{k};l_j\big)\mathrm{e}^{-\mathrm{i}\mathbf{k}\cdot\vec{\rho}_j} \tag{3.171}$$

and

$$\widetilde{D}_j^M(\mathbf{k},\mathbf{k}_1) = \widetilde{T}\big(\omega;\hat{k},\hat{k}_1;l_j\big)\left|\frac{\sin\phi_0}{\sin\phi_1}\right|\mathrm{e}^{-\mathrm{i}\mathbf{k}_1\cdot\vec{\rho}_j}, \tag{3.172}$$

where $l_j = z_M - z_j = (M - m_j)d \equiv M_j d$ is the depth below the surface where the emitter is located, and $\vec{\rho}_j$ is the position of the emitter within the unit cell, taking the origin as the lattice point of the unit cell in which the emitter is located.

The $\widetilde{T}(\omega;\hat{k},\hat{k};l_j)$ and $\widetilde{T}(\omega;\hat{k},\hat{k}_1;l_j)$ give the amplitude in the channel **k** at the top of the crystal for unit amplitude waves incident at the layer $m_j + 1$ in channels **k** and $\mathbf{k}_1$, respectively. The factors $\exp[-\mathrm{i}\mathbf{k}\cdot\vec{\rho}_j]$ and $\exp[-\mathrm{i}\mathbf{k}_1\cdot\vec{\rho}_j]$ give the relative phases of the contributions emerging at the top of the crystal in the **k** channel depending on the position of the emitter within the unit cell. The factor $\sin\phi_0/\sin\phi_1$ in (3.172) is the Jacobian $|\mathrm{d}\Omega_{k_1}/\mathrm{d}\Omega_k| = |k_z/k_{1z}| = \sin\phi_0/\sin\phi_1$, which converts a $\mathbf{k}_1$ solid angle into a **k** solid angle on reflection.

A general procedure for obtaining the $\widetilde{T}$ matrices is given in section 3.8. In the case of strong polarization mixing numerical procedures must be resorted to. For

the cases of no polarization mixing, $\widetilde{T}(\omega;\hat{k},\hat{k};l_j)$ and $\widetilde{T}(\omega;\hat{k},\hat{k}_1;l_j)$ are given by eqs. (3.116) and (3.117), respectively, with M replaced by $M_j = (M - m_j)$.

Bragg emission. For the Bragg channels, **k** is near a Bragg angle for some set of crystal planes and the wave field is determined by the **k** channel and a reflection channel $\mathbf{k}_1 = -g_1\hat{z} + \mathbf{k}_{xy} + \vec{\tau}_1$, which travels in the $-\hat{z}$ direction, as indicated in figure 17. The Bragg condition (3.161) is now

$$(g_0 + g_1)d = 2n\pi + 2\delta, \tag{3.173}$$

where δ is again given by $\delta = (kd\,\sin\theta)\Delta\phi/2\sin\phi_1$, as in the Laue case.

For Bragg emission,

$$\mathbf{A}_M(\mathbf{k}) = \widetilde{D}_j^M(\mathbf{k},\mathbf{k})\mathbf{J}_\perp(-\mathbf{k},\omega;j) + \widetilde{D}_j^M(\mathbf{k},\mathbf{k}_1)\mathbf{J}_\perp(-\mathbf{k}_1,\omega;j) \quad \text{(Bragg)}, \tag{3.174}$$

and channel **k** at the top of the crystal is fed coherently by the waves emitted by the atom at $\mathbf{R}_j$ into both the channel **k** and the channel $\mathbf{k}_1$, as shown schematically in figure 17.

The $\widetilde{D}$ matrices are now related to the Bragg transmission and reflection matrices $\widetilde{T}$ and $\widetilde{R}$, and there is a new complication not present in the off-Bragg and Laue cases: a wave **k** incident on layer $m_j + 1$ can be transmitted directly to layer M in the **k** channel by the Bragg transmission matrix $\widetilde{T}(\omega;\hat{k},\hat{k};M - m_j)$. But also the **k** wave can be reflected back into the $\mathbf{k}_1$ channel by the upper $M - m_j$ layers, and then reflected back into the **k** channel before being transmitted to the upper surface. The combined matrix for this process is

$$\widetilde{T}\big(\omega;\hat{k},\hat{k};M - m_j\big)\,\widetilde{R}\big(\omega;\hat{k},\hat{k}_1;m_j\big)\,\widetilde{R}\big(\omega;\hat{k}_1,\hat{k};M - m_j\big).$$

Or rather than a double reflection, there could be four reflections before transmission, and so on. As a consequence,

$$\widetilde{D}_j^M(\mathbf{k},\mathbf{k}) = \widetilde{T}\big(\omega;\hat{k},\hat{k};M - m_j\big)\big[1 - \widetilde{R}\big(\omega;\hat{k},\hat{k}_1;m_j\big)\,\widetilde{R}\big(\omega;\hat{k}_1,\hat{k};M - m_j\big)\big]^{-1}\mathrm{e}^{-\mathrm{i}\mathbf{k}\cdot\vec{\rho}_j}. \tag{3.175}$$

Similarly, a wave $\mathbf{k}_1$ incident on layer $m_j - 1$ can be reflected into the **k** channel by the lower m_j layers, and then transmitted through the upper $M - m_j$ layers, with the combined matrix being $\widetilde{T}(\omega;\hat{k},\hat{k};M - m_j)\widetilde{R}(\omega;\hat{k},\hat{k}_1;m_j)$. But again there can be multiples of double reflections between the parts of the crystal above and below the emitting atom at $\mathbf{R}_j$, as discussed above. The resulting $\widetilde{D}$ matrix is

$$\begin{aligned}\widetilde{D}_j^M(\mathbf{k},\mathbf{k}_1) = {}& \widetilde{T}\big(\omega;\hat{k},\hat{k};M - m_j\big)\big[1 - \widetilde{R}\big(\omega;\hat{k},\hat{k}_1;m_j\big)\,\widetilde{R}\big(\omega;\hat{k}_1,\hat{k};M - m_j\big)\big]^{-1} \\ & \times \widetilde{R}\big(\omega;\hat{k},\hat{k}_1;m_j\big)\left|\frac{\sin\phi_0}{\sin\phi_1}\right|\mathrm{e}^{-\mathrm{i}\mathbf{k}_1\cdot\vec{\rho}_j}.\end{aligned} \tag{3.176}$$

The Jacobian and phase factors have the same significance as in eqs. (3.171) and (3.172).

For the special cases of no polarization mixing, the $\widetilde{T}$ and $\widetilde{R}$ matrices are given by eqs. (3.86) and (3.81), with M replaced by $M - m_j$ or m_j, as appropriate. More generally, the numerical procedure must be used.

3.10.2. Reciprocity

In X-ray optics, the problem of diffraction when the source lies within the crystal was solved by von Laue [53] by using the classical reciprocity theorem. For X-ray optics, the theorem can be stated as follows [18, pp. 430–448]: "*If a source of radiation and a point of observation are interchanged, the intensity, measured in terms of electric displacement, is the same at the new place of observation as at the old*." This theorem allows one to solve the emission problem in terms of the solutions to the external source problem. As stated, however, the theorem only applies to E1 sources and a nonmagnetic scattering medium, or more exactly, a medium which is unchanged by time reversal.

The reciprocity theorem can, of course, also be applied in Mössbauer optics to relate the internal source problem to that of an external source; but its statement must be generalized somewhat to take into account the higher-order multipolarity of Mössbauer sources, and the possibly strong magnetic effects in the scattering medium. The general *classical* reciprocity theorem such as given by Landau [54] and utilized in [16] is valid for arbitrary multipolarity of the sources and for an absorbing medium, but it is not suitable for describing cases where magneto-optical effects occur, since then the assumed symmetry of the dielectric tensor ε_{ik} breaks down.

A more general theorem based on the supposed invariance of physical laws under time reversal is derived in [12]. The resulting reciprocity relation for single photon optics (eq. (46) of [12]) applies to arbitrary multipole currents, for photon propagation through a dispersive medium with arbitrary magneto-optical effects, and is valid for inelastic as well as elastic photon propagation. For the *coherent elastic wave* $\mathbf{A}(\mathbf{R}, \omega; j)$ of frequency ω, which is propagated through the crystal to a distant point $\mathbf{R}$ following an initial decay at $\mathbf{R}_j$ (either recoilless or with recoil), the theorem gives

$$\mathbf{A}_\perp(\mathbf{R}, \omega; j) = -\frac{\mathrm{e}^{\mathrm{i}kR}}{R} \sum_{\mathbf{e}_0 = \hat{x}, \hat{y}} \mathbf{e}_0 J_\mu^{0' f'}\left(\overrightarrow{\mathbf{k}}_j, \omega; j\right) A'_\mu(\mathbf{R}_j, \omega; \mathbf{e}_0). \tag{3.177}$$

Here $\hat{x}$ and $\hat{y}$ are any convenient orthogonal basis vectors perpendicular to $\mathbf{k}' = -\mathbf{k} = -(\omega/c)\widehat{R}$; $\overrightarrow{\mathbf{k}}_j = -\mathrm{i}\overrightarrow{\nabla}_j$, where the gradient is with respect to $\mathbf{R}_j$, the equilibrium position of atom j, and the gradient operates on the factors to the right as indicated; the current matrix element is the *absorption* process between the time reversed states, $|f'\rangle \rightarrow |0'\rangle$; and $A'_\mu(\mathbf{R}_j, \omega; \mathbf{e}_0)$ is the total coherent field at $\mathbf{R}_j$ due to an *external plane wave source* $\mathbf{e}_0 \exp(\mathrm{i}\mathbf{k}' \cdot \mathbf{x})$ incident in the $\mathbf{k}'$ direction on the *time-reversed scattering medium*, which is the external source problem already solved.

To use (3.177) to determine the $(\mathbf{k}, \omega)$ coherent wave at a distant point $\mathbf{R}$ following a decay $|0\rangle \rightarrow |f\rangle$ at $\mathbf{R}_j$, one first calculates the *coherent* wave $A'_\mu(\mathbf{R}_j, \omega; \mathbf{e}_0)$ at $\mathbf{R}_j$ caused by a plane wave of polarization $\mathbf{e}_0$ and frequency ω incident in the

$-\mathbf{k}$ direction on the medium in which the **B** field at each site is reversed (while the electric field gradient remains unchanged). The photon flux at **R**, given by inserting expression (3.177) for $\mathbf{A}_\perp(\mathbf{R},\omega;j)$ into the photon flux eq. (3.12), is then proportional to the excitation probability $|J_\mu^{0'f'}A'_\mu|^2$ for inducing the transition from the ground state $|f'\rangle = T|f\rangle$ to the excited state $|0'\rangle = T|0\rangle$ in the time reversed process. To obtain the recoilless Mössbauer fraction, the transition is taken as recoilless, while for the recoil fraction the transition is taken with recoil $\chi_\mathrm{f} \rightarrow \chi_0$.

Using this procedure, we can treat the various cases discussed above. Although the reciprocity approach is more cumbersome, it gives a useful insight into the emission problem.

3.10.3. Anomalous emission, magneto-optical effects, holographic phase determination

There are a number of interesting features of the internal source problem, among which are the following:

"Anomalous emission effect" for Mössbauer optics. If a Mössbauer emitter of multipolarity M1 or higher is located at a lattice site deep in a crystal (at a depth greater than the photoelectric absorption depth but less than the Borrmann penetration depth), and if the absorption from the remaining crystal sites is primarily the E1 photoelectric absorption, then a γ-ray emitted from the site into a Borrmann channel will emerge from the crystal. On the other hand, for an E1 emitter, such emission is strongly suppressed [13,39].

The effect is most easily seen using the reciprocity theorem, which states that the amplitude of the radiation field produced at a distant point in a direction $\hat{k}$ from the crystal is proportional to the coupling of the atom to the radiation field produced inside the crystal by a plane wave incident on the crystal in the direction $-\hat{k}$. In the present case the reciprocal problem is an external plane wave incident in a Borrmann channel, as discussed in section 3.8.1, and the diffraction effects lead to nodes in the electric field at regular lattice sites, and antinodes for the magnetic field and electric field gradients at such sites (figure 12). Hence, there is no coupling to an E1 oscillator at such a site, but strong coupling to an M1 or E2 oscillator, which, by reciprocity, implies the anomalous emission effect stated above. Alternatively, the effect occurs because the wave emitted directly into the $\hat{k}$ direction by the source interferes constructively or destructively with the wave which is Bragg reflected into the $\hat{k}$ direction by the crystal (figure 16), with the nature of the interference being determined by the multipolarity and position of the source. As discussed in [13,39], the interference is constructive if the source is M1 or higher, and located at a lattice site.

The polarization of the anomalous emission mode is parallel to the scattering planes, and the emitted radiation is narrowly collimated with a collimation angle $\delta\theta$ typically on the order of 10^{-4} rad. Thus, the effect is a natural source of polarized, collimated radiation.

The radiation field set up within the crystal by these deep crystal sources will also have E-field nodes at lattice sites, and B-field and EFG antinodes at lattice sites. Hence, this field can stimulate emission from similar emitters of multipolarity M1 or higher located at lattice sites.

As discussed in [92,93,95] and section 3.9.4, the effect is potentially useful for the construction of γ-ray lasers.

Magnetic Kossel cones. The Kossel pattern exhibits the crystal symmetry and affords a sensitive measure of crystal parameters. In X-ray optics, Kossel pattern analysis has been used to make precision determinations of lattice parameters and orientation, and to determine the variation of the parameters with temperature and strain, the components of the strain tensor, and the degree of crystal perfection [55]. In Mössbauer optics these features are also present and a new phenomenon can occur: the Mössbauer scattering is sensitive to the direction of the magnetic field and electric field gradient tensor at the nucleus, and if the internal field "unit cell" is greater than the chemical unit cell, there will appear extra Kossel cones ("magnetic Kossel cones") exhibiting the structure of the internal fields [13,39]. Thus, for example, analysis of the magnetic Kossel line pattern of rare-earth Mössbauer metals and alloys will permit accurate determinations of the spiral structures, and of their dependence on temperature and strain.

For example, if a magnetic crystal has a spiral axis $\hat{z}$ with a spiral angle θ, there will be Bragg or Laue channels $\mathbf{k}$ and $\mathbf{k}_1$ open when $(\mathbf{k} - \mathbf{k}_1 + n\vec{\theta})$ is equal to a reciprocal lattice vector, where $\vec{\theta} = (\theta/d_s)\hat{z}$ and d_s is the interplanar distance along the spiral axis $\hat{z}$. These lines will, of course, only appear if the internal fields are strong enough to cause appreciable hyperfine splitting.

Faraday effects. The most interesting effects in off-Bragg emission are the magneto-optical effects involved in the propagation of the photon through the surrounding medium. The matrix $\widetilde{D}_j^M(\mathbf{k},\mathbf{k}) = \widetilde{T}(\hat{k},\omega;l_j)$ given by eq. (3.63) determines the propagation of the emitted photon $|\mathbf{J}_\perp(-\mathbf{k},\omega;j)\rangle$ through the medium. As discussed in section 3.5, for a given frequency ω and direction of propagation $\hat{k}$, there are two eigenwaves $\mathbf{e}_\eta(\hat{k},\omega)$, $\eta = 1,2$, which are generally nonorthogonal and have different complex indices of refraction, $n_\eta = 1 + f_\eta$. This leads to Faraday and selective absorption effects, and as a consequence, for *recoilless emission*, the polarization state of the photon emitted from the crystal will generally differ from the polarization state at the source. The density matrix formalism for treating the polarization state of the emitted photon is discussed in [13].

Holography and phase determination. The problem of determining the structure of complex molecules by X-ray diffraction is greatly complicated by the fact that the reflected intensity only gives the magnitude $|A_\mathbf{h}|$ of the unit-cell scattering factor and *not* the phase $\phi_\mathbf{h}$.

The most widely used method to extract $\phi_\mathbf{h}$ is to use controlled variation of the structure factor, for example, by heavy atom replacement [56,57] or anomalous scattering [58]. In these procedures, the unit cell scattering amplitude is changed

from $A^0_{\mathbf{h}} = -r_0 F_{\mathbf{h}}$, where $r_0 = e^2/mc^2$ and $F_{\mathbf{h}} = |F_{\mathbf{h}}|\mathrm{e}^{\mathrm{i}\phi_{\mathbf{h}}}$ is the unit-cell structure factor, to $A_{\mathbf{h}} = A^0_{\mathbf{h}} + A^1_{\mathbf{h}}$, where $A^1_{\mathbf{h}}$ is the added amplitude due to the extra scattering (heavy atom, anomalous dispersion). Since the integrated reflected intensity is directly proportional to $|A_{\mathbf{h}}|^2$ for small crystals, $\phi_{\mathbf{h}}$ can be deduced from knowledge of $A^1_{\mathbf{h}}$ and measurement of $|A^0_{\mathbf{h}}|^2$ and $|A^0_{\mathbf{h}} + A^1_{\mathbf{h}}|^2$.

In [13,59–61] it was pointed out that internal source emission is a *holographic process*, and offers a sensitive method to determine the structure factor phases $\phi_{\mathbf{h}}$ of the chemical unit cell (and in the Mössbauer case, also the phases $\phi_{\mathbf{h}'}(\mathbf{B})$ for the structure of the internal field unit cells): the interference of the direct wave emitted in a given direction with that Bragg-reflected into this direction (figure 17) allows the phase of the latter to be obtained from the intensity distribution within the Kossel line, as in the holographic technique, where phase information is obtained by "beating" the diffracted wave with a primary reference wave.

If the source is located at a lattice site $\mathbf{R}_j$ near the top surface of the crystal, then the total amplitude of the wave traveling in the $\hat{k}$ direction is (see [60])

$$\sim \mathrm{e}^{-\mathrm{i}\mathbf{k}\cdot\mathbf{R}_j} + \mathrm{e}^{\mathrm{i}\phi_{\mathbf{h}}}\mathrm{e}^{-\mathrm{i}\mathbf{k}_1\cdot\mathbf{R}_j}\mathcal{D}(\Delta\theta/W_{\mathbf{h}}), \tag{3.178}$$

where $W_{\mathbf{h}}$ is the half-width of the total reflection region, and $\mathcal{D}(\Delta\theta/W_{\mathbf{h}})$ is the usual Darwin reflection amplitude. The cross term in the resulting intensity depends upon the phase of the structure factor, allowing $\phi_{\mathbf{h}}$ to be determined.

The holographic nature of internal source emission has more recently also been pointed out by Szöke [62], and has been utilized to do surface holography using photoelectron sources [63]. Furthermore, as pointed out by Timmermans et al. [64–66], if the neighboring atoms have spins, then due to exchange scattering, there is a "*spin hologram*" contribution to the interference between the direct and scattered electron waves which can be extracted to give the magnetic structure.

X-ray interferometry and phase determination. As just discussed, for the Kossel lines, the total field $\mathbf{A}(\mathbf{R},\omega;j)$ in the $\hat{k} = \widehat{R}$ direction, emitted by a source atom at the site $\mathbf{R}_j$, is a superposition of the directly emitted wave $\mathbf{k}$, and the wave Bragg-reflected from $\mathbf{k}_1$ into $\mathbf{k}$ by the crystal (figure 17 and eq. (3.178)). In the *time reversed process*, the total field at the site $\mathbf{R}_j$ due to a plane wave of frequency ω incident in the $-\hat{k}$ direction, is a superposition of the direct wave $(-\mathbf{k})$ and the wave Bragg-reflected $(-\mathbf{k})$ to $(-\mathbf{k}_1)$ by the crystal. The superposition of the two waves produces an X-ray standing wave pattern. By the reciprocity theorem eq. (3.177), the intensity $|\mathbf{A}(\mathbf{R},\omega;j)|^2$ at $\mathbf{R}$, which gives the Kossel line profile, is directly proportional to the excitation probability $|J_\mu^{0'f'}A'_\mu|^2$ for inducing the transition from the ground state $|f'\rangle = T|f\rangle$ to the excited state $|0'\rangle = T|0\rangle$ in the time reversed process. Thus, observing the fluorescence yield of an atom due to the field in the standing wave created by rocking through a Bragg peak is equivalent to observing the Kossel line intensity profile produced by the decay of that same atom, and consequently has the same phase information, as pointed out

by Hutton et al. [67] and Gog et al. [68]. X-ray holography using this technique has recently been demonstrated [69,70].

4. Coherent excitation of nuclei by synchrotron radiation pulses

Because of the low brightness of most radioactive Mössbauer sources, until recently nearly all Mössbauer experiments involved only resonance absorption, which, while valuable, does not exhibit to the fullest the interesting effects due to coherence in the emission or scattering of the γ-rays from the various nuclei in the sample. In 1974, however, Ruby [71] and Mössbauer [72] pointed out that the spectral brightness in the then existing synchrotron radiation sources at, e.g., the 14.4 keV ^{57}Fe resonance line exceeded that of 100% ^{57}Co radioactive sources. Since it was clear that with the use of wigglers or undulators the synchrotron brightness could be very much enhanced at the resonance lines, a number of groups undertook the quest of "filtering" out the "Mössbauer slice" from the white synchrotron beam. The first dramatic success was achieved by Gerdau et al. [73] in 1985, where filtering was first unambiguously achieved, and since that time there has been rapid progress and interest in the field [74].[13]

It is now clear that an important new field has been opened up involving *coherent* nuclear excitations induced by synchrotron radiation *pulses* traversing a piece of matter. Several important new areas of application are:

Inelastic scattering studies. Until recently, inelastic neutron scattering has been the primary method available for obtaining the low energy excitations (phonons, magnons, etc.) in condensed matter. X-ray inelastic scattering was not useful for such experiments because of poor energy resolution.

However, perfect Si crystal backscattering monochromators have been constructed at Brookhaven [75] and Hasylab [76], which have achieved resolutions of $\Delta E \approx$ 5–7 meV for X-ray energies. The use of such monochromators to filter synchrotron radiation and to measure energy gains or losses in the scattered beam will furnish another and perhaps more powerful means to determine condensed matter excitations.

To exceed the limit $\Delta E \approx 1$ meV obtainable by wavelength selecting monochromators, one must use nuclear resonance filters (frequency or energy selecting monochromators) where one can obtain submicrovolt resolution, $\Delta E < 10^{-6}$ eV at $E = 14.4$ keV (for ^{57}Fe filters), with a flux of the order of 10^5 photons/s/mm^2 or higher.

Resonant absorber Doppler shifting detectors capable of speeds up to $\approx$30 m/s have now been developed, making possible inelastic measurements corresponding to energy transfers of 10^{-5}–1 meV [77]. This should furnish a good method for measuring

[13] The current experimental situation using both synchrotron and conventional Mössbauer radiation sources is reviewed elsewhere in this issue. For a review of earlier work, see [74].

very slow relaxation and fluctuation processes ($\nu \approx 10^7$ s^{-1}) in the critical region, and faster processes up to $\approx 3 \times 10^{11}$ s^{-1} (1 meV).

There has been considerable recent progress in this field, as discussed in section 5.1 of this paper, and by Chumakov and Rüffer [78].

Interferometry, metrology, holography. Filtered synchrotron radiation opens up quite new possibilities in X-ray interferometry by utilizing the very long coherence length of the radiation.

The usual Bonse–Hart interferometer [79] is a large single crystal of Si or Ge, cut to have three parallel plates ("arms"), with a set of crystal planes running perpendicular to the faces of the plates. Set in a Laue transmission geometry, the first plate separates the incident X-ray radiation into two components (the direct and Bragg reflected beams), and Bragg reflection of the two beams in the second arm recombines the beams at the third plate, which acts as an analyzer. It is then possible to insert a very thin "transparent" wedge of material (several microns) into one of the paths to give an index of refraction change of the optical path length. In principle, observation of the interference pattern vs. wedge thickness can give an accurate determination of the index of refraction, and can, for example, be used to make precision determinations of the anomalous scattering near a K-shell absorption edge [80].

A restriction here is that the coherence length of the radiation is $l_c \approx 10^{-4}$ cm, which means path length differences are restricted to $\approx 10^{-4}$ cm (the Bragg scattering in the interferometer arms, or from a prior monochromatizing crystal, monochromatizes the X-ray radiation to ≈ 0.1 eV, giving a coherence length of $l_c = \hbar c/\Gamma \approx 2 \times 10^{-4}$ cm). Since the pathlength differences must be kept to less than l_c to obtain interference in the recombined beams, this effectively restricts us to transmission elements (e.g., a transparent thin wedge) in one of the beams.

However, if filtered synchrotron radiation is used as the source, then $\Gamma \approx 10^{-8}$–10^{-6} eV and the coherence length is $l_c \approx 2$ cm–20 m, and it would then be possible to use a scattering element in a Bonse–Hart interferometer. For example, in place of the transparent wedge, it would now be possible to insert two parallel cut grazing incidence reflectors for surface studies, where now the optical path length is changed by rotation of the reflectors. Another possibility would be to insert a multiple Bragg reflection etalon grating, used, for example, to make multiple passes through a monolayer. A backscattering monochromater has been demonstrated by Shvyd'ko et al. [81].

It is also possible to do long coherence length interferometry with unmonochromatized synchrotron radiation pulses by utilizing the long coherence time response of a resonance detector [82]. For example, a synchrotron radiation pulse of duration $\Delta t \approx 0.1$ ns sent through the two arms of an interferometer (e.g., Bonse–Hart, Michelson, ...) will emerge as two coherent sharp pulses, separated by a time $\Delta T \approx L/c$, where L is the optical path difference between the two arms. If the pulses then impinge on a film containing resonant Mössbauer nuclei, the nuclei are excited under the coherent superposition of two sharp pulses, giving an excitation probability proportional to

$\cos^2(\pi L/\lambda_0)$. This offers the interesting metrological possibility of measuring changes of the length $\Delta L \approx \lambda_0 \approx 1$ Å for L's up to $l_c \approx 2$ cm–20 m.

Structure determination. Another important application will be for the structure determination of complex biomolecules. The problem of making structure determinations by X-ray diffraction is greatly complicated by the fact that the reflected intensity only gives the magnitude of the unit-cell scattering factor and not the phase. For this reason, considerable effort has been devoted to devising methods for extracting phase information.

To determine the phase, the usual method employed is impurity substitution, in which one determines the phase of the unit cell scattering amplitude relative to the phase of the wave scattered from a limited number of impurity sites. In practice this is a tedious process, involving duplicate experiments on pure samples and impurity doped samples.

An alternate, and very powerful method is offered by Mössbauer diffraction [83,84]. In this case, one substitutes resonant ^{57}Fe for ^{56}Fe in the biomolecules to be studied, leaving the electronic scattering unchanged.

Because of the exceedingly sharp resonance, it is then possible to vary the phase and amplitude of the resonantly scattered wave by Doppler-shifting with negligible variation in the nonresonant electronically scattered wave. Consequently, the interference between the waves is easily varied in a controlled manner. As discussed by Black [83], and as demonstrated by Parak et al. [84], it is then possible to extract the phase of the chemical structure factor of the unit cell relative to the structure factor due to the resonant scattering at the Mössbauer sites. The problem is then reduced to determining the relative positions of the Mössbauer atoms within the unit.

(A related technique for phase determination is to tune near a K-shell absorption edge and use the frequency variation of the anomalous scattering $f'_K + \mathrm{i}f''_K$ over eV-regions. However, this contribution is typically only several electrons even in the immediate vicinity of a K shell, and more importantly, because of the continuum nature of the intermediate states involved, there is no sharp dispersion variation across the K edge. For example, the measurements of Materlik and Bonse [80] on Ni show that f'_K varies from ≈ -3 electrons at $\omega = \omega_K + 150$ eV, decreasing to ≈ -7.5 electrons at ω_K. In contrast, the real part of the resonant nuclear scattering amplitude for ^{57}Fe scatters as $+220$ electrons for $\omega = \omega_0 - \Gamma/2\hbar$, and as -220 electrons for $\omega = \omega_0 + \Gamma/2\hbar$, with $\Gamma = 5 \times 10^{-9}$ eV.)

However, in practice, because of the high collimation required and the limited brightness of natural sources, very long counting times are required ($\approx$ several counts per hour), making the Mössbauer experiments exceedingly difficult.

Filtered synchrotron radiation sources are ideal for such experiments, providing a pre-collimated beam with a brightness $\approx$3–4 orders of magnitude greater than that provided by a natural source, making the Mössbauer technique applicable to the analysis of significant biological molecules.

Hyperfine splitting, isomer shifts, ... by monitoring the quantum beats in the coherent forward and Bragg scattering channels. Synchrotron radiation from a source operating in the single-bunch mode consists of sharp pulses of about 10^{-10} s duration and about 10^{-6} s separation between pulses. Excited nuclear states of energy less than $\approx$100 keV commonly have lifetimes in the range $\hbar\Gamma^{-1} = 10^{-6}$–$10^{-10}$ s. If the pulse, monochromatized to perhaps 1 eV bandwidth at the nuclear transition, impinges on a small crystal containing the resonant nuclei, then the electronically scattered X-rays, photoelectrons, etc. will emerge promptly during the 10^{-10} s pulse, while those processes involving nuclear excitation will be delayed a mean time Γ^{-1}. Therefore, by using a timed detector which can recover from the prompt pulse in a time short compared to Γ^{-1}, the resonant and nonresonant events can be separated temporally.

There are "quantum beats" in the *coherently* scattered radiation in the forward and Bragg channels, arising from the interference between waves emitted from *different* sites [26]. The essential feature is that the sharp synchrotron radiation pulse excites the various nuclear excited state sublevels suddenly and coherently, which then "oscillate" at their various natural frequencies, giving beats in subsequent decays. These beats occur at frequencies

$$\Omega_{\mathrm{B}}\left(n, m, \rho; n', m', \rho'\right) = \omega_{nm}(\rho) - \omega_{n'm'}\left(\rho'\right) \tag{4.1}$$

corresponding to the difference frequencies of all allowed nuclear hyperfine transitions $\omega_{nm}(\rho)$ from all the different nuclear sites ρ, from which the hyperfine splittings of both the excited and ground states may be found, as well as any energy shifts between nuclei located in different chemical or magnetic sites. In contrast, the quantum beats occurring in the usual time dependent perturbed angular correlation (TDPAC) measurements are *spatially incoherent*, with the beats arising from the interference between transitions to the same ground state. Thus, the beat frequencies give only the splittings of the excited levels, with no information on ground state splittings or on shifts between different sites.

The quantum beats in the coherent scattering give a very sensitive measure of the hyperfine splittings and isomer shifts, which can be even more precise than the usual Mössbauer absorption measurements because the quantum beats give a direct measure of the energy differences, while the precision of the absorption measurements depends on the precision of the velocity control.

An important practical point is that because of the pulsed nature of the synchrotron radiation source, the quantum beats can be measured in the forward direction scattering following the pulse excitation [85]. Since coherent forward scattering occurs for any sample (crystalline, mosaic, amorphous), all normal Mössbauer experiments can be carried out in the time domain.

4.1. Nuclear exciton states

There are two approaches for treating the interaction of a synchrotron pulse with a system of nuclei. Because the temporal duration of the synchrotron pulse and its transit

time across the system are short compared to the lifetime of the nuclear resonance, the formation of the intermediate excited state and its subsequent decay can be treated as two independent quantum-mechanical processes. Alternatively, the interaction can be treated purely as a resonance scattering problem. The first approach brings out interesting new physics: the creation of nuclear excitons with synchrotron radiation pulses, and the nature of the subsequent exciton decay. The second approach, on the other hand, gives the simplest method for obtaining the scattered signal. The time dependent amplitude of the scattered signal is simply proportional to the Fourier transform of the frequency dependent reflection and transmission amplitudes $\widetilde{R}(\hat{k}_1, \hat{k}_0; \omega)$ and $\widetilde{T}(\hat{k}_1, \hat{k}_0; \omega)$ already obtained for the various cases of off-Bragg, Bragg, Laue and grazing incidence. In this subsection we discuss the exciton approach, and in the following subsection 4.2 we outline the scattering approach.

From the pure physics standpoint, the *nuclear exciton* produced by the synchrotron radiation pulse when it traverses a sample containing Mössbauer nuclei is a new state of matter exhibiting interesting effects of coherence, notably:

- *Speedup* of the decay (relative to that of an isolated excited nucleus) resulting from *superradiance* in the coherent channels (and a *slowdown* is also possible, resulting from *subradiance* in some coherent decay channels).
- *Quantum beats* resulting from the interference of waves of different frequencies from *different* nuclei, giving a time dependent spatially coherent decay rate, $\Gamma_c(t)$, varying periodically between superradiant and subradiant emission into the coherent channels.

4.1.1. Nuclear exciton

The important new element in the synchrotron pulse experiment is that because both the pulse duration and the transit time of the pulse across the crystal are short compared to the excited state lifetime $\hbar\Gamma^{-1}$, the pulse creates a collective nuclear excited state $|\psi_e(\mathbf{k}_0)\rangle$ which is a spatially coherent superposition of the various excited state hyperfine levels of all the nuclei in the crystal, with a spatial phasing wave vector $\mathbf{k}_0$ [26,28]. The subsequent radiative decay is radically affected by coherence, exhibiting both a speed-up due to "coherent enhancement" [2,10–13,25,26,28,32,86,87] and a quantum beat modulation of the decay rate [26,28,32].

As discussed in [26], the resulting recoilless excitation just after the pulse traverses the system is

$$\big|\psi_e(\mathbf{k}_0)\big\rangle = \sum_{l=1}^{N} e^{i\mathbf{k}_0\cdot\mathbf{R}_l} \sum_{n_l} c_{n_l m_l} |e_l n_l\rangle \big|G_0(l)\big\rangle |\chi_0\rangle, \tag{4.2}$$

where $\mathbf{k}_0 = c^{-1}\omega_0 \mathbf{n}_0$ ($\mathbf{n}_0$ is the direction of propagation of the incident pulse and ω_0 is the mean transition frequency for all the nuclei) and c_{nm} is the amplitude for exciting the nucleus at $\mathbf{R}_l$ from $|g_l m_l\rangle \rightarrow |e_l n_l\rangle$, with no change in the vibrational state $|\chi_0\rangle$,

and $|G_0(l)\rangle$ indicates that all the other nuclei ($l' \neq l$) are in their initial ground states $|g_{l'} m_{l'}\rangle$. For a nuclear dipole transition (E1 or M1), c_{nm} is given by

$$c_{n_l m_l} = \frac{\mathrm{i}}{\hbar}\sqrt{f}\langle e_l n_l|\vec{\mu}|g_l m_l\rangle \cdot \mathbf{F}_{\omega_0}, \tag{4.3}$$

where $\vec{\mu}$ is the nuclear dipole moment operator (E1 or M1), $\mathbf{F}_{\omega_0}$ is the resonant Fourier component of the incident synchrotron pulse $\mathbf{F}(t)$ ($\mathbf{F} = \mathbf{E}$ for E1 and $\mathbf{F} = \mathbf{B}$ for M1), and f is the Mössbauer factor.

$|\psi_{\mathrm{e}}(\mathbf{k}_0)\rangle$ is a *collective nuclear excited state*, i.e., a spatially coherent superposition of the various excited state hyperfine levels of all the nuclei in the crystal. In each contributing term, one nucleus is excited into one of its excited state hyperfine levels, and all the remaining nuclei remain in their initial ground states. The relative spatial phase is $\exp(\mathrm{i}\mathbf{k}_0 \cdot \mathbf{R}_l)$. Hence, $|\psi_{\mathrm{e}}(\mathbf{k}_0)\rangle$ is a *single exciton* collective state, with one excitation distributed coherently over the entire system, with a spatial phasing wave vector $\mathbf{k}_0$.

4.1.2. Radiative decay of the nuclear exciton

Because the temporal duration of the incident pulse is short compared to the lifetime of the nuclear resonance, it is legitimate to regard the formation of the intermediate excited state $|\psi_{\mathrm{e}}(\mathbf{k}_0)\rangle$ and its subsequent decay as two independent quantum-mechanical processes [88]. Consequently, we can use the general theory for γ emission discussed in section 3.10.

The initial state of the crystal is now the exciton state $|\psi_{\mathrm{e}}(\mathbf{k}_0)\rangle$ with one excitation spread coherently over all the nuclei of the system. The photon potential $A_\mu(z)$ due to a transition to a final crystal state $|\psi_{\mathrm{f}}\rangle$ corresponding to all Mössbauer nuclei being in their ground states is given by

$$A_\mu(z) = c^{-1}\langle\psi_{\mathrm{f}}|\sum_l \int \mathrm{d}^4x\, D_{\mu\upsilon}(z,x)J_\upsilon(x,l)\big|\psi_{\mathrm{e}}(\mathbf{k}_0)\big\rangle, \tag{4.4}$$

where $J_\upsilon(x,l)$ is the source current of the lth nucleus and $D_{\mu\upsilon}(z,x)$ is the photon propagator. If we neglect scattering, then $D_{\mu\upsilon}(z,x)$ is given by the free photon propagator $D^{(0)}_{\mu\upsilon}(z,x)$,

$$D^{(0)}_{\mu\upsilon}(z,x) = -4\pi g_{\mu\upsilon}\int \frac{\mathrm{e}^{-\mathrm{i}k(z-x)}}{k^2 + \mathrm{i}\varepsilon}\,\mathrm{d}^4k. \tag{4.5}$$

The source transition current $J_\upsilon(x,l)$ is given to good approximation by

$$J_\mu(x,l) = \mathrm{e}^{\mathrm{i}H_0 t_x} j^{(l)}_\mu(\mathbf{x})\mathrm{e}^{-\mathrm{i}(H_0 - \Gamma'/2)(t_x - \tau_l)}\mathbb{1}(t_x - \tau_l), \tag{4.6}$$

where $j^{(l)}_\mu(\mathbf{x})$ is the current-density operator for the atom l, Γ' is the width of the excited level, H_0 is the Hamiltonian for the complete crystal with electromagnetic interactions replaced by instantaneous Coulomb and magnetic interactions, and $\mathbb{1}(t)$ is the Heaviside step function ($\mathbb{1}(t<0) = 0$, $\mathbb{1}(t>0) = 1$). In (4.6) it is assumed that the excited nuclear state is produced at $t_x = \tau_l$. For a synchrotron pulse sweeping

across a crystal in the direction $\hat{n}_0$, arriving at the origin at $t = 0$, the lth nucleus is "turned on" at $\tau_l = c^{-1}\hat{n}_0 \cdot \mathbf{R}_l$.

In the first Born approximation, the width Γ' would simply be the excited state width of an isolated nucleus, $\Gamma' = \Gamma_\gamma + \Gamma_\alpha$. But the effects of coherent decay will radically effect Γ' as we discuss below. For our purposes, it suffices to calculate Γ' in the second Born approximation, using the Fermi Golden Rule if there is no hyperfine splitting (section 4.1.3), and the direct time dependent flux calculation if there is hyperfine splitting (section 4.1.6). The exact treatment of the excited state propagator for an initial exciton state $|\psi_e(\mathbf{k}_0)\rangle$ is discussed in section 6.

4.1.3. Spatially coherent and incoherent decay

The radiative decay of the exciton state

$$\big|\psi_e(\mathbf{k}_0)\big\rangle \rightarrow |\psi_f\rangle + \gamma_{\mathbf{k}} \tag{4.7}$$

can be either spatially coherent, giving highly directional emission into the coherent channels, or spatially incoherent, giving essentially isotropic emission into 4π sr.

Spatially coherent decay occurs when $|\psi_e(\mathbf{k}_0)\rangle$ makes a radiative transition to the original ground state, i.e., $|\psi_f\rangle = |\psi_0\rangle$. For the decay $|\psi_e(\mathbf{k}_0)\rangle \rightarrow |\psi_0\rangle + \gamma_{\mathbf{k}}$, the photon potential (for the *elastic* wave) becomes

$$A_\perp^{\rm el}(\mathbf{R}, t) = \frac{\mathbb{1}(t^*)}{R} \sum_l \mathbf{F}_{l,m_l}\big(t^*\big) \mathrm{e}^{-\mathrm{i}(\mathbf{k}-\mathbf{k}_0)\cdot\mathbf{R}_l}, \tag{4.8}$$

where $\mathbf{k} = c^{-1}\omega_0\mathbf{R}/R$, $t^* = (t - R/c)$ is the retarded time, and the emission amplitude from site $\mathbf{R}_l$ is

$$\mathbf{F}_{l,m_l}\big(t^*\big) = \sqrt{f} \sum_{n_l} \langle g_l m_l | c^{-1} \int \mathrm{d}\mathbf{x}\, \mathbf{j}_\perp(\mathbf{x}) \mathrm{e}^{-\mathrm{i}\mathbf{k}\cdot\mathbf{x}} | e_l n_l \rangle c_{n_l m_l} \mathrm{e}^{-\mathrm{i}(\omega_{n_l m_l} - \mathrm{i}\Gamma'/\hbar)t}. \tag{4.9}$$

The *coherent elastic wave*, obtained by ensemble averaging over $|\psi_0\rangle$, is then

$$A_\perp(\mathbf{R}, t) = \frac{\mathbb{1}(t^*)}{R} \sum_l \mathrm{e}^{-\mathrm{i}(\mathbf{k}-\mathbf{k}_0)\cdot\mathbf{R}_l} \mathbf{F}_c\big(t^*\big), \tag{4.10}$$

where the ensemble average emission amplitude $\mathbf{F}_c(t)$ is

$$\mathbf{F}_c(t) = \frac{C}{(2j_0+1)} \sum_{m_l} \mathbf{F}_{l,m_l}(t), \tag{4.11}$$

where C is the abundance of the resonant nuclear isotope. If there are several different resonant sites ρ within the unit cell, the sum in eq. (4.10) is also carried out over ρ, and $\mathbf{F}_c(t)$ will also depend on ρ.

Thus for spatially coherent decay $|\psi_e(\mathbf{k}_0)\rangle \rightarrow |\psi_0\rangle + \gamma_{\mathbf{k}}$, the emitted wave is a superposition of waves $\exp[-\mathrm{i}(\omega_{n_l m_l} - \mathrm{i}\Gamma')t]$ emanating from all the various sites $\mathbf{R}_l$ which add up to give highly directional emission, with the intensity modulated by the various difference frequencies.

Viewed as a scattering process, as discussed in section 4.2, the system resonantly scatters a photon $|\mathbf{k}_0\rangle$ in the incident synchrotron pulse to a final state $|\mathbf{k}\rangle$, with the nuclear system undergoing the transition $|\psi_0\rangle \rightarrow |\psi_{\rm e}(\mathbf{k}_0)\rangle \rightarrow |\psi_0\rangle$, i.e.,

$$\gamma_{\mathbf{k_0}} + |\psi_0\rangle \rightarrow \big|\psi_{\rm e}(\mathbf{k}_0)\big\rangle \rightarrow |\psi_0\rangle + \gamma_{\mathbf{k}}. \tag{4.12}$$

This is coherent elastic resonant scattering and corresponds to "multi-slit interference": it is impossible to tell at which nucleus the scattering took place, so the scattered wave amplitude is then the sum of the individual scattered wave amplitudes from all the nuclear sites, giving highly directional coherent scattering (as well as a weak diffuse contribution due to the "isotope effect").

If $|\psi_{\rm f}\rangle \neq |\psi_0\rangle$, the decay will be spatially incoherent (ignoring, for the moment, spatially coherent decay with recoil). For single photon decay, $|\psi_{\rm f}\rangle$ can differ from $|\psi_0\rangle$ only by the spin state of a single nucleus, e.g.,

$$|\psi_{\rm f}\rangle = \big|g_l m_l'\big\rangle\big|G_0(l)\big\rangle \quad m_l' \neq m_l. \tag{4.13}$$

In this case the lth site is "tagged" by "spin flip", and the emitted wave reduces to a single contribution,

$$A_\perp(\mathbf{R}, t) = \frac{\mathbb{1}(t^*)}{R} F_{l,m_l'}\big(t^*\big) \mathrm{e}^{-\mathrm{i}(\mathbf{k}-\mathbf{k}_0)\cdot\mathbf{R}_l}. \tag{4.14}$$

Thus, for spatially incoherent emission, $A_\mu(z)$ emanates from a single site $\mathbf{R}_l$, giving emission into 4π sr, with beat frequencies dependent only on the hyperfine splitting of the excited state of the nucleus at $\mathbf{R}_l$. Viewed as a scattering process, the scattering definitely occurred at the lth nucleus, and the scattered wave amplitude only contains this single contribution, giving essentially isotropic (diffuse) scattering.

Similarly, if $|\psi_{\rm e}(\mathbf{k}_0)\rangle$ decays by internal conversion, then one of the atoms will be tagged, now by the difference in the initial and final electronic states. As a consequence, there can be no spatial coherence in internal conversion decay.

Finally, the exciton may decay with the emission of one or more phonons in addition to the photon. Since the vibrational states are nonlocalized, this decay is spatially coherent if there is no spin flip. However, because of the continuum of phonon states, there is no coherent enhancement to these decay modes (the partial width is essentially $(1-f)\Gamma_\gamma$).

4.1.4. Coherent enhancement and coherent speedup

For an isolated nucleus, the total width for the excited level is $\Gamma = \Gamma_\gamma + \Gamma_\alpha$, where Γ_γ is the partial width for radiative decay and Γ_α is the partial width for internal conversion decay. For the synchrotron produced nuclear exciton state $|\psi_{\rm e}(\mathbf{k}_0)\rangle$, the total decay width is increased by the effect of spatially coherent radiative decay,

$$\Gamma \rightarrow \Gamma' = \Gamma_{\rm c} + \Gamma_\gamma' + \Gamma_\alpha, \tag{4.15}$$

where Γ_γ' is the partial width for spatially incoherent radiative decay and $\Gamma_{\rm c}$ is the partial width for spatially coherent decay $|\psi_{\rm e}(\mathbf{k}_0)\rangle \rightarrow |\psi_0\rangle + \gamma_{\mathbf{k}}$. If there is *no hyperfine*

splitting of the nuclei, then Γ_c will be time independent and can be calculated by the Fermi Golden Rule. For an E1 or M1 resonance,

$$\Gamma_c(\mathbf{k}_0) = \Gamma_{coh} N^{-1} (4\pi)^{-1} \int d\Omega(\mathbf{n}) \left[1 - \left(\mathbf{n} \cdot \hat{\varepsilon}_0\right)^2\right] \left|S(\mathbf{k} - \mathbf{k}_0)\right|^2, \tag{4.16}$$

where the diffraction factor $S(\mathbf{k} - \mathbf{k}_0)$ is given by

$$S(\mathbf{k} - \mathbf{k}_0) = \sum_{l=1}^{N} e^{-i(\mathbf{k}-\mathbf{k}_0)\cdot\mathbf{R}_l}. \tag{4.17}$$

Here $\mathbf{k}_0 = k_0\mathbf{n}_0$, $\mathbf{k} = k_0\mathbf{n}$, $\hat{\varepsilon}_0$ is the "appropriate" polarization of the incident synchrotron pulse ($\hat{\varepsilon}_0 = \mathbf{e}_0$ for E1, or $\hat{\varepsilon}_0 = \mathbf{b}_0 = \hat{k}_0\mathbf{e}_0$ for M1, respectively), and $\Gamma_{coh} = fC(2j_1+1)\Gamma_\gamma/(4j_0+2)$, where f is the Mössbauer factor, C is the abundance of the resonant nuclear isotope, and j_0 and j_1 are the spins of the nuclear ground and excited states.

The classical analogue is a phased array of dipole oscillators, oscillating with frequency ω_0 in the $\hat{\varepsilon}_0$-direction, with the amplitude of the radiator at $\mathbf{R}_l$ phased as $\exp(i\mathbf{k}_0 \cdot \mathbf{R}_l)$. The differential radiation rate is then

$$\frac{d\Re(\mathbf{k}_0)}{d\Omega(\mathbf{n})} = \frac{3}{2}\frac{\Gamma_\gamma}{\hbar}(4\pi)^{-1}\left[1 - \left(\mathbf{n} \cdot \hat{\varepsilon}_0\right)^2\right]\left|S(\mathbf{k} - \mathbf{k}_0)\right|^2. \tag{4.18}$$

$|S(\mathbf{k}-\mathbf{k}_0)|^2$ gives the relative intensity, due to the interference among the various source waves, of the radiation emitted in the $\mathbf{k}$ direction. The factor $[1 - (\mathbf{n} \cdot \hat{\varepsilon}_0)^2]$ gives the polarization dependence: each oscillator has an acceleration $\mathbf{a} \propto \hat{\varepsilon}_0 \exp(-i\omega t)$, and the emitted radiation in the $\mathbf{k}$ direction is proportional to the transverse projection $\mathbf{a}_\perp$ of the acceleration relative to the $\mathbf{k}$ direction. Integrating over $d\Omega(\mathbf{n})$ gives the total radiation rate for the system, $\Re(\mathbf{k}_0)$. Comparing with eq. (4.16), the partial width $\Gamma_c(\mathbf{k}_0)$ for spatially coherent decay $|\psi_e(\mathbf{k}_0)\rangle \rightarrow |\psi_0\rangle + \gamma_\mathbf{k}$ corresponds to the classical radiation rate per oscillator, $\Re(\mathbf{k}_0)/N$.

The relative intensity, $|S(\mathbf{k}-\mathbf{k}_0)|^2$, peaks to N^2 in directions $\mathbf{n}$ where constructive interference occurs for the wave amplitudes $\exp[-i(\mathbf{k} - \mathbf{k}_0) \cdot \mathbf{R}_l]$ emitted from all the nuclei. Thus in the small solid angle about $\mathbf{n}_0$ for which $(\mathbf{n} - \mathbf{n}_0) \cdot (\mathbf{R}_i - \mathbf{R}_j) \ll \lambda$ for all interatomic distances, $d\Re(\mathbf{k}_0)/d\Omega(\mathbf{n}) \approx N^2/4\pi$. The contribution to $\Re(\mathbf{k}_0)$ of this "forward direction" coherent radiation is then

$$\Re(\mathbf{k}_0) \approx \frac{\Gamma_{coh}}{\hbar}\frac{N^2}{4\pi}\Delta\Omega, \tag{4.19}$$

where $\Delta\Omega$ is the solid angle about $\mathbf{n}_0$ for which $(\mathbf{n} - \mathbf{n}_0) \cdot \left(\mathbf{R}_i - \mathbf{R}_j\right) < \lambda$ for all $\mathbf{R}_{ij}$.

$\Delta\Omega$ depends strongly on the dimensionality and shape of the crystal. If the radiators are uniformly distributed in a prism of dimensions $l_\parallel(\mathbf{k}_0)$, $l_\perp^{(1)}(\mathbf{k}_0)$ and $l_\perp^{(2)}(\mathbf{k}_0)$ relative to the direction $\mathbf{n}_0$, with the convention that $l_\perp^{(1)}(\mathbf{k}_0) \geqslant l_\perp^{(2)}(\mathbf{k}_0)$, and if $l_\parallel$ and $l_\perp \gg \lambda$, then there are three distinct cases:

(i) (1-D *crystal*) $\Delta\Omega \approx (4\lambda/l_{\parallel})$ if $l_{\perp}^{(1)} \approx l_{\perp}^{(2)} < \sqrt{\lambda l_{\parallel}}$;

(ii) (2-D *crystal*) $\Delta\Omega \approx (4\lambda/l_{\perp}^{(1)})(2\sqrt{\lambda/l_{\parallel}})$ if $l_{\perp}^{(1)} \approx l_{\parallel}$ and $l_{\perp}^{(2)} < \sqrt{\lambda l_{\parallel}}$; and

(iii) (3-D *crystal*) $\Delta\Omega \approx (\lambda/l_{\perp})^2$ if $l_{\perp}^{(1)} \approx l_{\perp}^{(2)} > \sqrt{\lambda l_{\parallel}}$.

In the opposite limit of long wavelengths, such that $\lambda \gg l_{\parallel}, l_{\perp}$ (0-D *crystal*), $\Delta\Omega \approx 4\pi$. Our main interest is in samples satisfying (iii), which is the usual situation, and we restrict our attention here to this case. The other three cases are discussed briefly in the following section.

For (iii) satisfied, we have

$$\frac{\Gamma_{\rm c}(\mathbf{k}_0)}{\hbar} = \frac{\Re(\mathbf{k}_0)}{N} \approx \frac{\Gamma_{\rm coh}}{\hbar}\left(\frac{N}{4\pi}\right)\left(\frac{\lambda}{l_{\perp}}\right)^2 = \frac{\Gamma_{\rm coh}}{\hbar}\pi n \lambda\!\!\!^{-2} l_{\parallel}, \tag{4.20}$$

where $n = N/(l_{\parallel} l_{\perp}^2)$ is the number of radiators per unit volume. Equation (4.20) shows that there is a coherent enhancement of the radiation rate per atom $\Re(\mathbf{k}_0)/N$ proportional to the number of atoms in a squared wavelength of the material in the thickness measured in the $\mathbf{n}_0$ direction. This is generally a very large number: if we take $\lambda \approx 1$ Å and $n \approx 0.1$ Å^{-3}, then $\pi n \lambda\!\!\!^{-2} \approx 10^{-2}$ Å^{-1}, so that a thickness of only ≈100 Å will double the radiation rate of properly phased atoms, and even for a very thin sample with $l_{\perp} \approx 1$ μm, condition (iii) allows $l_{\parallel} \leqslant 1$ cm, giving enhancements of ≈10^6. However, the actual length $l_{\parallel}$ over which coherence can occur will be limited by scattering and absorption processes: for the 14.4 keV resonance in ^{57}Fe, photoabsorption limits the coherence length to $l_{\parallel} \approx 2 \times 10^{-3}$ cm and the enhancements to ≈10^3. A very nice demonstration of the linear dependence of $\Gamma_{\rm c}$ on the thickness has been given by van Bürck et al. [89].

In addition to the enhancement due to coherence in the "forward" direction $\mathbf{n} \approx \mathbf{n}_0$, *in a crystal*, a further enhancement occurs if $\mathbf{k}_0$ makes a Bragg angle with a set of crystalline planes. Constructive interference then also occurs for those $\mathbf{k}$ ($\equiv k\mathbf{n}$) lying in the small solid angle about the ($\mathbf{k}_0 + \boldsymbol{\tau}$) direction ($\boldsymbol{\tau}$ is a reciprocal-lattice vector) such that $[\mathbf{k} - (\mathbf{k}_0 + \boldsymbol{\tau})] \cdot \mathbf{R}_{ij} \leqslant 2\pi$ for all $\mathbf{R}_{ij}$. For each open channel ($\mathbf{k}_0 + \boldsymbol{\tau}$), there will be a contribution [2,11,87]

$$\Gamma_{\rm c}^{(\tau)} = \Gamma_{\rm coh}\left[1 - \left(\mathbf{n}_{\tau} \cdot \hat{\varepsilon}_0\right)^2\right] \pi n \lambda\!\!\!^{-2} l_{\parallel}(\mathbf{k}_0 + \boldsymbol{\tau}), \tag{4.21}$$

where $l_{\parallel}(\mathbf{k}_0 + \boldsymbol{\tau})$ is the thickness of the crystal in the direction of ($\mathbf{k}_0 + \boldsymbol{\tau}$), and $\mathbf{n}_{\tau}$ is a unit vector in the direction of ($\mathbf{k}_0 + \boldsymbol{\tau}$). While the forward enhancement ($\tau = 0$) is always present, each additional channel ($\mathbf{k}_0 + \boldsymbol{\tau}$) only contributes for $\mathbf{k}_0$ within the small angular region $\Delta\phi \leqslant d/[m \cos(\phi_0) l_{\parallel}(\mathbf{k}_0 + \boldsymbol{\tau})]$ around the Bragg angle ϕ_0 ($d =$ interplanar spacing, $m =$ order of Bragg reflection).

Thus, if the incidence direction $\mathbf{n}_0$ is taken so that $\mathbf{k}_0$ satisfies the condition for a symmetric Bragg reflection from a thin crystal of resonant nuclei M-layers thick, then

there will be two coherent channels open, the reflection and transmission channels R and T, and the partial width for coherent decay will be

$$\Gamma_{\rm c}(\mathbf{k}_0) = \Gamma_{\rm c}^{(T)} + \Gamma_{\rm c}^{(R)}(\delta\phi), \tag{4.22}$$

where, for the coherent emission into the T-channel,

$$\Gamma_{\rm c}^{(T)} = \pi n \lambda\!\!\!^{-2} l_{\|}(\mathbf{k}_0)\Gamma_{\rm coh} \tag{4.23}$$

and for the coherent emission into the R-channel,

$$\Gamma_{\rm c}^{(R)}(\delta\phi) = \Gamma_{\rm c}^{(T)}\big[1 - \big(\mathbf{n}_1 \cdot \hat{\varepsilon}_0\big)^2\big]\left[\frac{\sin^2(M\delta)}{(M\delta)^2}\right]. \tag{4.24}$$

Here $\phi_0 = \phi_{0\rm B} + \delta\phi$ is the incidence angle with respect to the crystal planes, $\phi_{0\rm B}$ is the Bragg angle, d is the interplanar separation, and $\delta = kd\cos(\phi_{0\rm B})\delta\phi$. We have also assumed that the $\Delta\phi$-angular spread of the incident synchrotron pulse is small compared to the Bragg width, $\Delta\phi \ll \Delta\phi_{\rm B} \approx \lambda/(Md\cos\phi_{0\rm B})$. If $\Delta\phi \geqslant \Delta\phi_{\rm B}$, then $\Gamma_{\rm c}^{(R)}(\delta\phi)$ is integrated over the angular distribution of the incident pulse intensity. If $\hat{\varepsilon}_0 \perp \mathbf{n}_1$, then near Bragg ($\delta\phi \ll \Delta\phi_{\rm B}$), $\Gamma_{\rm c}$ doubles to $2\Gamma_{\rm c}^{(T)}$, which agrees with the enhanced width obtained in eq. (3.99) for excitation at Bragg by a near resonant monochromatic wave of frequency ω. For a sufficiently thick crystal, typically $M \approx 10^3$–10^4 layers, $\Gamma_{\rm c}$ will exceed $(\Gamma'_\gamma + \Gamma_\alpha)$, and coherent decay will dominate incoherent decay. The nuclear exciton then de-excites at the speeded-up rate $(\Gamma_{\rm c} + \Gamma'_\gamma + \Gamma_\alpha)/\hbar$, primarily via coherent radiative decay into either the R- or T-channel. This speed-up of coherent decay at Bragg has been observed, e.g., in [90].

Because the forward scattering channel ($\tau = 0$) is always open, an exciton $|\psi_{\rm e}(\mathbf{k}_0)\rangle$ created by a synchrotron radiation pulse is always superradiant (for a 3-D crystal geometry), regardless of whether $\mathbf{k}_0$ satisfies a Bragg condition or not. However, there is an important distinction between the Bragg- and off-Bragg cases. As discussed in section 6, in simple situations the Bragg mode excitation is a true semi-stationary state radiative eigenmode with an enhanced width $(\Gamma_{\rm c} + \Gamma'_\gamma + \Gamma_\alpha)$, while the off-Bragg (or Laue) excitation is in fact a superposition of radiative eigenmodes of slightly differing frequencies. In all cases, the *initial decay rate* of $|\psi_{\rm e}(\mathbf{k}_0)\rangle$ is $(\Gamma_{\rm c} + \Gamma'_\gamma + \Gamma_\alpha)/\hbar$ (where $\Gamma_{\rm c}$ depends on the number of open channels, as discussed above), but the character of the decay at delayed times $\gg \hbar/(\Gamma_{\rm c} + \Gamma'_\gamma + \Gamma_\alpha)$ is radically different, depending on whether the exciton $|\psi_{\rm e}(\mathbf{k}_0)\rangle$ is an eigenmode or not. In the case of an eigenmode, the scattered signal (emission probability) has a pure exponential decay $\propto \exp[-(\Gamma_{\rm c} + \Gamma'_\gamma + \Gamma_\alpha)t/\hbar)]$ at the enhanced decay rate. On the other hand, if $|\psi_{\rm e}(\mathbf{k}_0)\rangle$ is a superposition of eigenmodes, the superradiant components die out quickly, leaving a superposition of slowly damped components $\approx \exp[-(\Gamma'_\gamma + \Gamma_\alpha)t/\hbar)]$, with a spread of eigenmode frequencies, producing a slowly decaying "ringing" signal at delayed times. This delayed time behavior is discussed in sections 4.2 and 6.

4.1.5. Γ_c *in 0-, 1-, and 2-dimensions*

As noted above, the solid angle $\Delta\Omega$ of constructive interference depends strongly on the dimensionality and shape of the crystal (relative to the direction of the phasing vector $\mathbf{k}_0$).

For "*end-fire*" emission from a 1-*dimensional* shaped rod ($l_\parallel(\mathbf{k}_0) \gg l_\perp(\mathbf{k}_0)^2/\lambda$), the solid angle of constructive interference is $\Delta\Omega \approx (\pi\lambda/l_\parallel)$. For a linear chain of N atoms with an interatomic spacing d,

$$\frac{R_c(\mathbf{k}_0)}{N} \approx \frac{\lambda}{4d}\frac{\Gamma_{coh}}{\hbar}. \tag{4.25}$$

Thus, there is no appreciable enhancement for a one-dimensional array with $\lambda \leqslant d$.

For grazing "*surface mode*" emission from a 2-*dimensional* planar sample

$$l_\perp^{(1)}(\mathbf{k}_0) \approx l_\parallel(\mathbf{k}_0), \quad l_\perp^{(2)}(\mathbf{k}_0) \ll \sqrt{\frac{l_\parallel(\mathbf{k}_0)}{\lambda}},$$

and

$$\Delta\Omega \approx \frac{\lambda}{l_\perp^{(1)}} \cdot 2\sqrt{\frac{\lambda}{l_\parallel}}.$$

For a square array of $N = M^2$ atoms with an interatomic spacing d,

$$\frac{R_c(\mathbf{k}_0)}{N} \approx 2\pi\left(\frac{\lambda}{d}\right)^2\sqrt{\frac{l_\parallel}{\lambda}}\frac{\Gamma_{coh}}{\hbar}, \tag{4.26}$$

where $l_\parallel = Md$. This result also holds for a planar *crystal* if the orientation of $\mathbf{k}_0$ is such that a *surface mode channel* $\mathbf{k}_s$ is just opened (rather than for $\mathbf{k}_0$ being a surface mode). Thus for a planar sample and short wavelength resonance radiation $\lambda \leqslant d$, there is an enhancement of coherent decay $\propto\sqrt{l_\parallel/\lambda}$ of the exciton $|\psi_e(\mathbf{k}_0)\rangle$ if the phasing vector $\mathbf{k}_0$ just opens a surface mode for the plane.

In the opposite limit of long wavelegth resonances with $\lambda \gg$ the dimensions of the sample (0-*dimensional crystal*), there is constructive interference in all directions, so $\Delta\Omega = 4\pi$ and

$$\frac{R_c(\mathbf{k}_0)}{N} = N\frac{\Gamma_{coh}}{\hbar}. \tag{4.27}$$

Thus, for a 0-dimensional crystal Γ_c would be strongly enhanced, directly proportional to the number of nuclei N. Of course this long wavelength situation will not be realized for the Mössbauer transitions of interest to us, where always $\lambda \leqslant d$.

4.1.6. Spatially coherent quantum beats and temporal Pendellösung

If there is hyperfine splitting of the nuclear levels, or if there are shifts between the levels of nuclei located in different chemical sites, there will be periodic constructive/destructive interference between waves of different frequency emitted from the

different sites. This results in a striking "quantum beat" modulation of the spatially coherent decay rate,

$$\frac{\Gamma_{\rm c}}{\hbar} \to \frac{\Gamma_{\rm c}(t)}{\hbar}, \tag{4.28}$$

varying periodically between "superradiant" and "subradiant" emission into the coherent channels, with beat frequencies determined by the frequency differences among the various transition resonances. Furthermore, if there are several coherent channels open, the "superradiant" condition can oscillate between channels, giving a striking temporal Pendellösung effect for the probability for photon decay.

The coherent elastic photon potential $\mathbf{A}_\perp(\mathbf{R},t)$ for the spatially coherent decay $|\psi_{\rm e}(\mathbf{k}_0)\rangle \to |\psi_0\rangle + \gamma_{\mathbf{k}}$ is given by eqs. (4.9)–(4.11), where the decay width Γ' is given in the first Born approximation by $\Gamma' = \Gamma = \Gamma_\gamma + \Gamma_\alpha$, while in the second Born approximation,

$$\Gamma'\big(t^*\big) = \frac{1}{t^*}\int_0^{t^*} \big[\Gamma_{\rm c}(t) + \Gamma'_\gamma + \Gamma_\alpha\big]\,{\rm d}t. \tag{4.29}$$

$\Gamma_{\rm c}(t)$, Γ'_γ and Γ_α give the various partial widths of $|\psi_{\rm e}(\mathbf{k}_0,t)\rangle$ at time t, i.e.,

$$\frac{\rm d}{{\rm d}t}\big\langle\psi_{\rm e}(t)\big|\psi_{\rm e}(t)\big\rangle = -\frac{1}{\hbar}\big[\Gamma_{\rm c}(t) + \Gamma'_\gamma + \Gamma_\alpha\big]\big\langle\psi_{\rm e}(t)\big|\psi_{\rm e}(t)\big\rangle, \tag{4.30}$$

so that within the spirit of this approximation, $|\psi_{\rm e}(t)\rangle$ decays as

$$\big\langle\psi_{\rm e}(t)\big|\psi_{\rm e}(t)\big\rangle = {\rm e}^{-\Gamma'(t)t/\hbar}\big\langle\psi_{\rm e}(\mathbf{k}_0)\big|\psi_{\rm e}(\mathbf{k}_0)\big\rangle, \tag{4.31}$$

with $\Gamma'(t)$ as given above.

The *partial width* $\Gamma_{\rm c}(t)$ for *coherent emission* is given by

$$\Gamma_{\rm c}(t^*) = \frac{R^2\int {\rm d}\Omega_{\rm R}\, n_{\rm c}(\mathbf{R},t)}{\langle\psi_{\rm e}(t^*)|\psi_{\rm e}(t^*)\rangle}, \tag{4.32}$$

where the photon flux (probability/cm^2/s) for spacially coherent emission is given by

$$n_{\rm c}(\mathbf{R},t) = \left[\frac{\omega_0}{2\pi\hbar c}\right]\cdot\big|\mathbf{A}_\perp(\mathbf{R},t)\big|^2. \tag{4.33}$$

If there is no hyperfine splitting, then $\Gamma_{\rm c}(t) = \Gamma_{\rm c}$, the enhanced coherent decay width given by eq. (4.16). In the presence of splitting, $\mathbf{A}_\perp(\mathbf{R},t)$ is a superposition of waves of all the various resonance frequencies $\omega_{nm}(\rho)$ of all the nuclei within each unit cell, and there will be a "quantum beat" modulation of the coherent decay rate, with $\Gamma_{\rm c}(t)/\hbar$ varying between a strongly enhanced peak decay rate and a strongly suppressed minimum decay rate.

Because of the high directionality of $|S(\mathbf{k}-\mathbf{k}_0)|^2$, $\Gamma_{\rm c}(t)$ is the sum of the open channel contributions,

$$\Gamma_{\rm c}(t) = \sum_m \Gamma_{\rm c}^{(m)}(t). \tag{4.34}$$

$\Gamma_{\rm c}^{(m)}(t)/\hbar$ gives the instantaneous rate for radiative decay into the mth channel, so the expected signal $I_{\rm c}^{(m)}(t)$ in the channel (prob./s a photon is emitted into the channel) is

$$I_{\rm c}^{(m)}(t) = \frac{\Gamma_{\rm c}^{(m)}(t)}{\hbar} \cdot \big\langle \psi_{\rm e}(t) \big| \psi_{\rm e}(t) \big\rangle = \frac{\Gamma_{\rm c}^{(m)}(t)}{\hbar} \cdot {\rm e}^{-\Gamma'(t)t/\hbar} \cdot \big\langle \psi_{\rm e}(\mathbf{k}_0) \big| \psi_{\rm e}(\mathbf{k}_0) \big\rangle. \quad (4.35)$$

For the *spin flip* and *internal conversion incoherent decay modes*, there is no interference between waves from different sites, and at a particular site, the decay is $\sum c_{nm}|en\rangle \rightarrow |gm'\rangle$, so the quantum beats only exhibit the splittings of the excited levels. There is no information about the ground state splittings or of the energy shifts between different sites. Because there is no spatial coherence, there is no enhancement of the partial widths for incoherent decay, $\Gamma_\alpha + \Gamma'_\gamma$. Furthermore, Γ_α and the spin flip contribution to Γ'_γ are time-independent, in sharp contrast to $\Gamma_{\rm c}(t)$. The spatially incoherent decay goes into all directions, and in any particular direction a quantum beat modulation will be observed. But since the contributing waves arise from different ΔJ_z-"oscillators", there will be no net interference when integrated over d$\Omega_{\rm R}$. (There will, however, be a time dependence in the contribution to Γ'_γ, which arises from the diffuse elastic scattering associated with the isotope effect. But this is only a small contribution to the total width $\Gamma'(t)$ so we will not consider it further.)

A striking example of the quantum beat modulation of the coherent rate due to *spatial coherence* has been observed in the experiments on yttrium–iron–garnet (YIG) [91]. In YIG there are two inequivalent sites, $d1$ and $d2$, with a shift $\hbar\Omega_E \approx 6\Gamma$ between the resonance frequencies at the two sites arising from the different orientation of the electric field gradient (EFG) relative to the internal hyperfine field $\mathbf{B}_{\rm int}$ at the two sites. There is also hyperfine splitting at each site, resulting in additional higher frequency quantum beat modulations. But to simplify the discussion, we take an idealized case with a single unsplit resonance at each site, with two inequivalent sites ρ_{d1} and ρ_{d2} within each unit cell, and with a difference Ω_E between the resonance frequencies at the two sites.

With $\mathbf{k}_0$ set to satisfy the Bragg condition for a symmetric reflection from an M-layer crystal, the partial width for coherent decay is $\Gamma_{\rm c}(t) = \Gamma_{\rm c}^{(R)}(t) + \Gamma_{\rm c}^{(T)}(t)$, where for $m = R, T$,

$$\Gamma_{\rm c}^{(m)}(t) = \Gamma_{\rm c} \cdot \cos^2\big[(\Omega_E t - \phi_m)/2\big]. \quad (4.36)$$

Here ϕ_m gives the relative spatial phase of the $d1$ and $d2$ contributions for emission into the mth channel,

$$\phi_m = (\mathbf{k}_m - \mathbf{k}_0) \cdot (\rho_{d1} - \rho_{d2}), \quad (4.37)$$

and $\Gamma_{\rm c}$ gives the peak partial width for coherent emission into a single channel,

$$\Gamma_{\rm c} = \pi n \lambda\!\!\!^{-2} l_{\|}(\mathbf{k}_0)\Gamma_{\rm coh}. \quad (4.38)$$

The crystal "planes" now have unit cell thickness, with a separation d between plane centers, and n is the density of unit cells (/cm^3). We have also assumed $\hat{\varepsilon}_0 \perp (\mathbf{k}_0, \mathbf{k}_{(0-)})$

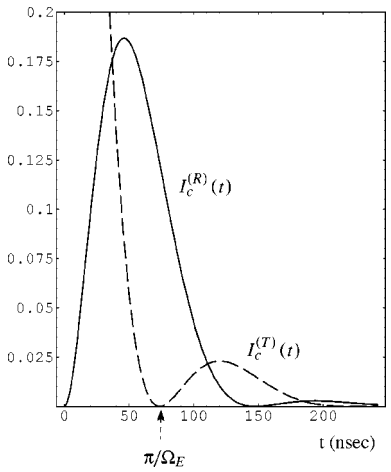

Figure 18. The probabilities/s for photon emission into the R- and T-channels (solid and dashed lines, respectively) following a pulse excitation of an ^{57}Fe enriched YIG crystal with $\mathbf{k}_0$ satisfying the condition for an (0 0 2) Bragg reflection.

and an exact Bragg condition, so that $[1-(\mathbf{n}_\mathrm{R}\cdot\hat{\varepsilon}_0)^2]\cdot[\sin(M\delta)/(M\delta)]^2=1$ for the reflection channel.

Thus, the decay rate $\Gamma_\mathrm{c}^{(m)}(t)/\hbar$ for coherent emission into each channel oscillates between superradiant and subradiant peaks occurring at the quantum beat frequency Ω_E. Furthermore, if the relative spatial phase factor $\phi_m \neq 2n\pi$, then the peak decay rates into the R- and T-channels occur at different times, with the time separation being a direct measure of ϕ_m.

For the (0 0 2) Bragg reflection in YIG, $\phi_{(R)}=\pi$ and $\phi_{(T)}=0$, so that the instantaneous partial widths for emission into the R- and T-channels are 180° out of phase,

$$\Gamma_\mathrm{c}^{(R)}(t)=\Gamma_\mathrm{c}\sin^2(\Omega_E t/2), \tag{4.39}$$

$$\Gamma_\mathrm{c}^{(T)}(t)=\Gamma_\mathrm{c}\cos^2(\Omega_E t/2). \tag{4.40}$$

Thus, for the (0 0 2) reflection, the total partial width $\Gamma_\mathrm{c}(t)$ for coherent decay is independent of time,

$$\Gamma_\mathrm{c}(t)=\Gamma_\mathrm{c}^{(R)}(t)+\Gamma_\mathrm{c}^{(T)}(t)=\Gamma_\mathrm{c}, \tag{4.41}$$

and the decay parameter $\Gamma'(t)$ also becomes time-independent,

$$\Gamma'(t)=\Gamma'=\Gamma_\mathrm{c}+\Gamma'_\gamma+\Gamma_\alpha. \tag{4.42}$$

The probabilities/s for photon emission into the R- and T-channels, eq. (4.35), are then

$$I_\mathrm{c}^{(R)}(t)=\mathrm{e}^{-\Gamma' t/\hbar}\sin^2(\Omega_E t/2)\cdot\frac{1}{\hbar}\big[\Gamma_\mathrm{c}\big\langle\psi_\mathrm{e}(\mathbf{k}_0)\big|\psi_\mathrm{e}(\mathbf{k}_0)\big\rangle\big], \tag{4.43}$$

$$I_\mathrm{c}^{(T)}(t)=\mathrm{e}^{-\Gamma' t/\hbar}\cos^2(\Omega_E t/2)\cdot\frac{1}{\hbar}\big[\Gamma_\mathrm{c}\big\langle\psi_\mathrm{e}(\mathbf{k}_0)\big|\psi_\mathrm{e}(\mathbf{k}_0)\big\rangle\big]. \tag{4.44}$$

In the reflection channel $R_{(0\,0\,2)}$, there is thus an initial complete suppression of the coherent decay, followed by a delayed enhanced probability for photon emission, as shown in figure 18. The decay rate $\Gamma_{\rm c}^{(R)}(t)/\hbar$ for coherent decay into R peaks at odd multiples of $\pi/\Omega_E \approx 74$ ns. Because the probability of excitation $\langle\psi_{\rm e}(t)|\psi_{\rm e}(t)\rangle$ is decaying proportional to $\exp(-\Gamma' t/\hbar)$, the observed signal $I_{\rm c}^{(R)}(t)$ peaks at earlier times $t_n = [(2n-1)\pi/\Omega_E - \Delta\tau]$, which are the positive time solutions of $\tan(\Omega_E t/2) = \hbar\Omega_E/\Gamma'$. For $\Gamma' = 4\Gamma$, as observed in the experiment in [91], $\Delta\tau \approx 32$ ns, and the first delayed peak occurs at $t_1 \approx 42$ ns. The enhanced total width $\Gamma' \approx 4\Gamma$ is due to coherent enhancement of the radiative width $\Gamma_{\rm c} \approx 3\Gamma \approx 30\Gamma_\gamma$, a 30-fold enhancement of the radiative decay rate. Equally remarkable is the initial complete suppression of coherent decay into R, followed by a delayed peak probability after 42 ns. This is in marked contrast to the radiative decay from an isolated nucleus, which follows an $\exp(-\Gamma t/\hbar)$ dependence.

For the transmission channel, the relative spatial phase is $\phi_{(T)} = 0$, giving initial constructive interference, and the coherent emission into $T_{(0\,0\,2)}$ is 180° out of phase with the emission into $R_{(0\,0\,2)}$. Thus, for the (0 0 2) Bragg reflection, the coherent decay should exhibit a striking "temporal Pendellösung" effect, oscillating back and forth between the T- and R-channels at frequency Ω_E.

This behavior can be changed by changing the order of the Bragg reflection. For example, for the (0 0 4)-Bragg reflection, the spatial phase factors are $\phi_{(R)} = \phi_{(T)} = 0 \pmod{2\pi}$, so in this case the R- and T-channels beat in phase with a $\cos^2(\Omega_E t/2)$ dependence, with the partial width for coherent decay being

$$\Gamma_{\rm c}(t) = \Gamma_{\rm c}^{(R)}(t) + \Gamma_{\rm c}^{(T)}(t) = 2\Gamma_{\rm c}\cos^2(\Omega_E t/2). \tag{4.45}$$

The decay parameter $\Gamma'(t)$, eq. (4.29), is now also time-dependent,

$$\Gamma'(t) = \Gamma_\alpha + \Gamma'_\gamma + \Gamma_{\rm c}\left(1 + \frac{\sin(\Omega_E t)}{\Omega_E t}\right), \tag{4.46}$$

and the probabilities/s for photon emission into the R- and T-channels are then

$$I_{\rm c}^{(R)}(t) = I_{\rm c}^{(T)}(t) = {\rm e}^{-\Gamma'(t)t/\hbar}\cos^2(\Omega_E t/2)\cdot\frac{1}{\hbar}\left[\Gamma_{\rm c}\left\langle\psi_{\rm e}(\mathbf{k}_0)\middle|\psi_{\rm e}(\mathbf{k}_0)\right\rangle\right]. \tag{4.47}$$

Thus, for the (0 0 4) reflection, in contrast to the (0 0 2) reflection, $\Gamma_{\rm c}(t)$ is time-dependent, with the probability for photon decay (into either channel) being initially strongly enhanced, followed by complete suppression of coherent decay at a time $\approx \pi/\Omega_E \approx 74$ ns.

4.1.7. Nuclear exciton states, Dicke superradiance, and γ-lasers

Steady state grazing is very unpromising because it would involve maintaining crystallinity during several natural lifetimes ($\approx 10^{-9}$–10^{-6} s) while each atom is discharging $\approx 10^4$ eV energy. Therefore, to prevent excessive heating, the radiation pulse must be emitted quickly, before the crystal is destroyed. Hence, "superradiance" appears essential for gamma lasing [21,43,44].

In the case of an initially inverted system, we find that multi-photon Dicke superradiance will take place in the mode for which the *single exciton* state $|\psi_e(\mathbf{k}_0)\rangle$ discussed above has the maximum decay rate $\Gamma_c(\mathbf{k}_0)/\hbar$:

For a long thin needle, with all N atoms initially excited, the initial decay rate for emission into the *end-fire mode* [21] is $N\gamma/\hbar$, where $\gamma = \Gamma_\gamma d\Omega/4\pi$ is the partial width for single atom decay into the end-fire mode, with $\Delta\Omega = (\lambda/d)^2$ and $d =$ needle diameter. However, coherent emission into the mode enhances the rate for subsequent emissions into the mode. According to Dicke [21], if p photons have already been emitted into the mode, then the rate of emission of the next photon is

$$R_{coh}(p+1) = \frac{\Gamma_{coh}}{\hbar}(p+1)(N-p), \tag{4.48}$$

where

$$\Gamma_{coh}(p+1) = (p+1)\gamma \tag{4.49}$$

is the probability/s of radiating into the end-fire mode per excited atom. Thus, $\Gamma_{coh}(p+1)$ exhibits a "coherent enhancement" over the single atom decay rate by a factor of $(p+1)$. The power $\hbar\omega R_{coh}(p+1)$ will maximize at $p = N/2$, giving

$$R_{coh}(N/2) = (N/2)^2\gamma, \tag{4.50}$$

but $\Gamma_{coh}(p+1)$ continues to increase, reaching its maximum, $N\gamma$ $(= \pi n \lambda\!\!\!^{-2} l_\parallel \Gamma_\gamma = \Gamma_c(\mathbf{k}_0)$, as discussed in section 4.1.4), at $p = N-1$, i.e., when only a *single excitation* remains. Thus, the *last state* in the cascade, the *single exciton* state $|\psi_e(\mathbf{k}_0)\rangle$, is the *most superradiant* (i.e., has the greatest decay rate per excited atom). Conversely, the single exciton state (mode) $|\psi_e(\mathbf{k}_0)\rangle$ with the greatest decay rate $\Gamma_c(\mathbf{k}_0)/\hbar$ will be the *favored superradiant decay mode* for an initially inverted system. Thus by studying the coherent enhancement of single exciton modes, in crystals as well as amorphous samples, we get direct information regarding the development of superradiance in an initially inverted system. As discussed in section 3.9, coherent multibeam modes resulting from crystallinity have greater coherent enhancements than any single beam modes and would in the case of an initially inverted crystal be the superradiant decay modes.

The connection between Dicke superradiance and single exciton states is very important because the coherent enhancement of single exciton modes is subject to experimental investigation now. Thus, it is of interest to investigate, both theoretically and experimentally, the optics of single exciton states induced in crystals by synchrotron radiation pulses, not only because of the intrinsic interest in this new field of optics, but also because the results will have a very important bearing on the possibility of γ-ray lasing/superradiance. Of particular interest will be thin crystal excitations in multibeam Bragg and Laue modes, as well as thick crystal excitations in multibeam Borrmann modes [92–95].

4.2. Coherent elastic scattering of synchrotron radiation pulses

The exciton approach brings out the interesting new physics involved in synchrotron pulse excitation of Mössbauer nuclei. However, a much simpler method for obtaining the scattered signal is to treat the interaction as a coherent elastic scattering problem.

Synchrotron radiation is a very bright, white source of radiation with fluxes in the 10 keV region ranging from 10^{12}–10^{14} photons/s per eV per mrad of Δ_y (see figure 19). The radiation is highly collimated about the plane of the synchrotron, with the divergence at 10 keV being $\Delta_x \approx 0.1$–0.2 mrad, with about 90% of the intensity associated with the component parallel to the plane of the orbit ($\hat{\varepsilon}_y$ in figure 19). There is also a stable periodic time structure, with the duration of each pulse being $\approx 10^{-10}$ s, and the separation between pulses, depending on the electron bunching, being $\approx 10^{-6}$ s for operation in the single bunch mode.

As discussed in [26,32,86], each synchrotron pulse consists of many photons emitted by the many electrons in the bunch incoherently, one with the other. The pulse from a given electron has a duration $\approx \lambda_c/c \approx 10^{-19}$ s, or, if this radiation is filtered to about 1 eV, the coherence time becomes $T_c \approx 10^{-15}$ s, which is still generally very short compared to the response time $I_c^{(s)}(t)$ of the coherently scattered signal (even with strong coherent enhancement, say $\Gamma_c \approx 100\Gamma$, the response time $\approx (100\Gamma)^{-1} \gg 10^{-15}$ s). The duration of the entire pulse depends on the bunching of the electrons and is typically $\approx 10^{-10}$ s. The scattered flux is then computed starting from eqs. (3.9)–(3.11), where $\mathbf{A}^0(t)$ represents a *one-photon* amplitude of duration on the

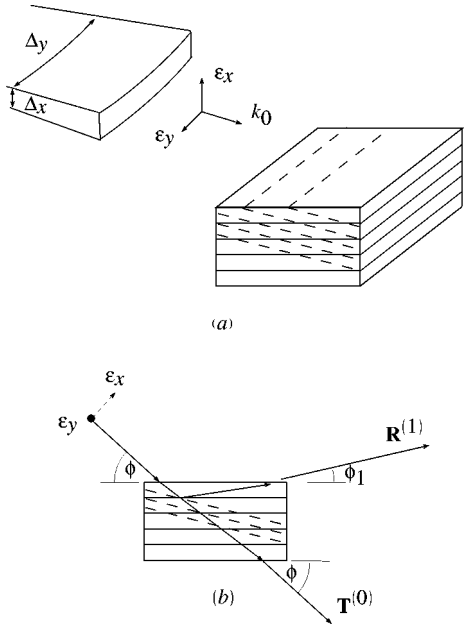

Figure 19. Schematic of scattering geometry.

order of the coherence time T_c. Because T_c is very short compared to the scattering response time, the time dependent amplitude of the coherent elastic scattered wave is simply proportional to the Fourier transform of the frequency dependent reflection and transmission amplitudes $\widetilde{R}(\omega;\hat{k}_1,\hat{k}_0)$ and $\widetilde{T}(\omega;\hat{k}_1,\hat{k}_0)$ already obtained for the various cases of off-Bragg, Bragg, Laue and grazing incidence:

The time-dependent coherent elastic photon flux which is scattered into the $\mathbf{k}_s$ channel following excitation of the crystal by a synchrotron pulse of polarization $\mathbf{e}_0$ incident at $t_0 = 0$ is given by

$$I^{(s)}(t,\phi) = \big[2\pi\hbar g I_{0p}(\phi)\big]\big|\mathbf{S}\big(t;\hat{k}_s,\hat{k}_0;\mathbf{e}_0\big)\big|^2, \tag{4.51}$$

where $\mathbf{S}(t;\hat{k}_s,\hat{k}_0;\mathbf{e}_0)$ gives the amplitude response to a δ-function pulse,

$$\mathbf{S}\big(t;\hat{k}_s,\hat{k}_0;\mathbf{e}_0\big) = \frac{1}{2\pi}\int_{-\infty}^{+\infty} \mathrm{d}\omega \mathbf{S}\big(\omega;\hat{k}_s,\hat{k}_0;\mathbf{e}_0\big)\mathrm{e}^{-\mathrm{i}\omega t}. \tag{4.52}$$

Here,

$$\mathbf{S}\big(\omega;\hat{k}_s,\hat{k}_0;\mathbf{e}_0\big) = \widetilde{S}\big(\omega;\hat{k}_s,\hat{k}_0\big)\mathbf{e}_0 \tag{4.53}$$

is the wave coherent elastically scattered into the $\mathbf{k}_s = (\omega/c)\hat{k}_s$ channel when a wave $\mathbf{k}_0 = (\omega/c)\hat{k}_0$ is incident on the crystal with polarization $\mathbf{e}_0$. For a reflection channel $\mathbf{k}_r$, $\mathbf{S}(\omega;\hat{k}_r,\hat{k}_0;\mathbf{e}_0)$ is the reflected wave $\mathbf{R}^r$; and for a transmission channel $\mathbf{k}_t$, $\mathbf{S} = \mathbf{T}^t$. $\mathbf{S}(\omega)$ is given in general by eq. (3.51), and for the special cases of off-Bragg, Bragg, grazing incidence, and Laue, by eqs. (3.63), (3.81, 3.86), (3.105) and (3.114), (3.115), respectively.

In (4.51), $I_{0p}(\phi)$ is the number of photons/eV per mrad^2 per synchrotron pulse incident on the crystal at the rocking angle ϕ, with polarization $\mathbf{e}_0$ at frequency ω_0; and $g = \sin\phi_s/\sin\phi_0$ is the geometrical factor relating the cross-sectional areas of the incident and scattered beams. For simplicity, we also assume that the crystal is oriented so that the scattering plane $(\mathbf{k}_0,\mathbf{k}_s)$ is perpendicular to the crystal surface. The Δ_y divergence is then maintained on scattering (see figure 19).

$I(t,\phi)\,\mathrm{d}t\,\mathrm{d}\phi\Delta_y$ then gives the expected number of photons scattered into the $\mathbf{k}_s$ channel between t and $t + \mathrm{d}t$. If the duration of the incident synchrotron pulse is appreciable compared to the response time of $|\mathbf{S}(t)|^2$, then the response must be folded over the initial pulse shape $P_0(t)$,

$$I^{(s)}(t,\phi) = 2\pi\hbar g I_{0p}(\phi)\int \mathrm{d}t_0\big|\mathbf{S}(t-t_0;\hat{k}_s,\hat{k}_0;\mathbf{e}_0)\big|^2 P_0(t_0). \tag{4.54}$$

In most cases there is no simple analytical solution for $\widetilde{S}(t;\hat{k}_1,\hat{k}_0)$, but instead one numerically computes the fast Fourier transform of $\widetilde{S}(\omega;\hat{k}_1,\hat{k}_0)$, which is calculated using the general procedure outlined in section 3.4. There are simple solutions in several important limiting cases, however.

4.2.1. Quantum beats in the Born approximation

In the first Born approximation,

$$\widetilde{S}\big(\omega;\hat{k}_1,\hat{k}_0\big) = M\widetilde{F}^{10} = n\lambda l_{\parallel}(\mathbf{k}_1)\tilde{f}(\omega). \tag{4.55}$$

Here $\widetilde{F}^{10}$ is the planar scattering amplitude as given in eq. (3.32) and M is the number of layers. In the second line, $l_{\parallel}(\mathbf{k}_1) = Md/\sin\phi_1$ is the thickness of the crystal in the $\mathbf{k}_1$ direction, and

$$\tilde{f}(\omega) = \sum_{\rho}\big[\tilde{f}_{\mathrm{e}}^{(\rho)} + \tilde{f}_{\mathrm{n}}^{(\rho)}(\omega)\big]\mathrm{e}^{-\mathrm{i}(\mathbf{k}_1-\mathbf{k}_0)\cdot\rho} \tag{4.56}$$

is the 2×2 matrix for the unit cell scattering amplitude. The resonant nuclear scattering amplitude $\tilde{f}_{\mathrm{n}}^{(\rho)}(\omega)$ is a sum of Lorentzian resonances corresponding to the various allowed transitions between the excited and ground state hyperfine levels at the unit cell site ρ,

$$\tilde{f}_{\mathrm{n}}^{(\rho)}(\omega) = \sum_{nm}\frac{f_0^{(\rho)}(nm;\hat{k}_1,\hat{k}_0)\Gamma/2}{[\hbar\omega - \hbar\omega_{nm}(\rho) + \mathrm{i}\Gamma/2]}. \tag{4.57}$$

The transform $\widetilde{S}(t;\hat{k}_1,\hat{k}_0)$ is then a superposition of damped harmonic waves,

$$\widetilde{S}\big(t;\hat{k}_1,\hat{k}_0\big) \propto \sum_{\rho}\mathrm{e}^{-\mathrm{i}(\mathbf{k}_1-\mathbf{k}_0)\cdot\rho}\sum_{nm}f_0^{(\rho)}(nm;\hat{k}_1,\hat{k}_0)\mathrm{e}^{-\mathrm{i}[\omega_{nm}(\rho)-\mathrm{i}\Gamma/2\hbar]t}, \tag{4.58}$$

and, hence, the intensity $|\mathbf{S}(t)|^2$ is modulated at the various quantum beat frequencies

$$\Omega_{\mathrm{B}}\big(n,m,\rho;n',m',\rho'\big) = \omega_{nm}(\rho) - \omega_{n'm'}\big(\rho'\big) \tag{4.59}$$

corresponding to the difference frequencies of all allowed nuclear hyperfine transitions $\omega_{nm}(\rho)$ from all the different nuclear sites ρ, from which the hyperfine splittings of both the excited and ground states may be found, as well as any energy shifts between nuclei located in different chemical or magnetic sites.

The electronic contribution to $\tilde{f}(\omega)$ gives a prompt time response which does not interfere with the slowly decaying signal from the nuclear resonances. (The frequency insensitive parts of f_{e} yield a delta-function response, and the absorption edge resonances with widths on the order eV give signals which decay out in $\approx10^{-15}$ s.)

The first Born approximation will give an accurate description of the resonant signal if the effects of coherent enhancement are small, i.e., if $\Gamma_{\mathrm{c}} \leqslant \Gamma_{\gamma}$. Since $\Gamma_{\mathrm{c}} \approx \pi n\lambda_0^2 l_{\parallel} f_{\mathrm{M}}\Gamma_{\gamma}$, where n is the density of resonators and f_{M} is the Mössbauer factor, the crystallite dimensions must be $l \leqslant 4\pi/nf_{\mathrm{M}}\lambda_0^2$, so typically a μm or less. For optically thick samples, the interaction among the resonators can lead to additional "*dynamical beats*" which must be subtracted from the quantum beat spectrum. The dynamical beats are discussed below.

4.2.2. Superradiant normal mode excitation at Bragg

For a symmetric Bragg reflection from a highly enriched thin film crystal of unsplit M1 Mössbauer nuclei, and for incident $\mathbf{e}_0 = \hat{\pi}$ radiation, $S(\omega; \hat{k}_1, \hat{k}_0; \mathbf{e}_0) = R(\omega, \delta)$ is given by the simple Lorentzian form of eq. (3.90), with an enhanced width $\Gamma'(\delta) = \Gamma'_\gamma + \Gamma_\alpha + \Gamma_c(\delta)$ and shifted resonance $\omega'_0(\delta) = \omega_0 + \Delta\omega_c(\delta)$, as given by eqs. (3.92) and (3.93). Here $\delta = k_0 d \cos\phi_0 \delta\phi$, where $\delta\phi$ is the rocking angle from exact Bragg at resonance. The transform time signal $R(t, \delta)$ is then a damped harmonic wave,

$$R(t, \delta) \propto \exp\{-\mathrm{i}[\omega'_0(\delta) - \mathrm{i}\Gamma'(\delta)/\hbar]t\}. \tag{4.60}$$

At exact Bragg ($\delta = 0$), the signal decays at the natural frequency ω_0 of the nuclear resonators, with the enhanced decay rate $(\Gamma + \Gamma_c)/\hbar$, with the Bragg enhancement being $\Gamma_c = 2\pi\lambda^2 l_\parallel(\mathbf{k}_0)\Gamma_{coh}$ as given by eqs. (3.99) and (3.90). Rocking off Bragg, the frequency is shifted above or below ω_0, depending on the sign of δ, and the decay rate decreases.

As discussed in section 3.6.2 and the appendix, the proper intermediate excited states in the scattering process are the collective normal mode exciton states, and at exact Bragg ($\delta = 0$) for a symmetric Bragg reflection, the phasing is such that *only* the superradiant *eigenmode* state $|\psi_e(\mathbf{q} = \mathbf{k}_0)\rangle$ is excited, with resonance occurring at the natural resonance frequency ω_0, and with the coherent decay width Γ_c given by eq. (3.99). Rocking off Bragg, in addition to the superradiant eigenmode, various other normal mode states are virtually excited, the weighted resonance energy is shifted from ω_0, and the effective width is decreased.

At exact Bragg, the eigenmode decays symmetrically into the forward ($\mathbf{k}_{0+}$) and reflected ($\mathbf{k}_{1-}$) channels.

4.2.3. Superradiance, dynamical beats, quantum beats and conversion electrons off-Bragg

For off-Bragg transmission (or transmission through a noncrystalline film), $\widetilde{S}(\omega; \hat{k}_0, \hat{k}_0) = \widetilde{T}(\omega; \hat{k}_0, \hat{k}_0)$ as given by eq. (3.63). If there is no hyperfine splitting, $\widetilde{T}$ is diagonal for any basis vectors $(\mathbf{e}_x, \mathbf{e}_y)$, and for any incident polarization the transmitted amplitude is

$$T(\omega) = \exp[\mathrm{i}n\lambda f_e l]\, \exp\big[\mathrm{i}\Gamma_c/(\hbar\omega_0 - \hbar\omega - \mathrm{i}\Gamma/2)\big], \tag{4.61}$$

where $\Gamma_c = \pi n \lambda^2 l \Gamma_{coh}$, the enhanced coherent scattering width of the exciton $|\psi_e(\mathbf{k}_0)\rangle$, as given by eq. (4.20). Correct to terms of order l^2 (Γ_c^2), the resonance factor can be expressed as a simple Lorentzian response, with enhanced total width $(\Gamma + \Gamma_c)$,

$$\exp\left[\frac{\mathrm{i}\Gamma_c}{\omega_0 - \omega - \mathrm{i}\Gamma/2}\right] = 1 + \frac{\mathrm{i}\Gamma_c}{(\hbar\omega_0 - \hbar\omega) - \mathrm{i}(\Gamma + \Gamma_c)/2} + \mathrm{O}\big(l^3\big). \tag{4.62}$$

This expression determines the short time behavior of the transform.

The time response is then given by (see [86])

$$T(t) = -\mathrm{i}\mathrm{e}^{-\mathrm{i}[\omega_0 - \mathrm{i}\Gamma/2\hbar]t} J_1\big(\sqrt{4\Gamma_\mathrm{c} t/\hbar}\big)\sqrt{\frac{\Gamma_\mathrm{c}}{t}}. \tag{4.63}$$

Here we have dropped a prompt $\delta(t)$ contribution and we have suppressed the electronic damping factor $\exp(\mathrm{i}n\lambda f_\mathrm{e} l)$. For *short times* ($t < 4\hbar/\Gamma_\mathrm{c} \approx$ the first zero of $J_1(\sqrt{4\Gamma_\mathrm{c} t/\hbar})/\sqrt{t}$),

$$T(t) \approx -\frac{\mathrm{i}\Gamma_\mathrm{c}}{\hbar}\mathrm{e}^{-\mathrm{i}[\omega_0 - \mathrm{i}(\Gamma+\Gamma_\mathrm{c})/2]t}, \tag{4.64}$$

which is just the transform of the Lorentzian response of eq. (4.62). For *long times* ($t > 4/\Gamma_\mathrm{c}$), using the asymptotic behavior $J_1(z) \sim \sqrt{2/\pi z}\cos(z - 3\pi/4)$,

$$T(t) \approx -\frac{\mathrm{i}\Gamma_\mathrm{c}}{\hbar}\mathrm{e}^{-\mathrm{i}[\omega_0 - \mathrm{i}\Gamma/2\hbar]t}\sqrt[4]{\frac{\Gamma_\mathrm{c}}{\hbar t^3}}\cos\left(\sqrt{4\Gamma_\mathrm{c} t/\hbar} - \frac{3\pi}{4}\right). \tag{4.65}$$

Thus, the delayed forward scattered signal following the creation of a nuclear exciton $|\psi_\mathrm{e}(\mathbf{k}_0)\rangle$ with $\mathbf{k}_0$ off-Bragg is

$$I_\mathrm{c}^{(T)}(t) = \begin{cases} (\Gamma_\mathrm{c}/\hbar)\mathrm{e}^{-\Gamma t/\hbar}\big[J_1\big(\sqrt{4\Gamma_\mathrm{c} t/\hbar}\big)\big]^2/t, & \\ \approx(\Gamma_\mathrm{c}/\hbar)^2\mathrm{e}^{-(\Gamma+\Gamma_\mathrm{c})t/\hbar}, & t < 4\hbar/\Gamma_\mathrm{c}, \\ \approx\sqrt{\Gamma_\mathrm{c}/\hbar t^3}\mathrm{e}^{-\Gamma t/\hbar}\cos^2\big(\sqrt{4\Gamma_\mathrm{c} t/\hbar} - 3\pi/4\big), & t > 4\hbar/\Gamma_\mathrm{c}. \end{cases} \tag{4.66}$$

In figure 20 we plot $I_\mathrm{c}^{(T)}(t)$ vs. t for an ^{57}Fe film with $\Gamma_\mathrm{c} = 4\Gamma$. The natural lifetime is $\Gamma^{-1} = 141$ ns. The solid line shows the exact transform, and the dashed line gives the short time solution, $\exp[-(\Gamma + \Gamma_\mathrm{c})t/\hbar]$. Figure 20(a) gives a linear plot over two natural lifetimes, and (b) gives a log plot over ten lifetimes. For comparison,

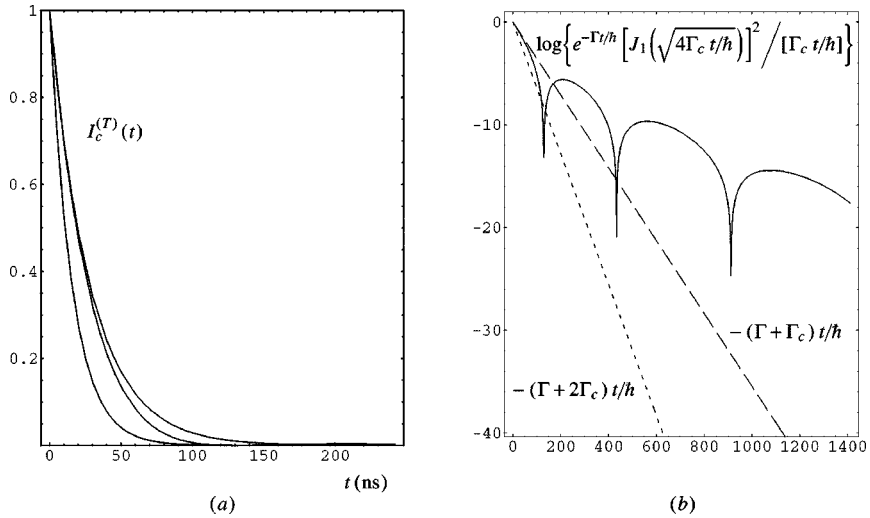

Figure 20. Off-Bragg time response.

the dotted line in each figure gives the thin film Bragg response coherently scattered into either the R- or T-channels, with $l_{\|}(\mathbf{k}_0)$ taken equal to the off-Bragg thickness l, so that $\Gamma_c(\text{Bragg}) = 2\Gamma_c$, and $I_c^{(R)} = I_c^{(T)} = \exp[-(\Gamma + 2\Gamma_c)t/\hbar]$.

Superradiance and dynamical beats. Looking at the linear plot, the interesting feature is that the decay is superradiant, for the reasons discussed in section 4.1.4, with $I_c^{(T)}$ closely following the simple superradiant decay, $\exp[-(\Gamma+\Gamma_c)t/\hbar]$, over the effective lifetime of the exciton. With high probability, the off-Bragg exciton $|\psi_e(\mathbf{k}_0\rangle$ decays during this superradiant period.

For delayed times $t \geqslant 4\hbar/\Gamma_c$, the decay of the off-Bragg exciton has a markedly different character: the fall-off is now slow, $\propto \exp(-\Gamma t/\hbar)/\sqrt{t^3}$, in contrast to the initial superradiant decay $\exp[-(\Gamma + \Gamma_c)t/\hbar]$, and there is the onset of dynamical beats, $\propto \cos^2(\sqrt{4\Gamma_c t/\hbar} - 3\pi/4)$.

In contrast to this complex off-Bragg decay, the Bragg exciton $|\psi_e(\mathbf{k}_0)\rangle$ has a simple exponential decay for all times, at the superradiant decay rate $\hbar(\Gamma + 2\Gamma_c)^{-1}$, as shown by the dotted lines in figures 20(a), (b).

From the normal mode approach, discussed in section 6, this very different behavior of the off-Bragg and Bragg cases can be understood as follows: the exciton $|\psi_e(\mathbf{k}_0)\rangle$ created by the synchrotron pulse is a Bloch wave of the form given by eq. (3.96). However, the Bloch waves are generally not the true radiative normal modes in a crystal, but instead, the proper forms of the eigenmodes for a parallel sided crystal have a sine or cosine modulation (coming in from the crystal faces) with a complex wave vector. Generally, the Bloch state $|\psi_e(\mathbf{k}_0)\rangle$ is a superposition of these radiative eigenmodes, which have a spread of eigenfrequencies and decay rates. The important exception is the case in which $\mathbf{k}_0$ satisfies a Bragg condition $\mathbf{k}_0 \cdot \tau = (1/2)\tau^2$, where τ is a reciprocal lattice vector which is perpendicular to the parallel faces (i.e., a symmetric Bragg reflection). In this case, $|\psi_e(\mathbf{k}_0)\rangle$ is a superradiant eigenmode, radiating at the natural resonance frequency ω_0, with a simple exponential decay at an enhanced decay width $(\Gamma + \Gamma_c)$, including the contributions from coherent decay into both the $\mathbf{k}_0$ and $\mathbf{k}_0 + \boldsymbol{\tau}$ directions,

$$\Gamma_c(\mathbf{k}_0) = \pi n \lambda^2 \big[l_{\|}(\mathbf{k}_0) + l_{\|}(\mathbf{k}_0 + \boldsymbol{\tau})\big]\Gamma_\gamma. \tag{4.67}$$

When $\mathbf{k}_0$ is off Bragg, then $|\psi_e(\mathbf{k}_0)\rangle$ is a superposition of radiative eigenmodes. An important general result, discussed in section 6, is that the eigenmodes are not Hermitian orthogonal. As a consequence, there will be interference effects between the different modes in the evolution of the exciton expectation value, $\langle\psi_e(\mathbf{k}_0;t)|\psi_e(\mathbf{k}_0;t)\rangle$. These interference effects lead to both the appearance of the dynamical beats, and to a "dephasing" of the expectation value, which contributes both to the initial superradiant decay, and to the weak $1/\sqrt{t^3}$ enhancement of the delayed decay of $\langle\psi_e(\mathbf{k}_0;t)|\psi_e(\mathbf{k}_0;t)\rangle$.

Correspondingly, the emitted wave packet $A(\mathbf{z},t)$ is a superposition of waves of the various normal mode frequencies, a spread of frequencies $\approx \pm\,\Gamma_c/\hbar$ about ω_0, leading to initial superradiance, dynamical beats and a weakly enhanced long time

decay of the emitted signal. For a simplified example, if the normal mode wave contributions entered with equal amplitude over a frequency range $\omega_0 \pm \Gamma_c/\hbar$, and if all modes decayed at the natural Γ, then the emitted signal would have dynamical beats of frequency $\Gamma_c/\hbar$ and a weakly enhanced long time decay $|T(t)|^2 \propto \exp(-\Gamma t)/t^2$:

$$T(t) \propto \int_{-\Gamma_c/\hbar}^{+\Gamma_c/\hbar} \mathrm{d}\omega \mathrm{e}^{-\mathrm{i}(\omega_0+\omega-\mathrm{i}\Gamma/2\hbar)t} = \frac{2\sin(\Gamma_c t/\hbar)}{t} \mathrm{e}^{-\mathrm{i}(\omega_0-\mathrm{i}\Gamma/2\hbar)t}. \tag{4.68}$$

This illustration is much too simple and does not give a proper description of the beats or long time decay, and there is no initial superradiance. But as shown in section 6, making the correct resolution of $|\psi_e(\mathbf{k}_0)\rangle$ into normal mode contributions, and using the correct complex mode frequencies, the numerically calculated signal $I_c^{(T)}(t)$ is essentially indistinguishable in form from the analytic transform eq. (4.66).

A simple alternative approach, which gives a different perspective to the problem, is discussed in [96]: directly solve for the time dependent response of the dipoles in each layer, acting under the transient radiation fields from all the other layers, following the initial prompt pulse excitation. The initial phasing of the dipoles within each layer is such that the layer will radiate equally into both the "forward" $\mathbf{k}_{0+} = \mathbf{k}_0$ direction and the "reflected" $\mathbf{k}_{0-}$ direction.

Initially, the phasing between different planes is such that there will be constructive interference in the *forward* direction $\mathbf{k}_0$ between radiation emitted from each plane layer – so that "behind" the film ($z > Md$), the field amplitude is enhanced M-fold, $E^{(+)}(z) = ME_0$, while at the $(m+1)$th layer inside the film, the forward propagating wave is enhanced m times, $E^{(+)}(md) = mE_0$.

If $\mathbf{k}_0$ is *off-Bragg*, then there is no constructive interference in the reflected $\mathbf{k}_{0-}$ channel and the problem is an asymmetrical "one-way communication": the mth layer acts under the influence of the *preceding* $(m-1)$ "upstream" layers, but the "downstream" $(M-m)$ layers have essentially no effect on the mth layer. In particular, there are no external forces acting on the first layer, and the dipoles in this layer decay at their natural frequency ω_0 and natural decay rate Γ (neglecting the small self action of the plane on itself). In contrast, in the Mth layer, the dipoles are driven by the fields from all the preceding layers, and there are two consequences: the component of the force which is 90° out-of-phase with the oscillator motion contributes to the damping of the oscillator, while the in-phase component acts to change the oscillator's phase relative to the "upstream" oscillators, which act under weaker driving forces. The phasing set by the synchrotron pulse is such that, *initially*, the radiative damping forces add layer by layer, so that the initial decay rate varies from $\Gamma/\hbar$ at the first layer to $(\Gamma + 2\pi n \lambda\!\!\!^{-2} l_{\|}(\mathbf{k}_0)\Gamma_\gamma)/\hbar$ at the Mth layer, with the *average* decay rate being $(\Gamma + \pi n \lambda\!\!\!^{-2} l_{\|}(\mathbf{k}_0)\Gamma_\gamma)/\hbar$, which is the effective off-Bragg superradiant decay rate of $|\psi_e(\mathbf{k}_0)\rangle$.

Due to the asymmetry of the forces, however, the "downstream" planes are eventually forced out-of-phase with the "upstream" planes, which results in both "dynamical beats", and a dephased $\exp(-\Gamma t/\hbar)/\sqrt{t^3}$ long time decay.

If, on the other hand, $\mathbf{k}_0$ satisfies the *symmetrical Bragg condition*, then the waves are constructive in both the $\mathbf{k}_{0+}$ and $\mathbf{k}_{0-}$ directions, and the problem becomes symmetrical: the driving forces on each oscillator are always equal, and normal mode motion results, with superradiant decay $\Gamma_{\rm c} = 2\pi n \lambda\!\!\!^{-2} l_{\parallel}(\mathbf{k}_0)\Gamma_\gamma$, and natural frequency ω_0.

A nice demonstration of the dynamical beats has been given by Kikuta [97].

Conversion electrons. As noted above, following the creation of an off-Bragg exciton $|\psi_{\rm e}(\mathbf{k}_0)\rangle$, there is a marked asymmetry in the subsequent decay rates across the film, with the initial decay rates varying from $\Gamma/\hbar$ at the first layer, to $(\Gamma+2\pi n \lambda\!\!\!^{-2} l_{\parallel}(\mathbf{k}_0)\Gamma_\gamma)/\hbar$ at the Mth layer, with the *average* decay rate being $(\Gamma + \pi n \lambda\!\!\!^{-2} l_{\parallel}(\mathbf{k}_0)\Gamma_\gamma)/\hbar$, which is the effective off-Bragg superradiant decay rate of $|\psi_{\rm e}(\mathbf{k}_0)\rangle$. This asymmetry of the planar decay rates can easily be detected by observing the incoherent resonant processes (conversion electrons, incoherently scattered gamma radiation, ...) occurring at different depths of the film. For example, conversion electrons emitted near the top surface will emerge during the natural lifetime $\hbar\Gamma^{-1}$, while conversion electrons emitted near the exit surface will primarily emerge during the much shorter excitation time $\hbar[\Gamma + 2\pi n \lambda\!\!\!^{-2} l_{\parallel}(\mathbf{k}_0)\Gamma_\gamma]^{-1}$, and then there will be subsequent weak oscillations.

Quantum beats. In the case of hyperfine splitting, the quantum beats $\Omega_{\rm B}$, which arise from the wave interference between different frequency transitions, will be modulated by the dynamical beats, which arise from the interaction between oscillators of the same natural frequency, as discussed above.

In the presence of hyperfine splitting, the transmission matrix $\widetilde{T}(\omega; \hat{k}_0, \hat{k}_0)$, eq. (3.63), is generally not diagonal, and there are strong Faraday type effects due to the orthogonal scattering $\mathbf{e}_x \leftrightarrow \mathbf{e}_y$. There is generally no simple analytical transform in this case, but $\widetilde{T}(t; \hat{k}_0, \hat{k}_0)$ is easily computed using the fast Fourier transform programs [85].

There are a few special cases where $\widetilde{T}(\omega; \hat{k}_0, \hat{k}_0)$ can be diagonalized: if $\mathbf{B}_{\rm int} \perp \mathbf{k}_0$ (e.g., a ferromagnetic or antiferromagnetic thin film with the magnetization lying in the plane of the film), then the linear vectors $\mathbf{e}_x \parallel \mathbf{B}_{\rm int}$, $\mathbf{e}_y \perp \mathbf{B}_{\rm int}$ are the basis vectors; and if $\mathbf{B}_{\rm int} \parallel \mathbf{k}_0$, the basis vectors are the circular polarizations $\mathbf{e}_{\pm 1}$. For these special cases, the diagonal elements of the transmission matrix are ($a = x, y$)

$$T_{aa}(\omega; \hat{k}_0, \hat{k}_0) = \exp(\mathrm{i}n\lambda f_{aa} l)$$
$$= \exp(\mathrm{i}n\lambda f_{\rm e} l) \exp\left\{ \sum_{m_0 M} \frac{\mathrm{i}\Gamma_{\rm c}(m_0 M; a)}{\hbar\omega_0(m_0 M) - \hbar\omega - \mathrm{i}\Gamma/2} \right\}, \quad (4.69)$$

where $\Gamma_{\rm c}(m_0 M; a) = n\lambda l f_0(m_0 M; a)\Gamma_\gamma$, with

$$f_0(m_0 M; a) = 4\pi\lambda \frac{C f_{\rm M}}{(2j_0+1)} \frac{\Gamma_\gamma}{\Gamma} C^2(j_0 L j_1; m_0 M) \left| \mathbf{e}_a^* \cdot \mathbf{Y}_{LM}^{(q)}(\hat{k}_0) \right|^2. \quad (4.70)$$

If there are several atoms per unit cell, as in the antiferromagnetic case, then n is the unit cell density, and the f_0 contributions must be summed over each site in the unit cell.

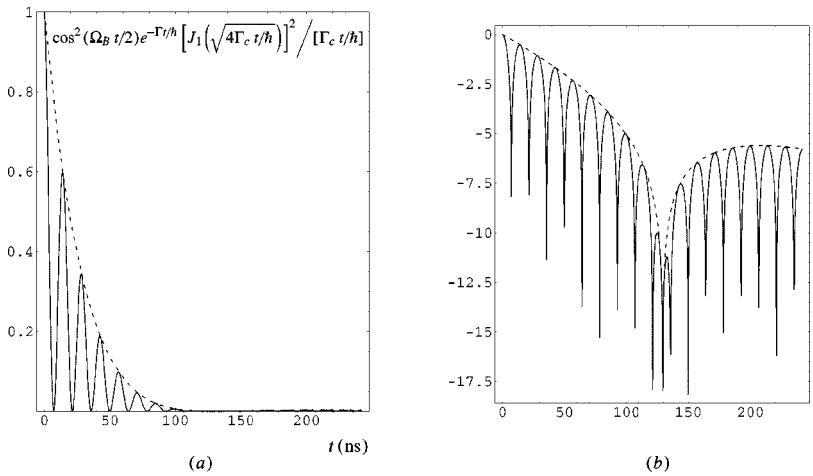

Figure 21. Off-Bragg quantum beat spectrum for a ferromagnetic ^{57}Fe film, with $\mathbf{B}_{\rm int}$ lying in the plane of the film and perpendicular to the linear polarization $\mathbf{e}_0$ of the incident synchrotron pulse: (a) gives a linear plot of $I_{\rm c}^{(T)}(t)$, and (b) gives a log plot of the signal.

Even though $\widetilde{T}(\omega)$ is diagonal, $T_{aa}(\omega)$ is a product of exponentials, one factor for each contributing resonance, and there is no simple transform for $\widetilde{T}(t)$. However, if the quantum beat frequencies are large compared to the natural width, i.e., $\Omega_{\rm B} \gg \Gamma/\hbar$, then correct to terms of order $\Gamma/\hbar\Omega_{\rm B}$,

$$T_{aa}\big(t;\hat{k}_0,\hat{k}_0\big) \approx -{\rm i}\sum_{m_0 M} {\rm e}^{-{\rm i}[\omega_0(m_0M)-{\rm i}\Gamma/2\hbar]t} J_1\big(\sqrt{4\Gamma_{\rm c}(m_0M;a)t/\hbar}\big)\sqrt{\frac{\Gamma_{\rm c}(m_0M;a)/\hbar}{t}}. \quad (4.71)$$

Here we have again dropped the prompt $\delta(t)$ contribution, and we have suppressed the electronic damping factor $\exp({\rm i}n\lambda f_{\rm e}l)$.

As an example, in figure 21 we show the quantum beat spectrum for a ferromagnetic ^{57}Fe film, with magnetization lying in the plane of the film and perpendicular to the linear polarization of the incident synchrotron pulse. In this case, only the two $M = 0$ transitions are excited (the $+1/2 \leftrightarrow +1/2$ and $-1/2 \leftrightarrow -1/2$ transitions), which have equal oscillator strengths, and a quantum beat frequency $\Omega_{\rm B} = \omega(+1/2,0) - \omega(-1/2,0) = 62.1\Gamma/\hbar$ between the two transitions. Equation (4.71) is then a good approximation, and the observed signal is

$$I_{\rm c}^{(T)}(t) \approx \frac{\Gamma_{\rm c}}{\hbar}\cos^2(\Omega_{\rm B}t/2){\rm e}^{-\Gamma t/\hbar}\big[J_1\big(\sqrt{4\Gamma_{\rm c}t/\hbar}\big)\big]^2/t. \quad (4.72)$$

In figure 21, we have taken the film thickness so that $\Gamma_{\rm c} = 4\Gamma$, as was done in figure 20 for the single resonance. The solid line gives $I_{\rm c}^{(T)}(t)$, as given by eq. (4.72), and the rapid oscillations give the quantum beats, with the period being $\tau = 2\pi/\Omega_{\rm B} = 14.3$ ns. The dotted curve gives the dynamical beat modulation ${\rm e}^{-\Gamma t/\hbar}[J_1(\sqrt{4\Gamma_{\rm c}t/\hbar})]^2/(\Gamma_{\rm c}t/\hbar)$, produced by each of the transitions separately. The important feature to notice is that

although the amplitude of the signal is modulated by the dynamical beat envelope, the quantum beat spectrum can still easily be discerned. A nice demonstration of this effect is given in [97].

If **B** is rotated, a very different quantum beat spectrum will be obtained. For example, if $\mathbf{B} \parallel \mathbf{e}_0$, then $\mathbf{e}_0$ couples to the four $M = \pm 1$ transitions ($\pm 1/2 \leftrightarrow \pm 3/2$, each with relative oscillator strength 1, and $\pm 1/2 \leftrightarrow \mp 1/2$, each with relative oscillator strength $1/3$). The resulting quantum beat pattern is shown below for grazing incidence reflection in figure 24(b).

4.2.4. Thick crystal pure nuclear Bragg reflection

Another important special case that has a simple analytical solution for the time transform is for a *pure nuclear Bragg reflection* from a *thick* crystal, with an unsplit (or well isolated) Mössbauer transition.

In a *thick* crystal, the initial excitation amplitude within the crystal exponentially decreases $\propto \exp(-n\sigma_e z/2 \sin\phi_0)$. The exciton produced, $|\psi_e(\mathbf{k}_0)\rangle$, is "asymmetrical" and no longer a simple Bloch wave as given by eqs. (3.96) or (4.2), and $|\psi_e(\mathbf{k}_0)\rangle$ is no longer a normal mode excitation even if $\mathbf{k}_0$ satisfies a symmetrical Bragg condition. As a consequence, the coherently scattered signal no longer exhibits a pure exponential decay $\propto \exp[-(\Gamma + \Gamma_c)t/\hbar]$, as for the thin crystal symmetric Bragg case, but instead has a more complex behavior discussed below.

By *pure nuclear reflection*, we mean that the electronic scattering is strongly suppressed, while the nuclear scattering contribution gives a strong reflection. One method for obtaining such reflections is to produce pure nuclear *Bragg* reflections by utilizing the unique features of the resonant nuclear scattering:

(1) The strength of the resonant scattering can greatly exceed that of the electronic scattering, and the scattering is isotropic (except for the multipole pattern). For example, an unsplit ^{57}Fe nucleus scatters as 440 electrons at the 14.4 keV resonance, while the electronic scattering is 26 electrons in the forward direction, dropping off to 7.6 electrons at 90°. Consequently, very pure nuclear Bragg reflections can be obtained from crystalline thin films approximately several thousand angstroms thick, which are optically thick for the resonant scattering but essentially transparent for the electronic scattering [98].

(2) The resonant scattering depends on the direction of the magnetic field and electric field gradient (EFG) at the nucleus, while the X-ray scattering is insensitive to internal fields, so magnetic superlattice Bragg reflections are possible in antiferromagnetic crystals [11,98–102]. EFG superlattice reflections have also been observed [102,103].

(3) The nuclear transitions are multipole oscillators which (excluding unsplit E1 transitions) have a quite different polarization response than the electronic system, which scatters essentially as an isotropic E1 oscillator. For a 90° scattering with $\mathbf{k}_f$ in the direction of the incident *linear* polarization $\mathbf{e}_0$, the electronic scattering vanishes, while there will generally be strong resonant scattering, so very pure

nuclear reflections can be obtained by 90° Bragg reflection of $\hat{\pi}$-polarized incident radiation [98].

(4) In complex systems with several atoms per unit cell, including ^{57}Fe, pure nuclear reflections can be obtained at special Bragg reflections where the unit-cell structure factor "accidentally" vanishes due to destructive interference [104].

(5) Grazing incidence techniques can also be used to obtain pure nuclear reflections, as discussed in the next section.

As a specific example, we consider a symmetric Bragg reflection from the (3 3 2) planes of an ^{57}Fe crystal, for which the Bragg scattering angle is $\theta_B = 89.46°$ for 14.4 keV radiation. In order to simplify the discussion, we assume no hyperfine splitting. If the crystal is oriented so that the linear polarization of the incident synchrotron pulse corresponds to $\hat{\pi}$-polarization for the scattering geometry, then the electronic scattering is strongly suppressed, since $\mathbf{k}_1 \parallel \hat{\pi}_0$, while the M1 nuclear resonance, which is driven by the $\hat{\sigma}$-polarized magnetic field of the incident radiation pulse, scatters very strongly in the $(\mathbf{k}_0, \mathbf{k}_1)$ plane perpendicular to $\widehat{\sigma}$. $R_\pi(\omega; \hat{k}_1, \hat{k}_0)$ is then given by eqs. (3.83) and (3.88), with the simplification that $\cos(2\phi_0) = 0$, so that the planar reflection arises entirely from the nuclear scattering, i.e., $F^{10}_{xx} = F_n$ in eq. (3.88).

For this special case there is a simple time transform[14] [32,86],

$$R(t, \delta\phi) = -\mathrm{i}\mathrm{e}^{-\mathrm{i}[\omega_0 + \omega_c(\delta\phi)]t}\mathrm{e}^{-\Gamma t/2}\frac{J_1[\omega_c(\delta\phi)t]}{t}, \tag{4.73}$$

where the *complex dynamical beat frequency* $\omega_c(\delta\phi)$ is given by

$$\omega_c(\delta\phi) \equiv \Delta\omega_c(\delta\phi) - \frac{\mathrm{i}\Gamma_c(\delta\phi)}{2\hbar} = \frac{\Gamma_c/2\hbar}{M_e\delta + \mathrm{i}}. \tag{4.74}$$

Here Γ_c is given by

$$\Gamma_c = 2\pi n \lambda\!\!\!^{-2} l_\parallel \Gamma_{coh}, \tag{4.75}$$

where

$$l_\parallel = \frac{2}{n\sigma_e} \equiv 2l_e, \tag{4.76}$$

and $M_e\delta$ is given by

$$M_e\delta = \frac{l_\parallel \sin\phi_0}{d}\delta = k_0 l_e \sin(2\phi_0)\delta\phi. \tag{4.77}$$

$\delta\phi$ is now measured from the actual Bragg (including the Thomson scattering index of refraction effect). $l_\parallel$ gives the thickness over which the initial excitation *amplitude* decreases by $1/\mathrm{e}$, and M_e gives the effective number of cooperating plane layers in the exciton $|\psi_e(\mathbf{k}_0)\rangle$.

[14] This result was presented by the authors at the *Workshop on New Directions in Mössbauer Spectroscopy*, Argonne (July 1977); and, independently, by Yu. Kagan at the *Moscow–Munich Mössbauer Workshop* (October 1977).

Just as for the thin crystal case given by eq. (3.99), Γ_c gives the enhanced partial width for coherent decay into two open channels (at exact Bragg), but now with the cooperation length $l_{\|}(\mathbf{k}_0)$ determined by the photoabsorption length l_e. However, because $|\psi_e(\mathbf{k}_0)\rangle$ is not an eigenmode, $(\Gamma_c+\Gamma)/\hbar$ only gives the initial decay rate. As we will see below, the "long time" development is characterized by an $\exp(-\Gamma t/\hbar)/t^3$ fall-off, and, rocking slightly off exact Bragg, by the onset of dynamical beats.

There are two distinct $\delta\phi$-regions to the response:

Very near exact Bragg such that $M_e\delta < 1$ ($\Rightarrow \delta\phi < \lambda\!\!\!^{-}/l_e$), then ω_c is primarily imaginary:

$$\omega_c(\delta\phi) \approx -\frac{i\Gamma_c}{2\hbar}. \tag{4.78}$$

Then for short times $t \leqslant 2\hbar/\Gamma_c$, so that $J_1(\omega_c t) \approx \omega_c t/4$, there is a pure exponential decay at the enhanced decay rate $(\Gamma_c+\Gamma)/\hbar$,

$$I_c^{(R)}\big(t < 2\hbar/\Gamma_c, \delta\phi < \lambda\!\!\!^{-}/l_e\big) \propto \exp\big[-(\Gamma_c+\Gamma)t/\hbar\big]. \tag{4.79}$$

For long times $t \gg 2\hbar/\Gamma_c$,

$$J_1(\omega_c t) \approx \sqrt{\frac{2}{\pi\omega_c t}}\cos\left(\omega_c t - \frac{3\pi}{4}\right) \approx \frac{i}{\sqrt{\pi\omega_c t}}\exp\left(\frac{\Gamma_c t}{2\hbar}\right),$$

and the decay becomes nonexponential,

$$I_c^{(R)}\big(t \gg 2\hbar/\Gamma_c, \delta\phi < \lambda\!\!\!^{-}/l_e\big) \propto \frac{\exp(-\Gamma t/\hbar)}{t^3}. \tag{4.80}$$

For $M_e\delta > 1$ ($\Rightarrow \delta\phi > \lambda\!\!\!^{-}/l_e$), ω_c is primarily real, and now becomes independent of the photoabsorption length l_e

$$\omega_c(\delta\phi) \approx \frac{\Gamma_c}{2\hbar M_e\delta} \approx \frac{2\pi n\lambda\!\!\!^{-3}\Gamma_{coh}}{\hbar\delta\phi}. \tag{4.81}$$

In this region, the initial decay is simply the natural decay $\exp(-\Gamma t/\hbar)$, while for delayed times $t > 1/\omega_c$, the decay again goes as $\exp(-\Gamma t/\hbar)/t^3$, but now modulated by dynamical beats of frequency $\omega_c(\delta\phi)$,

$$I_c^{(R)}\big(t > 1/\omega_c, \delta\phi > \lambda\!\!\!^{-}/l_e\big) \propto \frac{\exp(-\Gamma t/\hbar)}{t^3}\cos^2\left(\omega_c t - \frac{3\pi}{4}\right). \tag{4.82}$$

In figure 22 we illustrate these results for the (3 3 2) 90° pure nuclear Bragg reflection in ^{57}Fe, with the simplifying assumption of no hyperfine splitting. For this case, $l_e \approx 1.9\times10^{-3}$ cm, giving $\Gamma_c \approx 338\Gamma$ ($\approx$ a 3,000-fold enhancement over Γ_γ). Figure 22(a) shows the strong superradiant decay which occurs during the first few nanoseconds at exact Bragg $\delta\phi = 0$, while figure 22(b) gives a log plot over two natural lifetimes, and shows the delayed $\exp(-\Gamma t/\hbar)/t^3$ fall-off for $\delta\phi = 0$, and the dynamical beats $\omega_c(\delta\phi)$ for $\delta\phi = 0.01$ and 0.02 mrad.

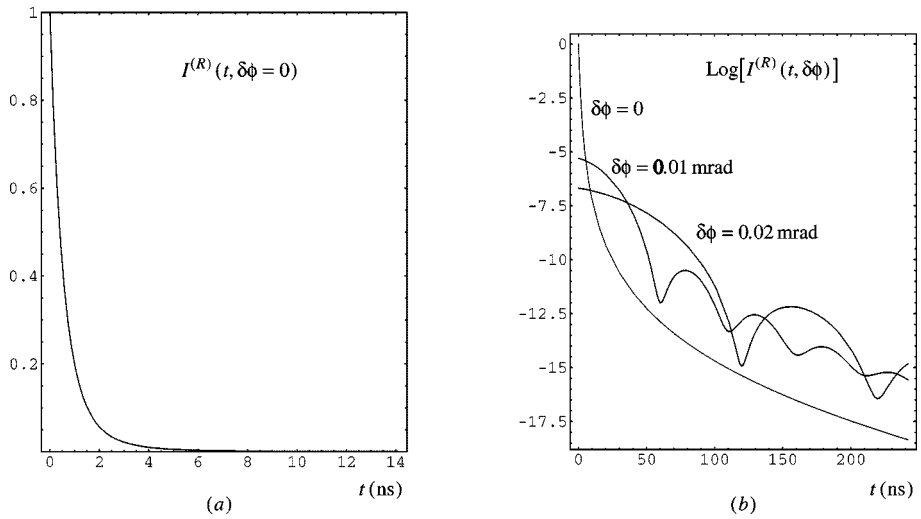

Figure 22. Time response $I_c^{(R)}(t, \delta\phi)$ for a pure nuclear Bragg reflection in a thick crystal of ^{57}Fe: (a) gives a linear plot of $I_c^{(R)}(t, \delta\phi)$ at exact Bragg ($\delta\phi = 0$), showing the superradiant decay which occurs during the first few ns; (b) gives a log plot of the signal for $\delta\phi = 0, 0.01$ and 0.02 mrad and shows the delayed $\exp(-\Gamma t/\hbar)/t^3$ fall-off for $\delta\phi = 0$, and the angle dependent dynamical beats for $\delta\phi \neq 0$.

Superradiant decay occurs only within the very narrow central region $\delta\phi < \lambda\!\!\!^{-}/l_e \approx 0.7 \times 10^{-6}$ rad. Outside of this central region, the most notable feature is the dynamical beats, with the beat frequency $\omega(\delta\phi)$ decreasing linearly with $\delta\phi$ as given by eq. (4.81). For ^{57}Fe, this gives a beat frequency of $\omega_c \approx 12\Gamma/\hbar$ for $\delta\phi = 0.01$ mrad, decreasing to $\omega_c \approx 1.2\Gamma/\hbar$ for $\delta\phi = 0.1$ mrad. Because of the rapid variation of ω_c with $\delta\phi$, the Bragg reflection dynamical beats will normally not be resolved: the incident synchrotron pulse typically has an angular spread $\Delta\phi \approx 0.1$ mrad, and the dynamical beat modulation will "wash out", $\langle \cos^2(\omega_c t - 3\pi/4) \rangle \approx 1/2$. The observed decay will then be $\exp(-\Gamma t/\hbar)/t^3$.

Just as in the off-Bragg case, it is the fact that the initial exciton $|\psi_e(\mathbf{k}_0)\rangle$ is a superposition of radiative eigenmodes, which leads to the dynamical beats and the weak $1/t^3$ enhancement of the long time decay.

4.2.5. Pure nuclear reflections at grazing incidence

An alternative method for producing pure nuclear reflections is to use grazing incidence reflection from mirrors coated with antireflection films, in which either the films or the substrate contain resonant Mössbauer nuclei [29,32,33]. The important point is that the index of refraction for near resonant radiation differs strongly from the index of refraction far off resonance, and as a consequence, it is possible to use thin-film interference techniques to strongly suppress the off-resonance reflectivity while maintaining a very bright reflection for near resonance radiation. Typically, nonresonant reflectivities can be suppressed to $\approx 10^{-4}$–10^{-3}, while maintaining reso-

nant reflectivities ≈70%. Furthermore, by using different combinations of films and substrates, the response can be tailored to give narrow bandpass widths $\Delta\omega \approx \Gamma/\hbar$ and correspondingly long delayed scattering times to optimize time filtering, or at the other extreme, to produce filters of very broad resonance width with $\Delta\omega \approx 100\Gamma/\hbar$, which would be ideal for a high resolution X-ray source.

Because this is an index or refraction technique, no crystals are needed and the system is free of the restrictions imposed by a crystalline Bragg condition. As a consequence, the filter can accept the full beam divergence of the synchrotron, and the system is stable against lattice parameter changes, such as might be caused by heating or radiation damage. Furthermore, the films are relatively easy to fabricate, and the techniques can be applied to a number of low-energy Mössbauer transitions.

The interesting features of the time response are again the *quantum beats* $\Omega_{\rm B}$ which determine the various hyperfine splittings; and, for an isolated resonance, the *coherent speedup* of the decay and the *dynamical beats*. Also, for multiple reflection from a system of m parallel mirrors, there is a *multiple-reflection delay* to the scattering, which can be a useful aid for time filtering.

As a specific example, we consider a resonant ^{57}Fe mirror coated with an impedance matched quarter-wave film of Te, for which the optimum parameters are $l_1 \approx 76$ Å and $\phi_0 = 4.4$ mrad – i.e., the ^{57}Fe mirror is coated with a 76 Å film of Te, and the grazing incidence angle is set for $\phi_0 = 4.4$ mrad. The electronic reflectivity is then suppressed to $|R_{\rm e}|^2 \approx 9.4 \times 10^{-4}$, while the peak resonant reflectivity is ≈0.7 [32].

The filter system is then taken as a system of m parallel mirrors of ^{57}Fe, each coated with a quarter-wave film of Te. The internal magnetic fields **B** in the separate mirrors will be assumed to be in parallel alignment.

For parallel alignment of the internal fields, the filter system has well-defined eigenpolarizations $\mathbf{e}_\eta(\hat{k}_0, \omega)$, $\eta = 1, 2$, which are determined by the resonant ^{57}Fe medium as given explicitly by eq. (3.58). The eigenpolarizations are generally frequency dependent and nonorthogonal, but for the special cases of $\mathbf{B} \parallel \mathbf{k}_0$, or $\mathbf{B} \perp \mathbf{k}_0$, or if there is no hyperfine splitting, then the bases are orthogonal and frequency independent. In particular, if $\mathbf{B} \parallel \mathbf{k}_0$, then the eigenpolarizations are the circularly polarized vectors $\mathbf{e}_{(\pm 1)}$; while if $\mathbf{B} \perp \mathbf{k}_0$, lying in the plane of the mirror, then the eigenpolarizations are the linear vectors $\hat{\sigma}$ and $\hat{\pi}$.

For the particular cases of orthogonal eigenbases, $I_{\rm c}^{(R)}(t, \phi)$ simplifies to

$$I_{\rm c}^{(R)}(t, \phi) = 2\pi\hbar I_{0{\rm p}}(\phi) \sum_{\eta=1,2} \left| R_\eta^{(m)}(t, \phi) \right|^2 \left| \mathbf{e}_\eta^* \cdot \mathbf{e}_0 \right|^2, \tag{4.83}$$

where $R_\eta^{(m)}(t, \phi)$ is now the Fourier transform of the eigenpolarization response $R_\eta^{(m)}(\omega, \phi)$ of the m-mirror system. As discussed in [32], the effect of the impedance-matched quarter-wave film is to effectively remove all electronic scattering, so that, to

a very good approximation, $R_\eta^{(m)}(\omega,\phi)$ is a pure nuclear reflection,

$$R_\eta^{(m)}(\omega,\phi)=\left[\frac{1-\beta_{\rm n}(\eta)}{1+\beta_{\rm n}(\eta)}\right]^m, \tag{4.84}$$

where

$$\beta_{\rm n}(\eta)=\left[\frac{1+n\lambda^2 f_{\rm n}(\eta)}{\pi(\phi^2-\phi_{\rm c}^2+{\rm i}n\lambda\sigma_{\rm e})}\right]^{1/2}. \tag{4.85}$$

Here $\phi_{\rm c}=[-2\lambda\Re(f_{\rm e})]^{1/2}\approx 3.8$ mrad is the X-ray grazing incidence critical angle for the ^{57}Fe substrate. The nuclear forward scattering amplitude $f_{\rm n}(\eta)$ is a superposition of oscillators,

$$f_{\rm n}(\eta)=\sum_{m_0M}\frac{f_0(m_0M;\eta)}{x(m_0M)-{\rm i}}, \tag{4.86}$$

where

$$x(m_0M)=\frac{2[E_1(j_1m_0+M)-E_0(j_0m_0)-\hbar\omega]}{\Gamma}, \tag{4.87}$$

and the oscillator strength of the m_0M resonance for $\mathbf{e}_\eta$ eigenpolarization is

$$f_0(m_0M;\eta)=\frac{2\lambda_0 f_M C}{2j_0+1}\frac{\Gamma_\gamma}{\Gamma}C^2(j_0Lj_1;m_0M)\left|\mathbf{e}_\eta^*\cdot\mathbf{Y}_{LM}^{(q)}(\hat{k}_0)\right|^2. \tag{4.88}$$

Here the notation is that of appendix A.2.

Isolated resonance: Dynamical effects. For a well isolated resonance with transition frequency $\omega(m_0M)$, we take

$$f_{\rm n}(\eta)=\frac{f_0(m_0M;\eta)}{x(m_0M)-{\rm i}} \tag{4.89}$$

in eq. (4.85). There is then a simple time transform [32]

$$R_\eta^{(m)}(t,\phi)=(-{\rm i})^m{\rm e}^{-{\rm i}[\omega(m_0M)+\omega_{\rm c}(m_0M)]t}{\rm e}^{-\Gamma t/2\hbar}\frac{mJ_m[\omega_{\rm c}(m_0M)t]}{t}, \tag{4.90}$$

where J_m is the mth-order cylindrical Bessel function and the *complex dynamical beat frequency* is given by

$$\begin{aligned}\omega_{\rm c}(m_0M;\phi;\eta)&\equiv\Delta\omega_{\rm c}(m_0M;\phi;\eta)-\frac{{\rm i}\Gamma_{\rm c}(m_0M;\phi;\eta)}{2\hbar}\\&=\frac{\pi n\lambda^2 f_0(m_0M;\eta)\Gamma}{\phi^2-\phi_{\rm c}^2+{\rm i}n\lambda\sigma_{\rm e}}.\end{aligned} \tag{4.91}$$

To emphasize the close connection between the grazing incidence and Bragg cases, we rewrite $\omega_{\rm c}$, in direct analogy to eq. (4.74), as

$$\omega_{\rm c}\equiv\Delta\omega_{\rm c}(\phi)-\frac{{\rm i}\Gamma_{\rm c}(\phi)}{2\hbar}=\frac{\Gamma_{\rm c}/2\hbar}{M_{\rm e}\delta'+{\rm i}}, \tag{4.92}$$

where now

$$\Gamma_{\rm c} = 2\pi n \lambda\!\!\!^{-} l_{\rm e} f_0(m_0 M;\eta)\Gamma \quad \text{(hyperfine splitting)} \tag{4.93}$$

$$= 2\pi n \lambda\!\!\!^{-2} l_{\rm e}\Gamma_{\rm coh} \quad \text{(no hyperfine splitting)}. \tag{4.94}$$

The effective cooperation length is again determined by photoabsorption, $l_{\rm e} = 1/n\sigma_{\rm e}$, and $M_{\rm e}\delta'$ is now defined as $M_{\rm e}\delta' \equiv k_0 l_{\rm e}(\phi^2 - \phi_{\rm c}^2)$. For ^{57}Fe coated with Te ($\phi =$ 4.4 mrad, $\phi_{\rm c} = 3.8$ mrad) with $\mathbf{B} \parallel \mathbf{k}_0$, then $\Delta\omega_{\rm c}(\phi) \approx 10\Gamma/\hbar$ and $\Gamma_{\rm c}(\phi) \approx 2.8\Gamma$ for the strong $M = \pm 1$ resonances.

From eqs. (4.83) and (4.90) the time spectrum is then

$$I_{\rm c}^{(R)}(t,\phi) \propto {\rm e}^{-(\Gamma+\Gamma_{\rm c})t/\hbar}\frac{|m\,J_m(\omega_{\rm c}t)|^2}{t^2}. \tag{4.95}$$

For short times $t < m|\omega_{\rm c}|^{-1}$, $J_m(z) \approx z^m/(2^m m!)$, so that

$$I_{\rm c}^{(R)}(t,\phi) \propto t^{2m-2}{\rm e}^{-(\Gamma+\Gamma_{\rm c})t/\hbar}. \tag{4.96}$$

For $t > m|\omega_{\rm c}|^{-1}$, $J_m(z) \sim \sqrt{2/\pi z}\cos(z - \pi/4 - m\pi/2)$, giving

$$I_{\rm c}^{(R)}(t,\phi) \propto \frac{{\rm e}^{-(\Gamma+\Gamma_{\rm c})t/\hbar}}{t^3}\big|\cos(\omega_{\rm c}t - \pi/4 - m\pi/2)\big|^2. \tag{4.97}$$

For $t \gg m\hbar(\Gamma_{\rm c}/2)^{-1}$, $|\cos(\omega_{\rm c}t)|^2 \approx \exp(\Gamma_{\rm c}t/\hbar)/4$, and the long time decay becomes

$$I_{\rm c}^{(R)}(t,\phi) \propto \frac{{\rm e}^{-\Gamma t/\hbar}}{t^3}. \tag{4.98}$$

For a *single mirror*, there is coherent enhancement of the initial decay, $\propto \exp[-(\Gamma + \Gamma_{\rm c})t/\hbar]$. For intermediate times, the decay is additionally modulated by dynamical beats, $\propto \exp[-(\Gamma + \Gamma_{\rm c})t/\hbar]\cos^2(\Delta\omega_{\rm c}t - 3\pi/4)$, while for long times, there is a weakly enhanced $\exp(-\Gamma t/\hbar)/t^3$ decay. The dynamical beats and the weakly enhanced long time decay have the same origin as for the off-Bragg and thick crystal Bragg cases: the initial exciton $|\psi_{\rm e}(\mathbf{k}_0)\rangle$ is a superposition of radiative eigenmodes, but the eigenmodes are not Hermitian orthogonal (but instead are transpose orthogonal), and as a consequence there is interference between the modes in the subsequent excitation probability $\langle\psi_{\rm e}(\mathbf{k}_0;t)|\psi_{\rm e}(\mathbf{k}_0;t)\rangle$, leading to both dynamical beats and a long time "dephasing" of the decay.

For *multiple reflections*, there is an inititial delay of the peak signal. Explicitly, the signal goes as $|J_m(\omega_{\rm c}t)/t|^2\exp[-(\Gamma + \Gamma_{\rm c})t/\hbar]$, which increases initially $\propto t^{2m-2}$, building up to a maximum at the delayed time $t_{\rm max} \approx (m-1)\hbar/(\Gamma + \Gamma_{\rm c})$.

The nature of this delayed response from the multi-mirror system is the following: since all mirrors are coated with anti-reflection films, only the first mirror sees the sharp synchrotron pulse ("white" over several eV about resonance). Following the initial pulse excitation, the first film sends out a long coherence length wave $\propto \exp[-{\rm i}(\omega_0 + \omega_{\rm c} - {\rm i}\Gamma/2\hbar)t]J_1(\omega_{\rm c}t)/t$. In the second film, the resonant absorption/re-emission of the nearly monochromatic incident wave gives a delay in the response. Classically, the near resonant incident wave must first build up the oscillations of the resonators in

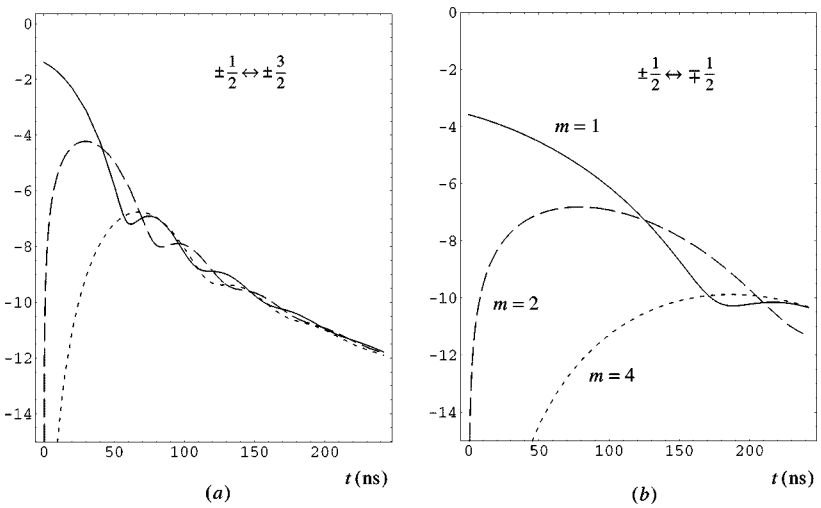

Figure 23. Time response $\log[I_c^{(R)}(t,\phi)]$ vs. t following excitation of an m-mirror system with a synchrotron pulse for $m = 1$, 2 and 4. The resonant ^{57}Fe mirrors are each coated with 76 Å of Te, so $\phi = 4.4$ mrad, and in all mirrors the internal fields are taken $\mathbf{B} \parallel \mathbf{k}_0$. Here we only include the effects of a single isolated resonance and in (a) use the parameters appropriate for the two strong $M = \pm 1$ resonances for which $\omega_c \approx (10 - i1.4)\Gamma/\hbar$; while in (b) we use the parameters appropriate for the two weak $M = \pm 1$ resonances for which $\omega_c \approx (3.3 - i0.5)\Gamma/\hbar$. In both figures, the solid straight line at the top is $-\Gamma t/\hbar$, indicating the natural decay of an isolated nucleus. In (a), the dotted straight line is $-(\Gamma + \Gamma_c)t/\hbar$, indicating the initial superradiant decay from a single mirror.

the second film before any appreciable radiation is sent out. Thus the initial response from the compound system is zero, as given explicitly by the t^2 dependence, and since the resonators of the second film respond collectively with a resonance half-width $\approx (\Gamma + \Gamma_c)$, the maximum response occurs after a delay $\approx \hbar/(\Gamma + \Gamma_c)$.

The features of enhanced decay, dynamical beats, and multiple-reflection delay are illustrated in figure 23, which shows the results for a system of parallel ^{57}Fe mirrors ($\phi_c = 3.8$ mrad), coated with a $\lambda/4$-antireflection film of Te ($l_{Te} = 76$ Å, and $\phi = 4.4$ mrad), and in all mirrors the internal fields are taken $\mathbf{B} \parallel \mathbf{k}_0$. The oscillating lines give $\log[I_c^{(R)}(t,\phi)]$ vs. t for $m = 1$, 2 and 4 parallel mirrors. Here we only include the effects of a single isolated resonance and in (a) use the parameters appropriate for the two strong $M = \pm 1$ resonances for which $\Delta\omega_c \approx 10\Gamma/\hbar$ and $\Gamma_c \approx 2.8\Gamma$; while in (b) we use the parameters appropriate for the two weak $M = \pm 1$ resonances for which $\Delta\omega_c \approx 3.3\Gamma/\hbar$ and $\Gamma_c \approx 0.9\Gamma$. The solid straight line at the top is $-\Gamma t/\hbar$, indicating the natural decay of an isolated nucleus, and the dotted straight line is $-(\Gamma + \Gamma_c)t/\hbar$, indicating the initial superradiant decay from a single mirror.

Quantum beats. The dynamical beats are a collective effect occurring for each isolated resonance. Whenever there is hyperfine splitting, the fundamentally more important quantum beats $\Omega_B(m_0 M)$, arising from the interference between the waves emitted by the various resonances, will be superimposed on the dynamical beat modulation.

For $\mathbf{e}_\eta$ eigenpolarization, the nuclear forward scattering amplitude $f_{\rm n}(\eta)$ is a superposition of contributing resonances, as given by eq. (4.86). There is then no simple time transform of $R_\eta^{(m)}(\omega,\phi)$, but if the quantum beat frequencies are large compared to the natural width, i.e., $\Omega_{\rm B} \gg \Gamma/\hbar$, then correct to terms of order $\Gamma/\hbar\Omega_{\rm B}$,

$$R_\eta^{(m)}(t,\phi) = \sum_{m_0 M} (-{\rm i})^m \, {\rm e}^{-{\rm i}[\omega_0(m_0M)+\omega_{\rm c}(m_0M;\eta)]t} \, {\rm e}^{-\Gamma t/2\hbar} \frac{m J_m[\omega_{\rm c}(m_0M;\eta)t]}{t}. \quad (4.99)$$

Because the complex dynamical beat frequencies $\omega_{\rm c}(m_0M;\eta)$ appear in the time-dependent exponential phase factor $\exp\{-{\rm i}[\omega_0(m_0M)+\omega_{\rm c}(m_0M;\eta)]t\}$ for each contributing transition in $R_\eta^{(m)}(t,\phi)$, then in the *initial development*, the dynamical beats will shift the quantum beats,

$$\Omega'_{\rm B} = \Omega_{\rm B} + \Omega_{\rm c}, \quad (4.100)$$

where the dynamical beat shift is

$$\Omega_{\rm c}\big(m_0M;m'_0M';\eta\big) = \Delta\omega_{\rm c}(m_0M;\eta) - \Delta\omega_{\rm c}\big(m'_0M';\eta\big). \quad (4.101)$$

However, at *delayed times* $t > m\hbar(\Gamma_{\rm c}/2)^{-1}$, then $\exp(-{\rm i}\omega_{\rm c})J_m(\omega_{\rm c}t) \sim \exp(-\pi/4 - m\pi/2)/\sqrt{2\pi\omega_{\rm c}t}$, and the natural beat frequencies $\Omega_{\rm B}$ are obtained.

The quantum beat spectrum depends on which transitions contribute to each eigenpolarization $\mathbf{e}_\eta$, and how the incident synchrotron polarization $\mathbf{e}_0$ couples to each eigenpolarization. As a consequence, the quantum beat spectrum is strongly dependent on the orientation of the **B**-field relative to $\mathbf{k}_0$ and $\mathbf{e}_0$.

As an example, let the incident synchrotron radiation be linearly polarized, and take the mirror surfaces oriented parallel to $\mathbf{e}_0$, so that $\mathbf{e}_0 = \widehat{\sigma}$ for the scattering geometry. Then, if $\mathbf{B} \parallel \mathbf{k}_0$, the eigenpolarizations are the circular bases $\mathbf{e}_{(\pm1)}$. Since $\widehat{\sigma} = [\mathbf{e}_{(+1)} + \mathbf{e}_{(-1)}]/\sqrt{2}$, the time spectrum is then

$$I_{\rm c}^{(R)}(t,\phi) \propto \frac{1}{2}\big[\big|R_{(+1)}^{(m)}(t,\phi)\big|^2 + \big|R_{(-1)}^{(m)}(t,\phi)\big|^2\big]. \quad (4.102)$$

For this orientation of **B**, $\mathbf{e}_{(+1)}$ couples only to the $M=+1$ transitions, and $\mathbf{e}_{(-1)}$ couples only to the $M=-1$ transitions. For ^{57}Fe, there are two $M=+1$ transitions, and two $M=-1$ transitions, and for pure Zeeman splitting, $\Delta E(M=+1) = \Delta E(M=-1) \approx 62.1\Gamma$. In this case, there is a single quantum beat frequency $\Omega_{\rm B} \approx 62.1\Gamma/\hbar$ in the spectrum. In figure 24(a) we show $I_{\rm c}^{(R)}(t,\phi)$ for a two-mirror system with $\mathbf{B} \parallel \mathbf{k}_0$. The "smearing" of the beats in the early development is due to the dynamical beat shifts $\Delta\Omega_{\rm c}(\pm1) \approx \mp 6.7\Gamma/\hbar$, which are in the opposite directions for two eigenwave contributions to $I_{\rm c}^{(R)}(t,\phi)$.

If the internal field is rotated so that $\mathbf{B} \perp \mathbf{k}_0$, with **B** lying in the plane of the film (i.e., $\mathbf{B} \parallel \widehat{\sigma}$), then the eigenpolarizations are the linear bases $\widehat{\sigma}$ and $\widehat{\pi}$. Since $\mathbf{e}_0 = \widehat{\sigma}$, the time spectrum then becomes

$$I_{\rm c}^{(R)}(t,\phi) \propto \big|R_\sigma^{(m)}(t,\phi)\big|^2. \quad (4.103)$$

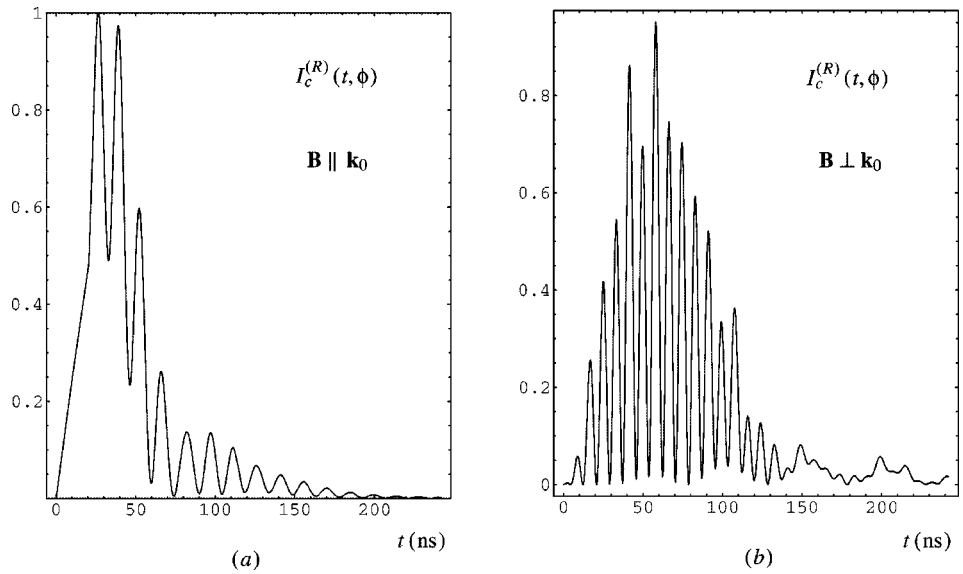

Figure 24. Time response $I_c^{(R)}(t, \delta\phi)$ vs. t following excitation by a synchrotron radiation pulse for an ^{57}Fe mirror system: two parallel mirrors coated with Te antireflection films. The rapid oscillations give the quantum beats. In (a) the internal fields of the two films are oriented $\mathbf{B} \parallel \mathbf{k}_0$, while in (b), $\mathbf{B} \parallel \mathbf{e}_0$.

For this orientation of $\mathbf{B}$, $\widehat{\sigma}$ couples to the four $M = \pm 1$ transitions of ^{57}Fe. For pure Zeeman splitting, this results in four distinct quantum beat frequencies Ω_B: $106.9\Gamma/\hbar$ between the strong $+1$ and -1 transitions, $62.1\Gamma/\hbar$ between the two $+1$ transitions or between the two -1 transitions, $44.8\Gamma/\hbar$ between the strong $+1$ and the weak -1 (or vice-versa), and $17.3\Gamma/\hbar$ between the weak -1 and the weak $+1$ transitions. The resulting beat pattern is shown in figure 24(b). The dominant feature is the sharp $\Omega_B = 106.9\Gamma/\hbar$ quantum beats due to the interference between the strongest two transitions, $\pm 1/2 \leftrightarrow \pm 3/2$. The irregular modulation of the peaks is due to the other quantum beat contributions. The dramatic change between figures 24(a) and (b) illustrates the sensitivity of the quantum beat spectrum to the directions of the hyperfine fields.

5. Resonant neutron optics

To this point we have been concerned with resonant X-ray and γ-ray optics, but the general features are universal for any type of resonant scattering. There are a number of neutron resonances with energies less than a few volts among the heavy nuclei [105,106]. With the advent of neutron spallation sources giving high intensities in the several eV region, it is now possible to use neutron resonance scattering for condensed matter investigations. We comment briefly here on two interesting aspects of resonant neutron optics.

For a neutron of incident energy E, the resonance coherent elastic scattering amplitude is

$$f_{\rm res} = \frac{\lambda\!\!\!^{-}_0 \Gamma_{\rm n}}{E_{\rm R} - E - {\rm i}(\Gamma_{\rm n} + \Gamma_\gamma)/2}, \tag{5.1}$$

where $\Gamma_{\rm n}$ is the partial width for the decay of the excited compound nucleus $|(A+1)^*\rangle$ to the ground state $|A\rangle$ with the emission of a neutron n ($|f_{\rm res}| \approx 16.6\times10^{-12}$ cm), Γ_γ is the partial width for $|(A+1)^*\rangle$ to decay to a lower energy state $|(A+1)\rangle$ with the emission of a photon, $E_{\rm R}$ is the resonance energy for the transition ${\rm n} + |A\rangle \rightarrow |(A+1)^*\rangle$, and λ_0 is the neutron wavelength at resonance. For simplicity, we have left out a statistical factor $(2j_1+1)/(2j_0+1)$.

Typically, the resonance energy $E_{\rm R} \approx 1$ eV, so $\lambda_0 \approx 0.3$ Å. The resonances have widths $\Gamma = \Gamma_{\rm n} + \Gamma_\gamma \approx$ 10–100 meV, and the branching ratio $\Gamma_{\rm n}/\Gamma_\gamma \approx 10^{-2}$–$10^{-1}$, so that at resonance $|f_{\rm res}| \approx 10^{-10}$–$10^{-11}$ cm, which is 1–2 orders of magnitude larger than the nonresonant (potential) scattering length, $b \approx 10^{-12}$ cm. For example, for ^{119}In, $E_{\rm R} = 1.5$ eV, $\Gamma_\gamma = 72$ meV, $\Gamma_{\rm n} = 3.3$ meV, so at resonance $|f_{\rm res}| \approx 16.6 \times 10^{-12}$ cm, while $b = 0.4 \times 10^{-12}$ cm.

Thus, just as for resonant γ-ray scattering, two notable features of resonant neutron scattering are that the scattering amplitudes near resonance are large compared to the nonresonant (potential) amplitudes, and the phase of the amplitude increases from 0 to π as one increases the energy of the incident neutron from well below the resonance to well above it.

One simplicity of resonant neutron scattering is that this is a scalar wave, and the scattering is primarily s-wave scattering, so there is no complex polarization or angular dependence as for resonant X-ray or γ-ray scattering.

An important distinction is that the scattering time $\hbar/\Gamma \approx 10^{-14}$–$10^{-13}$ s corresponds to medium collision times, in contrast to the fast X-ray scattering and the very slow Mössbauer γ-ray scattering. That is, speaking roughly, during the residence time ($\approx\hbar/\Gamma$) of the neutron in the compound nucleus, the nucleus (atom) executes an appreciable fraction of a vibration period. As a consequence, for *inelastic resonant neutron scattering*, the differential scattering cross-section of a small sample, rather than giving the van Hove $S(\mathbf{Q},\omega)$, gives $W(\mathbf{k}_0, \mathbf{k}_{\rm f})$ [1,105], which only reduces to S in the extremely fast collision limit. As an example, for incoherent scattering $S(\mathbf{Q},\omega) \rightarrow g(\mathbf{r},t)$, the self-correlation function of the scattering particles, while W gives an integral over a higher order correlation function that gives information on the *path* taken by the particle in moving a distance $\mathbf{r}$ in a time t.

Two interesting aspects of resonant neutron optics, which we briefly discuss, are the determination of molecular motions with neutron phasors, and neutron superradiance. A discussion of the suppression effect in resonant neutron optics is given in [107].

5.1. Determining molecular motions

The *structure* determination of large biological molecules is advancing very rapidly. But to understand the functioning of these molecules their motions must be determined, ultimately at the individual atoms' level, and there has been very little progress in this very important field.

One might have hoped, with the advances in high resolution microscopy, that in the near future these motions could be studied by focusing on a single molecule. However, because of the effects of the various possible illuminating radiations, this seems to be impossible at the atomic level of resolution (although X-ray microscopy at the ≈25 Å resolution level and neutron holography at the ≈100 Å resolution level remain open possibilities) [108]. This being the case, to determine the molecular motions at the atomic level we must prepare a macroscopic sample of identical molecules (generally a crystal) and deduce the motions in the individual molecules by measuring the radiation scattered by the ensemble.

In this case measurement of the inelastic differential scattering cross-section of a small sample, $\mathrm{d}^2\sigma/\mathrm{d}\Omega\,\mathrm{d}\omega$, gives $S(\mathbf{Q},\omega)$ [109]:

$$S(\mathbf{Q},\omega) = \int \mathrm{e}^{\mathrm{i}\mathbf{Q}\cdot\mathbf{r}}\mathrm{e}^{-\mathrm{i}\omega t} g(\mathbf{r},t)\,\mathrm{d}\mathbf{r}\,\mathrm{d}t, \tag{5.2}$$

where $\hbar\mathbf{Q}$ and $\hbar\omega$ are the momentum and energy transferred to the sample in the scattering process and

$$g(\mathbf{r},t) = \int \big\langle \rho(\mathbf{r}+\mathbf{x},t)\rho(\mathbf{x},0)\big\rangle\,\mathrm{d}\mathbf{x}, \tag{5.3}$$

where ρ is the scattering density (electron density for X-ray scattering and the nuclear scattering length density in the case of neutron scattering) and the angular brackets indicate the ensemble average.

$g(\mathbf{r},t)$ is the information on the sample which can be obtained from the scattering experiments. The *elastic scattering* measurements give $S(\mathbf{Q},0) \rightarrow g(\mathbf{r},\infty)$,

$$g(\mathbf{r},\infty) = \int \big\langle \rho(\mathbf{r}+\mathbf{x})\rho(\mathbf{x})\big\rangle\,\mathrm{d}\mathbf{x}, \tag{5.4}$$

the Patterson map of the molecule [110].

Except for the simplest molecules $g(\mathbf{r},\infty)$ cannot be solved to give the molecular structure $\langle\rho(\mathbf{r})\rangle$ (*phase of the structure factor problem* in crystallography). $g(\mathbf{r},\infty)$ has "peaks" at all the $N(N-1)+1$ interatomic vectors of the N atom molecule. Roughly it is the "N-ply" exposed image obtained by translating the molecule N times, bringing in turn each atom to a fixed point and exposing an image. For small molecules, with the knowledge of some chemistry, we can determine $\langle\rho(\mathbf{r})\rangle$ to within an enantiomorph from $g(\mathbf{r},\infty)$, but when N^2 becomes large it is very difficult to determine $\langle\rho(\mathbf{r})\rangle$ from the Patterson map.

Similarly, $g(\mathbf{r},t)$ is incapable of yielding the detailed structure and motion, the *dynamical structure*, of any but the simplest systems. For example, while the eigen-

values (frequencies) of the vibrational eigenmodes of a molecule can be determined from inelastic scattering measurements, the *eigenvectors*, which give the *amplitudes and phases of the displacements of the individual atoms, are not determined*.

This can be called the *phase of the "dynamic structure factor" problem* which will become acute when we try to study experimentally the concerted motions in large biomolecules. The methods of isomorphous replacement, heavy atom tagging, and anomalous scattering used to solve the problem in the time averaged static structure determinations can also be used to help in the dynamics determinations. There are differences, however: isomorphous replacements may not change the static structure, but may affect the motions appreciably. Also, X-ray scattering, so useful for static structure determinations, cannot be used to measure low energy vibrational motions until X-ray sources with energy resolution three or more orders of magnitude greater than present monochromators can yield are available. Thus, it appears necessary to rely on neutron scattering measurements, and the use of *resonant neutron phasors* may furnish the best method for solving the problem.

The resonance scattering amplitudes of the low energy neutron resonances are one to two orders of magnitude larger than nonresonance nuclear scattering amplitudes so that the resonance–nonresonance interference term in the cross-section for neutron scattering from a molecule containing a resonant atom is large. Furthermore, by varying the incident neutron energy the phase and amplitude of the resonantly scattered wave can be varied in a controlled manner. This makes it possible to determine [106,111]

$$g_{\mathrm{R}}(\mathbf{r},t) = \int \big\langle \rho(\mathbf{r}+\mathbf{x},t) R(\mathbf{x},0) \big\rangle \mathrm{d}\mathbf{x}, \tag{5.5}$$

where $R(\mathbf{x})$ is the probability density of the resonant atom. $g_{\mathrm{R}}(\mathbf{r},t)$ gives the positions and the motions of the N nonresonant atoms in the molecule relative to that of the resonant atom, whereas $g(\mathbf{r},t)$, as discussed above, just gives the time dependent Patterson map. Put another way, the resonant atom serves as a reference wave phasor which allows determination of the *dynamic* structure factor.

In summary, the determination of molecular motions is a very important chemical problem, and the use of nuclear resonance phasors can serve to determine these motions.

5.2. Neutron superradiance

As we discussed earlier, the decay of a system of γ-ray emitters is radically affected by the spatial coherence of the emitters, and, for example, can be either superradiant or subradiant, depending on the relative phases of the emitters.

Now in fact, if the initial coherent state corresponds to just a single excitation, then the nature of the emitted particle (i.e., whether it is a boson or a fermion) plays no role in determining the emission rate. Thus a spatially coherent system of neutron emitters will exhibit the same features of superradiance or subradiance.

This is simply a consequence of the quantum superposition principle: to compute the probability of a process, we add the amplitudes (with proper phases) of the

various ways the process can take place, and take the absolute square of the sum of the amplitudes. This leads, e.g., to the characteristic interference pattern for particles traversing a two-slit apparatus, but also, as a consequence, the same coherence effects that affect the decay rates of classical systems emitting classical waves (electric oscillators radiating electromagnetic waves, Helmholtz resonators radiating sound, etc.) apply to *particle emission* (electron, neutron, photon, etc.) decay rates in quantum systems [11,112,113].

For example, for two identical neutron emitters (nuclei) separated by a distance R, the semistationary single exciton states are the symmetric ($|+\rangle$) and antisymmetric ($|-\rangle$) combinations,

$$|\pm\rangle = \frac{1}{\sqrt{2}}\big[|e_1\rangle|g_2\rangle \pm |g_1\rangle|e_2\rangle\big], \tag{5.6}$$

where $|e_l\rangle = |(A+1)_l^*\rangle$ designates the excited state of the compound nucleus l, and $|g_l\rangle = |(A)_l\rangle$ designates the ground state of nucleus l. The corresponding decay widths $\Gamma_{(\pm)}$ for neutron emission, $|\pm\rangle \rightarrow |g_1\rangle|g_2\rangle + \mathrm{n}$, are given by

$$\Gamma_{(\pm)} \approx \Gamma_\mathrm{n}\left(1 \pm \frac{\sin(kR)}{kR}\right), \tag{5.7}$$

with eigenwidths $E_{(\pm)}$,

$$E_{(\pm)} = E_\mathrm{R} \mp \frac{\Gamma_\mathrm{n}}{2}\frac{\cos(kR)}{kR}. \tag{5.8}$$

If $kR \ll 1$, then the symmetric mode decays at twice the rate of a single nucleus ("superradiance") while the antisymmetric mode decays very slowly ("subradiance"). This corresponds classically to two electric dipoles oscillating together in phase (symmetric mode) or 180° out of phase (antisymmetric mode), which exhibits the same superradiant or subradiant behavior when $kR \ll 1$.

Similarly, for a *crystal* of such neutron radiators, the single exciton state $|\psi_\mathrm{e}(\mathbf{q})\rangle$,

$$\big|\psi_\mathrm{e}(\mathbf{q})\big\rangle = \sum_{l=1}^{N} \mathrm{e}^{\mathrm{i}\mathbf{q}\cdot\mathbf{R}_l}|e_l\rangle\big|G_0(l)\big\rangle, \tag{5.9}$$

will be superradiant or subradiant depending on the phasing vector $\mathbf{q}$: if $\mathbf{q} = \mathbf{k}_0 = (2\pi/\lambda_0)\mathbf{n}$, where λ_0 is the neutron resonance wavelength, then $|\psi_\mathrm{e}(\mathbf{k}_0)\rangle$ emits a neutron superradiantly at the coherently enhanced decay rate $\Gamma_\mathrm{c}(\mathbf{k}_0)$,

$$\Gamma_\mathrm{c}(\mathbf{k}_0)/\hbar = \pi n \lambda^2 L_\parallel(\mathbf{k}_0)\Gamma_\mathrm{n}, \tag{5.10}$$

with emission occurring in a narrow solid angle $\Delta\Omega \approx (\lambda_0/L_\perp)^2$ about $\mathbf{k}_0$ (where $L_\perp$ is the transverse dimension of the crystal $\perp \mathbf{k}_0$), while if $|\mathbf{q}| \neq |\mathbf{k}_0|$ the emission is subradiant. If the phasing vector $\mathbf{k}_0$ should satisfy a Bragg condition for neutron diffraction from the crystal, then there will be superradiant contributions $\Gamma_\mathrm{c}(\mathbf{k}_0 + \boldsymbol{\tau})$ for each open Bragg channel, just as for the γ-ray case.

For resonant γ-ray optics, it is possible to create superradiant single exciton states $|\psi_{\rm e}(\mathbf{k}_0)\rangle$ using synchrotron radiation pulse excitation. There are, of course, no such sources available for neutrons. However, the state $|\psi_{\rm e}(\mathbf{k}_0)\rangle$ is excited virtually when a nearly resonant neutron $E \approx E_{\rm R}$ is incident externally at a Bragg angle, and as the incidence energy E is tuned through resonance, the width of the Bragg scattered intensity will show an enhanced width $(\Gamma_{\rm c} + \Gamma_\gamma)$. This coherent enhancement of the width has recently been observed by Hastings et al. [114].

For γ-ray emission, the superradiant single exciton state $|\psi_{\rm e}(\mathbf{k}_0)\rangle$ is closely related to multiphoton Dicke superradiance: the single exciton state $|\psi_{\rm e}(\mathbf{k}_0)\rangle$ with the greatest decay rate $\Gamma_{\rm c}(\mathbf{k}_0)/\hbar$, is the favored mode of decay for an initially inverted system. Since there is single exciton superradiance for a system of neutron emitters just as for a system of γ-ray emitters, is it possible to have multineutron Dicke superradiance? The answer of course is no, because the Fermi statistics of the neutron prevents a superradiant cascade of neutrons into the endfire mode.

6. Radiative normal modes

In this final section, we discuss one of the most unique and fundamental aspects of Mössbauer γ-ray optics – collective nuclear states established by the radiative interaction between the nuclei.

Mössbauer γ-ray optics is rich and complex, with a variety of competing processes – sharp resonant scattering from the various nuclear hyperfine transitions, internal conversion absorption, Thomson scattering from the atomic electrons, photoelectric absorption, resonant and nonresonant magnetic X-ray scattering, etc. The most straightforward development of the coherent optics is in terms of the multiple scattering equations (3.5) and (3.6), with the effects of all the various processes incorporated on an equal footing in the coherent elastic scattering amplitudes f_j of each atom.

Some of the most interesting features involve the collective effects of the interactions between the nuclear oscillators, e.g., the "enhancement effect" at Bragg, and the superradiant or subradiant decay of a nuclear exciton. Since these phenomena only involve the nuclei, considerable insight can be gained by approaching the problem from a different point of view: solve directly for the *radiative normal modes* (*semi-stationary states*) of the *system of nuclei*. The scattering of an external plane wave $\mathbf{k}_0$ then involves virtual excitation of these modes as intermediate states; and the decay of a nuclear exciton is a superposition of exponentially decaying semi-stationary states.

In this section, we discuss the normal modes of decay of a system of identical resonators. We give the effective Hamiltonian equation of motion which determines the complex normal mode frequencies $\omega_{\rm n}$ and give simple sum rules which govern the real and imaginary parts of $\omega_{\rm n}$.

Because of retardation, the Hamiltonian is *symmetric* rather than Hermitian, and as a consequence, the eigenmodes $|\psi_{\rm n}\rangle$ satisfy a *transpose orthogonality* condition rather

than Hermitian orthogonality. This has an important consequence in the decay of a general superposition exciton state $|\psi_{\rm e}\rangle = \sum a_{\rm n}|\psi_{\rm n}\rangle$, because interference between the modes now leads to "dephasing" and to dynamical beats in the decay of the excitation probability $\langle\psi_{\rm e}(t)|\psi_{\rm e}(t)\rangle$.

Of particular interest is the decay of an exciton $|\psi_{\rm e}(\mathbf{k}_0)\rangle$ created by a *synchrotron pulse*. We show that if $\mathbf{k}_0$ satisfies the symmetric Bragg condition, then a single superradiant eigenmode is excited, and the subsequent decay is a simple enhanced exponential decay. If $\mathbf{k}_0$ is off-Bragg, then $|\psi_{\rm e}(\mathbf{k}_0)\rangle$ is a superposition of normal modes, and the spread of frequencies and Hermitian-nonorthogonality play an important role both in the initial superradiance and subsequent dynamical beats.

The development we give here follows [11,96,112,115].

6.1. Classical and quantum equations of motion

For a freely decaying system of identical classical electric dipole oscillators, each oscillating in the $\hat{x}_{\rm o}$ direction, $\mathbf{d}_i(t) = ex_i(t)\hat{x}_{\rm o}$, the coupled equations of motion are[15]

$$m\ddot{x}_i + m\Gamma\dot{x}_i + m\omega_0^2 x_i = e\hat{x}_{\rm o}\sum_{j\neq i}\mathbf{E}_{ij}(t), \tag{6.1}$$

where $\mathbf{E}_{ij}(t) = \mathbf{E}_j(\mathbf{R}_i, t)$ is the electric field at $\mathbf{R}_i$ due to dipole j ($\mathbf{E}_{ij}(t)$ is assumed to be uniform over the dimensions of the dipole, i.e., $|x_i| \ll \lambda$). For normal mode motion, each dipole oscillates as $x_j(t) = x_j \exp(-{\rm i}\omega t)$, where ω is the complex frequency of the mode. The field at $\mathbf{R}$ emitted by the jth oscillator is then

$$\mathbf{E}_j(\mathbf{R}, t) = \vec{\nabla}\times\left\{\vec{\nabla}\times\frac{1}{|\mathbf{R}-\mathbf{R}_j|}\mathbf{d}_j\exp\left[{\rm i}\big(k|\mathbf{R}-\mathbf{R}_j| - \omega t\big)\right]\right\}, \tag{6.2}$$

where $\mathbf{d}_j = ex_j\hat{x}_{\rm o}$. Equation (6.2) is valid for the "small source" approximation, which requires that the dimension of the oscillator $|x_j|$ be much smaller than the distance $|\mathbf{R}-\mathbf{R}_j|$ and the wavelength λ. For "Mössbauer radiators", $\lambda \approx 1$ Å and $|x_j| \approx 10^{-4}$ Å, so the condition $|x_j| \ll \lambda$ is well satisfied, and (6.2) would be a good approximation even for $|\mathbf{R}-\mathbf{R}_j| \approx 10^{-3}$ Å, well inside the atom.

Assuming normal mode oscillation, substituting (6.2) into (6.1), and linearizing the resulting equations in ω by making the replacements $\omega^2 - \omega_0^2 = (\omega+\omega_0)(\omega-\omega_0)$ $\rightarrow \approx 2\omega_0(\omega-\omega_0)$ and $\exp({\rm i}kR_{ij}) \rightarrow \approx \exp({\rm i}k_0R_{ij})$, gives an effective Hamiltonian equation of motion

$$\tilde{h}\mathbf{X} = \omega\mathbf{X}, \tag{6.3}$$

[15] Γ is customarily a frequency in classical electrodynamics, while Γ is customarily an energy in quantum electrodynamics ($=\hbar\Gamma_{\rm classical}$). Since the factors of $\hbar$ are not germane to the discussion here, in this section we suppress all factors of $\hbar$.

where, for the classical system of oscillators, $\mathbf{X}$ is the N-component state vector

$$\mathbf{X} = \begin{pmatrix} x_1 \\ x_2 \\ \vdots \\ x_N \end{pmatrix}, \tag{6.4}$$

and the Hamiltonian is

$$h_{ii} = \omega_0 - \frac{\mathrm{i}\Gamma}{2}, \tag{6.5}$$

$$h_{ij}(i \neq j) = -\frac{\Gamma_\gamma}{2}\kappa_{ij}\frac{\mathrm{e}^{\mathrm{i}k_0 R_{ij}}}{k_0 R_{ij}}. \tag{6.6}$$

In (6.6),

$$\kappa_{ij}\frac{\mathrm{e}^{\mathrm{i}k_0 R_{ij}}}{k_0 R_{ij}} = \frac{3}{2k_0^3}\hat{x}_\mathrm{o}\left\{\overset{\rightarrow}{\nabla}_i \times \left[\overset{\rightarrow}{\nabla}_i \times \frac{\exp(\mathrm{i}k_0|\mathbf{R}_i - \mathbf{R}_j|)}{|\mathbf{R}_i - \mathbf{R}_j|}\hat{x}_\mathrm{o}\right]\right\}, \tag{6.7}$$

so that

$$\kappa_{ij} \approx \begin{cases} \dfrac{3}{2}\left[3\left(\mathbf{n}_{ij}\cdot\hat{x}_\mathrm{o}\right)^2 - 1\right]\left[\dfrac{1}{(k_0 R_{ij})^2} - \dfrac{\mathrm{i}}{k_0 R_{ij}}\right] & \text{(near zone } R_{ij} \ll \lambda\text{)}, \\ \dfrac{3}{2}\left[1 - \left(\mathbf{n}_{ij}\cdot\hat{x}_\mathrm{o}\right)^2\right] & \text{(far zone } R_{ij} \gg \lambda\text{)}. \end{cases} \tag{6.8}$$

Equation (6.3) is an eigenvalue equation, which determines the complex normal mode frequencies ω_n ($n = 1, \ldots, N$) and the corresponding normal mode state vectors $\mathbf{X}_n$.

The corresponding *quantum system* is a system of nuclei with nondegenerate ground states $|a_l\rangle$ ($l = 1, \ldots, N$) and excited states $|b_l\rangle$. The normal modes of decay (semi-stationary states) are now nuclear exciton states:

$$\mathbf{X} = |\psi_\mathrm{e}\rangle = \sum_{l=1}^{N} c_l |b_l\rangle|G_0(l)\rangle = \begin{pmatrix} c_1 \\ c_2 \\ \vdots \\ c_N \end{pmatrix}, \tag{6.9}$$

where $|b_l\rangle|G_0(l)\rangle$ means that nucleus l is excited and all the remaining nuclei ($l' \neq l$) are in their ground states $|a_{l'}\rangle$.

An initially excited nucleus i will decay due to self-action (virtual radiative and internal conversion emission/absorption, and "mirror terms" involving virtual photon exchange with the other nuclei, as discussed in [12, appendix] and [2, appendix A]), and, if initially unexcited, can be excited by photon exchange from an excited nucleus j by the interaction $c^{-2} j_\mu(i)\,\delta_{ij}^{+}\,j_\mu(j)$ (see, e.g., [10, appendix B]). The equations of motion are obtained by taking the Fourier transform of the decaying exciton $G(t -$

$t_0)|\psi_e\rangle$. The excited state propagator $G(t-t_0)$ is obtained using the Green function approach of [2,10,12].

The resulting coupled quantum equations of motion, which determine the exponentially decaying semi-stationary states $\mathbf{X}_n$ and the complex mode frequencies ω_n, are of the same general form as the classical equations,

$$\tilde{h}\mathbf{X} = \omega\mathbf{X}, \tag{6.10}$$

where now the state vector $\mathbf{X}$ is the nuclear exciton, as given by eq. (6.9), and again

$$h_{ii} = \omega_0 - \frac{\mathrm{i}\Gamma}{2}, \tag{6.11}$$

$$h_{ij}(i \neq j) = -\frac{\Gamma_\gamma}{2}\kappa_{ij}\frac{\mathrm{e}^{\mathrm{i}k_0R_{ij}}}{k_0R_{ij}}, \tag{6.12}$$

but where now

$$\kappa_{ij}\frac{\mathrm{e}^{\mathrm{i}k_0R_{ij}}}{k_0R_{ij}} = -\frac{2}{\Gamma_\gamma}j_\mu^{ba}\big(\overrightarrow{\mathbf{k}}\big)\frac{\exp(\mathrm{i}k_0R_{ij})}{R_{ij}}j_\mu^{ab}\big(-\overleftarrow{\mathbf{k}}\big). \tag{6.13}$$

Here $\overrightarrow{\mathbf{k}} = -\mathrm{i}\overrightarrow{\nabla}_i$ and $\overleftarrow{\mathbf{k}} = \mathrm{i}\overleftarrow{\nabla}_i$, where the gradient is with respect to $\mathbf{R}_i$, the equilibrium position of atom i, and the gradients operate on the factors to the right or left as indicated. $j_\mu^{ba}(\mathbf{k}) = c^{-1}\int \mathrm{d}\mathbf{x}\langle\phi_b|\mathrm{e}^{\mathrm{i}\mathbf{k}\cdot\mathbf{x}}j_\mu(\mathbf{x})|\phi_a\rangle$ is the Fourier transform of the nuclear current density.

In the far field region, $R_{ij} \gg \lambda_0$, the longitudinal and scalar parts of the current–current contraction drop out, and the expression simplifies to

$$\kappa_{ij}\frac{\mathrm{e}^{\mathrm{i}k_0R_{ij}}}{k_0R_{ij}} = \frac{2}{\Gamma_\gamma}\mathbf{j}_\perp^{ba}\big(\overrightarrow{\mathbf{k}}\big)\cdot\frac{\exp(\mathrm{i}k_0R_{ij})}{R_{ij}}\mathbf{j}_\perp^{ab}\big(-\overleftarrow{\mathbf{k}}\big), \quad R_{ij} \gg \lambda_0. \tag{6.14}$$

In this limit, the operators $\overrightarrow{\mathbf{k}}$ and $\overleftarrow{\mathbf{k}}$ can be replaced by $\mathbf{k}_{ij} = k_0\mathbf{n}_{ij}$ (but often it is convenient to first take sums over sites j before applying the gradient operators).

To compare with the classical case, we take a system of "linear" E1 oscillators (i.e., $\Delta J_z = 0$), each with ground state $|a\rangle = |j_0 = 0,\ m_0 = 0\rangle$ and excited state $|a\rangle = |j_1 = 1,\ m_1 = 0\rangle$, and local quantization axis $\hat{z}_J$. Then $\mathbf{j}_\perp^{ab}(-\mathbf{k}_{ij}) = \sqrt{\lambda_0\Gamma_\gamma}\mathbf{Y}_{10}^{(\mathrm{e})}(\mathbf{n}_{ij})$, with $\mathbf{Y}_{10}^{(\mathrm{e})}(\mathbf{n}_{ij})$ given by eq. (A.22), giving $\kappa_{ij} = (3/2)[1-(\mathbf{n}_{ij}\cdot\hat{z}_J)^2]$, which agrees with the classical far zone result of eq. (6.8).

6.2. Eigenmodes

For either the classical or quantum systems, the determinant equation

$$\mathrm{Det}\big[\tilde{h} - \omega\tilde{\mathbf{1}}\big] = 0, \tag{6.15}$$

where $\tilde{\mathbf{1}}$ is the $N\times N$ unity matrix, determines the complex frequencies for the normal modes, $\omega_m = \omega'_m - \mathrm{i}\Gamma_m/2,\ m = 1,\ldots,N$. $\delta\omega_m = \omega'_m - \omega_0$ gives the frequency shift of the mth normal mode from the natural resonance frequency of a single oscillator;

and Γ_m gives the decay rate of the mode, which will generally be quite different from the decay rate Γ of an isolated nucleus.

Substituting ω_m for ω in the eigenvalue equation (6.10), and applying the transpose normalization condition of eq. (6.17) below, determines the mth eigenmode

$$|\psi_m\rangle = \sum_{l=1}^{N} c_l^m |b_l\rangle \big|G_0(l)\big\rangle = \mathbf{X}_m = \begin{pmatrix} c_1^m \\ c_2^m \\ \vdots \\ c_N^m \end{pmatrix}. \tag{6.16}$$

6.3. Orthogonality and sum rules

The Hamiltonian $\tilde{h}$ given by eqs. (6.5)–(6.7) or (6.7)–(6.13) is *symmetric* rather than Hermitian – i.e., $h_{ji} = h_{ij}$. As a consequence, the eigenmodes will be *transpose orthogonal*, rather than Hermitian orthogonal,

$$\big\langle \psi_m^{\mathrm{T}} \big| \psi_n \big\rangle = \mathbf{X}_m^{\mathrm{T}} \cdot \mathbf{X}_n = \delta_{mn}, \tag{6.17}$$

where $\langle \psi_m^{\mathrm{T}}| = \mathbf{X}_m^{\mathrm{T}}$ is the transpose state,

$$\big\langle \psi_m^{\mathrm{T}} \big| \equiv \sum_{l=1}^{N} c_l^m \langle b_l | \big\langle G_0(l) \big| = \mathbf{X}_m^{\mathrm{T}} = \big(c_1^m \;\; c_2^m \;\; \ldots \;\; c_N^m\big). \tag{6.18}$$

The Hamiltonian $\tilde{h}$ can be diagonalized by the similarity transformation,

$$\mathrm{U}\,\tilde{h}\,\mathrm{U}^{-1} = \widetilde{\omega}, \tag{6.19}$$

where $\widetilde{\omega}$ is the diagonal eigenvalue matrix, $\widetilde{\omega}_{mn} = \omega_m \delta_{mn}$. The $N \times N$ transformation matrix U is obtained from the eigenvectors $\mathbf{X}_m$ in the usual manner,

$$\mathrm{U} = \begin{pmatrix} \mathbf{X}_1^{\mathrm{T}} \\ \mathbf{X}_2^{\mathrm{T}} \\ \vdots \\ \mathbf{X}_N^{\mathrm{T}} \end{pmatrix}. \tag{6.20}$$

Because of the orthogonality condition (6.17), $\mathrm{U}^{-1} = \mathrm{U}^{\mathrm{T}}$. Since $\tilde{h}\mathbf{X}_m = \omega_m \mathbf{X}_m$, eq. (6.19) immediately follows.

Since similarity transformations leave the trace invariant, we have

$$\mathrm{Tr}\big(\tilde{h}\big) = \mathrm{Tr}\big(\widetilde{\omega}\,\big), \tag{6.21}$$

which gives

$$\sum_m \omega_m = N\left(\omega_0 - \frac{\mathrm{i}\Gamma}{2}\right). \tag{6.22}$$

Taking the real and imaginary parts of eq. (6.22) gives the "*sum rules*" for the eigenfrequency shifts and normal mode decay widths:

$$\sum_m \delta\omega_m = \sum_m \left(\omega'_m - \omega_0\right) = 0, \tag{6.23}$$

and

$$\frac{1}{N}\sum_m \Gamma_m = \Gamma. \tag{6.24}$$

The *frequency shift sum rule*, eq. (6.23), shows that for some modes the frequencies increase, while for others the frequencies decrease, such that the frequency shifts of all modes average to zero. The *decay width sum rule*, eq. (6.24), shows that the total decay widths of the various normal modes average to the decay width $\Gamma = \Gamma_\gamma + \Gamma_\alpha$ of a single oscillator.

The decay width of the mth mode can be expressed as $\Gamma_m = \Gamma_{\rm c}^{(m)} + \Gamma'_\gamma + \Gamma_\alpha$, where $\Gamma_{\rm c}^{(m)}$ is the partial width for *coherent radiative decay* in mode m, and $\Gamma'_\gamma + \Gamma_\alpha$ gives the total width for spatially incoherent radiative and nonradiative decay. Equation (6.24) can now be rewritten as a *sum rule for the coherent decay widths*,

$$\frac{1}{N}\sum_m \Gamma_{\rm c}^{(m)} = \Gamma_\gamma - \Gamma'_\gamma. \tag{6.25}$$

For a classical system, and for a nondegenerate quantum system, $\Gamma'_\gamma = 0$, and we assume this in all subsequent discussions.

Thus, some modes will have $\Gamma_{\rm c}^{(m)} < \Gamma_\gamma$, while for some $\Gamma_{\rm c}^{(m)} > \Gamma_\gamma$, such that the coherent radiative decay widths average to Γ_γ. For planar and crystalline arrays of nuclei, there will be *superradiant modes*, for which $\Gamma_{\rm c}^{(m)} \gg \Gamma_\gamma$, and *subradiant modes*, for which $\Gamma_{\rm c}^{(m)} \ll \Gamma_\gamma$.

6.4. Radiative decay of a normal mode

As a function of time, the mth mode develops as

$$\left|\psi_m(t-t_0)\right\rangle = G(t-t_0)|\psi_m\rangle = \mathbb{1}(t-t_0)\,\mathrm{e}^{-\mathrm{i}\omega_m(t-t_0)}|\psi_m\rangle, \tag{6.26}$$

and the (relative) probability of excitation decays exponentially,

$$\left\langle\psi_m(t-t_0)\middle|\psi_m(t-t_0)\right\rangle = \left|\mathbf{X}_m(t-t_0)\right|^2 = \mathrm{e}^{-\Gamma_m(t-t_0)}|\mathbf{X}_m|^2. \tag{6.27}$$

In the normal mode approach, all multiple scattering interactions between the resonators have been taken into account in the normal mode equation of motion, eq. (6.10), and the photon emitted from the system to an external point $(\mathbf{z}, t)$ is then simply a *freely propagating photon*, with no further multiple scattering,

$$A_\mu^{(m)}(\mathbf{z}, t) = \langle\psi_0|c^{-1}\int \mathrm{d}x\,\delta^+(z,x)j_\mu(\mathbf{x})G(t_x - t_0)|\psi_m\rangle. \tag{6.28}$$

Taking $t_0 = 0$, $\mathbf{z} = \mathbf{R}$, and assuming R is large compared to the dimensions of the system, gives

$$\mathbf{A}^{(m)}(\mathbf{R},t) = \sum_j \mathbb{1}\left(t - \frac{|\mathbf{R}-\mathbf{R}_j|}{c}\right) \frac{\exp[-\mathrm{i}\omega_m\,(t-|\mathbf{R}-\mathbf{R}_j|/c)]}{|\mathbf{R}-\mathbf{R}_j|} \mathbf{j}_\perp^{ab}\big(-\overleftarrow{\mathbf{k}}\big) c_j^m$$

$$\approx \mathbb{1}\big(t^*\big)\exp\big(-\mathrm{i}\omega_m t^*\big)\frac{\exp(\mathrm{i}k_m R)}{R}\mathbf{j}_\perp^{ab}(-\mathbf{k}_m)\big[\mathbf{X}^{\mathrm{T}}(-\mathbf{k}_m)\cdot\mathbf{X}_m\big]. \qquad (6.29)$$

Here $t^* = (t - R/c)$ is the retarded time, $k_m = (\omega_0 + \delta\omega_m)/c$, $\mathbf{k}_m = k_m\widehat{R}$, and we have introduced the "*phased vector*" $\mathbf{X}(\mathbf{k})$, with jth component $\exp(\mathrm{i}\mathbf{k}\cdot\mathbf{R}_j)$, so that

$$\big[\mathbf{X}^{\mathrm{T}}(-\mathbf{k}_m)\cdot\mathbf{X}_m\big] = \sum_j \mathrm{e}^{-\mathrm{i}\mathbf{k}_m\cdot\mathbf{R}_j} c_j^m. \qquad (6.30)$$

Equation (6.28) is the quantum version of *Huygens' principle* of classical optics: given the actual motions $\mathbf{x}_i(t)$ of a system of dipoles, the radiation field at any point $(\mathbf{z},t)$ is the superposition the freely propagating waves emanating from each source.

6.5. *Radiative decay of a general exciton state*

The N semi-stationary normal mode states $|\psi_m\rangle$ are a complete set of states for a single excitation in the system. Within this manifold, the resolvent operator is

$$\tilde{I} = \sum_m |\psi_m\rangle\big\langle\psi_m^{\mathrm{T}}\big|. \qquad (6.31)$$

Any single-exciton state $|\psi_{\mathrm{e}}\rangle$ can then be resolved into normal mode states,

$$|\psi_{\mathrm{e}}\rangle = \sum_m a_m|\psi_m\rangle, \qquad (6.32)$$

where the expansion coefficient is

$$a_m = \big\langle\psi_m^{\mathrm{T}}\big|\psi_{\mathrm{e}}\big\rangle. \qquad (6.33)$$

As a function of time, $|\psi_{\mathrm{e}}\rangle$ then develops as

$$\big|\psi_{\mathrm{e}}(t)\big\rangle = \sum_m a_m \mathrm{e}^{-\mathrm{i}\omega_m t}|\psi_m\rangle, \qquad (6.34)$$

and the photon potential for the emitted radiation is

$$\mathbf{A}(\mathbf{R},t) = \sum_m a_m \mathbf{A}^{(m)}(\mathbf{R},t), \qquad (6.35)$$

with the normal mode field $\mathbf{A}^{(m)}(\mathbf{R},t)$ given by eq. (6.29).

The expected flux (probability/cm^2/s) for finding a photon at $(\mathbf{R},t)$ is then given by $(\omega_0/2\pi\hbar c)|\mathbf{A}(\mathbf{R},t)|^2$, eq. (3.11). For a system of classical oscillators, $|\mathbf{A}(\mathbf{R},t)|^2$ is proportional to the expected energy flux, $\mathbf{S} = (c/4\pi)\mathrm{Re}(\mathbf{E}\times\mathbf{B}^*)$.

Since the semi-stationary states $|\psi_m\rangle$ are transpose orthogonal, rather than Hermitian (i.e., generally $\langle\psi_n|\psi_m\rangle \neq 0$), there can be *interference effects* between the modes in the decay of the excitation probability,

$$\big\langle\psi_{\rm e}(t)\big|\psi_{\rm e}(t)\big\rangle = \sum_{m,n} a_n^* a_m {\rm e}^{{\rm i}(\omega_n^* - \omega_m)t}\langle\psi_n|\psi_m\rangle. \tag{6.36}$$

These mode interference effects can lead to a "*dephasing*" of $\langle\psi_{\rm e}(t)|\psi_{\rm e}(t)\rangle$ and to the emitted signal $|\mathbf{A}(\mathbf{R},t)|^2$. In the case of a synchrotron pulse exciton $|\psi_{\rm e}(\mathbf{k}_0)\rangle$, this dephasing effect contributes to the initial superradiant decay if $\mathbf{k}_0$ is off-Bragg. These interference effects can also lead to *dynamical beats* in the emitted signal $|\mathbf{A}(\mathbf{R},t)|^2$. When this occurs, $\langle\psi_{\rm e}(t)|\psi_{\rm e}(t)\rangle$ will "flatten out" (i.e., the rate of decay ${\rm d}/{\rm d}t\,\langle\psi_{\rm e}(t)|\psi_{\rm e}(t)\rangle \approx 0$) whenever $|\mathbf{A}(\mathbf{R},t)|^2$ has a sharp minimum. In effect, the excitation is momentarily "*trapped*" within the system.

6.6. Normal mode excitation by coherent elastic scattering

For coherent elastic scattering of an incident photon A^0 by the system, the scattered photon potential $A^{\rm s}$ is, in the notation of (3.5),

$$A^{\rm s} = \delta^+ M A^0, \tag{6.37}$$

where M is the coherent elastic scattering operator for the *system*. The basic problem is to obtain M.

When treating Mössbauer γ-ray optics in its full complexity, the simplest procedure is to develop M in terms of single atom scattering, which leads to the simple multiple scattering eqs. (3.16) and (3.17), which determine the coherent elastic scattered wave.

For a system of two level nuclei, however, we can use the normal mode approach and calculate M directly for the system. The scattered wave is

$$A^{\rm s}_\mu(\mathbf{z},t) = \langle\psi_0| - {\rm i}c^{-2}\int \delta_+(z-x){\rm e}^{{\rm i}H_0 t_x} J_\mu(\mathbf{x}) G(t_x - t_y) J_\upsilon(\mathbf{y}) A^0_\upsilon(y) {\rm e}^{-{\rm i}H_0 t_x}\,{\rm d}x\,{\rm d}y|\psi_0\rangle, \tag{6.38}$$

where $J_\mu(\mathbf{x})$ is the current density operator for the *system* and $G(t)$ is the corrected propagator for exciton states. Inserting the resolvent operator $\tilde{I} = \sum_m |\psi_m\rangle\langle\psi_m^{\rm T}|$ to the left of $J_\upsilon(\mathbf{y})$, the resulting scattered photon potential, at a point $\mathbf{R}$ far removed from the system, is simply

$$\begin{aligned}\mathbf{A}^{\rm s}(\mathbf{R},\omega) &= \frac{{\rm e}^{{\rm i}kR}}{R}\sum_m \frac{\langle\psi_0|\mathbf{J}_\perp(-\mathbf{k})|\psi_m\rangle\langle\psi_m^{\rm T}|\mathbf{J}(\mathbf{k}_0)\cdot\mathbf{e}_0|\psi_0\rangle}{[\omega_m - \omega]}\,a_0 \\ &= \frac{{\rm e}^{{\rm i}kR}}{R}\big[\mathbf{j}^{ab}_\perp(-\mathbf{k})\mathbf{j}^{ba}(\mathbf{k}_0)\cdot\mathbf{e}_0\,a_0\big]\sum_m \left\{\frac{[\mathbf{X}^{\rm T}(-\mathbf{k})\cdot\mathbf{X}_m][\mathbf{X}_m^{\rm T}\cdot\mathbf{X}(\mathbf{k}_0)]}{Q_m(\omega)}\right\},\end{aligned} \tag{6.39}$$

where the resonance response denominator for the mth mode is

$$Q_m(\omega) = [\omega_m - \omega] = \omega_0 + \delta\omega_m - \omega - \mathrm{i}\frac{\Gamma_{\mathrm{c}}^{(m)} + \Gamma_\alpha}{2}. \tag{6.40}$$

In the second line of (6.39), **j**(**k**) is the Fourier transform of the nuclear current density operator for a *single nucleus*. **X**(**k**) is the notation introduced in eq. (6.29) for a "phased vector", with jth component exp(i**k** · **R**$_j$). The wave vector coupling of the incident photon to the mth mode is then

$$\left[\mathbf{X}_m^{\mathrm{T}} \cdot \mathbf{X}(\mathbf{k}_0)\right] = \sum_j c_j \mathrm{e}^{\mathrm{i}\mathbf{k}_0 \cdot \mathbf{R}_j}, \tag{6.41}$$

and the coupling to the emitted photon $\mathbf{k} = \omega/c\widehat{R}$ is

$$\left[\mathbf{X}^{\mathrm{T}}(-\mathbf{k}) \cdot \mathbf{X}_m\right] = \sum_j c_j \mathrm{e}^{-\mathrm{i}\mathbf{k} \cdot \mathbf{R}_j}. \tag{6.42}$$

From this perspective, the incident photon $|\hat{k}_0, \omega\rangle$ scatters by the virtual excitation/de-excitation of the exciton normal mode intermediate states $|\psi_m\rangle$, with the usual resonant frequency response $1/[\omega_m - \omega]$. The photon interacts with the system through the distributed system current J_μ(**x**), with the coupling to the system determined both by the polarization coupling to the individual nuclei, $\mathbf{j} \cdot \mathbf{e}_0$, and by the wave vector coupling to the mode, $[\mathbf{X}_m^{\mathrm{T}} \cdot \mathbf{X}(\mathbf{k}_0)]$. The wave vector coupling changes with the orientation of $\mathbf{k}_0$, and in some instances, such as in the *enhancement effect at Bragg*, it is possible to have *selective excitation* of a normal mode in the scattering.

6.7. Two nuclei

For two nuclei, $\tilde{h}$ is 2×2, and the solution for the normal mode frequencies is immediate:

$$\omega_{(\pm)} = \omega_0 - \mathrm{i}\frac{\Gamma}{2} \mp \frac{\Gamma_\gamma}{2}\frac{\kappa_{12}\mathrm{e}^{\mathrm{i}k_0 R_{12}}}{k_0 R_{12}}, \tag{6.43}$$

so that the frequency shifts of the two modes are

$$\delta\omega_{(\pm)} = \mp\frac{\Gamma_\gamma}{2}\frac{\kappa_{12}\cos(k_0 R_{12})}{k_0 R_{12}}, \tag{6.44}$$

and the coherent decay widths for the two modes are

$$\Gamma_{\mathrm{c}}^{(\pm)} = \Gamma_\gamma\left(1 \pm \frac{\kappa_{12}\sin(k_0 R_{12})}{k_0 R_{12}}\right). \tag{6.45}$$

The frequency shifts and coherent widths satisfy the sum rules $\delta\omega_{(+)} + \delta\omega_{(-)} = 0$, and $[\Gamma_{\mathrm{c}}^{(+)} + \Gamma_{\mathrm{c}}^{(-)}]/2 = \Gamma_\gamma$.

The corresponding eigenvectors are the symmetric and antisymmetric states

$$\mathbf{X}_{(\pm)} = \frac{1}{\sqrt{2}} \begin{pmatrix} 1 \\ \pm 1 \end{pmatrix}. \tag{6.46}$$

Since all vector components are real, $\mathbf{X}_{(\pm)}$ are Hermitian orthogonal as well as transpose orthogonal.

For $k_0 R_{12} \ll 1$, $\Gamma_c^+ \approx 2\Gamma_\gamma$ and $\Gamma_c^- \approx 0$. In this limit, the symmetric mode has an enhanced decay rate (superradiant), while the antisymmetric mode becomes nonradiative (subradiant).

This behavior is easy to understand classically. The symmetric mode corresponds to two oscillators oscillating together in-phase, which, for $k_0 R_{12} \ll 1$, doubles the dipole moment. The radiation fields are doubled and the radiation power is increased to four times that of a single oscillator. Since the total mechanical energy ε_T is also doubled, the decay rate for the system is $-(\mathrm{d}\varepsilon_\mathrm{T}/\mathrm{d}t)/\varepsilon_\mathrm{T} = 2\Gamma_\gamma$. In contrast, in the antisymmetric mode, the oscillators move 180° out of phase, and the radiation fields from the two oscillators interfere destructively, giving a very weak (electric quadrupole) radiative decay.

For coherent elastic scattering of an incident photon $|\hat{k}_0, \omega\rangle$, $\mathbf{A}^\mathrm{s}$ is given by (6.39), with the wave vector coupling to the incident and scattered photons now given by

$$\begin{aligned} \left[\mathbf{X}_{(\pm)}^\mathrm{T} \cdot \mathbf{X}(\mathbf{k}_0)\right] &= \left[\mathrm{e}^{\mathrm{i}\mathbf{k}_0\cdot\mathbf{R}_1} \pm \mathrm{e}^{\mathrm{i}\mathbf{k}_0\cdot\mathbf{R}_2}\right]/\sqrt{2}, \\ \left[\mathbf{X}^\mathrm{T}(-\mathbf{k}) \cdot \mathbf{X}_{(\pm)}\right] &= \left[\mathrm{e}^{-\mathrm{i}\mathbf{k}\cdot\mathbf{R}_1} \pm \mathrm{e}^{-\mathrm{i}\mathbf{k}\cdot\mathbf{R}_2}\right]/\sqrt{2}. \end{aligned} \tag{6.47}$$

We note, in particular, that the $\mathbf{X}_{(+)}$ mode can be selectively excited by taking $\mathbf{k}_0 \perp \mathbf{R}_{12}$, i.e., for this orientation, $[\mathbf{X}_{(-)}^\mathrm{T} \cdot \mathbf{X}(\mathbf{k}_0)] = 0$. For this case, the incident wave drives the two oscillators in phase, which is the symmetric mode.

This solution for $\mathbf{A}^\mathrm{s}$, using the normal mode approach, agrees with the multiple scattering solution worked out in [10, appendix B], as it should.

6.8. Planar array

For a planar array, we reverse the solution procedure, first obtaining the eigenmodes $\mathbf{X}_\mathbf{q}$ by symmetry, and then solving for $\omega_\mathbf{q}$ directly from the Hamiltonian equation $\tilde{h}\mathbf{X}_\mathbf{q} = \omega_\mathbf{q}\mathbf{X}_\mathbf{q}$.

Two-dimensional translational symmetry dictates that the eigenmodes should be 2-D Bloch waves

$$\left|\psi_\mathrm{e}(\mathbf{q})\right\rangle = \mathbf{X}_\mathbf{q} = \frac{1}{\sqrt{N}}\mathbf{X}(\mathbf{q}), \tag{6.48}$$

where, as before, $\mathbf{X}(\mathbf{q})$ is the phased vector with jth component $\exp(\mathrm{i}\mathbf{q}\cdot\mathbf{R}_j)$, and the N 2-D vectors $\mathbf{q}$ uniformly fill the first Brillouin zone. For simplicity, taking a square array with lattice spacing a, we have $\mathbf{q} = (2\pi/L)[n_x\hat{x} + n_y\hat{y}]$, with $L = \sqrt{N}\,a$, and $n_x, n_y \propto -\sqrt{N}/2, \ldots, +\sqrt{N}/2$. Or, in a continuum limit, the $\mathbf{q}$'s fill the first Brillouin zone ($-\pi/a \leqslant q_{x,y} \leqslant \pi/a$) with mode density $\rho(\mathbf{q}) = (L/2\pi)^2$.

Now these state vectors are, in fact, *Hermititian orthogonal* rather than *transpose orthogonal*,

$$\mathbf{X}^{\dagger}_{\mathbf{q}'} \cdot \mathbf{X}_{\mathbf{q}} = \delta_{\mathbf{q},\mathbf{q}'}, \tag{6.49}$$

or, in the continuum limit, $\mathbf{X}^{\dagger}_{\mathbf{q}'} \cdot \mathbf{X}_{\mathbf{q}} = (2\pi/L)^2\delta(\mathbf{q}-\mathbf{q}')$. However, we will see that the states $\mathbf{X}_{\mathbf{q}}$ and $\mathbf{X}_{-\mathbf{q}}$ are degenerate, i.e., $\omega_{-\mathbf{q}} = \omega_{\mathbf{q}}$. Thus, we can take the standing combinations $[\mathbf{X}_{\mathbf{q}} \pm \mathbf{X}_{-\mathbf{q}}]/\sqrt{2}$, which are transpose orthogonal. For most purposes, however, it is convenient to use the traveling wave solutions $\mathbf{X}_{\mathbf{q}}$. The proper resolvent operator is then $\tilde{I} = \sum_{\mathbf{q}} |\mathbf{X}_{\mathbf{q}}\rangle\langle\mathbf{X}_{\mathbf{q}}|$, rather than eq. (6.31).

Substituting $\mathbf{X}_{\mathbf{q}}$ into the Hamiltonian equation, and carrying out the resulting planar lattice sum as in (3.23), the complex mode frequency is

$$\omega_{\mathbf{q}} = \omega_0 + \delta\omega_{\mathbf{q}} - \mathrm{i}\frac{\Gamma_\alpha + \Gamma_{\mathrm{c}}^{(\mathbf{q})}}{2} = \omega_0 - \mathrm{i}\Gamma_\alpha - \left(\mathrm{i}\sum_s \beta_s - S\right), \tag{6.50}$$

where

$$\beta_s(\mathbf{q}) = -\frac{\pi n'}{g_s(\mathbf{q})}\left[j_\mu^{ba}(\mathbf{k}_{s+})j_\mu^{ab}(-\mathbf{k}_{s+}) + j_\mu^{ba}(\mathbf{k}_{s-})j_\mu^{ab}(-\mathbf{k}_{s-})\right]. \tag{6.51}$$

Here,

$$\mathbf{k}_{s\pm} = \mathbf{q} + \vec{\tau}_s \pm g_s(\mathbf{q})\hat{z}, \tag{6.52}$$

$$g_s(\mathbf{q}) = \sqrt{k_0^2 - (\mathbf{q}+\vec{\tau}_s)^2}, \tag{6.53}$$

where the $\vec{\tau}_s$ are the *planar* reciprocal lattice vectors, $n' = 1/a^2$ is the planar density of the nuclei, and S indicates that the real part of the self-action (radiation reaction of a single nucleus) is to be subtracted from $\mathrm{i}\sum\beta_s$. The sum over $\vec{\tau}_s$ breaks into two regions: those $\vec{\tau}_s$ for which $g_s(\mathbf{q})$ is real, which give *open radiation channels* to the normal mode field $\mathbf{A}^{(\mathbf{q})}$, given in eq. (6.57) below; and those $\vec{\tau}_s$ for which $g_s(\mathbf{q})$ is imaginary, $g_s(\mathbf{q}) = \mathrm{i}|g_s(\mathbf{q})|$, which give a nonradiative contribution to $\mathbf{A}^{(\mathbf{q})}$. The sum over all closed channels gives an exponentially damped contribution to $\mathbf{A}^{(\mathbf{q})}$ on the order of $\mathrm{e}^{-k_0|z|}/k_0|z|$. We denote the open channel sum as $\sum_{s<}$, and the closed channel sum as $\sum_{s>}$.

The partial width for coherent elastic decay in mode $\mathbf{q}$ is then

$$\Gamma_{\mathrm{c}}^{(\mathbf{q})} = \sum_{s<} \Gamma_{\mathrm{c}}^{(\mathbf{q})}(s), \tag{6.54}$$

where the partial width for emission into the symmetric open channels $\mathbf{k}_{s+}$ and $\mathbf{k}_{s-}$ is

$$\Gamma_{\mathrm{c}}^{(\mathbf{q})}(s) = \frac{2\pi n'}{g_s(\mathbf{q})}\left[\mathbf{j}_\perp^{ba}(\mathbf{k}_{s+})\cdot\mathbf{j}_\perp^{ab}(-\mathbf{k}_{s+}) + \mathbf{j}_\perp^{ba}(\mathbf{k}_{s-})\cdot\mathbf{j}_\perp^{ab}(-\mathbf{k}_{s-})\right]. \tag{6.55}$$

To compare with the classical case, we take a system of linear E1 oscillators (i.e., $\Delta J_z = 0$), each with ground state $|a\rangle = |j_0 = 0,\ m_0 = 0\rangle$ and excited state $|a\rangle =$

$|j_1 = 1,\ m_1 = 0\rangle$, and local quantization axis $\hat{z}_J$. If $\hat{z}_J$ lies in the plane of the nuclei (the x, y plane), then

$$\Gamma_{\rm c}^{(\mathbf{q})}(s) = 2\pi n' \lambda\!\!\!^{-2} \frac{k_0^2 - ((\vec{\tau}_s + \mathbf{q}) \cdot \hat{z}_J)^2}{k_0\, g_s(\mathbf{q})} \Gamma_{\rm coh}, \tag{6.56}$$

where $\Gamma_{\rm coh} = [(2j_1 + 1)\Gamma_\gamma/(4j_0 + 2) = (3/2)\Gamma_\gamma$. This result agrees with the classical treatment of [11].

The normal mode radiation field (Feynman photon potential) $\mathbf{A}^{(\mathbf{q})}$, obtained from eq. (6.29) by first carrying out the planar lattice sum before applying the gradient operator $\overleftarrow{\mathbf{k}} = \mathrm{i}\overleftarrow{\nabla}_{\mathbf{R}}$, is given by

$$\mathbf{A}^{(\mathbf{q})}(\mathbf{R}, t) = \mathbb{1}\big(t^*\big) \mathrm{e}^{-\mathrm{i}\omega_{\mathbf{q}} t^*} \frac{1}{\sqrt{N}} \sum_s \frac{\mathrm{i}2\pi n'}{g_s(\mathbf{q})} \mathrm{e}^{\mathrm{i}g_s(\mathbf{q})|z|} \mathrm{e}^{\mathrm{i}(\mathbf{q} + \vec{\tau}_s)\cdot \mathbf{R}_{xy}} \mathbf{j}_\perp^{ab}\big(-\overleftarrow{\mathbf{k}}\big). \tag{6.57}$$

This is a superposition of a finite number of open radiation channels, $\mathbf{k}_{s\pm}$, and a nonradiative contribution from the closed channels on the order of $\mathrm{e}^{-k_0|z|}/k_0|z|$. The open channels $\mathbf{k}_{s+}$ and $\mathbf{k}_{s-}$ are a symmetric pair above and below the x, y plane, each channel making an angle ϕ_s with the plane, where $\sin\phi_s(\mathbf{q}) = g_s(\mathbf{q})/k_0$ (see figure 8).

The expected flux (probability/cm^2/s) for finding a photon at $(\mathbf{R}, t)$ is $(\omega_0/2\pi\hbar c)$ $\times |\mathbf{A}^{(\mathbf{q})}(\mathbf{R}, t)|^2$ (eq. (3.11)). For the planar system, coherent emission goes into one of a finite number of open channels $\mathbf{k}_{s\eta}$ ($\eta = \pm$). The cross-sectional area for the $\mathbf{k}_{s\eta}$ channel is $L^2 \sin\phi_s$. Using just the $\mathbf{k}_{s\pm}$ contributions to $\mathbf{A}^{(\mathbf{q})}(\mathbf{R}, t)$, the probability/s that the state $|\psi_{\rm e}(\mathbf{q}), t\rangle$ de-excites by coherent γ-ray emission into either of the $\mathbf{k}_{s\pm}$ channels at time t is then given by

$$\rho_{\rm c}^{(\mathbf{q},s)}(t) = \Gamma_{\rm c}^{(\mathbf{q})}(s) \mathrm{e}^{-(\Gamma_\alpha + \Gamma'_\gamma + \Gamma_{\rm c}^{(\mathbf{q})})t}, \tag{6.58}$$

where $\Gamma_{\rm c}^{(\mathbf{q})}(s)$ is the partial width for emission into the symmetric open channels $\mathbf{k}_{s\pm}$, as given by (6.55), and $\Gamma_{\rm c}^{(\mathbf{q})} = \sum_s \Gamma_{\rm c}^{(\mathbf{q})}(s)$ is the partial width for emission into all open channels. Integrating (6.58) over t, the probability that $|\psi_{\rm e}(\mathbf{q})\rangle$ decays by coherent photon emission into the $\mathbf{k}_{s\pm}$ channels is

$$P_{\rm c}^{(\mathbf{q})}(s) = \frac{\Gamma_{\rm c}^{(\mathbf{q})}(s)}{\Gamma_\alpha + \Gamma'_\gamma + \Gamma_{\rm c}^{(\mathbf{q})}}. \tag{6.59}$$

For *coherent elastic scattering* of an incident photon $\mathbf{A}^0(\mathbf{z}, t) = a_0 \mathbf{e}_0 \exp[\mathrm{i}(\mathbf{k}_0 \times \mathbf{z} - \omega t)]$, using eq. (6.38), the scattered wave is

$$\mathbf{A}^{\rm s}(\mathbf{R}, \omega) = \sum_s \frac{\mathrm{i}\lambda_0 n'}{\sin\phi_s} \mathrm{e}^{\mathrm{i}g_s(\mathbf{q})|z|} \mathrm{e}^{\mathrm{i}(\mathbf{q} + \vec{\tau}_s)\cdot \mathbf{R}_{xy}} \frac{\mathbf{j}_\perp^{ab}(-\overleftarrow{\mathbf{k}}) \mathbf{j}_\perp^{ba}(\mathbf{k}_0) \cdot \mathbf{e}_0 a_0}{\omega_0 + \delta\omega_{\mathbf{q}} - \omega - \mathrm{i}(\Gamma_{\rm c}^{(\mathbf{q})} + \Gamma_\alpha)/2}, \tag{6.60}$$

where $\mathbf{q} = \mathbf{k}_{0xy}$ (reduced to the first Brillouin zone) in the denominator, and the notation for g_s and ϕ_s is now that of eq. (3.19), where the planar scattering was treated in the Born approximation. Equation (6.60) gives the exact result for elastic

scattering from a planar array of nuclei, including the planar self-action. We note that the incident $\mathbf{k}_0$ selectively excites the $\mathbf{q} = \mathbf{k}_{0xy}$ planar normal mode.

Planar surface mode and total transmission. The most interesting feature of the planar solution (6.60) is that total transmission can occur [11]. From (6.53) and (6.55), we see that for well defined directions of $\mathbf{k}_0$, there will exist a $\vec{\tau}_{s'}$ such that $g_{s'} = 0$ and $\Gamma_{\rm c}(s') = \infty$. The coherent width for emission into the s' channel is infinite and the nuclear excitation amplitudes are identically zero. The scattered wave is a single channel, parallel to the surface, with intensity equal to that of the incident wave, but the ratio of the total energy of this wave to the incident energy is zero (because of the $\sin\phi_{s'}/\sin\phi_0$ ratio of the cross-sectional areas). There is no forward scattering, so the total transmitted wave is $\mathbf{A}^0$ and the layer becomes perfectly transparent to the incident radiation. This phenomenon of surface mode channels in single layers, and in M-layer crystals, is discussed further in [96].

Exact planar vs. Born approximation. In our development of the generalized Darwin–Prins dynamical theory of X-ray and γ-ray optics, the scattering from each plane is treated in the Born approximation, and then the planes are coupled through their scattered radiation fields. The only approximation involved is the neglect of planar self-action. This approximation is in fact very good, except for the special case when a planar surface mode channel is just opened or just closed.

For a system of two level nuclei, we can use the exact planar result of eq. (6.60), and give an exact Darwin–Prins development, as carried out in [11]. However, the only difference between (6.60) and the Born approximation is the resonance denominator $Q(\omega)$: for the Born approximation, $Q(\omega) = \omega_0 - \omega - {\rm i}\Gamma/2$, while, with planar self-action, $Q(\omega) = \omega_0 + \delta\omega_{\mathbf{q}} - \omega - {\rm i}(\Gamma_\alpha + \Gamma_{\rm c}^{(\mathbf{q})})/2$, with $\mathbf{q} = \mathbf{k}_{0xy}$.

Now from (6.56), $\Gamma_{\rm c}^{(\mathbf{q})}(s) \approx 2\pi n'\Gamma_{\rm coh}/\sin\phi_s \approx 2\times 10^{-2}\Gamma_{\rm coh}/\sin\phi_s$, where we have taken $a \sim 2.5$ Å and $\lambda \sim 0.86$ Å. Thus, $\phi_s < 10^{-2}$ rad may double the coherent width (compared to an isolated nucleus), but since this is only a small fraction of the total width, ϕ_s less than about 10^{-3} rad is required to double the total width. Similarly, the frequency shift $\delta\omega_{\mathbf{q}}$ will normally be a negligible fraction of Γ_γ. Thus, for most orientations of $\mathbf{k}_0$, the Born approximation is quite accurate for treating the scattering of a single plane.

6.9. M-layer crystal

For an M-layer crystal, the invariance of the system under x, y translations by planar lattice vector displacements dictates that the normal modes will be 2-D Bloch waves $\mathbf{X}_{\mathbf{q}}$ in the x, y direction. Each plane layer sends out plane waves $\mathbf{k}_{s\pm}(\mathbf{q})$ which couple the layers together, and scatter into the same set of open channels. Since there are M plane layers, there will be M different linear combinations of the planar

solutions, giving M different normal modes within each **q**-manifold. Thus, the general form of the normal mode states is

$$\mathbf{X}_{\mathbf{q},l} = \mathbf{Z}_{\mathbf{q},l} \otimes \mathbf{X}_{\mathbf{q}}, \tag{6.61}$$

where $\mathbf{Z}_{\mathbf{q},l}$ is an M-component vector

$$\mathbf{Z}_{\mathbf{q},l} = \begin{pmatrix} c_1^{(\mathbf{q},l)} \\ c_2^{(\mathbf{q},l)} \\ \vdots \\ c_M^{(\mathbf{q},l)} \end{pmatrix}. \tag{6.62}$$

The new index l ($l = 1, 2, \ldots, M$) specifies the M different normal modes within each **q**-manifold. In mode $\mathbf{X}_{\mathbf{q},l}$, the exciton state is $|\psi_{\mathbf{q},l}\rangle = \sum_j c_j^{\mathbf{q},l} |b_j\rangle |G_0(j)\rangle$, and if the nucleus j lies in the mth layer, at the position $\mathbf{R}_j$, then $c_j^{\mathbf{q},l} = c_m^{(\mathbf{q},l)} \exp(\mathrm{i}\mathbf{q}\cdot\mathbf{R}_j)/\sqrt{N_{xy}}$.

The Bloch wave states $\mathbf{X}_{\mathbf{q}}$ factor out, and in the **q**-manifold, the Hamiltonian equation reduces to an $M \times M$ matrix equation

$$\tilde{h}^{(\mathbf{q})} \mathbf{Z}_{\mathbf{q},l} = \omega \mathbf{Z}_{\mathbf{q},l}, \tag{6.63}$$

where now

$$h_{nn} = \omega_0 + \delta\omega_{\mathbf{q}} - \mathrm{i}\frac{\Gamma_\alpha + \Gamma_{\mathrm{c}}^{(\mathbf{q})}}{2}, \tag{6.64}$$

$$h_{mn}(m \neq n) = -\frac{\mathrm{i}}{2} \sum_s \Gamma_{\mathrm{c}}^{(\mathbf{q})}(s) \exp\bigl(\mathrm{i}g_s|n-m|d\bigr). \tag{6.65}$$

In (6.65), for the closed channel contributions ($s>$), $\Gamma_{\mathrm{c}}^{(\mathbf{q})}(s)/2 = \beta_s(\mathbf{q})$, as given by (6.51).

The determinant equation, $\mathrm{Det}[\tilde{h}^{(\mathbf{q})} - \omega\tilde{\mathbf{1}}] = 0$, determines the complex frequencies $\omega_{\mathbf{q},l} = [\omega'_{\mathbf{q},l} - \mathrm{i}\Gamma_{\mathbf{q},l}/2] = [\omega_{0\mathbf{q}} + \delta\omega_{\mathbf{q},l} - \mathrm{i}(\Gamma_\alpha + \Gamma_{\mathrm{c}}^{(\mathbf{q},l)})/2]$ of the M normal modes, $l = 1, 2, \ldots, M$. The sum rules (6.23) and (6.25) hold globally, and within the **q**-manifold, we have the sum rules

$$\sum_{l=1}^{M} \delta\omega_{\mathbf{q},l} = \sum_{l=1}^{M} \bigl(\omega'_{\mathbf{q},l} - \omega_{0\mathbf{q}}\bigr) = 0 \tag{6.66}$$

and

$$\frac{1}{M} \sum_{l=1}^{M} \Gamma_{\mathrm{c}}^{(\mathbf{q},l)} = \Gamma_{\mathrm{c}}^{(\mathbf{q})} = \sum_{s<} \Gamma_{\mathrm{c}}^{(\mathbf{q})}(s). \tag{6.67}$$

The Hamiltonian $\tilde{h}^{(\mathbf{q})}$ is again symmetric, rather than Hermitian, so the eigenvectors $\mathbf{Z}_{\mathbf{q},l}$ satisfy the transpose orthogonality condition within the **q**-manifold, $\mathbf{Z}_{\mathbf{q},l}^{\mathrm{T}} \cdot \mathbf{Z}_{\mathbf{q},l'} = \delta_{ll'}$. An exciton state $|\psi_{\mathrm{e}}\rangle = \mathbf{Z}(0)$, which lies in the **q**-manifold (such as

state $|\psi_{\rm e}(\mathbf{k}_0)\rangle$ created by a synchrotron pulse, which lies in the $\mathbf{q} = \mathbf{k}_{0xy}$ manifold), will then develop in time as

$$\mathbf{Z}(t) = \sum_{l=1}^{M} a_l {\rm e}^{-{\rm i}\omega_{\mathbf{q},l}t}\mathbf{Z}_{\mathbf{q},l}, \tag{6.68}$$

where

$$a_l = \mathbf{Z}^{\rm T}_{\mathbf{q},l} \cdot \mathbf{Z}(0). \tag{6.69}$$

The field emitted by the crystal in the $(\mathbf{q}, l)$ normal mode is

$$\begin{aligned}\mathbf{A}^{(\mathbf{q},l)}(\mathbf{R},t) &= {\rm e}^{-{\rm i}\omega_{\mathbf{q},l}t}\sum_{s<}\frac{{\rm i}2\pi n'}{g_s(\mathbf{q})}{\rm e}^{{\rm i}\mathbf{k}_{s+}\cdot\mathbf{R}}\,\mathbf{j}_\perp(-\mathbf{k}_{s+})\,\mathbf{Z}^{\rm T}_{\mathbf{q},l}\cdot\mathbf{Z}(-g_s), \qquad z > (M-1)d,\\ &= {\rm e}^{-{\rm i}\omega_{\mathbf{q},l}t}\sum_{s<}\frac{{\rm i}2\pi n'}{g_s(\mathbf{q})}{\rm e}^{{\rm i}\mathbf{k}_{s-}\cdot\mathbf{R}}\,\mathbf{j}_\perp(-\mathbf{k}_{s-})\,\mathbf{Z}^{\rm T}_{\mathbf{q},l}\cdot\mathbf{Z}(g_s), \qquad z < 0.\end{aligned} \tag{6.70}$$

Here $\mathbf{Z}(\pm g_s)$ is the M-component phased vector with mth component $\exp(\pm{\rm i}g_s m d)$, with $m = 0, 1, \ldots, M-1$, so that $\mathbf{Z}^{\rm T}_{\mathbf{q},l}\cdot\mathbf{Z}(\pm g_s) = \sum_m c_m^{(\mathbf{q},l)}\exp(\pm{\rm i}g_s m d)$. For an initial exciton state $|\psi_{\rm e}\rangle = \mathbf{Z}(0)$, the subsequent emission field is a superposition of normal mode fields,

$$\mathbf{A}(\mathbf{R},t) = \sum_{l=1}^{M} a_l \mathbf{A}^{(\mathbf{q},l)}(\mathbf{R},t), \tag{6.71}$$

with a_l given by (6.69).

Symmetric two-wave approximation. We are particularly interested in the radiative decay of nuclear exciton states $|\psi_{\rm e}(\mathbf{k}_0)\rangle$ created by synchrotron pulses. Two important cases are for $\mathbf{k}_0$ off-Bragg, and for $\mathbf{k}_0$ satisfying the condition for a symmetric Bragg reflection. To treat these cases, it is sufficient to only include the coupling provided by the $\mathbf{k}_{0+}$ and $\mathbf{k}_{0-}$ channels, omitting the contributions of all other open channels $\mathbf{k}_{s\pm}$. This is essentially the usual two-wave approximation made in the dynamical theory of X-ray optics, restricting our attention to the symmetric case.

We take the scattering plane defined by $\mathbf{k}_{0+}$ and $\mathbf{k}_{0-}$ to be the (z, x)-plane, so that

$$\mathbf{q} = q\hat{x} = k_0\cos\phi_0\hat{x}, \tag{6.72}$$

$$g_0 = \sqrt{k_0^2 - q^2} = k_0\sin\phi_0, \tag{6.73}$$

$$\mathbf{k}_{0\pm} = \mathbf{q} \pm g_0\hat{z}. \tag{6.74}$$

This is the geometry shown in figure 8.

We will furthermore assume maximum coupling of the radiation fields to the nuclei. Assuming a linear $\Delta J_z = 0$, E1 nuclear transition, the quantization axis $\hat{z}_J$

should lie in the $\widehat{\sigma} = \hat{y}$ direction, perpendicular to the scattering plane. The partial width for coherent decay, eq. (6.56), then becomes

$$\Gamma_{\rm c}^{(\mathbf{q})}(0) = \frac{2\pi n' \lambda^2}{\sin\phi_0}\Gamma_{\rm coh}, \tag{6.75}$$

and the sum rule (6.67) becomes

$$\sum_{l=1}^{M} \Gamma_{\rm c}^{(\mathbf{q},l)} = M\Gamma_{\rm c}^{(\mathbf{q})}(0) = 2\pi n \lambda^2 l_{\|}\Gamma_{\rm coh}, \tag{6.76}$$

where $n = 1/(a^2 d)$ is now the volume density of nuclei in the crystal, and $l_{\|} = Md/\sin\phi_0$ is the thickness of the crystal in the $\mathbf{k}_{0\pm}$ directions. We note the right-hand side of (6.76) is precisely the superradiant decay width at Bragg as calculated by the Fermi Golden Rule in eq. (4.22).

For any particular number of layers M, we can now solve the determinant equation $\mathrm{Det}[\tilde{h}^{(\mathbf{q})} - \omega\tilde{\mathbf{1}}] = 0$ for the M eigenfrequencies $\omega_{\mathbf{q},l}$, and then substitute $\omega_{\mathbf{q},l}$ into the eigenvalue equation $\tilde{h}^{(\mathbf{q})}\mathbf{Z}_{(\mathbf{q},l)} = \omega_{\mathbf{q},l}\mathbf{Z}_{(\mathbf{q},l)}$ to determine the eigenmodes $\mathbf{Z}_{(\mathbf{q},l)}$. However, there is a better procedure, in which we first deduce the general form of the eigenstates, and then determine the eigenfrequencies.

We first rewrite the Hamiltonian equation (6.63) in component form,

$$Q_0(\omega)\, Z_m^{(\mathbf{q},l)} = \frac{\mathrm{i}}{2}\Gamma_{\rm c}^{(\mathbf{q})}(0) \sum_{n=0}^{M-1} Z_n^{(\mathbf{q},l)} \exp\bigl(\mathrm{i}g_0|n-m|d\bigr), \tag{6.77}$$

where $Q_0(\omega) = \omega_0 - \omega - \mathrm{i}\Gamma_\alpha$. We then try a trial solution of the form

$$Z_m = \mathrm{e}^{\mathrm{i}k'dm} \pm \mathrm{e}^{\mathrm{i}k'd(M-1-m)} = \mathcal{K}^m \pm \mathcal{K}^{M-1-m}, \qquad m = 0, 1, \ldots, M-1, \tag{6.78}$$

where k' is a complex parameter yet to be determined, and in the second line, we have introduced the notation $\mathcal{K} = \exp(\mathrm{i}k'd)$. We choose this form of trial solution based on the physical thinking that there exist two propagating waves inside the crystal. The eigenmodes are the stationary states formed by the superposition of the two waves, similar to the standing waves on a beaded string. Noting that $\mathcal{K}^m + \mathcal{K}^{M-1-m} = 2\mathcal{K}^{(M-1)/2}\cos[(M-1-2m)k'd/2]$ and $\mathcal{K}^m - \mathcal{K}^{M-1-m} = -2\mathrm{i}\mathcal{K}^{(M-1)/2}\sin[(M-1-2m)k'd/2]$, we call the "+" solutions "cosine solutions" and the "−" solutions "sine solutions".

Substituting (6.78) into (6.77) yields a *consistency equation* for Z_m to be a solution,

$$\mathcal{K}^{M+1} - \mathrm{e}^{\mathrm{i}g_0 d}\mathcal{K}^M \pm \bigl(1 - \mathrm{e}^{\mathrm{i}g_0 d}\mathcal{K}\bigr) = 0, \tag{6.79}$$

and a *dispersion equation*,

$$Q_0(\omega) = \frac{\mathrm{i}}{2}\Gamma_{\rm c}^{(\mathbf{q})}(0)\left[\frac{1}{1-\mathcal{K}\exp(\mathrm{i}g_0 d)} - \frac{1}{1-\mathcal{K}\exp(-\mathrm{i}g_0 d)}\right]. \tag{6.80}$$

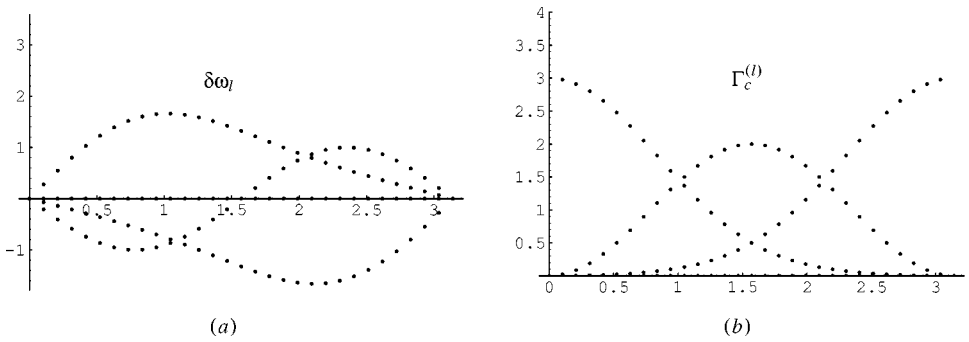

Figure 25. (a) Plot of the normal mode frequency shifts $\delta\omega_l$ as a function of $g_0 d$ for an $M = 3$ layer crystal. (b) The normal mode coherent decay widths $\Gamma_c^{(l)}$ vs. $g_0 d$. For both figures, the vertical scale is in units of $\Gamma_c^{(\mathbf{q})}(0)$, the coherent decay width for a single plane; and $g_0 d$ varies from 0 to π.

The consistency equation (6.79) constitutes two $(M+1)$-order equations, with the $(+)$ equations giving the cosine solutions and the $(-)$ equations giving the sine solutions. There are then $2M+2$ solutions to (6.79). Two of these solutions are "null" solutions, giving the null "mode" $\mathbf{Z} \equiv 0$. The null solutions are $\mathcal{K} = 1$, which is always a solution to the $(-)$ equation, and $\mathcal{K} = -1$, which is a solution to the $(+/-)$ equation if M is (odd/even). The remaining $2M$ solutions are paired, with each pair being an identical solution. If M is even, there are $M/2$ distinct cosine and sine solutions; while if M is odd, there are $(M+1)/2$ cosine solutions and $(M-1)/2$ sine solutions. In either case, there are M distinct eigenmodes $\mathbf{Z}_{\mathbf{q},l}$ for an M-layer crystal in the $\mathbf{q}$ subspace, which we designate by the index $l = 1, 2, \ldots, M$. The eigenmode frequency $\omega_{\mathbf{q},l}$ is obtained from the dispersion equation (6.80), by substituting the solution $\mathcal{K}_l$ of (6.79) which generates $\mathbf{Z}_{\mathbf{q},l}$ into the right-hand side of (6.80).

The solutions $\mathcal{K}_l$ of (6.79) are functions of $g_0 d$, or equivalently, of the mode angle ϕ_0. Changing g_0 changes the $\mathbf{q}$-manifold, $\mathbf{q} = k_0 \cos\phi_0 \hat{x}$. As a function of $g_0 d$, the configuration of the mode $\mathbf{Z}_{\mathbf{q},l}$ changes, as does the frequency shift of the mode, $\delta\omega_{\mathbf{q},l}$, and the partial width for coherent radiative decay, $\Gamma_c^{(l)}$. As $g_0 d$ varies from $0 \to \pi$, $\mathbf{k}_0$ varies from a symmetric Bragg condition ($\phi_0 = 0$), to off-Bragg ($g_0 d = \pi/2$), and back to the next higher order symmetric Bragg reflection ($g_0 d = \pi$).

In figure 25, we show the variation of the mode frequency shifts and coherent radiative widths vs. $g_0 d$ for the simplest nontrivial case of an $M = 3$ layer crystal. In (a) we show the frequency shifts $\delta\omega_l$ of the three modes. The shifts satisfy the sum rule $\sum_l \delta\omega_l = 0$. We note in particular that at Bragg, the frequency shifts all vanish; but off-Bragg, the frequencies are spread over a region $\approx 3\Gamma_c^{(\mathbf{q})}(0) = 2\pi n \lambda\!\!\!^{-2} l_{\|} \Gamma_{\rm coh}$.

In (b) we show the coherent decay widths $\Gamma_c^{(l)}$. The widths satisfy the sum rule $\sum_l \Gamma_c^{(l)} = 3\Gamma_c^{(\mathbf{q})}(0) = 2\pi \lambda\!\!\!^{-2} l_{\|} \Gamma_{\rm coh}$. The most interesting feature is that at Bragg, two of the modes become nonradiative, and one mode becomes superradiant with the coherent decay width being the full $3\Gamma_c^{(\mathbf{q})}(0)$ of the sum rule. For this mode, all the planar fields add in-phase, giving enhanced emission, while for the other two modes, the fields of the three planes exactly cancel.

- *These are general features for any* M: at Bragg, one mode becomes superradiant, with enhanced coherent decay width $\Gamma_{\rm c} = 2n\pi\lambda\!\!\!^{-2} l_{\|}\Gamma_{\rm coh}$, and all other modes are nonradiant. Off-Bragg, the widths are spread, consistent with the sum rule $\sum_l \Gamma_{\rm c}^{(l)} = 2\pi\lambda\!\!\!^{-2} l_{\|}\Gamma_{\rm coh}$, with a few modes being (weakly) superradiant, and most modes subradiant. The frequency shifts satisfy the sum rule $\sum_l \delta\omega_l = 0$, and at Bragg, all frequency shifts are zero. Off-Bragg, there is a broad spread of frequencies, with the total spread being $\Delta\omega \approx \Gamma_{\rm c} = 2\pi\lambda\!\!\!^{-2} l_{\|}\Gamma_{\rm coh}$. The remarkable behavior at Bragg is the essential point of the *coherent enhancement effect at Bragg* [11].

As a simple example, for $M = 2$ layers, the eigenmodes are the symmetric state (with corresponding oscillators $\mathbf{R}_j$ in each plane oscillating in-phase), and the antisymmetric state (with corresponding oscillators 180° out-of-phase), in direct analogy to two nuclei. At the $g_0 d = \pi$ Bragg, the symmetric state is nonradiative: the self field of each plane is exactly canceled by the field from the other plane, the radiation reaction on each oscillator then vanishes, and the oscillators have free undamped motion. Correspondingly, the emitted radiation fields from the two layers cancel and the mode is nonradiative. For the antisymmetric mode, the fields add, so the radiation reaction on each oscillator is doubled, and the mode decays superradiantly, at $2\times$ the rate of a single layer. For $g_0 d = 2\pi$, the roles are reversed – the symmetric mode is superradiant and the antisymmetric mode is nonradiative.

6.10. Superradiance and dynamical beats in the decay of a nuclear exciton

Of particular interest is the decay of an exciton $|\psi_{\rm e}(\mathbf{k}_0)\rangle$ created by a *synchrotron pulse*. If $\mathbf{k}_0$ satisfies the symmetric Bragg condition, then a single superradiant eigenmode is excited, and the subsequent decay is a simple enhanced exponential decay. If $\mathbf{k}_0$ is off-Bragg, then $|\psi_{\rm e}(\mathbf{k}_0)\rangle$ is a superposition of normal modes, and the spread of frequencies and Hermitian nonorthogonality play an important role both in the initial superradiance and subsequent dynamical beats.

The exciton $|\psi_{\rm e}(\mathbf{k}_0)\rangle$ created by a synchrotron pulse is a Bloch wave,

$$\big|\psi_{\rm e}(\mathbf{k}_0)\big\rangle = \frac{1}{\sqrt{N}}\sum_j {\rm e}^{{\rm i}\mathbf{k}_0\cdot\mathbf{R}_j}\big|b_j\big\rangle|G_0(j)\big\rangle, \tag{6.81}$$

where $\mathbf{k}_0 = (\omega_0/c)\hat{n}_0$, with $\omega_0 = (E_b - E_a)/\hbar$, and $\hat{n}_0$ the direction of the incident pulse. Hence, $|\psi_{\rm e}(\mathbf{k}_0)\rangle$ lies in the $\mathbf{q} = \mathbf{k}_{0xy}$ manifold of eigenmodes of an M-layer crystal. Factoring out the xy-Bloch states $\mathbf{X}_{\mathbf{q}}$, and suppressing the $\mathbf{q}$ index on all states and eigenfrequencies, the initial exciton state is

$$\big|\psi_{\rm e}(\mathbf{k}_0)\big\rangle = \frac{1}{\sqrt{M}}\mathbf{Z}(g_0) = \frac{1}{\sqrt{M}}\begin{pmatrix} 1 \\ {\rm e}^{{\rm i}g_0 d} \\ \vdots \\ {\rm e}^{{\rm i}g_0 d(M-1)} \end{pmatrix}. \tag{6.82}$$

Expanding in terms of eigenmodes,

$$\big|\psi_{\rm e}(\mathbf{k}_0)\big\rangle = \sum_{l=1}^{M} a_l \mathbf{Z}_l, \tag{6.83}$$

where

$$a_l = \frac{\mathbf{Z}_l^{\rm T}\cdot\mathbf{Z}(g_0)}{\sqrt{M}}. \tag{6.84}$$

The state then develops as

$$\big|\psi_{\rm e}(\mathbf{k}_0,t)\big\rangle = \sum_{l=1}^{M} {\rm e}^{-{\rm i}\omega_l t} a_l \mathbf{Z}_l, \tag{6.85}$$

and the excitation probability decays as

$$\big\langle\psi_{\rm e}(\mathbf{k}_0,t)\big|\psi_{\rm e}(\mathbf{k}_0,t)\big\rangle = \sum_{l,l'} a_{l'}^{*} a_l {\rm e}^{{\rm i}(\omega_{l'}-\omega_l)t}\mathbf{Z}_{l'}^{\dagger}\cdot\mathbf{Z}_l. \tag{6.86}$$

The eigenmodes are transpose orthogonal rather than Hermitian orthogonal, so generally $\mathbf{Z}_{l'}^{\dagger}\cdot\mathbf{Z}_l \neq 0$, and there are interference effects between the modes in the decay of $\langle\psi_{\rm e}(\mathbf{k}_0,t)|\psi_{\rm e}(\mathbf{k}_0,t)\rangle$.

The radiation field (Feynman photon potential) emitted by the crystal in the state $|\psi_{\rm e}(\mathbf{k}_0,t)\rangle$ is

$$\mathbf{A}(\mathbf{R},t) = \sum_{l=1}^{M} a_l \mathbf{A}^{(l)}(\mathbf{R},t), \tag{6.87}$$

where a_l is given by (6.84), and, in the symmetric two-wave approximation, the field of the lth normal mode is

$$\begin{aligned}\mathbf{A}^{(l)}(\mathbf{R},t) &= -\widehat{\sigma}C\frac{\rm i}{2}\Gamma_{\rm c}^{(\mathbf{q})}(0)\exp\big[{\rm i}(\mathbf{k}_{0+}\cdot\mathbf{R}-\omega_l t)\big]\mathbf{Z}_l^{\rm T}\cdot\mathbf{Z}(-g_0), \qquad z>(M-1)d,\\ &= -\widehat{\sigma}C\frac{\rm i}{2}\Gamma_{\rm c}^{(\mathbf{q})}(0)\exp\big[{\rm i}(\mathbf{k}_{0-}\cdot\mathbf{R}-\omega_l t)\big]\mathbf{Z}_l^{\rm T}\cdot\mathbf{Z}(g_0), \qquad z<0.\end{aligned} \tag{6.88}$$

Here $\widehat{\sigma}=\hat{y}$ is the polarization perpendicular to the $(\mathbf{k}_{0+},\mathbf{k}_{0-})$ scattering plane, $C=\sqrt{2/\lambda\Gamma_{\rm coh}}$, $\Gamma_{\rm c}^{(\mathbf{q})}(0)$ is the partial width for coherent decay per plane, as given by (6.75), and $\mathbf{Z}_l^{\rm T}\cdot\mathbf{Z}(\pm g_0)=\sum_m Z_m^{(l)}\exp(\pm{\rm i}g_0 d\,m)$, $m=0,\ldots,M-1$.

In figure 26(a), we show the coherent photon signal $|\mathbf{A}^{(+)}(t)|^2$ vs. t emitted by a synchrotron pulse exciton $|\psi_{\rm e}(\mathbf{k}_0,t)\rangle$ in the $\mathbf{k}_{0+}$ direction, for $\mathbf{k}_0$ on Bragg ($g_0 d=\pi$), and for $\mathbf{k}_0$ off-Bragg ($g_0 d=\pi/2$), for an $M=3$ layer crystal; and in (b) we show the corresponding decay of the excitation probability $\langle\psi_{\rm e}(\mathbf{k}_0,t)|\psi_{\rm e}(\mathbf{k}_0,t)\rangle$. In these figures, we have "turned off" the incoherent processes, i.e., have set $\Gamma_\alpha+\Gamma'_\gamma=0$. The Bragg decay has a simple exponential decay, both for $|\mathbf{A}^{(+)}(t)|^2$ and for $\langle\psi_{\rm e}(\mathbf{k}_0,t)|\psi_{\rm e}(\mathbf{k}_0,t)\rangle$, at the enhanced rate $\Gamma_{\rm c}=2\pi n\lambda^2 l_{\parallel}\Gamma_{\rm coh}$. The off-Bragg is more complex: there is an initial superradiant phase, decaying at half the Bragg rate, $\Gamma_{\rm c}/2$, indicated by the dashed

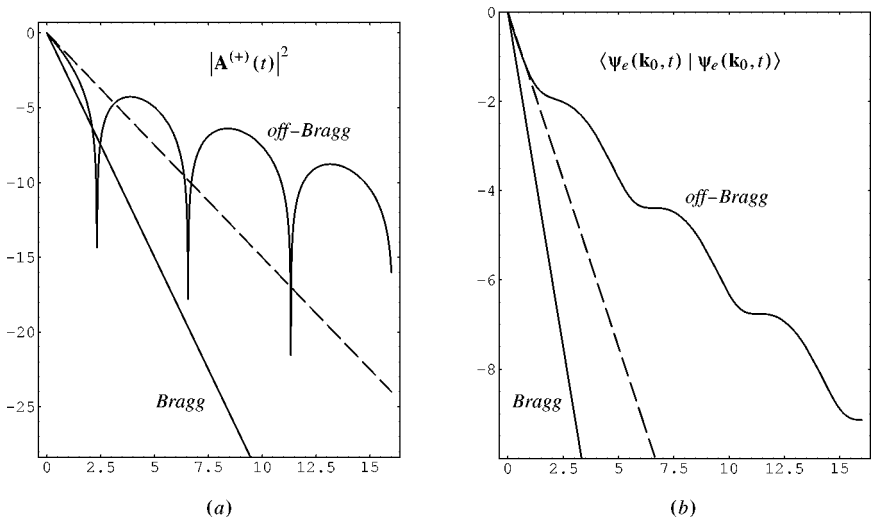

Figure 26. (a) The coherent photon signal $\log[|\mathbf{A}^{(+)}(t)|^2]$ vs. t emitted by a synchrotron pulse exciton $|\psi_{\rm e}(\mathbf{k}_0,t)\rangle$ in the $\mathbf{k}_{0+}$ direction, for $\mathbf{k}_0$ on Bragg ($g_0 d = \pi$), and for $\mathbf{k}_0$ off-Bragg ($g_0 d = \pi/2$). We have normalized the curves to unity at $t = 0$. The Bragg decay is superradiant, at the enhanced rate $\Gamma_{\rm c} = 2\pi n \lambda\!\!\!^{-2} l_{\|} \Gamma_{\rm coh}$. The dashed line shows the initial off-Bragg superradiant decay at the enhanced rate $\Gamma_{\rm c} = \pi n \lambda\!\!\!^{-2} l_{\|} \Gamma_{\rm coh}$. The number of crystal layers is $M = 3$. Time t is in units of $[\Gamma_{\rm c}^{(\mathbf{q})}(0)]^{-1}$. (b) The decay of the excitation probability $\log[\langle\psi_{\rm e}(\mathbf{k}_0,t)|\psi_{\rm e}(\mathbf{k}_0,t)\rangle]$ vs. t for $\mathbf{k}_0$ on- and off-Bragg, for a 3-layer crystal.

lines in (a) and (b). This is followed by a slowly decaying phase, in which the photon signal $|\mathbf{A}^{(+)}(t)|^2$ exhibits dynamical beats, periodically vanishing. Correspondingly, $\langle\psi_{\rm e}(\mathbf{k}_0,t)|\psi_{\rm e}(\mathbf{k}_0,t)\rangle$ "flattens out" (i.e., the rate of decay $\mathrm{d}/\mathrm{d}t\langle\psi_{\rm e}(\mathbf{k}_0,t)|\psi_{\rm e}(\mathbf{k}_0,t)\rangle \approx 0$) whenever $|\mathbf{A}(\mathbf{R},t)|^2$ has a sharp minimum. In effect, the excitation is momentarily "*trapped*" within the system.

This periodic behavior in the decay of $\langle\psi_{\rm e}(\mathbf{k}_0,t)|\psi_{\rm e}(\mathbf{k}_0,t)\rangle$ off-Bragg is due to the interference effects between the modes, which arise because the eigenmodes $|\psi_m\rangle$ are transpose orthogonal, rather than Hermitian, as noted in eq. (6.36). This interference also gives a "dephasing" effect due to the spread of frequencies, which plays a major role in the initial superradiant decay of $\langle\psi_{\rm e}(\mathbf{k}_0,t)|\psi_{\rm e}(\mathbf{k}_0,t)\rangle$.

At Bragg, a single superradiant eigenmode is excited, and the decay of $\langle\psi_{\rm e}(\mathbf{k}_0,t)|\psi_{\rm e}(\mathbf{k}_0,t)\rangle$ is a simple exponential, at the enhanced rate $\Gamma_{\rm c} = 2\pi n \lambda\!\!\!^{-2} l_{\|} \Gamma_{\rm coh}$.

Correspondingly, for Bragg excitation, the photon emission field is an eigenmode field, with the coherent photon signal having two equal strength channels, $|\mathbf{A}^{(+)}(t)|^2$ and $|\mathbf{A}^{(-)}(t)|^2$, in the $\mathbf{k}_{0+}$ and $\mathbf{k}_{0-}$ directions, respectively. Carrying out the calculation as in (6.58), the probability/s that the state $|\psi_{\rm e}(\mathbf{k}_0),t\rangle$ de-excites by coherent γ-ray emission into either the $\mathbf{k}_{0+}$ or the $\mathbf{k}_{0-}$ channel at time t is given by

$$\rho_{\rm c}(t) = \Gamma_{\rm c} \mathrm{e}^{-(\Gamma_\alpha + \Gamma'_\gamma + \Gamma_{\rm c})t}, \tag{6.89}$$

and integrating over t, the probability that $|\psi_{\rm e}(\mathbf{k}_0)\rangle$ decays by coherent photon emission is

$$P_{\rm c} = \frac{\Gamma_{\rm c}}{\Gamma_\alpha + \Gamma'_\gamma + \Gamma_{\rm c}}. \tag{6.90}$$

Off-Bragg, $|\psi_{\rm e}(\mathbf{k}_0)\rangle$ is a superposition of normal modes, and correspondingly, $\mathbf{A}(\mathbf{R},t)$ is a superposition of normal modes fields $\mathbf{A}^{(l)}(\mathbf{R},t)$, as given by (6.87). The combination of the modes, determined by the expansion coefficients a_l, is such that initially $|\mathbf{A}^{(-)}(t)|^2 \ll |\mathbf{A}^{(+)}(t)|^2$ – i.e., the system is phased so that there is initial constructive interference between the planar waves in the "forward" $\mathbf{k}_{0+}$ direction, but destructive interference in the $\mathbf{k}_{0-}$ direction. The decay is initially superradiant, but at half the Bragg rate $\Gamma_{\rm c}/2$ because the $\mathbf{k}_{0-}$ decay channel is shut down. As can be seen from figure 26(b), with about 80% probability, $|\psi_{\rm e}(\mathbf{k}_0)\rangle$ de-excites during this initial superradiant phase, so the probability for coherent decay into the $\mathbf{k}_{0+}$ channel is, approximately,

$$P_{\rm c} \approx \frac{\Gamma_{\rm c}/2}{\Gamma_\alpha + \Gamma'_\gamma + \Gamma_{\rm c}/2}. \tag{6.91}$$

Following this initial superradiant phase, the off-Bragg signal decays slowly, with the onset of "dynamical beats". This is a natural consequence of adding wave contributions spread over a frequency range $\Delta\omega \approx \Gamma_{\rm c}$. For example, if the normal mode wave contributions entered with equal amplitude over a frequency range $\omega_0 \pm \Gamma_{\rm c}/2$, and if all modes decayed at the natural Γ, then the emitted signal would have dynamical beats of frequency $\Gamma_{\rm c}/2$ and a weakly enhanced long time decay $|\mathbf{A}^{(+)}(t)|^2 \propto \exp(-\Gamma t)/t^2$:

$$\mathbf{A}^{(+)}(t) \propto \int_{-\Gamma_{\rm c}/2}^{+\Gamma_{\rm c}/2} {\rm d}\omega {\rm e}^{-{\rm i}(\omega_0+\omega-{\rm i}\Gamma/2)t} = \frac{2\sin(\Gamma_{\rm c}t/2)}{t} {\rm e}^{-{\rm i}(\omega_0-{\rm i}\Gamma/2)t}. \tag{6.92}$$

This example is much too simple, but it illustrates the beats and inverse power law type decay which arise from Fourier synthesis of bands of frequencies.

Making the correct resolution of $|\psi_{\rm e}(\mathbf{k}_0)\rangle$ into normal mode contributions, and using the correct complex mode frequencies, the signal $|\mathbf{A}^{(+)}(t)|^2$ is very close in form to the dynamical theory off-Bragg transform solution, $I_{\rm c}^{(T)}(t) = \exp(-\Gamma t)[J_1(\sqrt{4\Gamma_{\rm c} t})]^2/\Gamma_{\rm c} t$. This is illustrated in figure 27(a), for an $M = 10$ layer crystal, again with the incoherent processes turned off ($\Gamma_\alpha + \Gamma'_\gamma = 0$). The reason for the discrepancy is twofold: $I_{\rm c}^{(T)}(t)$ is a continuum approximation to a discrete problem, and, more importantly, the off-Bragg dynamical theory treatment is a single channel approximation which includes only forward scattering – i.e., only the $\mathbf{k}_{0+}$ channel is kept. The normal mode solution correctly accounts for the "back coupling" in the $\mathbf{k}_{0-}$ channel. As a consequence, $I_{\rm c}^{(T)}(t)$ is a poor approximation for a thin crystal, but the agreement becomes progressively better the larger the number of layers M.

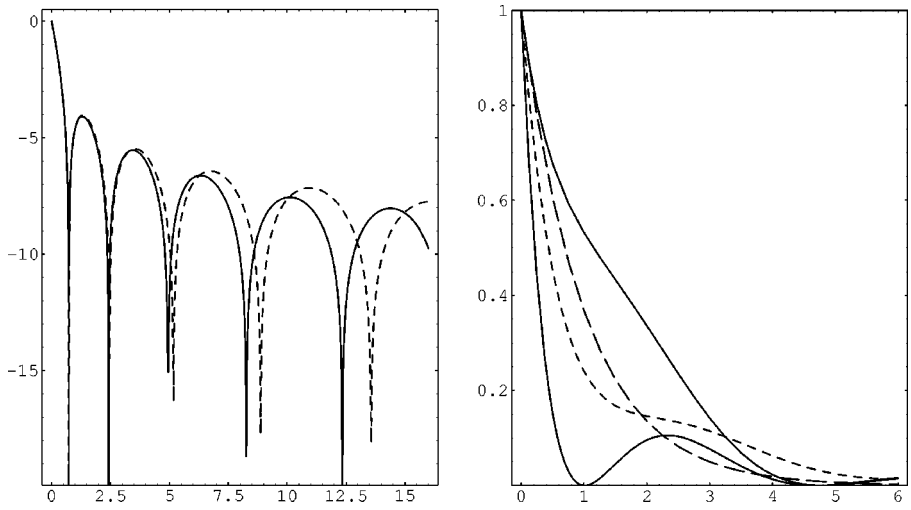

Figure 27. (a) Comparison of the exact normal mode solution (solid line) for $|\mathbf{A}^{(+)}(t)|^2$ for an off-Bragg exciton in an $M = 10$ layer crystal, and the approximate solution $\exp(-\Gamma t)[J_1(\sqrt{4\Gamma_c t})]^2/\Gamma_c t$ (dashed line). (b) The asymmetric probability distribution within the crystal for an off-Bragg exciton $|\psi_e(\mathbf{k}_0, t)\rangle$: the top solid line shows the relative probability $|Z_0(t)|^2$ that the top layer ($m = 0$) is excited at time t; the bottom solid line, the relative probability $|Z_{M-1}(t)|^2$ that the bottom layer ($m = M - 1$) is excited at t. The upper dashed line shows the free decay of a single plane. The lower dashed line shows the excitation probability $\langle\psi_e(\mathbf{k}_0, t)|\psi_e(\mathbf{k}_0, t)\rangle$. Here $M = 3$.

In figure 27(b), we show another very interesting feature of the off-Bragg solution, the asymmetric probability distribution within the crystal for an off-Bragg exciton $|\psi_e(\mathbf{k}_0, t)\rangle$. Here the top solid line shows the relative probability $|Z_0(t)|^2$ that the top layer ($m = 0$) is excited at time t; the bottom solid line, the relative probability $|Z_{M-1}(t)|^2$ that the bottom layer ($m = M - 1$) is excited at t. For a system of classical oscillators, the lines correspond to the total mechanical energy $\mathcal{E}(t)$ of oscillators in these planes. The upper dashed line shows the decay of an isolated single plane. The lower dashed line shows the excitation probability $\langle\psi_e(\mathbf{k}_0, t)|\psi_e(\mathbf{k}_0, t)\rangle$, as also shown in figure 26(b). Here we have taken $M = 3$. The first layer initially decays like an isolated single layer, but back reaction from the lower layers, although small, then slows the decay. The last layer, on the other hand, initially decays superradiantly, at the *Bragg decay rate*, $\Gamma_c = 2\pi n \lambda\!\!\!^{-2} l_\parallel \Gamma_{coh}$. Initially, the waves from all the "upstream" layers add constructively to act on the last layer, just as at Bragg. (In the Bragg case, *each* layer in the crystal sees the same enhanced field, and all layers decay superradiantly together.) As discussed in section 4.2.3, this marked asymmetry of the planar decay rates across the film can easily be detected by observing the incoherent resonant processes (conversion electrons, incoherently scattered γ-radiation, ...) occurring at different depths of the film.

Acknowledgement

Partial support for this work has been provided by the National Science Foundation under grant No. DMR-90-13058, and by the Welch Foundation under grant C-1049.

Appendix A

A.1. Electronic scattering

For X-ray scattering from the atomic electrons, the coherent elastic scattering amplitude (correct to second order in H_I) is given by [5,7,118]

$$f_{\mathrm{e}} = f_0 + f_{\mathrm{m}} + f_{\mathrm{r}}, \tag{A.1}$$

where f_0 is the Thomson contribution, f_{m} is the nonresonant magnetic scattering, and f_{r} is the resonance dispersion (or "anomalous") scattering contribution.

The Thomson scattering contribution is given by

$$f_0 = -r_0 f_{\mathrm{D}}(\mathbf{Q})\big\langle n(\mathbf{Q})\big\rangle \mathbf{e}_{\mathrm{f}}^{*} \cdot \mathbf{e}_0, \tag{A.2}$$

where $\mathbf{Q} = \mathbf{k}_0 - \mathbf{k}_{\mathrm{f}}$ is the momentum transfer, f_{D} is the Debye–Waller factor, and the form factor $\langle n(\mathbf{Q})\rangle$ is the ensemble average of the Fourier transform of the electron density,

$$\big\langle n(\mathbf{Q})\big\rangle = \sum_0 p_0 \left\langle \psi_0 \middle| \sum_j \exp(\mathrm{i}\mathbf{Q}\cdot\mathbf{r}_j) \middle| \psi_0 \right\rangle, \tag{A.3}$$

where $p_0(T)$ gives the statistical probabilities for the various possible initial states $|\psi_0\rangle$.

The nonresonant magnetic scattering contribution to the coherent elastic scattering can be expressed as

$$f_{\mathrm{m}} = \mathrm{i}\frac{\hbar\omega_0}{mc^2} r_0 f_{\mathrm{D}}(\mathbf{Q}) \left[\frac{1}{2}\big\langle L(\mathbf{Q})\big\rangle \cdot \mathbf{A}'' + \big\langle S(\mathbf{Q})\big\rangle \cdot \mathbf{B} \right], \tag{A.4}$$

where $\langle S(\mathbf{Q})\rangle$ and $\langle L(\mathbf{Q})\rangle$ are the ensemble averaged Fourier transforms of the spin and orbital magnetization densities,

$$\big\langle \mathbf{S}(\mathbf{Q})\big\rangle = \sum_0 p_0 \left\langle \psi_0 \middle| \sum_j \mathbf{s}_j \exp(\mathrm{i}\mathbf{Q}\cdot\mathbf{r}_j) \middle| \psi_0 \right\rangle, \tag{A.5}$$

$$\big\langle \mathbf{L}(\mathbf{Q})\big\rangle = \frac{1}{2}\sum_0 p_0 \left\langle \psi_0 \middle| \sum_j \big[f(\mathbf{Q}\cdot\mathbf{r}_j)\mathbf{l}_j + \mathbf{l}_j f(\mathbf{Q}\cdot\mathbf{r}_j) \big] \middle| \psi_0 \right\rangle, \tag{A.6}$$

where

$$f(x) = 2\sum_{n=0}^{\infty} \frac{(\mathrm{i}x)^n}{(n+2)n!}. \tag{A.7}$$

The polarization vectors are given by

$$\mathbf{B} = \big(\mathbf{e}_{\rm f}^* \times \mathbf{e}_0\big) + \big(\hat{\mathbf{k}}_{\rm f} \times \mathbf{e}_{\rm f}^*\big)\big(\hat{\mathbf{k}}_{\rm f} \cdot \mathbf{e}_0\big) - \big(\hat{\mathbf{k}}_0 \times \mathbf{e}_0\big)\big(\hat{\mathbf{k}}_0 \cdot \mathbf{e}_{\rm f}^*\big) - \big(\hat{\mathbf{k}}_{\rm f} \times \mathbf{e}_{\rm f}^*\big) \times \big(\hat{\mathbf{k}}_0 \times \mathbf{e}_0\big), \tag{A.8}$$

$$\mathbf{A}'' = \mathbf{A}' - \big(\mathbf{A}' \cdot \widehat{\mathbf{Q}}\big)\widehat{\mathbf{Q}}, \tag{A.9}$$

where

$$\mathbf{A}' = -4\big(\mathbf{e}_{\rm f}^* \times \mathbf{e}_0\big)\sin^2\theta, \tag{A.10}$$

with θ the scattering angle.

Finally, the resonance dispersion contribution to the coherent elastic scattering amplitude is

$$f_r = 2\pi\lambda f_{\rm D}(\mathbf{Q}) \sum_0 p_0 \sum_I \frac{1}{\lambda_{I0}} \left[\frac{\langle\psi_0|\mathbf{J}(-\mathbf{k}_{\rm f})\cdot\mathbf{e}_{\rm f}^*|I\rangle\langle I|\mathbf{J}(\mathbf{k}_0)\cdot\mathbf{e}_0|\psi_0\rangle}{E_I - E_0 - \hbar\omega - i\Gamma_I/2} - \frac{\langle\psi_0|\mathbf{J}(\mathbf{k}_0)\cdot\mathbf{e}_0|I\rangle\langle I|\mathbf{J}(-\mathbf{k}_{\rm f})\cdot\mathbf{e}_{\rm f}^*|\psi_0\rangle}{E_I - E_0 + \hbar\omega} \right], \tag{A.11}$$

where $\mathbf{J}(\mathbf{k}) = c^{-1}\int \mathrm{d}\mathbf{x}\, \mathrm{e}^{\mathrm{i}\mathbf{k}\cdot\mathbf{x}}\mathbf{J}(\mathbf{x})$ is the Fourier transform of the current density operator given by

$$\mathbf{J}(\mathbf{k})\cdot\mathbf{e} = \frac{e}{mc}\sum_j \mathbf{e}\cdot\big[\mathbf{p}_j + \mathrm{i}\hbar(\mathbf{s}_j \times \mathbf{k})\big]\exp(\mathrm{i}\mathbf{k}\cdot\mathbf{r}_j). \tag{A.12}$$

In all cases the appropriate phonon factor is the Debye–Waller factor. This is an immediate result for all nonresonant contributions, but also holds to good approximation for resonant X-ray scattering because the resonance widths Γ_I, typically ≈eV, are large compared to vibrational energies ε, typically ≈0.01 eV (hence, resonant X-ray scattering is a fast process, $\hbar/\Gamma_I \approx 10^{-16}$ s, compared to vibrational times, $\hbar/\varepsilon \approx 10^{-14}$ s).

A.1.1. Isotropic limit

For many cases the Mössbauer frequency is large in comparison to the atomic absorption edges. For example, for ^{57}Fe, the Mössbauer resonance energy is $\hbar\omega =$ 14.4 keV, while the highest energy atomic edges are K = 7.1 keV, $\mathrm{L}_1 = 0.85$ keV, $\mathrm{L}_2 = 0.79$ keV and $\mathrm{L}_3 = 0.78$ keV. In situations like this, where the frequency of the radiation is large compared to any of the atomic absorption edge frequencies, the dominant real contribution to the scattering amplitude f is the Thomson contribution f_0, and the dominant imaginary contribution comes from the photoelectric poles in the sum over intermediate states in $f_{\rm r}$ corresponding to photoemission of electrons from the various shells. In this limit, the coherent elastic X-ray scattering amplitude is given to good approximation by

$$f_{\rm e} = \mathbf{e}_{\rm f}^* \cdot \mathbf{e}_0 f_{\rm D}(\mathbf{Q})\left[-\big\langle n(\mathbf{Q})\big\rangle r_0 + \mathrm{i}\frac{\sigma_{\rm e}}{4\pi\lambda}\right], \tag{A.13}$$

where $\sigma_{\rm e}(\omega)$ is the photoelectric cross-section at the frequency ω, arising primarily from the tightly bound K- and L-shell electrons (so the form factor for scattering is near unity). In this approximation the polarization response is that of an isotropic electric dipole oscillator and gives no polarization mixing.

For frequencies near an atomic absorption edge however, the response is generally much more complex and interesting, with strong anisotropic scattering sensitive to the directions of the local fields (**B** and EFG).

A.1.2. Multipole expansion for the resonance dispersion contribution $f_{\rm r}$

Near absorption edges, very large resonant enhancements to the magnetic sensitive X-ray scattering occur, with amplitudes ranging from $0.1r_0$ to $100r_0$ [3,6,116]. This strongly enhanced "magnetic" X-ray scattering is actually electric multipole resonance scattering with the magnetic sensitivity arising from the effects of exchange and spin–orbit correlation [3]. To treat these interesting cases, it is necessary to make a multipole expansion of the currents in $f_{\rm r}$. The multipole development given here carries over directly for the nuclear resonant scattering amplitudes.

The interaction current $\mathbf{J}(\mathbf{k})\cdot\mathbf{e}$, given by eq. (A.12), can be expanded in multipole contributions following the standard treatments [8],

$$\mathbf{J}(\mathbf{k})\cdot\mathbf{e} = \sum_{q={\rm e,m}}\sum_{LM} J^{(q)}_{LM}\mathbf{Y}^{(q)*}_{LM}\big(\hat{k}\big)\cdot\mathbf{e}, \tag{A.14}$$

where $q =$ e or m designates an electric or magnetic multipole; $L = 1, 2, \ldots$ gives the order of the multipole, and the azimuthal index $M = -L, -L+1, \ldots, L$. The multipole moment operator $J^{(q)}_{LM}$ for the QL multipole ($Q =$ E or M) is a spherical tensor operator of order L given by

$$J^{\rm (e,m)}_{LM} = -\frac{4\pi {\rm i}^L k^L}{(2L+1)!!}\sqrt{\frac{L+1}{L}}\,Q^{\rm (e,m)}_{LM}. \tag{A.15}$$

For an electric 2^L-pole,

$$Q^{\rm (e)}_{LM} = E_{LM} + E_{LM}(s). \tag{A.16}$$

E_L and $E_L(s)$ denote, respectively, the charge and spin contributions of parity $(-1)^L$, leading to electric radiation, which to lowest order in r are given by

$$E_{LM} = \sum_j \big[e r_j^L Y_{LM}\big(\hat{r}_j\big)\big], \tag{A.17}$$

$$E_{LM}(s) = \frac{\hbar\omega}{mc^2}\sum_j \left\{ e\mathbf{l}_j\big[r_j^L Y_{LM}\big(\hat{r}_j\big)\big]\cdot\frac{\mathbf{s}_j}{L+1}\right\}. \tag{A.18}$$

For a magnetic 2^L-pole,

$$Q^{(\mathrm{m})}_{LM} \equiv M_{LM} = 2\mu_{\mathrm{B}} \sum_j \left\{ \nabla_j \left[r_j^L Y_{LM}(\hat{r}_j) \right] \cdot \left[\frac{\mathbf{l}_j}{(L+1)} + \mathbf{s}_j \right] \right\}, \tag{A.19}$$

where $\mu_{\mathrm{B}} = e\hbar/2mc$ is the Bohr magneton.

The vector spherical harmonics which enter eq. (A.14) are defined as

$$\mathbf{Y}^{(\mathrm{e})}_{LM}(\hat{k}) = \frac{1}{\sqrt{L(L+1)}} \nabla_k Y_{LM}(\hat{k}), \tag{A.20}$$

$$\mathbf{Y}^{(\mathrm{m})}_{LM}(\hat{k}) = \hat{k} \times \nabla_k Y_{LM}(\hat{k}). \tag{A.21}$$

For the spherical harmonics Y_{LM} we use the conventions of Rose [117]. For reference we give the explicit forms of the vector spherical harmonics $\mathbf{Y}^{(q)}_{LM}(\hat{k})$ for E1, M1, and E2 transitions: for E1,

$$\mathbf{Y}^{(\mathrm{e})}_{10} = -\sqrt{\frac{3}{8\pi}} \sin(\theta)\mathbf{e}_\theta, \qquad \mathbf{Y}^{(\mathrm{e})}_{1\pm1} = \sqrt{\frac{3}{16\pi}} \mathrm{e}^{\pm \mathrm{i}\phi} \left[\mp \cos(\theta)\mathbf{e}_\theta - \mathrm{i}\mathbf{e}_\phi \right]. \tag{A.22}$$

Here $\mathbf{e}_\theta$ and $\mathbf{e}_\phi$ are the usual spherical polar unit vectors, and θ and ϕ are the polar and axial angles specifying the photon direction $\mathbf{k}$, with the z axis coinciding with the quantization axis $\mathbf{z}_J$ determined by the direction of the internal field at the nucleus. For an M1 transition,

$$\mathbf{Y}^{(\mathrm{m})}_{10} = \mathrm{i}\sqrt{\frac{3}{8\pi}} \sin(\theta)\mathbf{e}_\phi, \qquad \mathbf{Y}^{(\mathrm{m})}_{1\pm1} = \sqrt{\frac{3}{16\pi}} \mathrm{e}^{\pm \mathrm{i}\phi} \left[\mathbf{e}_\theta \pm \mathrm{i}\cos(\theta)\mathbf{e}_\phi \right], \tag{A.23}$$

and for an E2 transition,

$$\begin{aligned} \mathbf{Y}^{(\mathrm{e})}_{20} &= -\sqrt{\frac{15}{32\pi}} \sin(2\theta)\mathbf{e}_\theta, \\ \mathbf{Y}^{(\mathrm{e})}_{2\pm1} &= \sqrt{\frac{5}{16\pi}} \mathrm{e}^{\pm \mathrm{i}\phi} \left[\mp \cos(2\theta)\mathbf{e}_\theta - \mathrm{i}\cos(\theta)\mathbf{e}_\phi \right], \\ \mathbf{Y}^{(\mathrm{e})}_{2\pm2} &= \sqrt{\frac{5}{16\pi}} \mathrm{e}^{\pm \mathrm{i}2\phi} \left[(1/2)\sin(2\theta)\mathbf{e}_\theta \pm \mathrm{i}\sin(\theta)\mathbf{e}_\phi \right]. \end{aligned} \tag{A.24}$$

The polarization dependence for the QL multipole of the current expansion (A.14) is determined by the Lth rank spherical tensor,

$$T^{(q)}_{LM}(\mathbf{e}, \hat{k}) = \mathbf{e}^* \cdot \mathbf{Y}^{(q)}_{LM}(\hat{k}), \tag{A.25}$$

made up of the vectors $\mathbf{e}$ and $\hat{k}$, and being linear in the components of $\mathbf{e}$. For an EL transition, this is expressed as products of the components of $\mathbf{e}$ and $\hat{k}$ by

$$\mathbf{e}^* \cdot \mathbf{Y}^{(\mathrm{e})}_{LM}(\hat{k}) = \sqrt{\frac{4\pi(2L+1)}{3(L+1)}} \sum_{\mu=-1}^{+1} C(1, L-1, L; \mu, M-\mu, M) Y_{L-1,M-\mu}(\hat{k}) Y_{1\mu}(\mathbf{e}). \tag{A.26}$$

For an ML transition, the polarization factor is

$$\mathbf{e}^* \cdot \mathbf{Y}^{(\mathrm{m})}_{LM}(\hat{k}) = \sqrt{\frac{4\pi(2L+1)}{3(L+1)}} \sum_{\mu=-1}^{+1} C(1, L-1, L; \mu, M-\mu, M) Y_{L-1,M-\mu}(\hat{k}) Y_{1\mu}(\mathbf{b}), \tag{A.27}$$

where $\mathbf{b} = \hat{k} \times \mathbf{e}$ is the B-vector of the radiation field. Alternatively, using the circularly polarized bases $\mathbf{e}_\mu$ ($\mu = \pm 1$) transverse to $\hat{k}$, the polarization factors are given in terms of the rotation matrices $D^{(L)}_{\mu M}$ by

$$\mathbf{e}^*_\mu \cdot \mathbf{Y}^{(\mathrm{e})}_{LM}(\hat{k}) = \sqrt{\frac{2L+1}{8\pi}} D^{(L)}_{\mu M}(\hat{k}), \tag{A.28}$$

$$\mathbf{e}^*_\mu \cdot \mathbf{Y}^{(\mathrm{m})}_{LM}(\hat{k}) = (\mu) \sqrt{\frac{2L+1}{8\pi}} D^{(L)}_{\mu M}(\hat{k}). \tag{A.29}$$

Using the current multipole expansion, f_r is then given by

$$f_\mathrm{r} = 4\pi\lambda \sum_{q'L'M'} \sum_{qLM} \left[\mathbf{e}^*_\mathrm{f} \cdot \mathbf{Y}^{(q')}_{L'M'}(\hat{k}_\mathrm{f})\right] \left[\mathbf{Y}^{(q)*}_{LM}(\hat{k}_0) \cdot \mathbf{e}_0\right] F^{(q'q)}_{L'M';LM}, \tag{A.30}$$

where

$$F^{(q'q)}_{L'M';LM} = f_\mathrm{D}(\mathbf{Q}) \sum_0 p_0 \sum_I \frac{1}{\lambda_{I0}} \left[\frac{\langle\psi_0|J^{(q')\dagger}_{L'M'}|I\rangle\langle I|J^{(q)}_{LM}|\psi_0\rangle}{E_I - E_0 - \hbar\omega - \mathrm{i}\Gamma_I/2} - \frac{\langle\psi_0|J^{(q)}_{LM}|I\rangle\langle I|J^{(q')\dagger}_{L'M'}|\psi_0\rangle}{E_I - E_0 + \hbar\omega} \right]. \tag{A.31}$$

This result is still a completely general expression for f_r. An important point to note is that the dependence on the photon polarizations $\mathbf{e}_0$ and $\mathbf{e}^*_\mathrm{f}$ and the photon directions $\hat{k}_0$ and $\hat{k}_\mathrm{f}$, given by the factor $[\mathbf{e}^*_\mathrm{f} \cdot \mathbf{Y}^{(q')}_{L'M'}(\hat{k}_\mathrm{f})][\mathbf{Y}^{(q)}_{LM}(\hat{k}_0) \cdot \mathbf{e}_0]$, has now been separated out from the current matrix elements and frequency response given by the factor $F^{(q'q)}_{L'M';LM}$. The polarization dependence gives an important "handle" for analyzing scattering experiments.

In most situations, a near resonant transition is a pure multipole transition, so $q' = q$ and $L' = L$. Due to crystal field effects however (local symmetry, bonding orbitals, ...), J_z is generally not conseved, and it is possible to have $M' \neq M$.

A.1.3. QL-multipole transition with $M' = M$

An important special case is coherent elastic scattering from a pure multipole transition with $M' = M$. This will be the situation when crystal field effects can be ignored, and even in the presence of crystal fields, this condition will often hold (e.g., E1 or M1 transitions in a cubic symmetry field). The resonance contribution is then

$$f_{QL} = 4\pi\lambda \sum_{qLM} \left[\mathbf{e}^*_\mathrm{f} \cdot \mathbf{Y}^{(q)}_{LM}(\hat{k}_\mathrm{f})\right] \left[\mathbf{Y}^{(q)*}_{LM}(\hat{k}_0) \cdot \mathbf{e}_0\right] F^{(q)}_{LM}, \tag{A.32}$$

where $F_{LM}^{(q)} = F_{LM;LM}^{(qq)}$ as given by eq. (A.31), where now the sum over intermediate states is just over the near resonant excited state sublevels.

As noted in section 2.4, the polarization response $[\mathbf{e}_\mathrm{f}^* \cdot \mathbf{Y}_{LM}^{(q)}(\hat{k}_\mathrm{f})\mathbf{Y}_{LM}^{(q)}(\hat{k}_0)^* \cdot \mathbf{e}_0]$ is precisely the polarization response of a qL, $\Delta J_z = M$ *classical oscillator*. Furthermore, the overall form of the polarization response is dictated by symmetry considerations and can depend only on $\mathbf{e}_0$, $\mathbf{k}_0$, $\mathbf{e}_\mathrm{f}^*$, $\mathbf{k}_\mathrm{f}$ and the local quantization axis $\mathbf{z}_J$, since these are the only defined directions in the scattering (in the absence of crystal fields). For a QL transition, the explicit $\mathbf{Y}_{LM}^{(q)}$ expressions give the scattering amplitude [3]

$$f_{QL} = \sum_{l=0}^{2L} A_l(\omega) P_l\big(\mathbf{e}_\mathrm{f}^* \mathbf{k}_\mathrm{f}; \mathbf{e}_0 \mathbf{k}_0; \mathbf{z}_J\big), \tag{A.33}$$

where the polarization factors P_l contain $\mathbf{z}_J$ to the lth power, and the amplitudes A_l are combinations of the $F_{LM}^{(q)}$.

For $E1$ *transitions*, the polarization factors are

$$P_l = \begin{cases} \mathbf{e}_\mathrm{f}^* \cdot \mathbf{e}_0, & l = 0, \\ -\mathrm{i}\big(\mathbf{e}_\mathrm{f}^* \times \mathbf{e}_0\big) \cdot \mathbf{z}_J, & l = 1, \\ \big(\mathbf{e}_\mathrm{f}^* \cdot \mathbf{z}_J\big)(\mathbf{e}_0 \cdot \mathbf{z}_J), & l = 2, \end{cases} \tag{A.34}$$

and the corresponding resonant amplitudes are

$$A_l = \frac{3}{16\pi} \begin{cases} F_{11}^{(\mathrm{e})} + F_{1-1}^{(\mathrm{e})}, & l = 0, \\ F_{11}^{(\mathrm{e})} - F_{1-1}^{(\mathrm{e})}, & l = 1, \\ 2F_{10}^{(\mathrm{e})} - F_{11}^{(\mathrm{e})} - F_{1-1}^{(\mathrm{e})}, & l = 2. \end{cases} \tag{A.35}$$

For a *magnetic dipole transition* (M1), the P_l are given by (A.34) with the E-polarization vectors $\mathbf{e}$ replaced by the B-polarization vectors $\mathbf{b} = \hat{\mathbf{k}} \times \mathbf{e}$, and the A_l are given by (A.35) with the $F_{1M}^{(\mathrm{e})}$ replaced by the $F_{1M}^{(\mathrm{m})}$.

For an $E2$ *transition*, the polarization factors are

$$P_l = \begin{cases} \big(\hat{\mathbf{k}}_\mathrm{f} \cdot \hat{\mathbf{k}}_0\big)\big(\mathbf{e}_\mathrm{f}^* \cdot \mathbf{e}_0\big) + \big[\mathbf{e}_0 \leftrightarrow \hat{\mathbf{k}}_0\big], & l = 0, \\ -\mathrm{i}\big(\hat{\mathbf{k}}_\mathrm{f} \cdot \hat{\mathbf{k}}_0\big)\big(\mathbf{e}_\mathrm{f}^* \times \mathbf{e}_0\big) \cdot \mathbf{z}_J + \big[\mathbf{e}_0 \leftrightarrow \hat{\mathbf{k}}_0\big] & \\ \quad + \big[\mathbf{e}_\mathrm{f}^* \leftrightarrow \hat{\mathbf{k}}_\mathrm{f}\big] + \big[\mathbf{e}_0 \leftrightarrow \hat{\mathbf{k}}_0, \mathbf{e}_\mathrm{f}^* \leftrightarrow \hat{\mathbf{k}}_\mathrm{f}\big], & l = 1, \\ \big(\hat{\mathbf{k}}_\mathrm{f} \cdot \hat{\mathbf{k}}_0\big)\big(\mathbf{e}_\mathrm{f}^* \cdot \mathbf{z}_J\big)\big(\mathbf{e}_0 \cdot \mathbf{z}_J\big) + \big[\mathbf{e}_0 \leftrightarrow \hat{\mathbf{k}}_0\big] & \\ \quad + \big[\mathbf{e}_\mathrm{f}^* \leftrightarrow \hat{\mathbf{k}}_\mathrm{f}\big] + \big[\mathbf{e}_0 \leftrightarrow \hat{\mathbf{k}}_0, \mathbf{e}_\mathrm{f}^* \leftrightarrow \hat{\mathbf{k}}_\mathrm{f}\big], & l = 2, \\ -\mathrm{i}\big(\hat{\mathbf{k}}_\mathrm{f} \cdot \mathbf{z}_J\big)\big(\hat{\mathbf{k}}_0 \cdot \mathbf{z}_J\big)\big(\mathbf{e}_\mathrm{f}^* \times \mathbf{e}_0\big) \cdot \mathbf{z}_J + \big[\mathbf{e}_0 \leftrightarrow \hat{\mathbf{k}}_0\big] & \\ \quad + \big[\mathbf{e}_\mathrm{f}^* \leftrightarrow \hat{\mathbf{k}}_\mathrm{f}\big] + \big[\mathbf{e}_0 \leftrightarrow \hat{\mathbf{k}}_0, \mathbf{e}_\mathrm{f}^* \leftrightarrow \hat{\mathbf{k}}_\mathrm{f}\big], & l = 3, \\ \big(\hat{\mathbf{k}}_\mathrm{f} \cdot \mathbf{z}_J\big)\big(\hat{\mathbf{k}}_0 \cdot \mathbf{z}_J\big)\big(\mathbf{e}_\mathrm{f}^* \cdot \mathbf{z}_J\big)\big(\mathbf{e}_0 \cdot \mathbf{z}_J\big), & l = 4. \end{cases} \tag{A.36}$$

The corresponding resonant amplitudes are

$$A_l = \frac{5}{16\pi}\begin{cases} F^{(\mathrm{e})}_{22} + F^{(\mathrm{e})}_{2-2}, & l=0,\\ \frac{1}{2}\big(F^{(\mathrm{e})}_{22} - F^{(\mathrm{e})}_{2-2}\big), & l=1,\\ \big(F^{(\mathrm{e})}_{21} + F^{(\mathrm{e})}_{2-1}\big) - \big(F^{(\mathrm{e})}_{22} + F^{(\mathrm{e})}_{2-2}\big), & l=2,\\ \frac{1}{2}\big[2\big(F^{(\mathrm{e})}_{21} - F^{(\mathrm{e})}_{2-1}\big) - \big(F^{(\mathrm{e})}_{22} - F^{(\mathrm{e})}_{2-2}\big)\big], & l=3,\\ 6F^{(\mathrm{e})}_{20} - 4\big(F^{(\mathrm{e})}_{21} + F^{(\mathrm{e})}_{2-1}\big) + \big(F^{(\mathrm{e})}_{22} + F^{(\mathrm{e})}_{2-2}\big), & l=4. \end{cases} \tag{A.37}$$

In a spiral antiferromagnet, each order $l > 0$ will give rise to a distinct magnetic satellite about the central Bragg peak [3]. The appearance of two harmonic satellites is a characteristic signature of a dipole resonance (E1 or M1). The first order E1 harmonic does not allow $\sigma \to \sigma$ scattering, while the first order M1 harmonic does not allow $\pi \to \pi$ scattering. Quadrupole resonances (E2 or M2) will have four harmonics, and, generally, allow all the possible combinations of $\sigma \to \sigma, \pi$ and $\pi \to \pi, \sigma$ scattering.

A.1.4. Effective spin-orbital operators and quasi-elastic resonant scattering

The expressions (A.33)–(A.37) are useful for determining the local magnetic field direction, but are not in a useful form for relating the observed scattering cross-sections to the expected moments $\langle \mathbf{L}\rangle$, $\langle \mathbf{S}\rangle, \ldots$ of the valence shell being probed. This information is available though: As shown by Luo et al. [5,6], for the important case of quasi-elastic scattering, if the "fast collision" approximation can be made, then indeed there is a simple relation between the scattering and the spin-orbital moments. For a pure EL transition, the scattering amplitude (A.30) becomes

$$f_{\mathrm{r}} = 4\pi\lambda \sum_{k=0}^{2L} \sum_{q=-k}^{k} m_k T^{(k)*}_q \big(\mathbf{e}^*_{\mathrm{f}} \hat{k}_{\mathrm{f}} \mathbf{e}_0 \hat{k}_0\big)_{\mathrm{E}L} \big\langle \psi_{\mathrm{f}} \big| M^{(k)}_q(\mathbf{l}_i, \mathbf{s}_i) \big| \psi_0 \big\rangle, \tag{A.38}$$

where the $M^{(k)}_q(\mathbf{l}_i, \mathbf{s}_i)$ are kth rank spin-orbital multipole moments depending only on the $\mathbf{l}_i$ and $\mathbf{s}_i$ operators of the valence electrons for the valence shell involved in the resonance, with each contribution $M^{(k)}_q(\mathbf{l}_i, \mathbf{s}_i)$ having a distinct polarization and wave vector dependence $T^{(k)*}_q(\mathbf{e}^*_{\mathrm{f}} \hat{k}_{\mathrm{f}} \mathbf{e}_0 \hat{k}_0)$. The factor m_k contains products of Clebsch–Gordan coefficients, a squared radial matrix element for the transition involved, and a complex resonance denominator. Thus, for an E1 transition, the scattering amplitude operator contains up to quadrupole spin-orbital moments, and for an E2 transition up to hexadecapole moments. The odd moments are odd under time reversal T and, hence, purely magnetic, while the even-order moments are even under T, and include the charge multipole moments (giving nonmagnetic Templeton effects).

"Quasi-elastic" resonant scattering means that after the scattering, the total number of valence electrons in the final state is the same as that of the initial state, but the two states may have different quantum numbers (e.g., different $L, S, J, \ldots$). Quasi-

elastic resonant scattering includes elastic scattering ($|\psi_{\rm f}\rangle = |\psi_0\rangle$) as well as spin-wave and higher multipole-wave excitations.

The "fast collision" approximation means that the collision time $T = |\Delta\omega - {\rm i}\Gamma/2\hbar|^{-1}$ is short compared to $\hbar/\Delta E_I$, the time scale over which the torques exerted amongst the core hole and the intermediate state valence electrons affect the evolution of the intermediate state. Here $\hbar\Delta\omega = E_I - E_0 - \hbar\omega$ is the deviation of the incident radiation from resonance, and ΔE_I is the spread of the intermediate levels E_I. Under this condition, the spread ΔE_I can be ignored, and there is a single resonance denominator for the transition. We note that, even if $\Gamma \leqslant \Delta E_I$, the fast collision approximation can be assured by simply tuning off-resonance several ΔE_I.

The polarization factors $T_q^{(k)*}(\mathbf{e}_{\rm f}^*\hat{k}_{\rm f}\mathbf{e}_0\hat{k}_0)$ are the spherical tensors made by coupling $\mathbf{e}_0\cdot\mathbf{Y}_{LM}^{(e)*}(\hat{k}_0)$ and $\mathbf{e}_{\rm f}^*\cdot\mathbf{Y}_{LM'}^{(e)}(\hat{k}_{\rm f})$. For an $E1$ transition, $T_0^{(0)} \propto \mathbf{e}_{\rm f}^*\cdot\mathbf{e}_0$, $\mathbf{T}^{(1)} \propto \mathbf{e}_{\rm f}^*\times\mathbf{e}_0$, and the $T_q^{(2)}$ ($q = -2,\ldots,+2$) are the second rank tensors made up from products of $\mathbf{e}_{\rm f}^*$ and $\mathbf{e}_0$.

The expressions for the spin-orbital multipole moment operators $M_q^{(k)}(\mathbf{l}_i,\mathbf{s}_i)$ are given by Luo [6,5]. If total **L**, **S** are conserved for the valence shell being probed (for the ground state and low lying excitations), then the operators can be expressed in terms of **L** and **S**, $M_q^{(k)} = M_q^{(k)}(\mathbf{L},\mathbf{S})$. The simplest situation occurs for quasi-elastic scattering within a manifold of good total **J**, in which case $M_q^{(k)} = M_q^{(k)}(\mathbf{J}) \propto T_q^{(k)}(\mathbf{J})$, the kth order spherical tensor obtained from **J**. This is often a good approximation for transitions to the 4f valence shell of rare earth ions. For an E1 transition, such as the $3d_{3/2,5/2} \rightarrow 4f$ transitions at the M_4 and M_5 edges, the vector part of the effective scattering operator is $\propto (\mathbf{e}_{\rm f}^*\times\mathbf{e}_0)\cdot\mathbf{J}$, and the quadrupole part is $\propto T_{-q}^{(2)}(\mathbf{e}_{\rm f}^*\otimes\mathbf{e}_0)T_q^{(2)}(\mathbf{J})$. The expressions for $M_q^{(k)}(\mathbf{L},\mathbf{S})$ and $M_q^{(k)}(\mathbf{J})$ have been worked out by Hu [118].

The simple relation between $f_{\rm r}$ and the spin-orbital operators $M_q^{(k)}(\mathbf{l}_i,\mathbf{s}_i)$ is of considerable importance for the interpretation of resonant X-ray scattering experiments. The coherent elastic scattering gives sharp Bragg peaks and satellites which measure the long range order of the thermal expectation values of these moments, and the diffuse inelastic scattering gives information about coherent and incoherent excitations, and short range correlations.

Of particular interest, below the ordering temperature T_N, the inelastic resonant scattering can determine the dispersion curves $\omega(\mathbf{q})$ for spin wave excitations, just as for inelastic neutron scattering, but moreover, because of the higher spin-orbital moments entering $f_{\rm r}$, the inelastic resonant X-ray scattering couples to quite new types of spin-charge wave excitations – quadrupolar, octupolar, and hexadecupolar waves.

Just above T_N, the frequency integrated diffuse critical scattering depends upon the instantaneous moment–moment correlations $\langle M_q^{(k)\dagger}(i)M_q^{(k)}(j)\rangle$ between the ith and jth sites. This includes the short range spin–spin correlations $\langle\mathbf{s}_i\mathbf{s}_j\rangle$, just as for neutron scattering, but also gives quite new information about the correlations of higher order moments above T_N.

A.2. Resonant nuclear scattering

For the sharp resonant γ-ray scattering by the nucleus, the coherent elastic scattering amplitude is

$$f_{\rm n} = f_M \sum_0 p_0 \sum_I \left[\frac{\langle\psi_0|\mathbf{J}(-\mathbf{k}_{\rm f})\cdot\mathbf{e}_{\rm f}^*|\psi_I\rangle\langle\psi_I|\mathbf{J}(\mathbf{k}_0)\cdot\mathbf{e}_0|\psi_0\rangle}{E_I - E_0 - \hbar\omega - {\rm i}\Gamma_I/2} \right], \tag{A.39}$$

where **J**(**k**) is the Fourier transform of the nuclear current density operator and $f_{\rm M}$ is the Mössbauer phonon factor. Here ψ represents the state of the crystal, excluding the vibrational state, and E represents its energy (e.g., ψ includes the magnetic state of the crystal and the internal state of the nucleus). Finally, Γ_I is the total width of the excited state ψ_I, including the radiation width Γ_γ and the internal conversion width Γ_α.

In the fast relaxation cases (relaxation times very much smaller than the nuclear Larmor precession times $\tau_{\rm L}$), we may take ψ and E in eq. (A.39) as the state and energy of the nucleus i in the external fields and the "static effective fields" of the surrounding medium. Similarly, in the slow relaxation limit, ψ and E may be taken as the state and energy of the *atom* i, but unless the hyperfine energy is negligible relative to the electronic Larmor frequency, one can no longer consider the transitions between nuclear states in an effective field but must allow for the dynamic effects of the nucleus plus atomic electrons as a coupled quantum-mechanical system. The modifications necessary when the relaxation times are on the order of $\tau_{\rm L}$ are discussed briefly in section A.2.5.

The usual situation is the fast relaxation limit. The states ψ_0 and energies E_0 are then the hyperfine levels of the nuclear ground state, produced by the interaction of the ground state magnetic dipole moment of the nucleus with the effective magnetic field $\mathbf{B}_{\rm int}$ arising from the s-electron density at the origin, and the coupling of the quadrupole moment of the nucleus in the ground state with the electric field gradient (EFG). Similarly, the ψ_I and E_I are the hyperfine levels of the excited state of the nucleus involved in the Mössbauer transition. The ground and excited states will be states of good angular momentum, j_0 and j_1, but J_z need not be conserved. Because the ground state hyperfine splittings are typically $\approx 10^{-8}$ eV $\approx 10^{-4}$ K, the initial state is normally equally likely to be in any of the $(2j_0+1)$ hyperfine substates, and $p_0 = C/(2j_0+1)$, where C is the enrichment fraction for the Mössbauer isotope.

A.2.1. Coaxial **B** *and EFG*

If the effective fields acting on the nucleus have a common axis of symmetry ($\hat{z}$), then the ground and excited nuclear states are states of good J_z.

Mössbauer transitions occur with well-defined multipolarity E1, M1, E2, and in a few cases, M1–E2. The multipole expansion of the Fourier transform nuclear current density **J**(**k**) is given by (A.14). The matrix elements of the current multipole moment operator $J^{(q)}_{LM}$ are evaluated in terms of the radiative width $\Gamma_\gamma(QL)$, i.e., the width associated with the emission of (QL)-multipole radiation. (The ratio of the radiative

widths gives the mixing ratio δ^2, i.e., $\delta^2(\mathrm{E2/M1}) = \Gamma_\gamma(\mathrm{E2})/\Gamma_\gamma(\mathrm{M1})$.) Denoting the spin of the states explicitly, $|\psi_0\rangle = |a, J_0, m_0\rangle$ and $|\psi_I\rangle = |n, J_1, m_1\rangle$, we have

$$\langle\psi_0|J^{(q)\dagger}_{LM}|\psi_I\rangle = C(j_0 L j_1; m_0 M m_1)|\chi(QL)|\mathrm{e}^{\mathrm{i}\eta(QL)}, \tag{A.40}$$

where $\chi(QL)$ is the reduced matrix element (for emission). Substituting (A.14) into the width expression

$$\Gamma_\gamma = \lambda_0^{-1}\sum_{\mathbf{e}}\sum_{m_0}\int \mathrm{d}\Omega_k|\langle\psi_0|\mathbf{J}(-\mathbf{k})\cdot\mathbf{e}^*|\psi_I\rangle|^2, \tag{A.41}$$

we obtain

$$|\chi(QL)| = \sqrt{\lambda_0\Gamma_\gamma(QL)}. \tag{A.42}$$

The phase $\eta(QL)$ of the reduced matrix element is only important for mixed multipole transitions. For such transitions, Lloyd has shown that if T invariance is valid for γ emission/absorption, then $\eta(QL) - \eta(Q'L') = 0$ or π [119].

For a pure QL Mössbauer transition with conserved J_z, the coherent elastic scattering amplitude is

$$f_\mathrm{n} = 4\pi\lambda\sum_{M=-L}^{L}\left[\mathbf{e}^*_\mathrm{f}\cdot\mathbf{Y}^{(q)}_{LM}(\hat{k}_\mathrm{f})\right]\left[\mathbf{Y}^{(q)*}_{LM}(\hat{k}_0)\cdot\mathbf{e}_0\right]F^{(q)}_{LM}(\omega), \tag{A.43}$$

where now $F^{(q)}_{LM}$ is given by

$$F^{(q)}_{LM}(\omega) = \frac{C f_\mathrm{M}}{2j_0+1}\frac{\Gamma_\gamma}{\Gamma}\sum_{m_0=-j_0}^{j_0}\frac{C(j_0 L j_1; m_0 M)^2}{x(m_0 M) - \mathrm{i}}, \tag{A.44}$$

with $x(m_0M) = 2[E(j_1; m_0+M) - E(j_0; m_0) - \hbar\omega]/\Gamma$. Alternatively, we can express f_n as

$$f_\mathrm{n} = \sum_{l=0}^{2L} A_l(\omega) P_l\left(\mathbf{e}^*_\mathrm{f}\mathbf{k}_\mathrm{f}; \mathbf{e}_0\mathbf{k}_0; \mathbf{z}_J\right), \tag{A.45}$$

where the amplitude factors A_l and the polarization factors P_l are given by eqs. (A.34)–(A.37) for E1, M1 and E2 transitions, with the $F^{(q)}_{LM}$ now given by eq. (A.44).

For a mixed M1–E2 transition,

$$f_\mathrm{n} = 4\pi\lambda\sum_{q'L'}\sum_{qLM}\left[\mathbf{e}^*_\mathrm{f}\cdot\mathbf{Y}^{(q')}_{L'M}(\hat{k}_\mathrm{f})\right]\left[\mathbf{Y}^{(q)*}_{LM}(\hat{k}_0)\cdot\mathbf{e}_0\right]F^{(q'q)}_{L'M;LM}, \tag{A.46}$$

where

$$F^{(q'q)}_{L'M;LM} = \frac{Cf_{\mathrm{M}}}{(2j_0+1)} \mathrm{e}^{\mathrm{i}[\eta(Q'L')-\eta(QL)]} \frac{\sqrt{\Gamma_\gamma(Q'L')\Gamma_\gamma(QL)}}{\Gamma} \times \sum_{m_0=-j_0}^{j_0} \frac{C(j_0L'j_1;m_0M)C(j_0Lj_1;m_0M)}{x(m_0M)-\mathrm{i}}.$$

Here both (qQL) and $(q'Q'L')$ are summed over (mM1) and (eE2).

A.2.2. Isotropic limit

An important special case is the "isotropic limit" (magnetically disordered state for which the splittings are negligible compared to Γ, e.g., ^{57}Fe). In this case all amplitudes $A_l(\omega)$ in eq. (A.45) have the same resonance denominator, and f_{n} is independent of the direction of the quantization axis $\mathbf{z}_J$ which enters the expressions for $P_l(\mathbf{e}^*_{\mathrm{f}}\mathbf{k}_{\mathrm{f}};\mathbf{e}_0\mathbf{k}_0;\mathbf{z}_J)$. The calculation is simplified by averaging over all directions of $\mathbf{z}_J$. The resulting coherent elastic scattering amplitudes for E1, M1, and E2 in the isotropic limit are

$$f_{\mathrm{E1}} = \frac{\lambda C f_{\mathrm{M}}}{[x-\mathrm{i}]} \frac{2j_1+1}{4j_0+2} \frac{\Gamma_\gamma}{\Gamma} \big(\mathbf{e}^*_{\mathrm{f}} \cdot \mathbf{e}_0\big), \tag{A.47}$$

$$f_{\mathrm{M1}} = \frac{\lambda C f_{\mathrm{M}}}{[x-\mathrm{i}]} \frac{2j_1+1}{4j_0+2} \frac{\Gamma_\gamma}{\Gamma} \big(\hat{k}_{\mathrm{f}} \times \mathbf{e}^*_{\mathrm{f}}\big) \cdot \big(\hat{k}_0 \times \mathbf{e}_0\big), \tag{A.48}$$

$$f_{\mathrm{E2}} = \frac{\lambda C f_{\mathrm{M}}}{[x-\mathrm{i}]} \frac{2j_1+1}{4j_0+2} \frac{\Gamma_\gamma}{\Gamma} \big[\big(\hat{k}_{\mathrm{f}} \cdot \hat{k}_0\big)\big(\mathbf{e}^*_{\mathrm{f}} \cdot \mathbf{e}_0\big) + \big(\hat{k}_{\mathrm{f}} \cdot \mathbf{e}_0\big)\big(\hat{k}_0 \cdot \mathbf{e}^*_{\mathrm{f}}\big)\big], \tag{A.49}$$

where $x = 2[E_1 - E_0 - \hbar\omega]/\Gamma$.

A.2.3. J_z not conserved

Here we discuss the modifications (for the fast relaxation limit) when J_z is not conserved. This can arise from crystal field effects, e.g., an EFG tensor which is not axially symmetric, or an axially symmetric EFG tensor which is not coaxial with $\mathbf{B}_{\mathrm{int}}$. It is then possible to have cross terms $M' \neq M$ in the absorption and emission matrix elements in the scattering process. (But we note again that even in the presence of crystal fields, the condition $M' = M$ will often hold, e.g., E1 or M1 transitions in a cubic symmetry field.)

The asymmetry terms will mix the states of good J_z, and the eigenstates for the level $|n, J_n\rangle$ are given by

$$|\psi_{\mathrm{n}}\rangle \equiv |n, J_n, \mu_n\rangle = \sum_{m_n} K(\mu_n, m_n)|n, J_n, m_n\rangle. \tag{A.50}$$

The index μ_n takes on the same values as m_n, and the $K(\mu_n,m_n)$ are the elements of the unitary transformation matrix which diagonalizes the interaction Hamiltonian. The (QL) multipole component of the current matrix element for emission becomes

$$\big\langle \psi_0 \big| J^{(q)\dagger}_{LM} \big| \psi_I \big\rangle = G_{LM}(\mu_0\mu_1)\sqrt{\lambda\Gamma_\gamma(QL)}, \tag{A.51}$$

where

$$G_{LM}(\mu_0\mu_1) = \sum_{m_0} K(\mu_0 m_0)^* K(\mu_n; M + m_0) C(j_0 L j_1; m_0 M). \tag{A.52}$$

The coherent elastic scattering amplitude for a pure QL resonance is then

$$f_{QL} = 4\pi\lambda \sum_{M'} \sum_{M} \left[\mathbf{e}_{\mathrm{f}}^* \cdot \mathbf{Y}^{(q)}_{LM'}(\hat{k}_{\mathrm{f}})\right] \left[\mathbf{Y}^{(q)}_{LM}(\hat{k}_0) \cdot \mathbf{e}_0\right] F^{(q)}_{LM';LM}, \tag{A.53}$$

where

$$F^{(q)}_{LM';LM} = \frac{C f_{\mathrm{M}}}{2j_0 + 1} \frac{\Gamma_\gamma}{\Gamma} \sum_{\mu_0} \sum_{\mu_1} \frac{G_{LM'}(\mu_0\mu_1) G_{LM}(\mu_0\mu_1)^*}{x(\mu_0\mu_1) - \mathrm{i}}. \tag{A.54}$$

Here $x(\mu_0\mu_1) = 2[E(j_1\mu_1) - E(j_0\mu_0) - \hbar\omega]/\Gamma$.

As a simple example we consider a $(j_0 = 1/2) \leftrightarrow (j_1 = 3/2)$ M1 transition where the effective Hamiltonian of the nucleus is given by

$$\mathcal{H} = \mathcal{H}_0 + \hat{g}\beta B J_z + \widehat{Q}\left[3J_z^2 - J^2 + \frac{1}{2}\eta\left(J_{(+)}^2 + J_{(-)}^2\right)\right]. \tag{A.55}$$

The asymmetry term, $\propto\eta(J_{(+)}^2 + J_{(-)}^2)$, mixes J_z states which differ by $\Delta J_z = \pm 2$. Thus, for the $j_0 = 1/2$ ground state, J_z is still conserved and the eigenstates are $|\alpha_0, j_0, m_0\rangle$, $m_0 = \pm 1/2$, while for the excited level, there is mixing between $m_1 = 3/2$ and $m_1 = -1/2$, and between $m_1 = 1/2$ and $m_1 = -3/2$. The resulting transformation matrix is

$$\widetilde{K}(\mu_1 m_1) = \begin{pmatrix} a_{3/2} & 0 & b_{3/2} & 0 \\ 0 & a_{1/2} & 0 & b_{1/2} \\ b_{-1/2} & 0 & a_{-1/2} & 0 \\ 0 & b_{-3/2} & 0 & a_{-3/2} \end{pmatrix}, \tag{A.56}$$

where

$$a_\lambda = \left[1 + \varepsilon_\lambda^2\right]^{-1/2}, \qquad b_\lambda = \varepsilon_\lambda a_\lambda,$$
$$\varepsilon_{\pm 3/2} = \frac{[(3Q \pm Z)^2 + 3Q^2\eta^2]^{1/2} - (3Q \pm Z)}{Q\eta\sqrt{3}}, \qquad \varepsilon_{\pm 1/2} = -\varepsilon_{\mp 3/2},$$

with $Z = g\beta B$. We note that $\varepsilon_\lambda \to 0$ as $\eta \to 0$.

Thus, the polarization for a photon emitted by the $|3/2\mu = 3/2\rangle \to |1/2, 1/2\rangle$ transition, which would be $\propto \mathbf{Y}^{(m)}_{11}(\hat{k})$ for J_z conserved, now contains an admixture of $\mathbf{Y}^{(m)}_{1-1}(\hat{k})$, i.e., the polarization is proportional to

$$C(1/2, 1, 3/2; 1/2, 1)\mathbf{Y}^{(m)}_{11}(\hat{k}) + \varepsilon_{3/2} C(1/2, 1, 3/2; 1/2, -1)\mathbf{Y}^{(m)}_{1-1}(\hat{k}).$$

For the $|3/2, \mu = 3/2\rangle \to |1/2, -1/2\rangle$ transition, which is not allowed for J_z conserved, the amplitude and polarization of the emitted photon is proportional to $[\varepsilon_{3/2} C(1/2, 1, 3/2; 1/2, -1)\mathbf{Y}^{(m)}_{1-1}(\hat{k})]$.

A.2.4. Screening effects

When a photon is emitted from a nucleus, the scattering of the photon by the surrounding electron cloud of the atom gives rise to a complex index of refraction for passage of the photon through the electron cloud. In effect, the radiation emitted by the nuclear transition induces multipole currents in the electron cloud, and the radiation emitted by these induced electronic currents interferes with the primary radiation from the nucleus.

The effect of the electronic scattering is to replace the bare nuclear current $\mathbf{j}^{fn}$ by the "screened" nuclear current $\mathbf{J}^{fn}$,

$$\mathbf{J}_{\perp}^{fn}(-\mathbf{k}) = \mathbf{j}_{\perp}^{fn}(-\mathbf{k})[1 + \delta(QL) + \mathrm{i}\xi(QL)], \tag{A.57}$$

$\mathbf{J}^{fn}$ being just the bare nuclear current multiplied by the screening factor $n(QL) = 1+\delta(QL)+\mathrm{i}\xi(QL)$. The parameter $\delta+\mathrm{i}\xi$ will be referred to as the *screening parameter*, or, alternatively, as the *interference parameter*.

The contribution $\delta(QL)$ gives the effect of the induced electronic currents which are in phase, or 180° out of phase, with the nuclear current. Typically, $\delta(QL)$ values are small ($\approx 10^{-5}$–$10^{-2} \ll 1$), and in emission give only a small correction to the nuclear radiation width, which can generally be neglected. On the other hand, the imaginary part $\mathrm{i}\xi(QL)$, although small ($\approx 10^{-3}$–10^{-1}), gives a phase shift to the emitted multipole wave which can lead to observable effects, as discussed below.

Screening also affects resonant γ-ray scattering from the nucleus, which is a combined absorption–emission process. The effect of screening again modifies the "emission current" $\mathbf{j}_{\perp}^{fn}(-\mathbf{k})$ by the factor $[1+\delta(QL)+\mathrm{i}\xi(QL)]$ as given in eq. (A.57), and similarly, the screening modifies the "absorption current" $\mathbf{j}_{\perp}^{na}(\mathbf{k}_0)$ by the same screening factor. The overall effect of the screening processes in γ-ray scattering is then to modify the nuclear scattering amplitude f_{n} by the factor $(1+\delta+\mathrm{i}\xi)^2 \approx 1 + 2\delta(QL) + \mathrm{i}2\xi(QL)$. In particular, for coherent elastic scattering by a pure QL Mössbauer transition, the modified scattering amplitude is f_{n}, as given by eq. (A.43), times the factor $1 + 2\delta(QL) + \mathrm{i}2\xi(QL)$.

The total cross-section for resonant scattering and absorption is then given by the optical theorem, $\sigma_n = (4\pi\lambda)\Im[f_{\mathrm{n}}(\mathbf{k}_0, \mathbf{e}_0; \mathbf{k}_0, \mathbf{e}_0)]$. For each $(m_0 M)$ resonance, $\Im[(1+\mathrm{i}2\xi)/(x(m_0M)-\mathrm{i})] = (1+2\xi x)/(1+x^2)$. In the limit of no hyperfine splitting, the resonant cross-section becomes

$$\sigma_n = \sigma_0 \frac{1 + 2\xi x}{x^2 + 1}, \tag{A.58}$$

where σ_0 is the total cross-section at exact resonance.

Thus the screening gives a small dispersion term $[2\xi x/(x^2+1)]\sigma_0$ to the total cross-section. The effect of this contribution is to give a small asymmetry to the Mössbauer absorption spectrum, and to shift the minimum of the spectrum from $x = 0$ to $x \approx \xi$. Although the screening effect is small, the induced dispersion can be important in isotope shift measurements.

For absorption experiments, the imaginary part of the screening parameter, $\xi(QL)$, which gives the dispersion term, arises from the interference between coherent competing processes, and for this reason we refer to ξ as the interference parameter.

The dominant contribution to ξ arises from the interference between nonresonant photoelectric absorption and resonant absorption followed by internal conversion. Since both processes have the same initial and final states (assuming no nuclear spin flip), they are coherent and, hence, interfere. This contribution to $\xi(QL)$ we call *conversion screening*.

A second contribution to ξ arises from the interference between resonant scattering from the nucleus and nonresonant scattering from the atomic electrons. We refer to this contribution as *Rayleigh screening*. In most cases the primary contribution to ξ is from conversion screening, but in a few isolated cases Rayleigh screening is dominant.

The magnitude of the screening effect is dependent on the multipolarity of the Mössbauer transition, but not as strongly as one might expect. In the case of Rayleigh screening the strongest effect occurs if the Mössbauer transition is E1. This is because the scattering from the atomic electrons is dominantly E1, so if the resonant transition is M1 or higher, the final photon states are almost orthogonal, i.e., $\int f_{\mathrm{n}}^{*} f_{\mathrm{e}}\, \mathrm{d}\Omega \approx 0$, and it is only the small admixture of higher multipole orders in the Rayleigh scattering which lead to a nonzero Rayleigh screening contribution ξ_{R}.

In the case of conversion screening we might expect a similar result since photoelectric absorption is also primarily E1. However, this conclusion is not correct, and in particular, the screening parameters ξ for E2 transitions are often larger than those for E1 transitions. This occurs because for a QL multipole nuclear transition, the interference parameter $\xi(QL)$ is proportional to $\sqrt{\sigma_{\mathrm{pe}}(QL)\sigma_{\mathrm{ic}}(QL)}$, where $\sigma_{\mathrm{pe}}(QL)$ is the QL multipole contribution to the photoelectric absorption cross-section, and $\sigma_{\mathrm{ic}}(QL)$ is the cross-section for internal conversion–absorption at resonance. For an E2 transition, the photoelectric partial cross-section σ_{pe}(E2) is much less than the E1 contribution, i.e., $\sigma_{\mathrm{pe}}(\mathrm{E2}) \ll \sigma_{\mathrm{pe}}(\mathrm{E1})$, but, on the other hand, internal conversion is much stronger for an E2 transition than for a corresponding E1 transition, so that $\sigma_{\mathrm{ic}}(\mathrm{E2}) \gg \sigma_{\mathrm{ic}}(\mathrm{E1})$. This amplification of the internal conversion cross-section just offsets the reduction of the photoelectric partial cross-section, so that generally $\xi(\mathrm{E2}) \sim \xi(\mathrm{E1})$.

Various aspects of this problem are treated in [2,120–122], and extensive calculations of the screening parameters are given by Goldwire [123].

A.2.5. Relaxation effects

Up to now, we have assumed the "fast relaxation limit", which is the usual situation, in which the atomic relaxation processes are very fast relative to the lifetime of the excited Mössbauer state and to the nuclear Larmor precession period, τ_{L}. In this limit, we can take ψ and E in eq. (A.39) as the state and energy of the nucleus i in the external fields and the "static effective fields" of the surrounding medium.

If the relaxation times are on the order of τ_{L}, then it is convenient to write (A.39) in the form

$$f_{\mathrm{n}} = \mathrm{i}\int_0^\infty \mathrm{d}t \mathrm{e}^{\mathrm{i}(\omega + i\Gamma/2\hbar)t} \times \left\langle \langle \chi_0\phi_0 | \mathrm{e}^{-\mathrm{i}\mathbf{k}_{\mathrm{f}}\cdot\mathbf{r}(t)} G_0^\dagger(t)\mathbf{e}_{\mathrm{f}}^* \cdot \mathbf{J}(-\mathbf{k}_{\mathrm{f}}) G_0(t)\mathbf{J}(\mathbf{k}_0)\cdot\mathbf{e}_0 \mathrm{e}^{\mathrm{i}\mathbf{k}_0\cdot\mathbf{r}(0)} | \chi_0\phi_0\rangle \right\rangle, \quad \text{(A.59)}$$

where $G_0(t) = \exp(-\mathrm{i}H_0 t)$. Here we are concerned only with coherent elastic scattering, and the brackets $\langle\ \rangle$ indicate that the ensemble average is to be taken. To calculate the resonance response of the scattering operator, it is necessary to calculate the current–current correlation function.

Equation (A.59) is directly analogous to the correlation formulations for Mössbauer absorption or emission spectra in the presence of relaxation, such as developed by Afanas'ev and Kagan [124,125], Bradford and Marshall [126], and Blume and Tjon [127,128], and the same methods for solving for the correlation function can be applied here.

Just as in the absorption and emission cases, the resonance response of f_{n} is only a simple Breit–Wigner response in the fast relaxation limit. When the relaxation time is on the order of τ_{L}, the resonances can be shifted or split, the effective widths can be broadened or narrowed, and lines corresponding to normally forbidden transitions can be obtained.

References

[1] G.T. Trammell, Phys. Rev. 126 (1962) 1045.
[2] J.P. Hannon and G.T. Trammell, Phys. Rev. 186 (1969) 306.
[3] J.P. Hannon, G.T. Trammell, M. Blume and D. Gibbs, Phys. Rev. Lett. 61 (1988) 1245.
[4] M. Hamrick, MA thesis, Rice University (1991); Ph.D. thesis, Rice University (1994).
[5] J. Luo, Ph.D. thesis, Rice University (1994).
[6] J. Luo, G.T. Trammell and J.P. Hannon, Phys. Rev. Lett. 71 (1993) 287.
[7] M. Blume, in: *Resonant Anomalous X-Ray Scattering*, eds. G. Materlik, C.J. Sparks and K. Fischer (North-Holland, Amsterdam, 1994) p. 495.
[8] V.B. Berestetskii, E.M. Lifshitz and L.P. Pitaevskii, *Relativistic Quantum Theory* (Addison-Wesley, Reading, MA, 1971).
[9] R.P. Feynman, *Quantum Electrodynamics* (Benjamin, New York, 1962).
[10] J.P. Hannon and G.T. Trammell, Phys. Rev. 169 (1968) 315.
[11] G.T. Trammell, in: *Chemical Effects of Nuclear Transformations, Proc. of the IAEA Symposium on the Chemical Effects of Nuclear Transformations*, Prague (October, 1960), Vol. I (International Atomic Energy Agency, Vienna, 1961) p. 75.
[12] J.P. Hannon, N.J. Carron and G.T. Trammell, Phys. Rev. B 9 (1974) 2791.
[13] J.P. Hannon, N.J. Carron and G.T. Trammell, Phys. Rev. B 9 (1974) 2810.
[14] A.M. Afanas'ev and Yu.M. Kagan, Zh. Eksper. Teoret. Fiz. 48 (1965) 327 (JETP 21 (1965) 215).
[15] Yu.M. Kagan, A.M. Afanas'ev and I.P. Perstnev, Zh. Eksper. Teoret. Fiz. 54 (1968) 1539 (JETP 27 (1968) 819).
[16] P.A. Alexandrov and Yu. Kagan, Zh. Eksper. Teoret. Fiz. 59 (1970) 1733 (JETP 32 (1971) 942).
[17] J.T. Hutton, J.P. Hannon and G.T. Trammell, Phys. Rev. A 37 (1988) 4269.

[18] R.W. James, *The Optical Principles of Diffraction of X-Rays* (Bell, London, 1948) pp. 52–90, 413–436.
[19] M. Blume and O.C. Kistner, Phys. Rev. 171 (1968) 417.
[20] R.M. Housley, R.W. Grant and V. Gonser, Phys. Rev. 178 (1969) 514.
[21] R.H. Dicke, Phys. Rev. 93 (1954) 99; and in: *Quantum Electronics*, Vol. I, eds. P. Grivet and N. Bloembergen (Columbia Univ. Press, New York, 1964) p. 35.
[22] C. Muzikar, JETP 14 (1962) 833.
[23] M.I. Podgoretskii and I.I. Raizen, JETP 12 (1961) 1023.
[24] D.F. Zaretskii and V.V. Lomonosov, JETP 21 (1965) 243.
[25] A.M. Afanas'ev and Yu.M. Kagan, Zh. Eksper. Teoret. Fiz. Pis. Red. 2 (1965) 130 (JETP Lett. 2 (1965) 81).
[26] G.T. Trammell and J.P. Hannon, Phys. Rev. B 18 (1978) 165; and Phys. Rev. B 19 (1979) 3835.
[27] J.P. Hannon and G.T. Trammell, in: *Resonant Anomalous X-Ray Scattering*, eds. G. Materlik, C.J. Sparks and K. Fischer (North-Holland, Amsterdam, 1994) p. 565.
[28] J.P. Hannon and G.T. Trammell, Physica B 159 (1989) 161.
[29] J.P. Hannon, N. Hung, G.T. Trammell, E. Gerdau, M. Mueller, R. Rüffer and H. Winkler, Phys. Rev. B 32 (1985) 5068 and 5081.
[30] R. Röhlsberger, this issue, sections III-1.4 and IV-1.3.
[31] A.I. Chumakov et al., this issue, section IV-1.2.
[32] J.P. Hannon, G.T. Trammell, M. Mueller, E. Gerdau, R. Rüffer and H. Winkler, Phys. Rev. B 32 (1985) 6363 and 6374.
[33] J.P. Hannon, G.T. Trammell, M. Mueller, E. Gerdau, H. Winkler and R. Rüffer, Phys. Rev. Lett. 43 (1979) 636.
[34] Yu. Kagan and A.M. Afanas'ev, Z. Naturforsch. 28a (1973) 1351.
[35] A.M. Afanas'ev and Yu. Kagan, JETP 37 (1973) 987.
[36] V.G. Kohn, JETP 78 (1994) 357.
[37] T. Joko and A. Fukuhara, J. Phys. Soc. Japan. 22 (1967) 597.
[38] A.M. Afanas'ev and V. Kohn, Acta Crystallogr. A 33 (1977) 178.
[39] J.P. Hannon and G.T. Trammell, in: *Mössbauer Effect Methodology*, Vol. 8, ed. I.J. Gruverman (Plenum, New York, 1973) p. 25.
[40] Yu. Kagan, Soviet. Phys. JETP Lett. 20 (1974) 11.
[41] J.P. Hannon and G.T. Trammell, Optics Commun. 15 (1975) 330.
[42] G.C. Baldwin, M.S. Field, J.P. Hannon, J.T. Hutton and G.T. Trammell, J. Phys. (Paris) Colloq. 47 (1986) C10-299.
[43] G.C. Baldwin, J.C. Solem and V.I. Gol'danskii, Rev. Mod. Phys. 53 (1981) 687;
G.C. Baldwin and R.V. Khokhlov, Physics Today (February, 1975) 32;
G.C. Baldwin and J.C. Solem, Rev. Mod. Phys. 69 (1997) 1085.
[44] G.T. Trammell and J.P. Hannon, Optics Commun. 15 (1975) 325.
[45] G.T. Trammell, J.T. Hutton and J.P. Hannon, J. Quant. Spectrosc. Radiat. Transfer 40 (1998) 693.
[46] A.L. Schallow and C.H. Townes, Phys. Rev. 112 (1958) 1940.
[47] W.E. Lamb, Jr., Phys. Rev. A 134 (1964) 1429.
[48] J.T. Hutton, J.P. Hannon and G.T. Trammell, Phys. Rev. A 37 (1988) 4280.
[49] J.P. Hannon and G.T. Trammell, in: *Mössbauer Effect Methodology*, Vol. 8, ed. I. Gruverman (Plenum, New York, 1973) p. 25.
[50] J.P. Hannon and G.T. Trammell, in: *Mössbauer Effect Methodology*, Vol. 9, ed. I. Gruverman (Plenum, New York, 1973) p. 181.
[51] J.T. Hutton, G.T. Trammell and J.P. Hannon, Phys. Rev. B 31 (1985) 6420.
[52] J.T. Hutton, G.T. Trammell and J.P. Hannon, Phys. Rev. B 31 (1985) 743.
[53] M. von Laue, *Röntgenstrahleninterferenzen* (Academische Verlagsgesellschaft, Frankfurt am Main, 1960) p. 430.

[54] L.D. Landau and E.M. Lifshitz, *Electrodynamics of Continuous Media* (Addison-Wesley, Reading, MA, 1960) p. 288.
[55] R. Tixier and C. Wache, J. Appl. Cryst. 3 (1970) 466.
[56] D.M. Blow and F.H.C. Crick, Acta Cryst. 12 (1959) 794.
[57] T.L. Blondell and L.N. Johnson, *Protein Crystallography* (Academic Press, New York, 1976).
[58] G. Wendin, Phys. Scripta 21 (1980) 535.
[59] J.P. Hannon and G.T. Trammell, in: *Mössbauer Effect Methodology*, Vol. 9, ed. I.J. Gruverman (Plenum, New York, 1973) p. 181.
[60] J.T. Hutton, G.T. Trammell and J.P. Hannon. Phys. Rev. B 31 (1985) 743.
[61] M. Tegze and G. Faigel, Europhys. Lett. 16 (1991) 41.
[62] A. Szöke, in: *Short Wavelength Coherent Radiation: Generation and Applications*, eds. D.T. Attwood and J. Bokker, AIP Conf. Proc. 147 (American Institute of Physics, New York, 1986).
[63] J.J. Barton, Phys. Rev. Lett. 61 (1988) 1356.
[64] E.M.E. Timmermans, G.T. Trammell and J.P. Hannon, J. Appl. Phys. 73 (1993) 6183.
[65] E.M.E. Timmermans, G.T. Trammell and J.P. Hannon, Phys. Rev. Let. 72 (1994) 832.
[66] E.M.E. Timmermans, G.T. Trammell and J.P. Hannon, Phys. Rev. B 58 (1998) 5637.
[67] J.T. Hutton, G.T. Trammell and J.P. Hannon, Phys. Rev. B 31 (1985) 6420.
[68] Th. Gog, D. Novikov, J. Falta, A. Hille and G. Materlik, J. Physique IV (1994) C9-449.
[69] M. Tegze and G. Faigel, Nature 380 (1996) 49.
[70] T. Gog, P.M. Len, G. Materlik, D. Bahr, C.S. Fadley and C. Sanchez-Hanke, Phys. Rev. Lett. 76 (1996) 3132.
[71] S.L. Ruby, J. Phys. (Paris) C 6 (1974) 209.
[72] R.L. Mössbauer, in: *Anomalous Scattering*, eds. S. Ramaseshan and S.C. Abrahams (Munksgaard, Copenhagen, 1975) p. 463.
[73] E. Gerdau, R. Rüffer, H. Winkler, W. Tolksdorf, C.P. Klages and J.P. Hannon, Phys. Rev. Lett. 54 (1985) 835.
[74] E. Gerdau and U. van Bürck, in: *Resonant Anomalous X-Ray Scattering*, eds. G. Materlik, C.J. Sparks and K. Fischer (North-Holland, Amsterdam, 1994) p. 589;
G.V. Smirnov and A.I. Chumakov, ibid. p. 609;
U. van Bürck and G.V. Smirnov, Hyp. Interact. 27 (1986) 219.
[75] G. Faigel, D.P. Siddons, J.B. Hastings, P.E. Haustein, J.R. Grover, J.P. Remeika and A.S. Cooper, Phys. Rev. Lett. 58 (1987) 2699.
[76] E. Burkel, *Inelastic Scattering of X-rays with Very High Energy Resolution* (Springer, New York, 1991).
[77] W. Sturhahn, T.S. Toellner, E.E. Alp, X. Zhang, M. Ando, Y. Yoda, S. Kikuta, M. Seto, C.W. Kimball and B. Dabrowski, Phys. Rev. Lett. 74 (1995) 3832.
[78] A.I. Chumakov and R. Rüffer, Hyp. Interact. 113 (1998) 59.
[79] U. Bonse and M. Hart, Z. Phys. 1941 (1966) 1; Physics Today (August 1970) 26.
[80] U. Bonse and G. Materlik, Z. Physik 253 (1972) 232.
[81] Y.V. Shvyd'ko, E. Gerdau, J. Jäschke, O. Leupold, M. Lucht and H.D. Rüter, Phys. Rev. B 57 (1998) 3552.
[82] G.T. Trammell, invited talk at *The Internat. Conf. on Applications of the Mössbauer Effect (ICAME '89)*, Budapest (unpublished).
[83] P.J. Black, Nature 206 (1965) 1223.
[84] F. Parak, R.L. Mössbauer, V. Biebel, H. Formanek and W. Hoppe, Z. Phys. 244 (1971) 456.
[85] J.B. Hastings, D.P. Siddons, U. van Bürck, R. Hollatz and U. Bergmann, Phys. Rev. Lett. 66 (1991) 770.
[86] Yu.M. Kagan, A.M. Afanas'ev and V.G. Kohn, Phys. Lett. A 68 (1978) 339; J. Phys. C 12 (1979) 615.

[87] G.T. Trammell and J.P. Hannon, Phys. Rev. Lett. 61 (1988) 653.
[88] J.J. Sakurai, *Advanced Quantum Mechanics* (Addison-Wesley, Reading, MA, 1973) p. 56.
[89] U. van Bürck, D.P. Siddons, J.B. Hastings, U. Bergmann and R. Hollatz, Phys. Rev. B 46 (1992) 6207.
[90] U. van Bürck, R.L. Mössbauer, E. Gerdau, R. Rüffer, R. Hollatz, G.V. Smirnov and J.P. Hannon, Phys. Rev. Lett. 59 (1987) 355.
[91] E. Gerdau, R. Rüffer, R. Hollatz and J.P. Hannon, Phys. Rev. Lett. 57 (1986) 1141; and 58 (1987) 2359.
[92] Yu. Kagan, Soviet Phys. JETP Lett. 20 (1974) 11.
[93] G.T. Trammell and J.P. Hannon, Optics Commun. 15 (1975) 330.
[94] G.T. Trammell, J.T. Hutton and J.P. Hannon, J. Quant. Spectrosc. Radiat. Transfer 40 (1988) 693.
[95] J.T. Hutton, J.P. Hannon and G.T. Trammell, Phys. Rev. A 37 (1988) 4280.
[96] J.P. Hannon, T.-X. Shen and G.T. Trammell, to be submitted to Phys. Rev. B.
[97] S. Kikuta, in: *Resonant Anomalous X-Ray Scattering*, eds. G. Materlik, C.J. Sparks and K. Fischer (North-Holland, Amsterdam, 1994) p. 635.
[98] G.T. Trammell, J.P. Hannon, S.L. Ruby, P. Flinn, R.L. Mössbauer and F. Parak, in: *Workshop on New Directions in Mössbauer Spectroscopy*, Argonne (1977), AIP Conf. Proc., No. 38, ed. G.J. Perlow (AIP, New York, 1978) p. 46.
[99] G.V. Smirnov, V.V. Sklyarevskii, R.A. Voskanyan and A.N. Artem'ev, Zh. Eksper. Teoret. Fiz. Pis'ma Red. 9 (1969) 123 (JETP Lett. 9 (1969) 70).
[100] V.A. Belyakov and Ya.N. Aivazian, Zh. Eksper. Teoret. Fiz. 56 (1969) 346 (JETP 29 (1969) 191); Phys. Rev. B 1 (1970) 1903.
[101] U. van Bürck, G.V. Smirnov, R.L. Mössbauer, H.J. Maurus and N.A. Semioschkina, J. Phys. C 13 (1980) 4511.
[102] H. Winkler, R. Eisberg, E. Alp, R. Rüffer, E. Gerdau, S. Lauer, A.X. Trautwein, M. Grodzicki and A. Vera, Z. Phys. B 49 (1983) 331.
[103] R.M. Mirzababaev, G.V. Smirnov, V.V. Sklyarevskii, A.N. Artem'ev, A.N. Izrailenko and A.V. Bobkov, Phys. Lett. A 37 (1971) 441.
[104] P.J. Black and J.P. Duerdoth, Proc. Phys. Soc. London 84 (1964) 169.
[105] G.T. Trammell, in: *Condensed Matter Research Using Neutrons Today and Tomorrow*, NATO ASI Series, Vol. 112, eds. S.W. Lovesey and R. Scherm (Plenum Press, New York, 1984) p. 277.
[106] R.E. Word and G.T. Trammell, Phys. Rev. B 24 (1981) 2430.
[107] Yu. Kagan and A.M. Afanas'ev, JETP 22 (1966) 1032.
[108] J.R. Breedlove and G.T. Trammell, Science 170 (1970) 1310.
[109] S.W. Lovesey, *Theory of Neutron Scattering from Condensed Matter* (Clarendon, Oxford, 1984).
[110] A.L. Patterson, Phys. Rev. 46 (1934) 372.
[111] F. Lu, Ph.D. thesis, Rice University (1989).
[112] T.-X. Shen, MA thesis, Rice University (1991).
[113] X. Hu, MA thesis, Rice University (1993).
[114] J.B. Hastings, D.P. Siddons and M. Lehman, Phys. Rev. Lett. 64 (1990) 2030.
[115] J.P. Hannon, MA thesis, Rice University (1965).
[116] D. Gibbs, D.R. Harshman, E.D. Isaacs, D.B. McWhan, D. Mills and C. Vettier, Phys. Rev. Lett. 61 (1988) 1241.
[117] M.E. Rose, *Elementary Theory of Angular Momentum* (Wiley, New York, 1957) p. 32.
[118] X. Hu, Ph.D. thesis, Rice University (1997).
[119] S.P. Lloyd, Phys. Rev. 83 (1951) 716.
[120] J.P. Hannon and G.T. Trammell, Phys. Rev. Lett. 21 (1968) 726.
[121] G.T. Trammell and J.P. Hannon, Phys. Rev. 180 (1968) 337.
[122] Yu.M. Kagan, A.M. Afanas'ev and V.V. Voitovetskii, JETP Lett. 9 (1969) 91.
[123] H.C. Goldwire, Jr., and J.P. Hannon, Phys. Rev. B 16 (1977) 1875.

[124] A.M. Afanas'ev and Yu. Kagan, JETP Lett. 18 (1964) 1139.
[125] A.M. Afanas'ev and Yu. Kagan, JETP Lett. 20 (1965) 743.
[126] E. Bradford and W. Marshall, Proc. Phys. Soc. London 87 (1966) 731.
[127] M. Blume and J.A. Tjon, Phys. Rev. 165 (1968) 446.
[128] M. Blume, Phys. Rev. 174 (1968) 351.